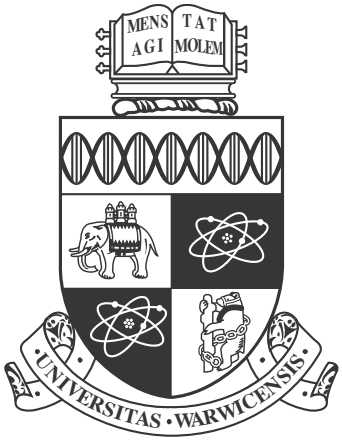

Molecular Simulation of Ice Growth Inhibition by Biomimetic Antifreeze Macromolecules

by

Alaina Emanuella O. Emmanuel

Thesis

Submitted to the University of Warwick

for the degree of

Doctor of Philosophy

Chemistry

December 2015

THE UNIVERSITY OF
WARWICK

Contents

List of Tables

List of Figures

Acknowledgments

Firstly, I would like to express my sincere gratitude to my supervisors Dr. Rebecca Notman and Dr. Matthew I. Gibson for their tremendous support during my Ph.D, their patience and immense knowledge. Thank you for the opportunity to join your groups and it has been a privilege getting to know you both and to learn from you. I could not have imagined having better advisers for my Ph.D study.

A special thank you to the members of my advisory panel, Dr. Rachel O'Reilley and Prof. Mark Rodger for their insightful comments and for the hard questions. My sincere thanks also goes to our collaborators, Dr. Thomas Congdon, for his expertise and experiments, and Dr. David Quigley for making the lattice structures available. I would also like to thank Dr. Scott Habershon and Prof. David R. Nutt who graciously agreed to my examiners and for their invaluable feedback towards the final stages of my degree. Additionally, I would like to thank the Leverhulme Trust for funding this research, the contributions from the Centre for Scientific Computing and the facilities provided by the MidPlus Centre of Excellence and the University of Warwick.

I would also like to thank my friends and the Notman group for the stimulating discussions, the company whilst working, and for all the fun we have had in the last four years: Kara Lin, Lewis Egan, Mary Kyobula, Kasra Razmkhah, Bola Ola, Amanda Vuong, David O'Neill and everyone in Lab 3.

Last but not the least, I would like to thank my family, including Dr. Clementina Emmanuel, Dr. and Mrs Jude Adeghe, Prof. Pandi Kubeyinje, Dr. Temisan Ige, Mrs. Ivie Okoro, Prof. Omare Otote and Grandma Yemi. Thank you for your unconditional love, prayers and support.

Declarations

I confirm that my thesis has been prepared in accordance with the University's guidelines on the presentation of a research thesis. This thesis is submitted to the University of Warwick in support of my application for the degree of Doctor of Philosophy. It has been composed by myself, except where acknowledged in the text, and has not been submitted in any previous application for any degree.

Abstract

Many polar fishes, insects and plants have evolved to produce biological antifreezes known as antifreeze proteins and glycoproteins (AF(G)Ps). These proteins reduce the size of ice crystals, thereby mitigating the structural damage that ice crystals cause to their cells.

Recent experimental work has shown that synthetic polymers, namely poly(vinyl alcohol) (PVA) and poly(hydroxyproline) (PHYP) can also reproduce some of the properties of native AF(G)Ps. This has enormous potential for use in cryobiological storage, such as the cryopreservation of organs in medicine and food preservation, because synthetic polymers are highly tunable and scalable. As a results, they can be tailored to create ideal antifreeze polymer, with high availability.

Unfortunately the mechanism by which AFGPs and their synthetic mimics function remains a mystery. The ability to understand how these proteins and their synthetics mimic work will aid the rational design of an ideal synthetic antifreeze polymer.

In this thesis, we use a computational technique known as molecular dynamics simulation to investigate the molecular mechanism of action for antifreeze active (PVA and HYP) and inactive polymers (poly(ethylene glycol)) at the ice/water interface.

The main results from this study are that the all the polymers decrease the growth velocity of ice. They achieve this by disrupting the rate of water addition to the ice crystals and can arrest ice growth through temporary immobilization onto the ice lattice. The emerging difference between IRI active and inactive polymers lies in the polymers' abilities to pause the crystallization process during their immobilization. Overall, the results from this study lead us to conclude that PVA and PHYP function

in very different ways and that neither of the antifreeze active polymers function *via* a pre-ordering mechanism because none of the polymers increase the orientational order of water vicinal molecules.

Abbreviations

AF(G)P	Antifreeze proteins and glycoproteins
AFG	Antifreeze glycoproteins
AFP	Antifreeze proteins
AMBER	Assisted Model Building with Energy Refinement
ASASA	Apolar or hydrophobic solvent accessible surface area
BA	Biological antifreeze
BAR	Bennett Acceptance Ratio
CHARMM	Chemistry at HARvard Macromolecular Mechanics
DIS	Dynamic ice shaping
DMSO	Dimethyl sullfoxide
EXP	Exponential Averaging
FF	forcefield
GROMACS	GROningen MAchine for Chemical Simulations
GTE	Gibbs-Thomson effect
H-Bond	Hydrogen bonds
H-Bonding	Hydrogen bonding
HBN	Hydrogen bond network
HYP	Hydroxyproline
$\mathbf{I}_c$	Cubic ice

I_h	Hexagonal ice
IBS	Ice binding site
IRI	Ice recrystallisation inhibition
LJ	Lennard jones
MC	Monte Carlo
MD	Molecular dynamics
MLGS	Mean largest grain size
N_H	Number of hydrogen bonds
NPH	Isoenthalpic-isobaric ensemble
NPT	Isobaric-isothermal ensemble
NVE	Microcanonical ensemble
NVT	Canonical ensemble
OPLS	Optimized potential for liquid simulations
PDB	Protein data bank
PEG	Poly(ethylene glycol)
PEO	Poly(ethylene oxide)
PHYP	Poly(hydroxyproline)
PME	Particle mesh ewald
PPI	Poly(proline) type one
PPII	Poly(proline) type two
PSASA	Polar or hydrophilic solvent accessible surface area
PVA	Poly(vinyl alcohol)
PVC	Poly(vinyl chloride)
PVP	Poly(vinyl pyrrolidone)
Q_4	Tetrahedral order parameter (using four closest neighbours)

QLL Quasi-liquid layer

R_g Radius of gyration

RDF Radial distribution function

RMSD Root-mean-square deviation

RMSF Root-mean-square fluctuation

SASA Solvent accessible surface area

sfAFP Snowflea antifreeze protein

SPME Smooth particle mesh ewald

Stdev Standard deviation

T_g Glass transition temperature

TI Thermodynamic Integration

T_m Melting tempertaure

TH Thermal hysteresis

TH_m Melting thermal hysteresis

tmAFP Tenebrio molitor antifreeze protein

TSASA Total solvent accessible surface area

wfAFP Winter flounder antifreeze protein

Chapter 1

Introduction

1.1 Statement of the Problem

The growth of ice crystals within tissues is a serious threat to the cryo-preservation of organs, food and crops in cold climates. They cause mechanical damage, dehydrate the cells and even create pockets of high salinity which disrupt the normal function of the tissue. In the UK alone, the waiting list for organ transplantation currently exceeds 7,000[20], therefore creating a huge emphasis on protecting the limited organs available. Inspired by antifreeze proteins and glycoproteins (AF(G)Ps)– proteins which permit the survival of organisms in sub-freezing climates – researchers are now seeking better and cheaper synthetic methods of preventing the growth of ice crystals or reducing them to manageable sizes.

Our collaborators recently demonstrated the remarkable ability of low concentrations of poly(vinyl alcohol) (PVA) to preserve mammalian red blood cells after freeze-thawing.[21] Unfortunately however the molecular mechanisms of the antifreeze actions of PVA remain unknown. Molecular dynamics (MD) simulations, provides atomistic resolution which is not accessible to experiments such as the "splat" assays[22]. It is a powerful tool, which can give important insights into the polymer-mediated inhibition of the ice growth, because it directly examines the interactions of antifreeze macromolecules with ice. By using MD computer simulations we can begin to address this challenge by correlating the structural properties of this polymer with different antifreeze characteristics *e.g.* thermal hysteresis, dynamic ice shaping or reduced ice recrystallization, and facilitate the design of new, improved antifreeze polymers for specific control over crystal size and morphology.

Our simulations have focused on three polymers; PVA, poly(ethylene glycol) (PEG) and poly(hydroxyproline) (PHYP) in solution, and at the ice/water inter-

face using the TIP4P/Ice water model. Our initial work has focused on PVA and its antifreeze inactive isomer, PEG, so we have simulated various chain lengths of each polymer in solution and at the ice/water interface.

One hypothesis for the mechanism of action is that the antifreeze molecules structure liquid water in either:

1. an ice-like configuration, which could promote binding to a growing ice crystal,
2. or in a disordered configuration that could inhibit ice crystal growth.

Our simulations indicate that PVA does not have significant ordering or disordering effect on surrounding water molecules in solution. In stark contrast, PHYP dramatically reduces the tetrahedral order of nearby water molecules by up to 25% in solution. This suggests that the two antifreeze active polymers function in different ways.

Slowed growth of the ice crystals was observed at the ice/water interface for all polymers because their presence slowed the rate of water addition to the growing ice crystal. We find that the growth of ice is also completely arrested by the polymers for short periods of time, owing to the temporary immobilization of the polymers at the ice/water interface. The greatest effect is seen in the antifreeze active polymers, which present hydroxyl groups with a close spatial match to the oxygen atoms on the prism plane. For instance, the O-O separation of PVA in solution is 0.46 nm (compared to 0.31 nm and 0.39 nm in PEG). This suggests that the lattice matching provides an important role in the antifreeze mechanism of PVA and PHYP.

Compared to the 40 year *in situ* and *in silico* studies into the antifreeze activities of AF(G)Ps, MD simulation studies of ice nucleation and growth in the presence of synthetic antifreeze biomimics are still in their infancy. This study forms an important contribution to this relatively new branch of *in silico* studies. To the best of our knowledge, we present the first simulations of long synthetic antifreeze polymers, PVA, PEG and PHYP at the ice/water interface. Our results provide new insights into the atomistic mechanism of ice growth inhibition of PVA and PHYP and therefore presents a novel contribution to the growing antifreeze community.

1.2 Background

1.2.1 Ice structure, crystallization and growth

The most common ice form on Earth is hexagonal ice (I_h), which is stable at 73–273 K and 1 atm, meaning that this isoform of ice is readily available in nature.

Although eighteen other crystalline phases exist depending on the temperature and pressure, I_h can be distinguished by its hexagonal symmetry. It possesses a regular structure of water molecules where a single oxygen atom is bonded to four hydrogen atoms; two of which are covalent bonds and the others are weaker hydrogen bonds. Consequently, four equidistant water molecules surround each water molecule and so the ice lattice structure is held firmly in place.

Many of the physical processes and interactions we observe in both water and ice are predominantly due to the extensive hydrogen bonding network (HBN) and their bond angles. For instance, the characteristic trait that ice — with a density of $0.9164\,\mathrm{g\,cm^3}$ — is less dense than liquid water ($0.9998\,\mathrm{g\,cm^3}$) at $273.15\,\mathrm{K}$.[23] In fact it is well known that near tetrahedral arrangements of water molecules permeate through the ordered ice lattice, with typical bond angle closer to 109.5°, whereas those found in liquid water are normally slightly smaller (<104.5°).[24,25]

Although water and ice are ubiquitous in nature, a substantial amount of research is still needed for us to fully understand the solid and liquid phases, and various transition states between them, particularly about the quasi liquid layer (QLL) – a state approx. 0.10–0.15 nm[26] thick that lies between liquid and solid forms of ice.

Crystallization of liquid water to ice is a two-step process composed of nucleation and ice crystal growth. Nucleation is described as the first step in the formation of a new phase, where small, stable clusters of ice-like water molecules are formed within a parent phase, like a body of liquid water.[27] The sizes of these clusters fluctuate; some grow, whilst others completely melt away. Once a cluster reaches a critical size, the embryo will continue to grow into a crystal, which in turn facilitates the growth of a new phase.

The classical nucleation theory is conventionally used to describe this whole process in terms of free energy.[28] Water molecules at the surface of the crystal have fewer neighbours and are not able to form the optimum number of hydrogen bonds (H-bonds) so they experience a higher free energy than molecules within the crystal.[6] As the cluster grows, the surface-area-to-volume ratio increases and molecules that populate the surface are less well bound to their neighbours than those in the bulk. This causes the nucleus to be unstable, as a result, water molecules migrate back into the QLL and initial liquid phase. Beyond a critical size, a smaller surface-area-to-volume ratio occurs and the initial energy cost of maintaining a growing solid/liquid interface no longer outweighs the benefits of crystal growth. In fact, the old phase becomes increasingly metastable and a small fluctuation in density or another external property can spur the sudden growth of the new phase.[27]

Under laboratory conditions, pure water can withstand supercooling up to 236 K before ice is spontaneously formed. In this instance nucleation is described as homogeneous and is unlikely to occur for two reasons. Firstly, the probability of nucleation is hampered by the free energy penalty for creating an interface. Secondly, water in most conditions contains small particles in them that act as seeds, templates or platforms for ice crystal nucleation, and so decrease the interfacial energy.

This type of nucleation is more likely to happen and is known as heterogeneous nucleation. Depending on the particle's resemblance to the molecular structure and orientation of ice, they allow water molecules to become quickly oriented, similar to an ice nucleus.[29,30] Therefore these particles can actually be used to facilitate crystal growth and exert greater control over the rate of nucleation.[27] It is thought organisms also attempt to alter or manage ice crystal growth within their systems using this same approach, which we discuss later in greater detail.

Hexagonal ice (Fig. 1.1) has three different faces: the secondary prism plane $(11\bar{2}0)$, which is the fastest to grow and also the most stable[31], the prism plane $(10\bar{1}0)$, and finally the basal plane (0001), which grows in the direction of the c-axis.

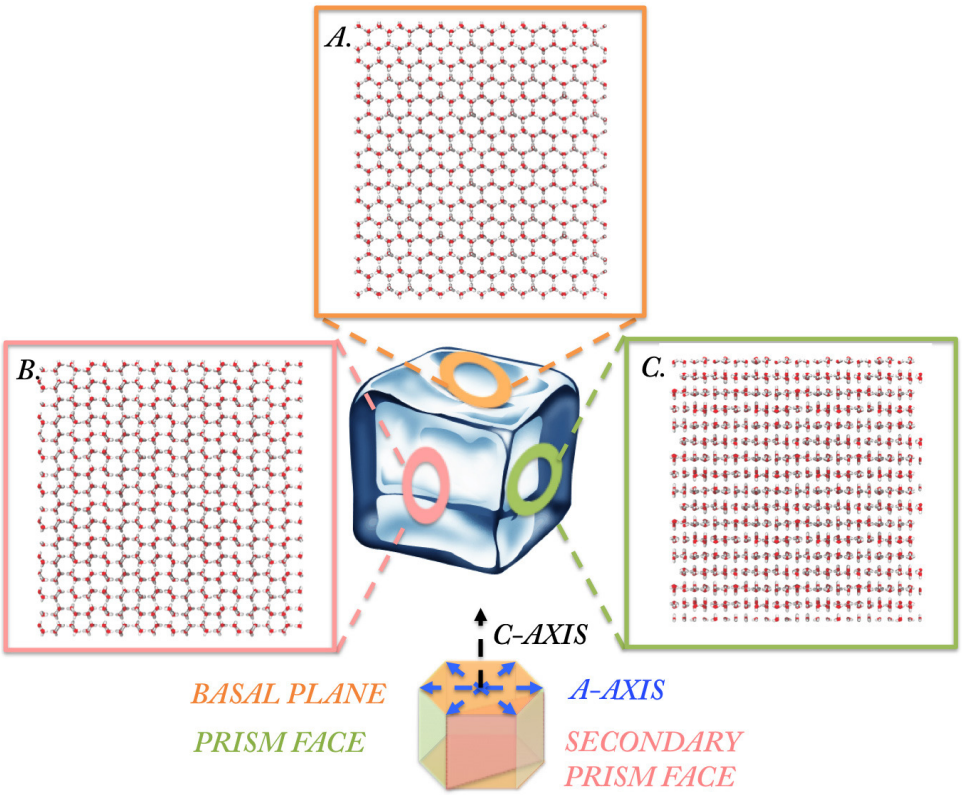

Figure 1.1: Three types of faces on the I_h crystal. A. basal plane, B. secondary prism plane and C. prism face.

In this thesis we will refer to heating or supercooling (ΔT) as the difference between the melting temperature of ice (T_m) and a temperature (T) of interest. *i.e.* $\Delta T = T - T_m$, where positive and negative signs will be included to indicate higher and lower temperatures respectively. Ordinarily, at slight undercooling (up to $\Delta T \approx -2$ K *i.e.* 271 K),[32] ice crystals start to grow into spherical shapes in the absence of any ice shaping additives. However, at greater undercooling ($\Delta T \approx -5$ K) anisotropic growth occurs due to increasing disparity in growth rates between the various faces of ice. For instance the secondary prism plane is known to grow much faster than the other planes and continued addition of water to the plane builds them out until it eventually grows itself out of existence. As a result the initial spherical crystals eventually turn into hexagonal prisms or columns with the smoothest, and slowest faces exposed[3,32–35]. It is important to note that crystal growth rate is restricted by the degree of supercooling because the diffusion and re-orientation of

water molecules become rate-limiting steps.

Using ellipsometry Furukawa *et al* discovered that for each of the planes or faces of ice, their crystal habit and QLL thickness were also, unsurprisingly, dependent on the temperature.[36,37] Similarly Pruppachar reported that the growth rates of basal planes on small, free-standing crystals could be described by a square dependence on supercooling between 273.15–264.15 K. *i.e.* $v(cm\,s^{-1}) = 0.035 \mid \Delta T \mid 2.2$.[38,39] More formulas for growth rates derived from various research are shown in Table 1.1. However Pruppacher's piece of work is the most frequently cited in ice growth simulation papers. In this study the maximum growth rates were observed at ∼255 K with approximately 10.5 $cm\,s^{-1}$ velocity. Unlike earlier investigations, the study encompassed a large range between 272.65–253.15 K and showed that at temperatures lower than 261.15 K (higher supercooling), the square dependence was lost and became linear. At a narrow temperature range of 264.15–261.15 K, an unusual pattern appeared: the growth rates of individual repeats became noticeably more scattered. However its worth noting that standard deviations or errors were not shown for this study.[38] Slightly faster growth rates were also determined for the prism planes under sampled temperatures, but empirical relations were not reported in many of these studies.[40]

Authors	**Plane**	**Temperature (K)**	**Rates**
Hallet[40]	B	273.15-253.15	$0.08\mid \Delta T\mid^{1.9}$
Pruppachar[38,39]	B	273.15-264.15	$0.035\mid \Delta T\mid^{2.2}$
Hillig & Turnbull[41,42]	-	-	$0.16\mid \Delta T\mid^{1.7}$
Lindenmeyer & Chalmers[43,44]	B	271.15-266.65	$0.0228\mid \Delta T\mid^{2.39}$
Tirmizi & Gill[45]	B & P	272.95-272.15	$0.0187\mid \Delta T\mid^{2.09}$

Table 1.1: Tabulated growth rates of the basal (B) and the prism (P) planes of ice on small, free-standing crystals. In each cited article, the rates are reported on a logarithmic scale.

1.2.2 Three Macroscopic Antifreeze Properties

In the last section we discussed some of the crystal growth behaviours of ice in the absence of additives. In the presence of additives, crystal ice growth behaves differently. In this section we present three macroscopic properties of antifreeze molecules, which we will later use to characterize the antifreeze behaviour of our polymers and compare to what has already been done in experiments. The three properties are ice recrystallization inhibition (IRI), thermal hysteresis (TH) and

dynamic ice shaping (DIS).

Ice recrystallization inhibition

During thawing or storage in a freezer, larger ice crystals normally grow at the expense of neighbouring smaller ones in order to reduce the interfacial energy of the system. This process is known as ice recrystallization and is often likened to a form of Ostwald ripening. Antifreeze molecules that inhibit or slow this process give rise to the term ice IRI.[3,46] This particular antifreeze property is thought to be the most useful of the three, particularly for cryopreservation, because it can potentially reduce ice crystals to manageable sizes.

Ice recrystallisation is affected by surface adsorbing polymers or proteins, which interfere with the movement of water molecules within the ice boundaries, *e.g.* ice surface modifications (*e.g.* during surface adsorption), disruption of water diffusion rates and manipulation of liquid channel thickness between the ice grains.[3,46,47] Because even non-ice-adsorbing macromolecules are sometimes able to manipulate water diffusion rates, the inclusion of small solutes like salt or sugars are often used to differentiate between adsorbing and non-adsorbing polymers whilst testing for IRI. The reason for this is that salts like NaCl are able to increase the size of the liquid channels, counteracting any non-specific, retarding effects on water mobility.[3,46–48]

IRI is widely investigated using the "splat" assay first developed by Knight *et al* [22], although other techniques have also been developed.[49] The set-up of a splat assay is shown in Fig 1.2. In this test a syringe containing the solution of interest is suspended approximately 2 m above a 193.15 K chilled glass plate and a small drop is released. On immediate contact the drop is quickly frozen, and annealed at a warmer temperature close to 267.15 K, yielding a polycrystalline wafer after 30 minutes. A high-resolution camera is used to continuously monitor this droplet and its crystals from start to finish. At the end of the experiment, image analysis tools like ImageJ[50] are used to determine the mean ice grain size (MIGS) or the mean largest grain size (MLGS) from a number of randomly selected or largest crystals in the field of view respectively. The results are then compared to a negative control, typically a phosphate-buffered saline (PBS) solution, which serves as a solvent for the most part. The final results are normally reported as a percentage of the negative control,[1,7,8,22,51,52] and sometimes by quoting the lowest concentration at which IRI activity is observed.

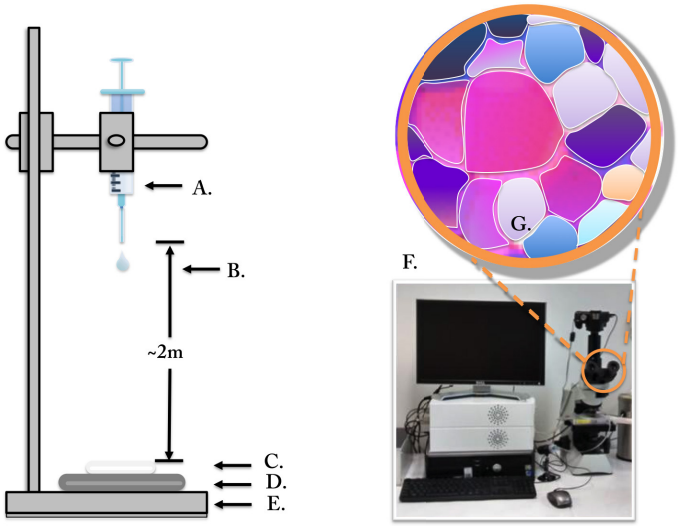

Figure 1.2: Splat assay set up. A. syringe, B. distance, C. chilled glass plate, D. cooling aluminium plate, E. stand, F. imaging system G. schematic of micrograph.

Thermal hysteresis

TH is possibly the most studied of the three antifreeze properties. Ordinarily the melting and freezing temperature of ice crystals are one and the same. In the presence of antifreeze molecules this might change: thermal hysteresis describes the scenario when the freezing temperature falls beneath the melting temperature and the difference between the two is called the TH gap. TH is thought to be caused by direct and irreversible adsorption onto specific planes of a growing ice crystal surface.[1] As a result of direct pinning onto the surface, the local area becomes microscopically curved and energetically unfavorable to grow any further (Fig. 1.3). This is known as the Kelvin effect or sometimes Gibbs-Thomson effect.[53] The size of the TH gap varies from molecule to molecule, however at temperatures within the TH region, ice crystals does not grow or shrink.[3] In the literature, TH is usually described as non-colligative, which means that TH antifreeze molecules does not lower the freezing point in proportion to their concentrations.[54] Rather, they typically work more effectively than expected at lower concentrations.

In order to assess this antifreeze property, a nanolitre osmometer is also used to accurately monitor the temperature and ice crystal size at time intervals.[3] Alternatively a differential scanning calorimeter can be used to automate the process, without the need for microscopic observation.[55]

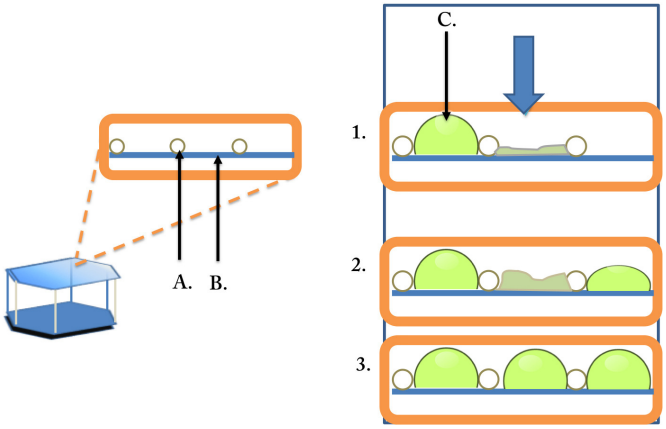

Figure 1.3: A schematic illustrating the accumulation of water (green) onto the ice surface (blue) in the presence of antifreeze molecules (white). The blue arrow highlights this process between adjacent antifreeze molecules. A. antifreeze molecule, B. growing ice front, C. accumulating water molecules.

Dynamic ice shaping

As mentioned earlier, ice crystals typically grow out into spherical shapes at temperatures close to the T_m (up to $\Delta T \approx -2\,K$). However in the presence of antifreeze molecules the ice crystal shape may become altered as it grows within the TH region (or at temperatures close to the T_m), because certain antifreeze molecules have the ability to interact closely with certain planes of ice.[3] The name for this process is dynamic ice shaping (DIS), and it can be monitored using a range of techniques, mainly hemispheral etching and by use of a nanolitre osmometer.[3]

1.2.3 Essential Polymer Physics

Later we will introduce the use of synthetic polymers, and it is important to understand that the physical properties of large polymers can be described using statistics. These descriptions typically base themselves on one of various models of polymers' motion *e.g.* Brownian motion, the random walk, which is the simplest, or the self-avoiding walk. The founder of this field is Paul Flory who also determined the radius of gyration (R_g) for a polymer as a function of chain length (the Flory exponent (V)) under theta conditions (the conditions at which polymers will behave as an ideal chain[56]). The R_g describes how collapsed a polymer is in solution, and is calculated using Eq 1.1, where m_i is the mass of atom i and r_i is its position. It is the root-mean-square distance of a collection of atoms from the polymer's centre of

mass (r_{mean}).

$$R_g = \sqrt{\frac{\sum_{i=1}^{n} m_i (r_i - r_{mean})^2}{\sum_{i=1}^{n} m_i}} \tag{1.1}$$

$$R_g \propto {M_w}^V \tag{1.2}$$

Equation 1.2 defines how R_g scales with chain length and molecular weight (M_w). In a good solvent ($V \approx 0.588$)[57] or θ-solvent ($V \approx 0.5$), a single polymer chain is fully extended or more swollen in solution, while in a bad solvent the chain is more compact or spherical in order to minimize polymer-solvent interactions ($V \approx 0.333$)[58]. However for proteins, which typically have a well-defined secondary structure, it merely reflects how compact or extended it is in solution.

Experimentally, the R_g is normally determined using static light scattering techniques like small angle neutron scattering (SANS) or X-ray scattering.[56,59] It is important to note that the experimental R_g is reported as an ensemble average and that the polymers that make up the ensemble solution are in fact polydisperse, (although the degree of polydispersity depends on the type of polymerization used). Therefore direct comparison of experimental R_g and those obtained from computational simulations with a single polymer solution may be an oversimplification.

1.2.4 Antifreeze Proteins and Glycoproteins

In the North and South Poles where the climate is continuously icy and the salty ($\sim$0.45 M)[60] sea waters rest at approximately 271.25 K,[61] the evolution of biological antifreezes has enabled the survival of fish,[62] insects,[63] plants, bacteria and even fungi.[2,64,65] Two types of these biological antifreezes exist: antifreeze proteins (AFP) and antifreeze glycoproteins (AFGP). From here on we shall refer to them both collectively as AF(G)Ps.

To date AFPs have been investigated using a vast array of techniques; NMR spectroscopy,[66,67] X-ray spectroscopy and chromatography to name a few, and these have been used to reveal their large range of structures.[60,68,69] As a result, AFPs have been characterized according to secondary structures, interactions and size, and thus far they are classified into 4 groups (Table 1.2)[70]. Briefly, type 1 and 4 are α-helical and contain large amounts of alanine (>60%), whilst type 2 is cysteine rich and predominantly held together by disulphide bonds, and finally type 3 typically consists of a globular, β-sandwich structure.[1,60,68]

Characteristic	AFGP	Type 1 AFP	Type 2 AFP
Mass kDa	2.6–33.0	3.3–4.5	11.0–24.0
Key properties	AAT repeat & disaccharide	Alanine-rich α-helix	Disulphide bonded
Natural sources	Antarctic notothonoids	Right-eyed flounders	Sea raven, Smelt, Heerring

Characteristic	Type 3 AFP	Type 4 AFP
Mass kDa	6.5	12.0
Key properties	β-sandwich	Alanine-rich helical bundle
Natural sources	Ocean pout, Eel pout	Longhorn sculpin sculpin

Table 1.2: Types of AF(G)Ps and their characteristic properties. Adapted from Ref. 1 and Ref. 2. AAT = Alanine-Alanine-Threonine repeats

AFGPs however are composed of regularly repeating structures, similar to synthetic polymers. Their monomers are glycotripeptide units of $[\text{Ala-Ala-Pro/Thr}]_{4-50}$,[71,72] with a disaccharide (β-d-galactosyl-(1,3)-α-N-acetyl-d-galactosamine) attached onto the threonine residue via a glycosidic link (Fig. 1.4).[62,72] To date only 8 classes have been identified and are often grouped as large (AFGP-1–5) or small (AFGP-6–8). Compared to AFPs, AFGPs are less studied because they are structurally complex and so are often problematic to synthesize or purify in the quantities needed for experimental studies to be made.[72,73] As a result, there is actually less known about them despite the fact that they were the first to be isolated.[61]

AF(G)Ps are able to exhibit TH, DIS and IRI activities, which are several orders of magnitude (300–500 times[68]) greater than their colligative properties.[61,64,74] In addition to this they have also been shown to alter the growth rates of ice.[60,64] AF(G)Ps do not necessarily display all three antifreeze properties at once; some may, for instance, only have IRI properties and negligible TH properties.[2]

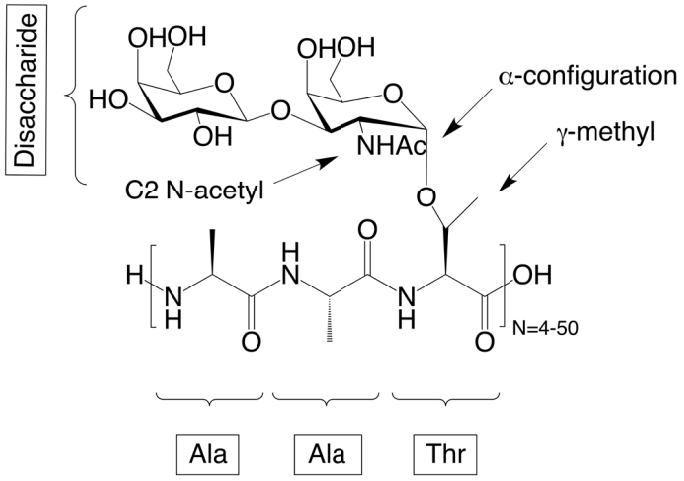

Figure 1.4: Chemical structure of AFGPs.

1.3 Key experimental studies

In this section we explore the key experimental studies for both biological antifreezes, for small and synthetic molecules.

1.3.1 Previous experiments on the mechanisms of AF(G)Ps

Discovery of AF(G)Ps

The first biological antifreeze (BA) was discovered in Notothonoid fish in the 1950s[64] and elucidation of the mechanism first began in the 1960s by Devries and Wolschang[61]. Since then the structure function relationship of AF(G)Ps has been explored in order to further understand these proteins and their mechanism(s).

Thus far no one has been able to provide a theorem comprehensive enough to account for every experimental observation without some serious unanswered questions undermining its explanation. Rather, a few reasonable observations or theories have been put forward, all of which have some gaps that need closing. The predominantly accepted theory is the step-pinning mechanism described earlier in the TH section, however some clarity is still needed to understand which interactions mediate the ice binding mechanism.[75] In this section we discuss what has been explored, and why. Please note that this section predominantly focuses on AFGPs because they closely resemble polymers, and their structural differences to AFPs suggest that their mechanisms and interactions may also differ greatly.

Predominant mechanism

The adsorption inhibition mechanism was first mentioned by Raymond *et al* in 1977 and coined the name step-pinning.[53] Soon after, Knight *et al* extended the mechanism to give the mattress model, a competing theory with similar criticisms (to be mentioned later).[76,77] The main difference between the two models is that the former assumes growth occurs in a stepwise fashion and suggests that AF(G)Ps block growth at steps (Fig. 1.5), while the latter proposes that inhibition occurs perpendicular to the surface (Fig. 1.3).[78] In both models, the mechanism or interactions by which the molecules arrive at the ice interface is not declared in the theory. Rather they describe that the adsorption of AF(G)Ps onto the interface results in an energetically unfavourable, curved surface between adsorbed AF(G)Ps where water molecules attempt to incorporate into the ice lattice (See § 1.2.2). These water molecules cannot overgrow the AFPs whilst within the TH region,[79] so the ice crystal neither grows nor melts. However at temperatures lower than the TH the ice crystal will grow uncontrollably. These theories explains why it is possible for the freezing point depression to occur, and inherently explains why TH is always accompanied by DIS, while the reverse does not necessarily mean the presence of TH.[3,73,80]

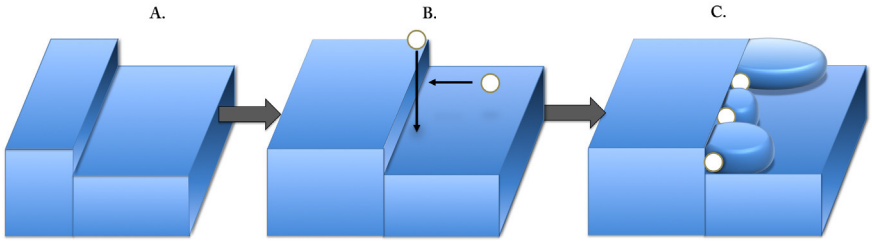

Figure 1.5: Schematic of AF(G)Ps blocking ice growth at a step sites. Key: A. and B. are at 273 K while C. occurs at T<273 K.

To investigate the mechanism of AF(G)P, ice hemisphere etching (IHE) studies are commonly employed. This technique is the process of freezing the dilute AF(G)P solutions just below their TH region so as to incorporate the molecules completely into the crystal. Normally the crystal is grown is such a way that all the interfacial orientations are equally exposed to the solution. On sublimation, the surfaces of ice crystals reveal faint patches (or etches) where AF(G)Ps are, or were once pinned onto specific planes of ice.[1,4,77] The use of IHE demonstrated that the AF(G)Ps become irreversibly pinned. These experiments also reveal how

single ice crystal growth habits changed around different AF(G)Ps because they had affinities for different planes of ice, normally the prism or secondary prism planes (a-axis), while growth along the basal plane (c-axis) remained uninhibited. If the temperature is dropped low enough, the basal plane will continue to advance gradually forming a tiered structure. As a result the final crystal morphologies are often "needle-like" crystals or hexagonal at low supercoolings rather than circular disks, as they would otherwise be (Fig. 1.6). In exceptional cases, hyperactive AF(G)Ps are able to interact closely with the basal planes as well — however, these traits are often reserved for AF(G)Ps from insects which endure harsher climates than plants or notothonoid fish.[81] This multi-plane behaviour is presumably responsible for their larger TH levels of up to 6°C and tendency to form hexagonal plates rather than needles.[2,82]

Both models propose that AF(G)Ps become trapped in the ice during freezing, and are therefore adsorbed irreversibly to the growing ice crystal. This is evidenced in experiments and so these models have become widely accepted mechanisms. There is also recent evidence to suggest that some AFPs permit superheating (TH_m) of ice crystals, which is in support of the adsorption inhibition mechanisms.[83–85] Celik *et al* investigated superheating of ice crystals in the presence of AFPs and the correlation between TH and TH_m at a melting rate of $0.02°C\,min^{-1}$. Under these conditions TH_m is considerably higher for hyperactive AFPs, just like with TH, and approximately a tenth of the TH values.[83,84] They also demonstrated that the replacement of an AFP solution around an ice crystal at T_m did not induce melting of the crystal.[86] This experiment provided a strong case that the AFPs did not exist in reversible equilibrium as bound states on the ice crystal and unbound states in solution.[85] Hall and Lips[78] suggest that for the adsorption to be irreversible (and consequently accompanied with a large free energy), more AF(G)Ps must be adsorbed onto the ice at both small and large concentrations, rather than the concentration dependent profiles we typically see. The authors state that this process only appears to be irreversible – they propose that the AF(G)Ps are instead slowly and temporarily blocking the addition of water molecules.[3,78] Their proposal explains why TH_m is a fraction of TH values and allows for a smaller free energy, however it does not explain why significant crystal growth is not observed prior to inhibition. To resolve debates like these, it is important to have a closer look at the types of interactions between ice and the antifreeze proteins or polymers.

Importance of complementation Both direct and indirect experimental methods have confirmed that AF(G)P binds to the surface of the growing ice crys-

tal.[1,77,85–89] The earliest proposals for the mechanism uses evidence that AFGPs compliment the ice lattice structures in certain planes, and so suggests that they are able to bind directly to the ice interface (or regions close to it).[3,75,83,90] AFGPs are decorated with sugars, which carry restricted hydroxyl groups capable of hydrogen bonding (H-bonding) with "dangling" atoms on the exposed ice interface.[79] Upon testing this theory studies found that substitution of these hydroxyl groups could be tolerated but often resulted in reduced TH and DIS activity.[3,72,91] However removal of 60% or more of the galactosyl residues resulted in complete loss of antifreeze activity.[87] Early CD studies revealed that subsets of AFGPs can be either coils or left-handed helices, with hydrophilic groups bristling on one side of the helix while the hydrophobic residues line the opposite side.[3,87] These studies also revealed that the steric N-acetyl group helped to maintain protein neutrality and to conserve the secondary structure necessary for both DIS and TH to function.[3,72,91] Overall these provide a combined effort to keep the hydroxyl groups in place for efficient interactions with ice.

NMR techniques were used to reveal that low molecular weight AFGPs are rod shaped at low temperatures and become increasingly flexible coils at higher temperatures and molecular weight, similar to polymers.[87] This is an interesting contrast to most AFPs that are often described as flat and /or rigid structures, and furthermore suggests that these two types of proteins (and even mimics) may have two completely different mechanisms. NMR spectroscopy was also used to probe the spacing between the hydroxyl groups and highlight that every tripeptide unit was separated by 0.931 nm[3,4], which corresponds to distances found between 2 units on the prism plane (0.904 nm)[3,4] – the same planes where growth would normally become inhibited. Similarly, AFPs have complimentary hydrophilic regions with each polar residue separated by identical distances (*e.g.* 0.45 nm for winter flounder).[79] These spaces vary from protein to protein, yielding different patterns that are attributed to inhibition of specific planes in different ways. As a result, they exhibit varying DIS behaviours and form spicular or hexagonal shaped crystals that are non-identical (Fig. 1.6) – even for proteins from the same AFP class.[79,80]

A combination of these attributes explained why, under laboratory condition, TH values as high as 1°C could be achieved by AF(G)Ps at concentrations as low as 0.1 mg ml^{-1}.[2] Moreover, their ability to change the surface characteristics of a growing ice crystal is indicative of a high level of specificity,[92] especially as $\sim$20.2 mg ml^{-1} of NaCl salts would be required in order to achieve the same degree of undercooling.[23] Similar observations were also found in studies of fish serum, which differentiated the contributions of salt and AFGPs to the overall antifreeze activity,

and concluded that ∼50–60% was a result of just 10–15 mg ml^{-1} AFGPs.[79,93–98]

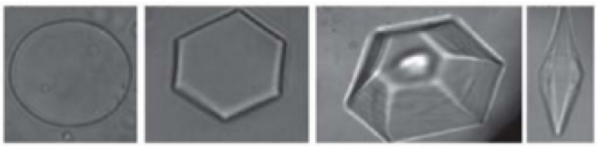

Figure 1.6: Different effects of dynamic ice shaping by AFPs. Image taken from Ref. 3. A. no additives B. and C. show dilute solutions of AFP and D. shows a hexagonal bipyramid at high concentrations.

Importance of hydrophobicity Due to a combination of the aforementioned attributes, AF(G)Ps were assumed to interact with ice directly via complimentary interactions such as H-bonding. However there are disputes as to whether H-bonding alone sufficiently explains the irreversibility seen by AFGP ice inhibition — particularly as the ice/water interface is not a sharp transition but a gradual one with the QLL at the center. Knight *et al* [4] attempted to address this problem by suggesting the hydroxyl groups of the glycoproteins become incorporated into the growing ice lattice as described in (Fig. 1.7) and so the AFP/QLL or AFP/ice contact line effectively changes, resulting in more H-bonding between the two structures.

In spite of these suggestions, substantial considerations have recently been given to the involvement of hydrophobic interactions.[3,99,100] As mentioned earlier, most AF(G)Ps display some level of amphiphilicity; in fact the presence of hydrophilic and large hydrophobic regions (∼60% alanine in some cases) suggest that the hydrophobicity also play a strong role in the antifreeze mechanism. It could not be coincident that most known antifreeze proteins have evolved independently with amphiphilic properties.[101] To give an example, DeVries and Lin[79] found that the Type 1 winter flounder AFP has 0.45 nm separation between threonine and aspartate residues, with clusters of up to seven hydrophobic residues separating them. Ultimately these indicate a use for hydrophobic regions as well, mainly pointing at a role that maintains fixed spacing between polar groups.

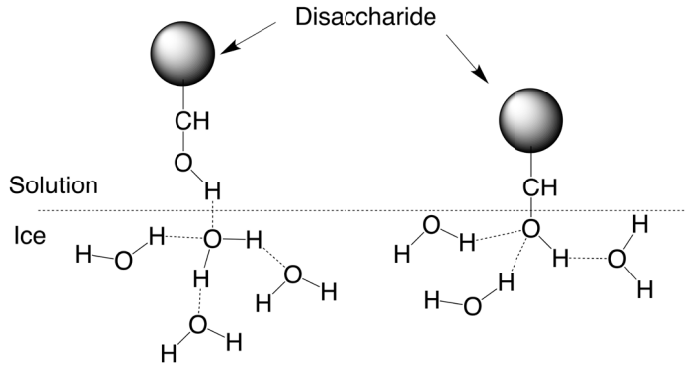

Figure 1.7: Two possible mechanism for interaction of AF(G)Ps with ice surfaces. In the first option, the AFGP remains completely in solution and a single H-bond is formed between ice and its disaccharide (left). Alternatively, Knight *et al* [4] proposed that parts of the AFGP reside in the ice surface rather than H-bonding to the ice; the hydroxyl group is fully shared with the crystal (right)

The recent ability to resolve the flat ice binding faces of Type 1 AFPs also revealed that they largely consist of hydrophobic groups, which creates an additional purpose to the seemingly resolved role of apolar groups.[102] Substitution studies of hydrophilic amino acids with hydrophobic residues in Type 1 AFPs demonstrate that H-bonding is not crucial for antifreeze activity. Replacement of Thr with Val (hydrophobic) retains some TH and DIS activity.[99,103] To give an example, the replacement of four out of six Thr residues (approx. 67% Thr) with Val at $10\,\mathrm{mg\,ml^{-1}}$ retains ∼50% TH activity.[103] Similar results were also found in another study where two of four Thr were substituted with Val and only resulted in a 10–20% loss in activity.[99] However substitution with Ser (hydrophilic) results in little or no recognizable antifreeze activity, which is surprising. In the referenced studies[99,103] no mention of IRI was made, but these results indicate that hydrophobic groups — specifically γ-methyl groups — are necessary or at least equally responsible for the adsorption of Type 1 AFP onto ice.

It is possible that the van der Waals contributions from the non-polar groups and their hydrophobic interactions forces surrounding waters into a packing arrangement (presumably "ice-like") so as to minimize interactions with the hydrophobic face and maximize the HBN between themselves.[4]

Alternatively, the mechanism may be driven by an entropic gain as a result of the exclusion of water molecules from the ice surface and also from the hydrophobic surface (desolvation). Additionally, upon binding to ice the hydrophobic solvent accessible area (PSASA) would become masked.[99] In this instance the hydrophilic

groups support this function by increasing or securing the complementarity of the AFP/ice fit, ensuring buried surface area is exposed for maximum entropy gain.[99] These hydrophobic contributions to the mechanism might also explain why it is possible some AFPs like TisAFP6,[102] with flat, but irregular β-structures can still have antifreeze activity (TH). Computer simulations have contributed greatly to these types of studies and are discussed further in the computational section.

1.3.2 Advantage of Synthetic Mimics

Designing synthetic AF(G)P mimics with tailored antifreeze properties is an attractive prospect because they can be produced at batch levels required to meet the high demands for improved cold storage in medicine and commerce.[73] This route provides a better alternative to the exhaustive process of isolation and purification of AF(G)Ps.[73] A synthetic approach also means that a diverse range of structures can be built so they are ideal for systematic structure-function studies, in order to create an ideal antifreeze that might not be accessible in nature. Two other reasons prevent their use as cryoprotectants and cold storage of biological tissues: (1.) TH values associated AF(G)Ps are hardly large enough for the low temperatures used (>93.15 K).[6], (2.) As a result the DIS abilities or explosive crystal growth at temperatures lower than TH present a mechanical hazard to the cells.[6,21]

1.3.3 Small molecules

C- and N- linked analogues

The production of AFGP in batch is limited by the orientation of the anomeric carbon-oxygen bond (O-link).[3,6,21,73] So Ben *et al* explored the inhibition of ice growth using synthetic C-linked analogues[6,73](Fig. 1.8). These small mimics (N= 4, 6 and 9) have little to no TH (∼0–0.06°C), and due to their DIS properties, they can form hexagonally shaped crystals, but still exhibit some IRI properties comparable to native AFGP-8.[6] This indicates that the mimics do not really interact with the ice lattice, but when they do it is on a preferential plane.[6] To some degree the latter is consistent with findings for native AF(G)Ps, and smaller chain lengths (N= 1 and 3) had no IRI activity at all. The authors systematically investigated the effects of backbone composition, lengths of side groups and the type of carbohydrate used. The results demonstrated that increasing distances between the side groups and the backbone beyond 2 or 3 carbons resulted in a complete loss of IRI activity. The same result was achieved by substituting galactose moieties with others sugars known to have cryoprotective properties (*i.e.* glucose, mannose and talose).[2,6] This lays out

the extent to which IRI relies on structure and orientation, particularly for the C2 hydroxyl group – where a change from an axial position to equatorial meant a 50% reduction in IRI activity – and less seriously on the equatorial C4 hydroxyl group.[6] Based on these findings, they linked IRI performance to the hydration properties of sugars attached to these mimics.[73,104]. Their most potent analogues bore sugars that can produce larger hydration spheres, and effectively preoccupy surrounding water molecules from advancing the QLL or ice interface. Instead they help to distort the amorphous phase.[3,6]

The lack of TH and DIS in C-linked analogues translates to little or no cytotoxicity during cold storage of mammalian cells (*i.e.* human embryonic liver cells).[5,6] Studies of AF(G)P mimics like these have shown that IRI can be dissociated from the other 2 antifreeze properties. It has also been demonstrated that although DIS can sometimes be dissociated from TH, it is not possible to have TH without DIS.[3,73,80] This makes the two properties undesirable and shifts considerable attention to maximizing the third antifreeze property, IRI. In nature, similar approaches have already been employed by freeze tolerant organisms[105] which also use IRI active sugars whilst, freeze avoidant species rely more on AF(G)Ps. Seeing as DIS is most tolerant of structural modifications, aside from the need for a well-defined secondary structure and neutral moiety, one approach could be to subdue DIS by designing synthetic analogues with a different type of secondary structures.[3,6,72,91]

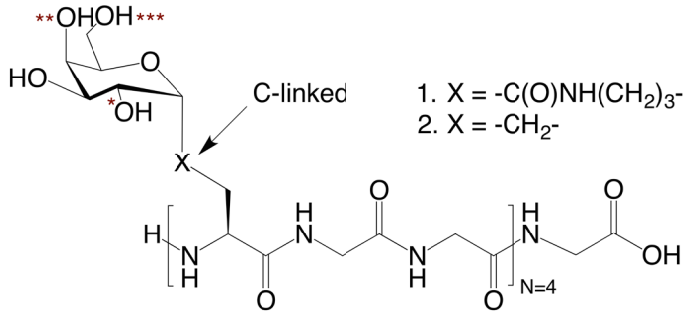

Figure 1.8: Structures of potent C-linked AFGP analogues. 2. Has IRI activity comparable to AFGP-8 in PBS solution and produces an MLGS of 20% at 5.5 µM. * marks C2 hydroxyl group (HO2), ** marks C4 hydroxyl groups (H04) and *** marks C6 hydroxyl groups (HO6). Taken from Ref. 5 and Ref. 6.

Non-protein "antifreezes"

Biological tissues using non-protein cryoprotective agents can be cryopreserved

using vitrification, the rapid cooling of a liquid to a glassy state without crystallization.[21] In order to protect mammalian cells, some conventional formulations include molecules such as carbohydrates[6], salts, glycerol[106], or dimethyl sulfoxide (DMSO).[6,107] The latter two are most commonly used, and are normally applied at concentrations of 5–10% (v/v) DMSO or glycerol, and 95–90% (v/v) Fetal Bovine Solution.[108] The disadvantage of using these cryoprotective agents are that they are only favourable for a few types of cells (erythrocytes and spermatocytes) and non-ideal because of high cytotoxicity — especially in the case of DMSO — and glycerol's weak cryoprotective abilities.[108]

1.3.4 Polymer antifreezes

In the search for an ideal antifreeze macromolecule, researchers assessed the antifreeze properties of a library of synthetic polymers[48,52], first started by Knight *et al* [48] in 1995. Those which have received most attention are poly(vinyl alcohol) (PVA)[48], poly(hydroxyproline) (PHYP)[48], poly-l-histidine[48], zirconium acetate (ZA)[6,109,110], silane coupling agents (SCA)[106] and polyampholytes[108]. These have been largely studied rather than using synthetic glycopeptide conjugates like C-linked analogues because they are less challenging to make and often produce greater yields.

Poly(vinyl alcohol)

Inada *et al* [48] first observed atactic PVA as an antifreeze polymer in 1995. They found that polydispersed, low grade $PVA_{318-2273}$ (86–98%) exhibited relatively strong IRI in comparison to other polymers. These were qualitative observations and no comments were made for TH and DIS.[46] Later studies conducted by the group found that PVA exhibited small amounts of TH ($\sim$0.037 K at 50 mg ml^{-1})[52,111,112] and DIS by interacting with non-basal planes of ice.[113] [52] They also showed that[114] PVA of 80–98 kDa could be as effective at IRI as AFGP-8 or AFP Type 1 (3.3 kDa) at equimolar concentrations.[52,114] However in a separate study Ben *et al* 's first generation C-linked analogues were almost 80 times less active in comparison.[6,52] These highlight the effectiveness of PVA and consequentially PVA serves as a good starting point to study IRI in order to develop an ideal IRI polymer. This is further compounded by earlier studies on a range of structurally diverse polymers (carboxylic acids, amides, amines, and alcohols), which revealed that only polymers with hydroxyl groups could achieve significant IRI activity.[52] Even PVA's structural isomer, PEG showed negligible IRI, TH or DIS activity[3,7,52], which makes

sense because it has a functional group that cannot meet the aforementioned requirements; the oxygen group neither protrudes out of the polymer backbone, nor can it act as both H-bond donor and acceptor.[7]

In 2013 Congdon *et al* [7] carried out an extensive study on narrowly polydispersed PVA. They argue that the purity and polydispersity of the polymer will affect the integrity of these studies, which Inada previously demonstrated in the case of poly-l-histodine.[48] They investigated the effects of increased acetylation, poly(vinylpyrrolidone) (PVP) block copolymerization and the influence of 7 chain lengths (between 10–351 units) on the IRI activity. The concentrations tested ranged from 0.005–1 mg ml^{-1}, and revealed that PVA_{351} (34.5 kDa) could be IRI active from as low as 0.05 mg ml^{-1} after just 30 minutes. Their results are shown in Fig. 1.9. At 1 mg ml^{-1} PVA_{10} produced crystals with 80% MLGS, while all other chain lengths (N= 19, 30, 56, 154, 246 and 351) produced 15–25% MLGS and had similar profiles for the concentration dependence of IRI activity. Somewhere between 10–19 repeat units; there exists a minimum chain length where IRI activity is "switched on", but at longer chain lengths the IRI activity increased steadily until a critical point.[7] Larger polymers, (N= 246 and 351, 22.7–34.5 kDa) reached this point at much lower concentrations of 0.1 mg ml^{-1}, in comparison to ∼0.3–0.8 mg ml^{-1} for much smaller polymers (N= 19–154, 1.7–14.6 kDa).[7] It therefore appears that, like AF(G)Ps, larger polymers may be more effective and so can be used at lower concentrations.

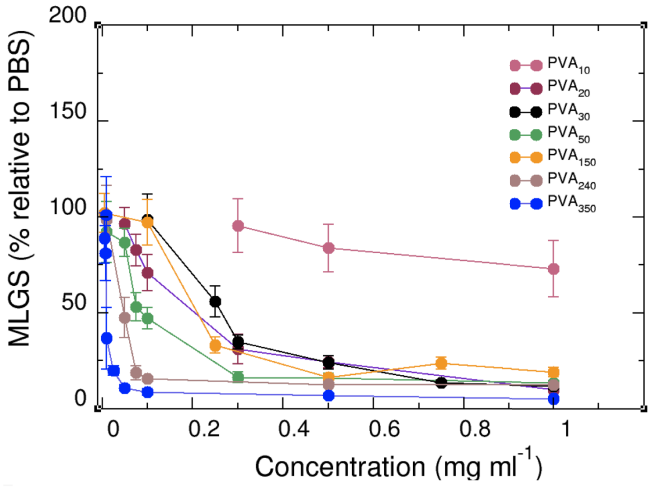

Figure 1.9: IRI activity of PVA polymers in PBS solution. Error bars represent standard deviations (stdevs) between repeats. Taken from Ref. 7.

It is important to acknowledge three more things. Firstly, that these studies primarily deal with atactic PVA which means that their hydroxyl groups are oriented at random with respect to the chain. It is easy to believe that combined with the positive size dependence[7,52] of IRI activity, this indicates that higher densities of hydroxyl groups may in fact influence a corresponding increase in IRI activity, rather than just a complementary fit to ice from OH-OH distances on PVA alone.[73] This notion is further corroborated by a decline in IRI activity by introducing acetyl spacer side groups into the PVA backbone. For instance a change from 10 to 30 mol% acetylation resulted in complete loss of IRI for a $2\,\mathrm{mg\,ml^{-1}}$ solution. However this reasoning was questioned by findings that other glycopolymers with higher OH densities per unit mass than PVA were found to have lower IRI.[115,116] Similar conclusions were also made when PVA was compared to carbohydrates[8](Fig. 1.10). It brings to light the influence and need for quantitative assessments of other factors such as the relative degrees of backbone flexibility, hydrophobicity, water hydration and water ordering or disordering. For instance, it is possible that as a result of greater flexibility, these PVA polymers can adopt plethora conformations and maximize their interactions with the ice. In the light of these considerations, it suddenly becomes unclear if the introduction of acetyl group adversely affects IRI because of a change in flexibility or the discontinuity within either the hydrophobic face or hydrophilic groups.[7]

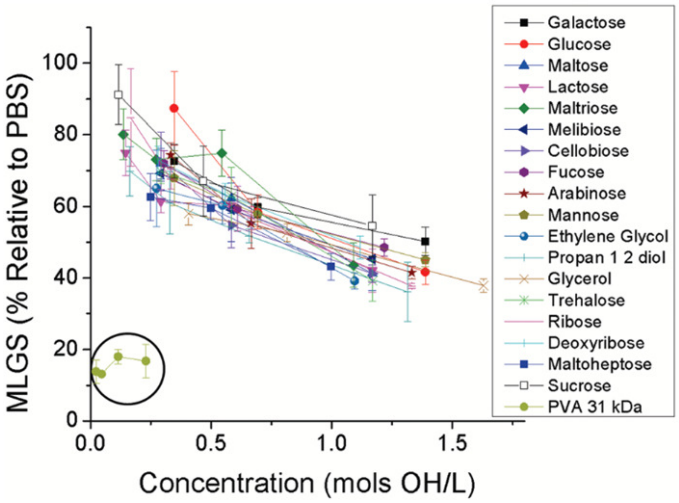

Figure 1.10: IRI activity of PVA and glycopolymers normalised for the number of hydroxyl groups present. Solutions were made using PBS solution and PVA_{31} is encircled for clarity. Error bars represented stdevs between repeats. Taken from Ref. 8.

Secondly, the splat assay shows both nucleation and the growth of ice crystals. It is difficult to distinguish which of the two PVA and other IRI inhibitors affect, however Wang *et al* [117] demonstrated that both stages are affected. Further studies have also confirmed their finding and show that nucleators like bacterial ice nucleation proteins[118] or silver iodide[30] have had their activities suppressed by the presence of PVA.

Finally, an advantage of PVA is that it is non-toxic[119] and already in use for a range of pharmaceutical applications from eye drops to tablet coatings and even thickeners. Deller *et al* [21] recently demonstrated that for both sheep and human erythrocites, cell viability was enhanced by 0.1 wt% PVA_{200} (9 kDa), which is almost 100 times less than typical fractions used for DMSO. This study tested the compatibility of PVA with human blood and the findings mean that more blood cells will be rapidly available for transfusions after thawing, seeing as there is not an urgent need for PVA to be removed post surgery, unlike with DMSO.[21]

Poly(hydroxyproline)

Poly-l-hydroxyproline (PHYP) has also been shown to exhibit high degrees of IRI activity and nearly non-existent TH in pure water at moderate concentrations[48] or low degrees of polymerization. In 2009, Gibson *et al* reported the first quanti-

tative studies of the IRI activities of PHYP and they found that its IRI activity is concentration dependent. For N= 44 (5.7 kDa) the IRI activities were comparable to PVA_{80} at 3.5 mmol L^{-1}, producing a mean largest grain size of 175µm, which is approximately 34% smaller than the MLGS of the PBS negative control.[52] Interestingly, PHYP possesses a PPII helical secondary structure, similar to AFGPs.[120,121] Even more interestingly, compared to the structure of PVA polymer, albeit atactic in structure, PHYP is not considered facially amphiphilic and highlights the independence of IRI on this feature.

Zirconium (IV) acetate

Normally ice in a colloid suspension grows into lamellar structures with dendritic surfaces however in the presence of 13–100 g L^{-1} Zirconium acetate (ZrA), homogeneous sized hexagonal pores form along the direction of growth within the crystals.[110,122] At smaller cooling rates the pores are bigger and become faceted, which is believed to be a direct consequence of ZrA interacting with the ice crystal interface. For instance pores of 4.5 µm are produced at a cooling rate of 20°C min^{-1} and increases to 100 µm at 0.5°C min^{-1}.[110] ZrA or ($Zr(OH)_3A^{2-}$) and has recently been revealed to have IRI activity[109], because it slows the growth of ice buffer solution (pH= 3.5–4.5)[6,109,110] while the true amount of thermal hysteresis activities still remain largely under debate.[109,110,122] Similar to PVA and AF(G)Ps, it is thought that the arrangement of the chemical groups like OH matches the periodicity of atoms on the ice surface. Due to this feature, ZrA could participate in in H-bonding with dangling atoms on the ice surface and it is possible that ZrA so may also reside at the interface of the ice/water boundary or distort the diffusion rates of nearby migrating water molecules.

1.4 Key simulation studies

MD simulations provide an atomistic view of the dynamics of a system and can therefore be used to look closely into the mechanism of antifreeze activity (Fig. 1.11). In this section key simulation studies in the literature are discussed in order to provide an overview in the relevant areas of ice growth without any additives, properties of antifreeze molecules in solution and the behaviour of antifreeze additives in the presence of ice.

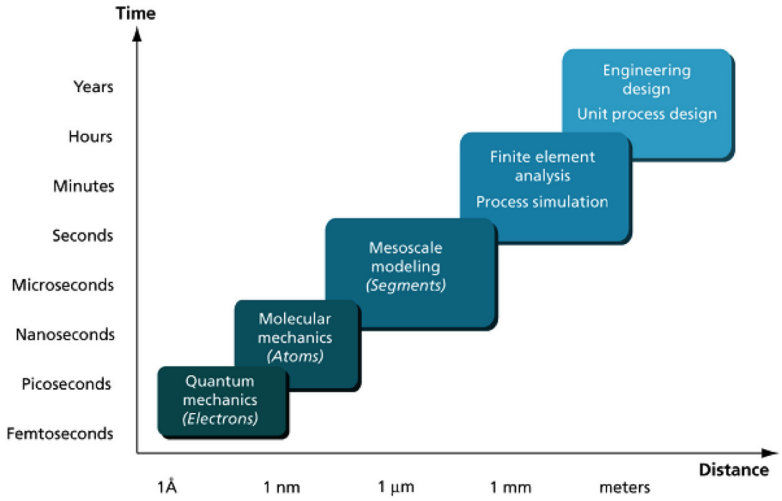

Figure 1.11: Schematic of timescales accessible to various computational techniques, where MD simulations fall within the category of molecular mechanics (CCP5 course material).

1.4.1 Simulations of small antifreeze molecules

Simulation of small antifreeze molecules in the presence of ice is rare. Rather they tend to be in systems of supercooled water, and focus on salts like NaCl or small organic molecules that are typically polyols *e.g.* carbohydrates or alcohols. Previous simulations of salt, sugars and AFP analogues are discussed here in this section, particularly findings which are relevant to later discussions.

Salts

MD simulations of salts in the presence of ice appear to be the most popular of the small "antifreeze" molecules, largely because of their applications in other areas like the process of brine rejection. It is common knowledge that salts do not incorporate easily into the ice lattice, and so are rejected out of the growing ice region. In the presence of salts, the freezing and melting point is depressed however the molecular mechanism has not yet been elucidated. Recently, Vrbka and Jungerwith [123] studied the brine rejection mechanism in the presence of a growing cubic ice crystal. They found that during ion density fluctuations, a new layer of ice opportunistically forms in regions where the NaCl ions had temporarily vacated. Over a trajectory period of 60–630 ns, they studied freezing of dilute aqueous solutions (0.15 M and 0.3 M) at T_m+15 and T_m-15. [123] Consistent with expectations, a local concentration gradient

was produced as the salts were rejected into an unfrozen region, forming a glassy area that would become even less likely to freeze.

Complete freezing of a pure water system was obtained after 250 ns, while the time taken in the presence of salts typically increased. In this study, a 0.15 M solution resulted in a 20% increase in the time taken to freeze (300 ns), whereas doubling the concentration led to a remarkable 100% increase (500 ns).[123] These observations of the freezing point depression and the glassy QLL are not uncommon, and have been reported elsewhere for different planes of ice, water models and a range of salt concentrations.[9,124]

For example, in 2006 Carignano *et al* [124] studied the I_h ice growth of both the prism and the basal plane in contact with a saline solution with similar concentrations (0.2 M) and undercoolings. Their simulation was conducted at approximately T_m-18 Kand used a 6-point water model for increased accuracy of the phase diagram of water. Peculiarly, the growth kinetics for the prism plane changed in the presence of salts and less so for the basal plane. The basal plane experienced approximately 30% reduction in growth rate and the prism plane was split into three stages. In the first stage, the initial growth rate was the same and faster than the basal plane however it came to a metastable state for about 2.5 ns. This period translates to approximately 30% of the simulation time needed for complete freezing of the system in the presence of salts. The author explains that these differences in kinetics are a direct result of the surface roughness on the two planes. Modelling work on the basal plane revealed a layer-by-layer growth mechanism, which produces a smoother surface, while the prismatic plane is much more random, disorganized and rough.[125,126] To place the observation into context, no isolated ions were found at the end of simulations and the authors concluded that complete freezing would not be possible unless the ions were fully paired or clustered together. The resulting decrease in entropy from pairing would encourage crystallization of the liquid phase.

Ordinarily, the prism plane's roughened surface offers an abundance of binding sites for faster ice growth however in this instance, it shelters ions from their pairs delaying the freezing process. It is interesting to note that the growth rate in the third stage is faster than the first, however the authors do not comment on this. It is plausible to suggest that in stage three, the collision of ice-like water molecules with salt ions prior to pairing may roughen the surface even further and therefore speed up the growth rate at subfreezing temperatures.[124] It also explains why concentrated solutions have been shown to increase the rate of melting at higher temperatures[127] (particularly as the larger ions, which can do more damage to the lattice or roughening, have repeatedly been proven to approach much closer to the

ice/water interface.[127–129])

These types of simulations produce melting or freezing rates comparable to experiment[124,127], and so provide a reliable protocol for identifying the freezing point depression that can be applied to larger antifreeze molecules. They have also revealed important information about ice/water systems. For instance, there has been a long standing dispute as to whether super-cooled water spontaneously crystallizes to cubic ice and quickly transitions into hexagonal ice. Recent studies have exposed that the introduction of stacking faults in both I_h and cubic ice (I_c) polymorphs in contact with brine solution can produce layers of I_c or I_h respectively.[9,123,124] In multiple studies Carignano *et al* [9,124] also noticed the presence of stacking faults as the ice crystal grew, but these were only observed for the basal plane[9,124] and not the prism plane[124]. The authors[9] demonstrated that the differences between these two polymorphs could easily be identified in a snapshot by tracing a guide line through the center lattice honeycomb structure, layer by layer (ie from left to right). I_h is characterized by a zig-zag pattern and I_c is marked by a straight line (Fig. 1.12). In the referenced simulation, they noted that this transition between I_c and I_h was a rare event, which occurred approximately every 50 ns. Most importantly they identified that the cause of this transition was the constant local freezing and re-melting of the ice layer because it produced the opportunity for the rearrangement of the lattice waters. These observations are important and cannot be readily dismissed as artefacts of the simulation system, mainly because so many different set-ups were used across these studies and still independently reach similar conclusions.

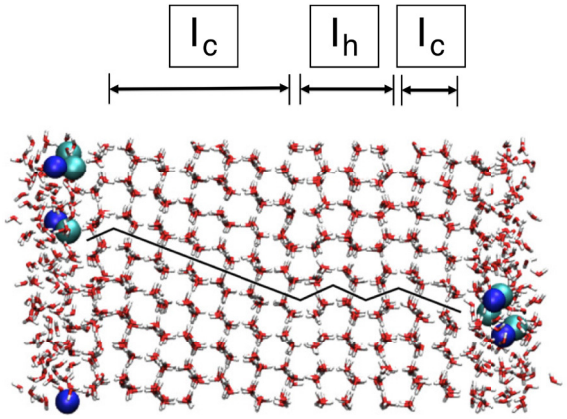

Figure 1.12: Illustration of how to differentiate between I_h and I_c polymorphs. Water molecules are shown in red and white. NaCl salts are shown in blue and green. Image taken from Ref. 9.

Sugars

In 1989, Brady[130] published the first MD simulation of α-d-glucose in water and shortly after the forcefield was revised to improve the description of glycosidic links on proteins.[131] These parameters were mainly intended for protein-sugar or membrane-sugar complexes however some simulations of carbohydrates were soon used to study the effects on hydrating water because of the correlation with their cryoprotective capabilities.[132] For instance, trehalose and sucrose are known cryoprotectants typically found in animals and plants respectively.[133] So they are expected to have a lot of antifreeze related properties in common, especially as both disaccharides are composed of fructose and glucose in a glycosidic link.[133]

Once such interesting study was produced ten years ago by Bordat *et al* .[132] They studied three disaccharides – trehalose, sucrose and maltose — and the effects of varying concentrations (0%, 4%, 16%, 33%, 49% and 66%) or temperatures (273–373 K, in 20 K intervals) on surrounding water. In a system consisting of 512 SPC/E water molecules, they investigated the size of the H-bonded clusters and the tetrahedrality of water using an orientational order parameter. In accordance with experimental work[132], and later simulations,[134] they found that below a threshold concentration of 40% and at cold temperatures (273 K), the disaccharide could not be distinguished in their disrupting effect of the HBN.[132] Above this threshold, which is close to the experimental value of 50%, trehalose was most disruptive, followed by sucrose and then maltose as expected.[132,134,135] This expectation is largely based on

NMR studies by Ablett *et al* [47], and others[47,135] that have identified a correlation between a higher glass transition temperature with reducing ice recrystallization rates. Using the orientational order parameter Bordat *et al* [132] demonstrated that trehalose has a greater hydration sphere than the other two disaccharides. As a result, it can disrupt more and so produces many more neighbouring, small clusters of HBN than other disaccharides.[132] This too, has been demonstrated before.[136] Interestingly, the orientational order parameter did not reveal any shift among the three sugars' profiles suggesting that they adopt comparable conformations in solution. Instead, increasing the concentrations of trehalose produced a profile similar to that reported by Debenedetti for pure water as the temperature is increased.[134,137]

To date, similar comparative studies of mono- and polysaccharides in unfrozen water continue to stress the protective capabilities of the solution directly correlates with concentration, and attribute their properties — including slowed water diffusion rates — to their water/sugar H-bonding behaviours.[134,138] In terms of atomistic mechanism, the most widely accepted theory is the disruption of water interactions meaning that the sugar cannot easily be incorporated into the lattice. However prior to this Crowe *et al* first proposed an alternative called the water replacement theory.[139] They suggest that sugars replaced hydrating waters around biomolecules thereby protecting them from freezing over and denaturing.[132,139] Sum *et al* [140] considered this interaction possible with the lipid bilayer to protect it from the extracellular ice and suggested that trehalose could H-bond to the phospholipid bilayer. They constructed a simulation that revealed minuscule changes when trehalose interacted with the phospholipid heads[140] and ultimately negated Crowe's assumption that biomolecules are H-bonded to the sugars during the freezing process.[132] Recently, similar attempts have been made to study if and how carbohydrates protect proteins in solution from thermal denaturation, however these methods focus on questionably high, "desiccating" temperatures, presumably past the boiling points of the water model used and the T_g of the carbohydrates.[141,142].

1.4.2 Simulations of AF(G)Ps

MD simulation is particularly useful as direct measurements of the ice-AFP interactions, which are not readily available to current solution-based experimental techniques.[143] Molecular modelling of AFPs and free energy calculations lend some support to the range of mechanistic viewpoints which emphasize the importance of hydrophilic lattice matching groups[144,145], and more recently, hydrophobic groups[68,146] which have been discussed earlier. The third hypothesis, which was only touched on, is that the antifreeze molecules accumulate at the ice water in-

terface and remodel the ice surface by influencing or assisting the development of their own binding site.[75,147–149] Each of these theories, introduces questions like: Is ice more hydrophobic than water? How does the protein differentiate between ice, QLL and water all of which are so chemically similar?[75] The most recent simulations aim to address these questions and select or rule out the aforementioned theories. Investigators typically draw their conclusions by studying the properties of the system such as H-bonding, water ordering or disordering, hydration numbers or protein solvation, facial alignment toward ice or "recognition" of ice, distance from the QLL, hydroxyl group spacing, solvent accessible surface areas or contact areas, free energy calculations and so on. The work of McDonald[145,150], Jorgensen[144], Haymet[26,68,72,103,143,151], Madura[151–155], Wierzbicki[143,153,154,156], Nada[157–160] and Granham[102,149], in particular, present landmark contributions in understanding the detailed mechanism using MD simulations.

The first simulations

Two independent groups conducted and reported the first simulations studies of antifreeze proteins and glycoproteins in solution: McDonald *et al* [145] in 1993 and Jorgensen *et al* [144]. These largely focused on conformations and the spacing between the hydrophilic residues at room temperature (300 K)[145] and supercooled water (273.15 K)[144] using 3-point water models and the CHARMM[145] or AMBER[144] FF. Like the experiments, early solution studies[144,145] pointed towards the key role of hydrophilic groups because they typically found that Thr residues had spacing, which matched those on specific (201) planes of ice. Take the study by Jorgensen *et al* [144] for instance; following a short 0.12 ns NPT simulation, they found that that HPLC-6 winter flounder protein (the most studied AFP) had equally spaced Thr hydroxyls (close to 1.67 nm) on one side of the helix, which matched the [0112] direction of ice. These findings are closely in line with etching results produced by Knight *et al* [77] between 263 K–258 K, and other molecular modelling studies.[153,161,162] By taking a snapshot and calculating the root-mean-square deviation (RMSD) from the protein's initial structure, the authors were able to confirm that HPLC-6 was linear for the most part, and maintained its helical structure at 273.15 K.[144] Using the same, all-atom RMSD calculation at 300 K and similar number of water molecules — albeit a different forcefield and system set-up — McDonald *et al* [145] found that the same HPLC-6 protein was stable but actually remained bent at the center, particularly at lower temperatures; 30° bent at 300 K and 60° at 237 K. Both referenced studies displayed average RMSDs between 0.225–0.325 nm after just 0.07–0.16 ns, however neither of the two studies confirmed these claims

to secondary structure using Ramachandran plots, which are typically used in MD simulations of proteins. In order to capture a snapshot of the mechanism, the first few simulations of AF(G)Ps were done in contact with ice in *vacuo*. In an effort to minimize the complexity of the simulation set up, these were traditionally simulated without the presence of liquid water and therefore the absence of the ideal QLL.[154] These systems were initially thought to be a reasonable approximation however a vacuum is actually an ill representation of water[151], and further still, there is increasing experimental evidence that the AFGPs might in fact work at the QLL interface.[103]

Around the same time Karim and Haymet became the first to introduce the simulation set up which described the QLL — a 1–1.5 nm wide transition region between the two phases of water — using the TIP4P water model.[26,163] Several other ice/water simulations have been performed since then to confirm these results. These regions are typically identified using an order parameter such as self-diffusion, average density, translation order, all of which provides an inflection point whilst crossing between the two phases.[26,154,163,164] Seeing as an accurate description of the protein's interactions would depend on a realistic description of the ice-water interface, Karim and Haymet's protocol was quickly adopted by McDonald *et al* [150], and others,[146,150,151] so that AFGP/water/ice interfaces became common practice for simulation of AFGPs; however at the time the ice lattice was typically fixed in position.[146,150] Later this was naturally followed up with the practice of unconstrained ice simulations in the presence of water, also first achieved by Dalal *et al* ,[151] in order to relieve simulations of structural artefacts that propagate into the QLL, and could potentially result in altered freezing times.[26]

The introduction of the ideal QLL

With the introduction of an idealized interface, and a better description of the QLL, investigators began to report that the lattice matching theory was not the predominant mechanism and moved away from this stand. In 1995 McDonald *et al* [150] simulated the AFPs at the idealized interface for just 0.10 ns at 203 K using an NVT ensemble. They found a good fit for their AFP at the interface, however the protein was oriented in such a way that the Thr faced away from the interfacial region and so it was proposed that direct binding via lattice matching may not be the only plausible mechanism to successfully bind onto the ice interface. They also noted that their starting structure formed a twist in the protein that later "promoted" a bent helix for the remainder of the simulation.[150,154] In a similar study five years later, and using a longer trajectory of 0.40 ns, Madura *et al* argued

that given sufficient time, the Thr residues would in fact reorient or remain oriented towards ice at 180 K. It's important to note that in these simulations the AFPs were first placed in the QLL in a configuration where they formed H-bonds with the ice at the start of the simulation.[154] They did not notice any bending of the helix however they found that one of the proteins "rolled" onto its side, moving the non-polar Leu residues from the QLL layer parallel to the ice surface, and allowing them to also interact with the ice. Similar to McDonald, they did find that the ends of the protein began to unwind at the N-terminus, producing non-helical regions when close to the ice, while at the QLL, promoting helicity.[154] In agreement with Houston *et al* [147] they postulate that the third mechanism could be most appropriate; they imply that AFPs don't bind to any plane in particular but reorient in order help to generate the binding site.[154]

Recent breakthroughs

Also in agreement with Houston *et al* [147], Garnham *et al* [149] and Sharp[75] independently highlight that both types of interactions (hydrophobic and hydrophilic), most likely work in conjunction to mediate the ice binding mechanism. This stand negates the concept of a dominant interaction and may even place the 30-year debate at rest. In the past two years there have been monumental discoveries and simulations about the antifreeze mechanism, which support this finding. Garnham *et al* made one such discovery in reporting the first X-ray structure to capture ice-like water molecules hydrating a bacterial AFP known as MpAFP.[149] The reason why this is so rare and important is that crystal structures normally capture multiple AFPs, which are close enough to each other that they distort the few surrounding crystal waters that separate them. However on this occasion the authors found a region of unaffected and solvent exposed ice binding site.[75,149] From studying the hydration of these proteins, the authors postulate that the proteins residing in the QLL order water around itself into an ice-like configuration using hydrophobic groups, (rather than binding to a plane and releasing surrounding waters for an entropic gain). The ice-like structures are anchored by H-bonds to polar groups on the protein backbone or side chain (at the edge) and so the protein can approach the ice lattice with its own "ice" ligand or binding site, which they termed an "anchored clathrate".[75,149] This theory was first proposed based on MD simulations by Nutt and Smith in 2008[148] and Garnham *et al* go on to describe that the most effective anchoring would be achieved by polar groups spaced by apolar groups. This is not necessarily the same way that the polymers function however; this theory explains why most reported ice binding faces are flat and hydrophobic.[148] It explains the

unusual concentration dependence. It explains why the type 3 AFPs function as antifreezes, although they are globular and not bristled with many OH groups. It also explains occasions where it is possible to observe a decrease in TH during mutation studies by changing hydrophobic residues to hydrophilic, as well as the reverse across different AFP classes (*e.g.* Ala $\longrightarrow$ Thr in Type 3 or Thr $\longrightarrow$ Ala in Type 1).[75] A delicate balance of the two interactions might therefore be in order and if this were the correct route; a new question arises as to what this balance may be.

Garnham *et al* expanded further that with this as a predominant mechanism one would expect to see high residence times of a number of water molecules at the ice binding face (IBS), which they do across different classes of AFP[149]. Once a certain number of these slowed water molecules (*i.e.* "a quorum") are achieved the ligand formation begins. Notably the mobility of liquid water is hampered at the QLL[26,154,163] where the protein resides, which makes the concept of quorums forming at the IBS even more feasible at low temperatures. In solution, these quorums are likely to be affected by higher temperatures as well as by mutation studies, so Garnham *et al* also recommend that the relationship between TH and mutation studies be re-examined on the basis of IBS hydration, rather than hydrophobicity alone.[149] Note that this does not appear to be the case for hyperactive AFPs.[165]

Rightly so, Nada and Furukawa raised the question of inherent bias in setting up the AFP's initial environment in simulations — how do we decide where to place the AFP at the start of the simulation?[160] Ideally, the AFP would be unconstrained and allowed to migrate from the liquid phase itself as it would in experiments, rather than placing the AFP directly onto the QLL in order to save simulation time.[153,160] Particularly as experiments have no way of guiding investigators to identify how far into the QLL that the proteins may reside. Considering that in experiments, the AFP solutions are frozen and the ice-water interface begins to grow, it is crucial to observe the AFPs in these growth environments as well, rather than at static temperatures which maintained stable ice crystals alone.

A recent study by Wierzbicki *et al* also already addressed this criticism.[143] They used potential mean force (PMF) profiles to show the free energy penalty in placing the Type 1 AFP at a range of distances from the midpoint of the QLL. Based on the PMF results they suggested that the hydrophobic face (Thr-Ala-Ala) would be the most likely to approach the ice as it interacted more favourably with the ice than the hydrophilic face ((Thr-Ala-Asx), and so could draw closer. The basic assumption was that a face specific adsorption was required. The authors found that the lowest energy penalty was produced whilst approx. 0.75 nm away from the center of the ice/water interface, which coincides with the start of the QLL envi-

ronment. Using the hydrophobic face, they calculated a -3.5 kJ mol^{-1} free energy difference compared to bulk water as reference. This is approximately 0.5 kJ mol^{-1} more favourable than for the hydrophilic face at its optimum distance of 0.9 nm, which happens to fall outside the QLL region and inside bulk water.[143] They also found two interesting details. Firstly, that the hydrophobic face in contact with the QLL encouraged an additional number of 13 close contacts (or H-bonds) than compared to the bulk, while no real difference was observed for the hydrophilic face. Similarly, they found that the contact surface area of the protein increased with the hydrophobic face from 85.7 nm to 89.2 nm and again, no real difference was observed for the Thr-Ala-Asx face.[143] These findings, which were reported in also 2007 support the proposal and observations made later by Garnham *et al* [149] in 2011.

In the past, the same faces had been studied[143] and conflicting findings were reported, however this only goes to show how insufficient sampling from short trajectories or poor system set ups (*e.g.* in *vacuo* environments) can affect the representation of the real life mechanism. Newer studies by Nada and Furukawa[158–160], Todde *et al* [166,167] and Kuiper *et al* [168] are discussed in later sections. These authors have all made important contributions by making improvements to the system set up, the water models they select to accurately represent the phase diagram of water, and they thoroughly characterize the AFP in the presence of these ideal environments under much longer timescales – in the presence of stable crystals and during crystal growth.

1.4.3 Polymer simulations

Proline based polymers

Simulations of hydroxyproline or proline are typically produced to investigate the influence of substitution on the protein side chains or backbones to the secondary structure of a protein (or water structure around a protein). Take collagen for instance, where hydroxylation of prolines occurs and stabilizes the triple helix. Park *et al* (2005)[169] explored the importance of ring puckering conformations on this process using MD simulation. They found that previous attempts to include hydroxyproline in calculations had not given the correct puckering as known to experiments. So they proposed a new set of parameters, which reproduced the correct puckering preference at 300 K using the AMBER FF.[169]

A recent paper by Yu *et al* [170] demonstrated that the rigid, and hydrophilic proline molecules induced slow diffusion dynamics in vicinal water molecules. The water molecules also experienced an increased distortion of their HBN and a loss

in tetrahedral orientation. For instance, a solution consisting of 96.2% water and 20% w/w proline, produced a 15% drop in tetrahedral orientation compared to bulk water. The reason for this behavior is that a 5-membered proline ring, which is similar to poly(hydroxyproline), passes on its rigidity to vicinal waters. Clusters of surrounding water molecules exhibited H-bonding angles, which are restricted to 79° and 99° rather than the ideal 109° for tetrahedral orientations. In this study they used the OPLS-AA FF, and the TIP4P water model at room temperature to investigate the properties of proline concentration between 0–76% w/w.

Another recent study by Nizaga *et al* [171] examined the backbone solvation of three homopolymers poly(proline) (PPRO), poly(hydroxyproline) (PHYP) and poly(hydroxyproline-β-galactose) (PHYP-Gal), each 9 units long. As is common in these types of simulations, they used AMBER and TIP3P water model for 100 ns. α-, β-, PPI- and PPII helices are three well known helical secondary structures which proteins can adopt, and these are characterized by the respective backbone dihedral conformations (ϕ, ψ) are equal to (60°, 50°), (120°, 120°), (75°, 160°) and (75°, 145°) respectively. They probed the differences in solvent-polymer backbone interactions between PPI and PPII helical conformations within the three polymers. In agreement with experiments, they found that both PHYP and PHYP-Gal polymers preferred a PPII helical conformation in water because it obtained greater number of H-bond interaction with the water solvent than with PPI.

Interestingly neither PHYP nor PPRO exhibited any significant intramolecular interactions in the PPII conformation, and as a result these polymers obtained similar, high levels of interactions with the solvent. In contrast, glycosylation reduced the number of H-bond interactions with the solvent. The authors also found that aliphatic solvents such as alcohols could completely change the polymer's preference to the PPI helix and so they concluded that a small or large change in hydrophilicity could be induced by adding groups like sugars and by careful solvent selection respectively. The group proposes that the galactosyl residue may alter the solvent accessible surface area, in order to interact with the protein backbone. Of the three homopolymers, it was the only one to exhibit intramolecular interactions (between the galactosyl O6 hydroxyl group and the protein C=O carbonyl group) and these lasted for approximately 5% of the simulation trajectory. This study goes to show that polymer or protein secondary structure can be governed by solution-polymer interactions (or its side chains), at times more so than the intramolecular interactions. It reiterates that the changes in conformation might also be important in elucidating mechanisms such as the ice binding of protein.

Poly(ethylene glycol) polymers

A number of simulations of PEG (aka polyethylene oxide or PEO for short) in solution have been reported in the literature. Due to their amphiphilic nature, these polymers are soluble in water as well a vast range of organic solvents like methanol, chloroform and benzene. MD simulations by Hezaveh *et al* [172] have been used to understand the interactions of PEO_{2-43} with these solvents at 298 K.[172] They modelled the polymer using united atom models and the GROMOS/OPLS-UA FF. The PEO O-C-C-O dihedrals adopted gauche conformations in water and trans conformations in apolar solvents, which is consistent with available NMR data. For the R_g the power law dependence with chain lengths for PEO also showed good agreement with experiments. They reported expansion of polymers in polar solvents (methanol) and contraction in apolar solvents (chloroform, carbon tetrachloride and n-heptane), relative to bulk water and as indicated by the R_g calculations.

Lee *et al* also calculated the R_g for PEO_{9-27} oligomers using a revised C35r CHARMM FF. They obtained an exponent of 0.515 ± 0.023 which relates the R_g to molecular weight.[173] Although the value is also in agreement with experiments it is still smaller than the expected 0.588, and deviates further than the value achieved whilst using the OPLS FF (0.59).[172] Oelmeier *et al* [174] conducted a similar study using PEO_{6-81} and the AMBER FF. They studied single polymer chains in solution for 10–30 ns and obtained an exponent of 0.54. In agreement with these previous simulations, PEO was described as a random coil in solution with a preference for the gauche conformations. Unsurprisingly this forcefield also yielded a Flory exponent between 0.5–0.535, which is acceptable but still lower than the experimental value.[174]

Poly(vinyl alcohol)

Simulations of PVA have been used to understand the miscibility of binary blends or polymer melts for a range of applications; coatings, adhesives and hydrogels. Hydrogels are of particular interest because they are used extensively in biomedical applications such as drug delivery, tissue engineering and pervaporation membranes (used to separate mixtures of liquids).[175] They are formed from network of crosslinked polymers, which have the ability to retain water, so their structure is largely characterized by crosslinking density, and has the ability to influence the diffusion or release of molecules. Because the swelling of PVA membranes in aqueous solution results in a decrease in mechanical strength, early studies predominantly focused on the effect of percentage water content on the state and structure of water in PVA.

These targeted cross-linking systems typically include multiple polymers or polymers with long chain lengths, which match the behaviour of real polymeric systems. A few groups – Tamai *et al* [176–178], Müller Plathe *et al* [57,179,179,180], Wu *et al* [181], Zhang *et al* [182] and Chiessi *et al* [183] – performed extensive MD simulations of PVA in water. Through their works, these authors have demonstrated that the solubility of PVA declines in the presence of supercooled water, and highlight that temperature may in fact have more of an influence on the structure of PVA than just the water content.[181] As a result, more recent studies concern themselves with the influence of water and temperature on the behavior of PVA, while only a handful focus on shorter chain lengths in dilute solutions.[57,181,184] Advantages of these new systems are largely due to the fact that there are fewer segmental motions and so the time required for relaxation/equilibration is drastically less demanding. They are also useful towards the efforts in characterizing the polymers as function of chain length, obtaining scaling factors for properties used to characterize polymers. Below is a brief summary of the literature.

PVA and swelling Zhang *et al* [182] and Muller-Plathe *et al* [179] studied the swelling properties of PVA and its hydrogels in binary solutions of water and ethanol. Results from their MD simulations showed that PVA swells with increasing water content in alcohol-water mixtures. These findings were observed by calculating the free volume using a solvent sized probe to trace the contours of polymers and obtain the exposed O'Connelly surface. As as a direct result of increased mobility and disorder of PVA chains, the densities of swollen PVA decreases with increasing swelling.[182] Their study found that a solution containing 15%, 30% and 45% weight water, caused syndiotactic PVA_{50} networks to swell by 22.13%, 39.10% and 84.21% respectively. The reason for this is that large holes formed, which water molecules inhabit and these increase in size for systems with greater water content. Diameters of up to 0.90–1.10 nm were found to occupy 0.36% of the system containing the most amount of water. Inside the membranes, they also found a selective absorption for 76.61–81.30%, water rather than the larger ethanol molecules. A continuation of the work revealed that the calculated diffusion coefficient of the carbon backbones were 2.95, 10.83 and $22.7 \times 10^{-8}\,\mathrm{cm^2\,s^{-1}}$ at 323.2 K. However the diffusion rates of water were not consistent with experimental values or trends at low water contents, which casts a shadow over the reliability of hydration properties and highlights the importance of careful selection of water models used.[182]

PVA in the cold In 1993, Tamai and Tanaka studied atactic PVA_{21-161} hydrogels subjected to both supercooled and warm temperatures between 200–400 K using 28–100% w/w SPC/E water and the AMBER/OPLS FF.[176,178]

PVA and water diffusion Müller-Plathe reported a concentration (and temperature) dependence of water diffusion in atactic PVA_{400} for systems between 3–100% weight water. They found that at cooler temperatures and higher water content, PVA drastically reduced the rate of water diffusion. At 300 K, they found that the SPC water model's self-diffusion constant was $3.32 \times 10^{-5}\,cm^2\,s^{-1}$ and in a 34% water solution fell by an appreciable 91%. At 375 K the constant dropped by 87% to $1.3 \times 10^{-5}\,cm^2\,s^{-1}$. These studies employed short timescales of 2–16 ns.[180]

PVA and temperatures Wu *et al* [181] investigated the influence of temperature on an atactic PVA_{300} in 21% weight water (200 TIP4P water molecules) in 10 ns production runs. They studied temperatures between 200–420 K using 20 K intervals. They found that a cooperative behaviour between the PVA chain and water were responsible for the T_g, by evaluating the total number of H-bonds per hydroxyl group for water-water, water-polymer and polymer-polymer interactions. They arrived at this conclusion because a marked transition occurs in the H-bond number of water-polymer interactions, at the T_g temperature, while negligible changes occur at this temperature for the other two categories. Although the OPLS-AA FF could be used to model atoms in PVA, Wu *et al* took partial charges from the COMPASS FF and applied them using the OPLS-AA FF and the GROMACS simulation software. This approach is not recommended because it creates an untested hybrid of forcefield parameters which requires evaluation. They found a T_g of 283 K, which is drastically different from the experimental value of 385 K, although it lies between the T_g values for pure water (134 K) and PVA. It goes to show the importance of careful forcefield selection (Wu attributes this to the large rate of cooling).[181]

In another study, Tesei *et al* [183] investigated atactic PVA_{30} in 97% (w/w) water and three different temperatures; 293 K, 303 K and 323 K over a 90 ns period. They explored the effects of two different GROMOS FFs and they found the later version was more suitable because they represented the results from aqueous experiments best. The differences between the two were largely due to variations in intensity of interactions between the polymer and water. The chain size, polymer conformation and H-bonding of PVA were studied. They used the R_g to describe polymer chain extension and found that bimodal or trimodal distribution fits were useful depending on the forcefield used. Their study revealed that temperature

induced transitions between a globular form and extended coils in solution. The R_g distribution for the better forcefield was trimodal, with peaks at 0.80–0.84 nm, 1.03–1.06 nm and 1.34–1.60 nm, which begin to converge at elevated temperatures.

PVA and tacticities Although tacticities of a polymer greatly affects its properties, few simulations have addressed the effects on PVA, even though it may be important for its IRI potency. Remarkably this too has not yet been explored in experiments. In 2013 Norjahan and Choi [185] investigated the effects of tacticity as well as temperature (200–550 K) on specific volumes, the thermal expansion coefficient, the glass transition temperatures and the solubility of the PVA_{400} polymers. They used the OPLS-AA FF and the TIP4P water model, which has a melting temperature of 232 K. This means that over a 100 ns period, they explored a temperature range between T_m-32 K and T_m+318 K, using a 10 K interval. They found that aside from overestimated heat capacities, the systems reproduced the thermal properties found in experiments, and whilst within the amorphous phase all the properties of the stereoisomers produced similar values except for the solubility parameters. The isotactic structure was the most soluble, followed by the atactic and finally the syndiotactic structure. Surprisingly they found that the T_g was insensitive to tacticity in MD simulations, however an average T_g of 350 K was obtained, which falls within the experimental range of 325–375 K. [185]

Antifreeze protein analogues

There are even fewer simulations investigating antifreeze protein analogues or polymers with the intent of investigating their properties for antifreeze purpose. To our knowledge, and to this respect, Tam *et al* [116], Corzana *et al* [186] and Kim *et al* [187] presented the only simulations of antifreeze analogues in solution between 2006 and 2010. Tam *et al* [116] also produced a complimentary review and study of C-linked antifreeze glycoprotein analogues, using both experiments and *in silico* methods. The AFGP analogue system was modelled in solution for 10 ns at 300 K using the AMBER FF and the TIP3P water model, consisting of 2000–3000 water molecules. The authors found that the intermediate side chain lengths of three carbons was necessary for IRI activity, whilst values smaller or greater than this exhibited no IRI activity (*i.e.* one, two or four carbons). Their simulations studies reveal that the IRI active structures adopted a unique conformation in solution that permits folding into the peptide backbone, and buries the hydrophilic face of the carbohydrates away from the bulk solvents. This folding behaviour characteristically brings the carbohydrate moiety closer to the peptide backbone, which can form a hydrophobic

pocket that may be used to approach the QLL. Conversely, the IRI inactive peptides have their hydrophilic moieties completely exposed.

Interestingly they did not manage to identify any H-bonds between the amide protons and other H-bond acceptors. They also noticed that the more potent IRI active peptides (with longer side chains) hosted weaker H-bonding between the C4 and C6 galactosyl hydroxyl groups (HO4 and HO6), than than the less potent one. (Please see Fig. 1.8 for an example for carbon numbering). They suggest that, as with carbohydrate systems, the interaction of HO4/HO6 atoms with adjacent water molecules is crucial to IRI potency, rather than for interactions between AFGP-analogues.[116] To test this theory further, the energy penalty was also calculated as a function of rotating the linker bond between the carbohydrate side groups in relation to the protein backbone. They found that the energy penalty was highest for the IRI active peptides, which is consistent with their hypothesis. They propose the stereochemistry of these hydroxyl groups, and the folding of the carbohydrate moiety is directly related to regulation of the hydration environment of the peptides (as previously shown with O4 hydroxyls on carbohydrates).[116] Especially in the light of recent work by Davidovic *et al* [116,188], which reported, that cold induced denaturing of proteins is often accompanied with an unchanged hydration sphere at 273 K. If this is certainly the case then these IRI active C-linked AFGPs analogues may be able to help with modulation of the hydration state accordingly.

Although the referenced IRI experiments were undertaken at the same temperature as Davidovic *et al* [116,188], the same cannot be said for the simulation studies conducted at room temperature. In order to confirm their speculations, new simulations would need to be conducted to re-evaluate the behaviour of the truncated peptides at 273 K and possibly even in contact with ice. From their study it is clear that the side chain length is important for conformational changes in order to influence hydration of the AFGP analogues, which in turn affect their potency.[116]

Similar to Tam *et al* [116], Corzana *et al* [186] conducted modelling studies which also support these findings that the carbohydrate moiety's interaction with surrounding water influences the conformation of the peptide, its flexibility and the structuring of vicinal water molecules.

1.5 Aims and Objectives of the Thesis

The aim of this thesis is to use MD simulation to model antifreeze polymers at the ice/water interface in order to identify what interactions are responsible for their mechanisms of action. We use the proposed mechanisms which have been outlined

in section 1.3 as a starting point for our study . The remainder of this thesis is outlined as follows. Chapter 1 summarises the motivation for this study and provides a review of the key experiments, which have contributed towards our understanding of the mechanism of AF(G)Ps and their mimics. Chapter 2 presents a summary of the simulation theory. In Chapter 3, we examine the ability of TIP4P/Ice water model to predict the properties of liquid water and melting point of ice. This chapter is also a forcefield validation for the mixing of TIP4P/Ice water model with the OPLS-AA forcefield. The solution properties of PVA and PEG are reported in Chapter 4. In this chapter we characterised properties of both polymers in solution prior to placement at the ice/water interface in Chapter 5. Chapter 6 presents our work of poly(hydroxyproline) in solution and in the ice/water systems. Finally, we conclude with a brief discussion and present an overview of future directions.

Chapter 2

Computer Simulation Methodology

A central aim of scientific research is to enable a deeper knowledge of how things work. By studying the motion of their constituent molecules, researchers can begin to understand the mechanisms for chemical reactions, molecular recognition and many other processes. Molecular dynamics (MD) is a computational technique used to simulate the movement of molecules or atoms over time. It uses mathematical models to calculate the potential energy from interactions between large numbers of atoms in the system, and generates a trajectory by numerically integrating Newton's equations of motion (Eq. 2.1) at regular intervals, updating the atom positions. $\boldsymbol{F}_i$ is the force, m_i is the mass and $\boldsymbol{a}_i$ is the acceleration, $\boldsymbol{v}_i$ is the velocity and $\boldsymbol{r}_i$ is the position of the atom, i.

$$\mathbf{F_i} = m_i \mathbf{a_i} = m_i \frac{\delta \mathbf{v_i}}{\delta t} = m_i \frac{\delta^2 \mathbf{r_i}}{\delta t^2} \tag{2.1}$$

MD simulations provide atomistic resolution and describe the dynamics and static properties of a system. Given the use of an accurate model system, sufficient sampling time and a suitable number of molecules to average over, these inherent features mean MD simulations provide strong predictive capabilities, and so they are also used to supplement experiments where sampling is untenable *via* traditional experiments or techniques.

2.1 Statistical mechanics

The thermodynamic and structural properties of a system can be described by either macroscopic (volume, pressure, temperature, number of particles) or microscopic properties (momentum, ($\mathbf{p_i} = \mathbf{v_i}\, m_i$) and $\mathbf{r_i}$ positions). Classical computational simulations measure the instantaneous position and velocities of 10^2–10^6 particles at a given time, while experiments measure the average properties of a system over time and a large number of particles in the order of 10^{23}. For example, X-ray crystallography and NMR spectroscopy can provide 3D structures of biomolecules and details about the their local motion.[189]

Statistical mechanics is applied to make the classical computational simulations comparable to experiments so that they can be useful for interpreting results or guiding future experiments, and one can extract these averages from the simulations. It links the microscopic properties to the macroscopic ones such as heat capacities, diffusion coefficients and pressure by applying a statistical distribution functions to set of configuration in a systems which has reached equilibrium.

An ensemble describes the collection of microstates, while the phase space represents the space in which all possible states of the system are represented. Each microstate corresponds to a unique point in the phase space: $\mathbf{\Gamma} = \mathbf{r_1}, ..., \mathbf{r_N}, \mathbf{p_1}, ..., \mathbf{p_N}$, where N is the number of atoms. This is a 6N-dimensional space, consisting of 3N positions ($\mathbf{r} = r_x, r_y, r_z$) and 3N momenta ($\mathbf{p} = p_x, p_y, p_z$).

The time evolution of the system can be described as a trajectory through phase space, so given an infinite trajectory, it is possible to explore all parts of the phase space of ergodic systems that have reached equilibrium. So, longer simulation trajectory would cause the averages to converge towards the true value of the measured thermodynamic properties. By sampling many microstates which span the part of phase space that satisfies the constraints placed on the system, a picture is formed of the probability distribution for a given microstate to occur at time t. This is known as the time average (Eq. 2.3), while the experimental average is known as the ensemble average (Eq. 2.2).

$$\langle A \rangle_{time} = \lim_{\tau \to \infty} \int_{t=0}^{\tau} A(\mathbf{p}, \mathbf{r}) dt \approx \frac{1}{M} \sum_{t=1}^{M} A(\mathbf{p}, \mathbf{r}) \tag{2.2}$$

A is the observable of interest, M is the number of time steps, τ is a large, finite number of steps and $A(\mathbf{p}, \mathbf{r})$ is the instantaneous value of A.

$$\langle A \rangle_{ensemble} = \int\int A(\mathbf{p}, \mathbf{r}) \rho(\mathbf{p}, \mathbf{r}) d\mathbf{p} d\mathbf{r} \tag{2.3}$$

The integration is over all possible variables of $\mathbf{r}$ and $\mathbf{p}$ and the functional form of the probability density, ρ, is determined by the chosen fixed macroscopic variables, which in turn define the statistical ensemble itself. (Eq. 2.5).

$$\beta \equiv \frac{1}{k_B T} \tag{2.4}$$

$$\rho(\mathbf{p}, \mathbf{r}) = \frac{1}{Z} e^{-\beta E_s} \tag{2.5}$$

E_s is the total energy of the system when it is in a microstate, s. In this thesis, we are only concerned with the canonical ensemble (NVT); a fixed number of particles, constant system volume and temperature, and the isothermal-isobaric ensemble (NPT); a fixed number of particles, constant system pressure and temperature. Eq. 2.6 describes the canonical partition function, Z, where the incorporation of Eq. 2.6 into Eq. 2.5 provides the probability that the system occupies a certain microstate at constant volume and temperature. Similarly, Eq. 2.6 describes the isothermal-isobaric partition function where P and V stand for pressure and volume of the microstates respectively.

$$Z = \sum\nolimits_s e^{-\beta E_s} \tag{2.6}$$

$$Z = \sum\nolimits_s e^{-\beta (E_s - P V_s)} \tag{2.7}$$

2.1.1 Ergodicity for polymers

The timescales of polymers motions are dependent on chain length and entanglements, which mean that it can take a relatively long time for systems with large polymers to equilibrate in comparison to smaller molecules. This feature makes it challenging to produce meaningful simulations of N-body polymeric systems unless one is able to further improve on ergodic sampling. As mentioned earlier (see § section 1.2.3), polymers behave as ideal chains under theta conditions and become extended in solution.[56]). One can argue that non-ergodicity effects should be small provided that one starts from an extended configuration, uses small polymer chains, studies single polymer systems and uses sufficiently long simulation timescales. Fig. 2.1 gives the typical timescales that are found in experiments for

different types of motions including biological polymers such as DNA.

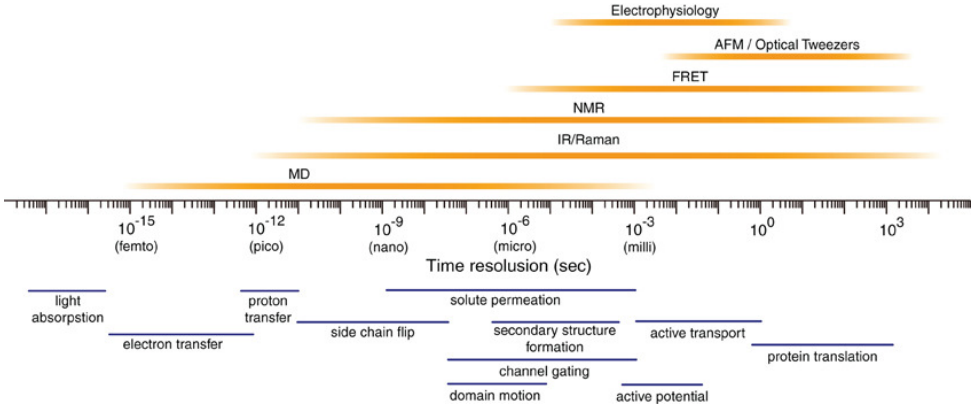

Figure 2.1: Schematic of the timescales of select atomic or molecular motions and various instruments that can be used to probe these motions: Atomic Force Microscopy (AFM), Fluorescence Resonance Rnergy Transfer (FRET), Infrared Radiation (IR) and Nuclear Ragnetic Resonance (NMR). Image reprodcued from Ref. 10.

2.2 Forcefields

Interactions between atoms must be adequately described in MD simulations. A forcefield is a set of mathematical equations, which describe the potential energy (U) of a system of particles (Eq. 2.8). In a nutshell, forcefields determine which atoms are allowed to interact and how. These include descriptions of bonded and non-bonded terms, which are discussed in the next section, and they also detail constants such as the atomic masses and radii.

$$U = U_{bonded} + U_{non-bonded} = (U_{bond} + U_{angle} + U_{dihedral}) + (U_{electrostatic} + U_{vdw}) \quad (2.8)$$

Among the vast range of forcefields, some of the most commonly used are CHARMM[190,191], AMBER[192], GROMOS[193] and the OPLS forcefield[194], all of which were derived from a combination of experiments and quantum mechanical studies of small molecules. These in turn yield more reasonable models of proteins and organic systems. However, the onus lies on individuals to determine whether these parameters are transferable to their own systems and molecules of interest.

2.2.1 Bonded interactions

Bonded interactions are treated as ball and stick models of atoms, which oscillate harmonically. There are 3 types: bond stretching, angle bending and dihedral angle rotation (Fig. 2.2). For each unique pair of atoms, covalent bonds (U_r) are described by the functional form in Eq. 2.9.

$$U_r = \sum k_r(r_{ij} - r_{eq})^2 \tag{2.9}$$

The forcefield details an equilibrium distance (r_{eq}) between the two atoms and any deviations away from that distances incurs an energy penalty, which is added to the potential energy. The functional form for angles (U_θ), proper dihedrals (U_Φ) and improper dihedrals (U_Ψ) are also treated in a similar fashion (Eq. 2.10–2.12 respectively). U_Ψ is the torsonial energy associated with maintaining a planar geometry or the correct chirality of a molecule. In each equation k_r, k_θ are force constants, k_Ψ is the peak height, n is the frequency, and Ψ is the phase. All constants are highlighted in red and sums are over a combination of atoms pairs, triplets or quadruplets for bonds, angles and dihedrals respectfully.

$$U_\theta = \sum k_\theta(\theta_{ijk} - \theta_{eq})^2 \tag{2.10}$$

$$U_\Phi = \sum k_\Phi(1 + cos(n\Phi - \Phi)) \tag{2.11}$$

$$U_\Psi = \sum k_\Psi(\Psi_{ijkl} - \Psi_{eq})^2 \tag{2.12}$$

2.2.2 Non-bonded interactions

Non-bonded interactions are composed of two parts; the van der Waals and Coulombic terms. Calculations for this part of the simulations are typically the most computationally expensive part of MD simulations, because interactions need to be evaluated between thousands of atoms at each time step. As users, we often have to make trade-offs between the accuracy and efficiency of these calculations. In order to run longer simulations we therefore aim to reduce the cost of computation and favour efficiency. In practice, one way of doing this is to calculate only the interactions between pairs of atoms, rather than all possible combinations like triplets or quadruplets and so on.

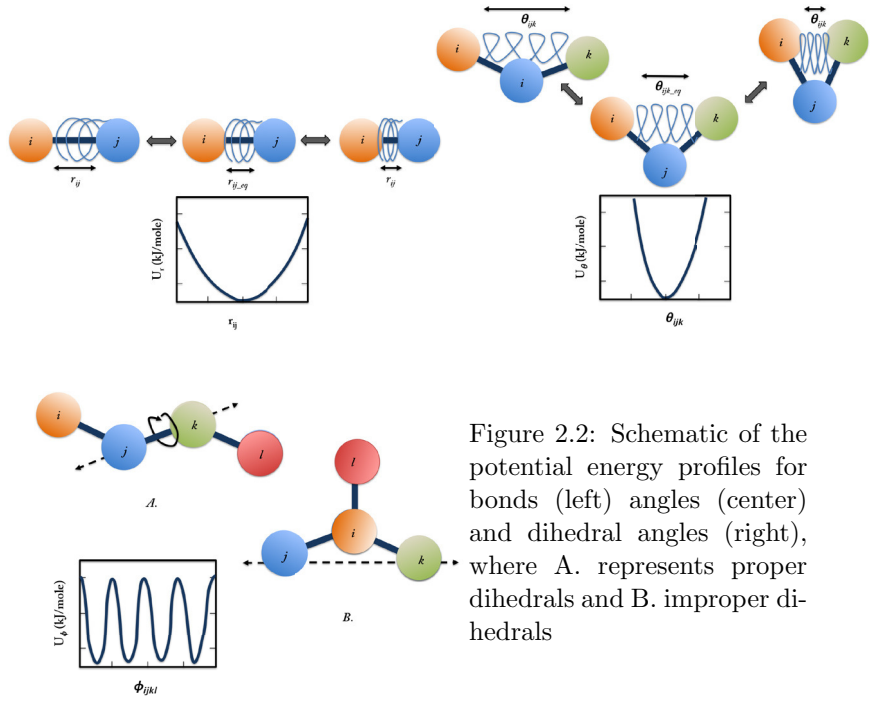

Figure 2.2: Schematic of the potential energy profiles for bonds (left) angles (center) and dihedral angles (right), where A. represents proper dihedrals and B. improper dihedrals

Van der Waals

Van der Waals forces are described by the Lennard Jones (LJ) 6-12 potential (U_{LJ}); where attractive forces are long range (r_{ij}^{-6}) while repulsive forces dominate at shorter (r_{ij}^{-12}) distances (Eq. 2.13–2.15). To further reduce the cost of computation, cut-off distances are typically used with van der Waals interactions, and atoms that are separated by distances greater than the cut-offs are ignored or approximated. The reason why cut-offs can be used in this instance is because van der Waals interactions decay rapidly to zero as distances increase. As a result, by the time they reach the cut-off distances, their potential energies are so small that they are considered negligible. To date there are various methods for applying LJ tail corrections (also commonly referred to as cut-offs), for example the truncation, SHIFT and SWITCH methods.[195] Truncation means that interaction energies are simply set to zero at the cut-off distance or discontinued. However, this abrupt change can lead to poor energy conservation and infinitely large artificial forces in the latter case. The SHIFT method essentially shifts the entire potential energy surface (*i.e.* the LJ potential curve) so that the interaction potential energy is zero at the cut-off distance and it typically results in higher energies and smaller equilibrium distances

between the atoms. Finally, the SWITCH method serves as a combination of the two. Two cut-off distances are defined and within the small range between them the interaction potential gradually settles to zero, using a smooth scaling function. A schematic of the tail correction schemes is shown in Fig. 2.3.

$$U_{LJ} = 4\epsilon_{ij}((\sigma_{ij}/r_{ij})^{12} - (\sigma_{ij}/r_{ij})^{6}) \tag{2.13}$$

where a geometric average is used to calculate the two parameters in the OPLS-AA FF for:

$$\sigma_{ij} = (\sigma_{ii}\sigma_{jj})^{\frac{1}{2}} \tag{2.14}$$

$$\epsilon_{ij} = (\epsilon_{ii}\epsilon_{jj})^{\frac{1}{2}} \tag{2.15}$$

$$\tag{2.16}$$

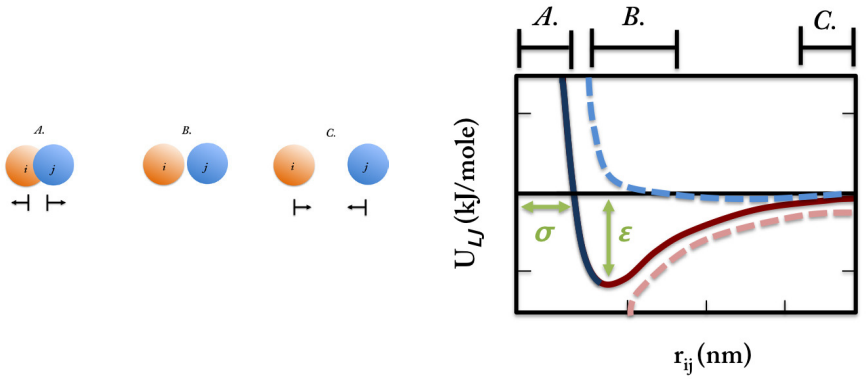

Figure 2.3: Schematic of the LJ potential, where (A) describes the dominance of the repulsion term at short distances (blue), (B) is the optimum energy and equilibrium distance and (C) is the attractive term at long distances (red)

Coulomb potentials

The Coulomb potential is used as the functional form for modelling electrostatic interactions between a pair of charged atoms. The formula is shown in Eq. 2.17, where q_i is the charge for atom i, r_{ij} is the distance between atoms i and j and ϵ_0 is the dielectric constant (also known as the permittivity).

$$U_{Coulombic} = \frac{q_i q_j}{4\pi\epsilon_0 r_{ij}} \tag{2.17}$$

Compared to van der Waals, electrostatics is considered longer-range which means that it takes much longer to decline with distance. To be exact it declines as r^{-1}. It is therefore ideal to completely avoid truncation-style cut-offs, which can lead to huge errors and unphysical results. As electrostatic interactions play a serious role for many properties seen in real systems such as transport properties and protein folding, other methods are commonly used for these interactions, mainly switching functions (mentioned earlier) or Ewald summation techniques.[196]

Ewald summations

Ewald summation is a technique for calculating electrostatic interactions, which also considers periodic images (see § 2.4.5). It works by splitting summations into long- and short-range components. The short-range contributions fall within the cut-off distance and so are treated as normal (*i.e.* in real space), while the long-range contributions are calculated using a Fourier Transform (FT).

The Ewald sum scales as $O(N^2)$ for a system of N atoms, so variant methods such as the Particle Mesh Ewald (PME)[197,198] have been developed to speed up calculations (by an order of O(NlogN)). The PME algorithm uses a cardinal B-spline interpolation; it partitions the simulation box into a 3D grid and uses Fast FT to interpolate the charges from the long-range contributions onto the nodes of the grid. The charges are summed over the grid in Fourier space and the resulting charges are then interpolated back into real space.

2.2.3 Water forcefields: 3-site and 4-site models

Water forcefields describe how water molecules are represented in simulations. The most common water forcefields are typically 3-site or 4-site rigid models (discussed in Chapter 3). These are ordinarily designed to mimic one or more properties of real water using a combination of experiments and computational techniques. Over the years various water models have been developed to account for the different properties of water such as dielectricity, density, heat of vaporization and the phase diagram of water. The different types of explicit water models are ordinarily classed according to the number of sites, flexibility (or rigidity) and polarisability. Both types of water models are depicted in Fig. 2.4. A 3-site water model is planar and has 3 atoms; an oxygen atom that carries a partial negative charge and two hydrogen

atoms that are positive. In contrast, a 4-site water model has an added, massless dummy atom that resides at the bisector of the water molecule. In this model the negative charge is moved away from the oxygen and placed on the dummy atom in order to represent the lone pairs of the oxygen. Compared to the 3-site water models this change is known to improve the electrostatic distribution around water molecules in the condensed phase.[199–201]

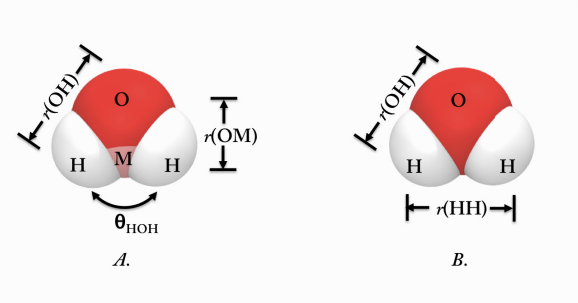

Figure 2.4: Schematic of (A) a 4-site water model and (B) a 3-site water model, where O-H bond lengths typically vary between 0.0957–0.100 nm and HOH angles between 104.52°–109.5°.

Today, the refinement of water models have advanced to support the different simulation parameters such as Ewald style treatments of the electrostatics, and not solely the properties of water. Unsurprisingly, the greater the model's complexity, the longer the time taken for computation especially considering the enormous number of water molecules required for solvation. To avoid this, implicit solvation can also be used, where water molecules are represented by a distance dependent dielectric-screening function. This approach reproduces the average behaviour of water molecules screening the interaction between two non-solvent molecules, however the disadvantage is that interesting interactions between water molecules and non-solvent molecules cannot be reproduced.[202]

In 2002, Guilliot *et al* [203] produced a comprehensive review of the older water models, in order to help us decide which one is best to use. The way that the polymers are able to interact with both ice and surrounding water is very much dependent on which model is chosen. Seeing as water is ubiquitous in nature and plays a crucial role in almost every biological and synthetic process, we need to pick a reliable model to ensure our simulations are useful. In this report, we predominantly work with a 4-point water model called TIP4P/Ice[204] water model, which has been designed to describe the phase diagram of water. Its use, advantages and

forcefield parameters are discussed further in Chapter 3.

2.3 Potential energy minimization

Energy minimization methods (EM) are conducted to obtain the equilibrium configuration of molecules, which is often necessary to produce stable and experimentally relevant MD simulations. Initial structures are usually obtained from NMR or X-ray studies or built using a program, and then they are typically converted into lower-energy states of interest. EM can be achieved by using algorithms like the Steepest descent or the Conjugate gradient methods, which are used to search for local minima. These minimizations remove unreasonable or close contacts between given atoms in a system, which are often undesirable and unrealistic. Due to the complex nature of the potential energy surface, these algorithms typically bring the state to a local energy minimum, and not necessarily the global energy one. A schematic of this is shown in Fig. 2.5. To achieve the latter, simulated annealing and other computational techniques are often used.

In this work, we use the steepest decent algorithm, which is a first derivative algorithm and so is much faster than second derivative alternatives. The steepest descent conceptually works by re-evaluating the gradient of the potential energy as it is calculated. After each step, a displacement is added to the coordinates in the direction of the force and the size of this displacement or step is increased if the energy is lower than the previous calculated energy. Otherwise the step is reduced and the same loop is reiterated for a user-defined number of iterations, until convergence is reached, where the total energy of the system plateaus as a function of time. [202]

2.4 Molecular dynamics

In molecular dynamics simulations, starting coordinates for each atom are taken from experiments like X-ray crystallography, NMR spectroscopy or electron microscopy and initial velocities are randomly assigned to every atom from the Maxwell-Boltzmann distribution. This method for assigning initial velocities encourages equilibration distribution which would normally be expected at the temperature of interest. This approach is much better than initializing all the velocities to zero which is also fairly simple task, however would result in less stable structures because the atoms experience a thermal shock.

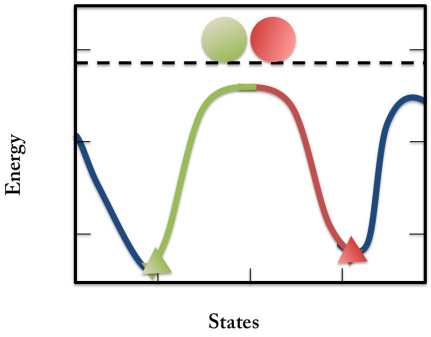

Figure 2.5: Schematic of a 1D cross section of the potential energy surface. The dashed line is the starting point for 2 different structures. The colours show their resulting end states at their different local minima, where green is the global minimum of the system.

Consider an atom i, of mass m_i, which moves from position $\mathbf{r_0}$ to $\mathbf{r_1}$, after a period of time $\delta\, t$ because it has an initial velocity of $\mathbf{v_0}$ (Eq. 2.18). The move to this new position, $\mathbf{r_1}$, can be described by (Eq. 2.19).

$$\mathbf{v_0} = \frac{\mathbf{r_1} - \mathbf{r_0}}{\delta t} \tag{2.18}$$

$$\mathbf{r_1} = (\mathbf{v_0}\, \delta t) + \mathbf{r_0} \tag{2.19}$$

The net force acting on atom i at this new position, is a direct consequence of all its interaction with every other particle in the system. The potential energy from bonded and non-bonded interactions are summed in order to produce a potential energy profile. Eq.2.20 describes the relationship between potential energy and force, which says that the force can be calculated from the negative gradient of the potential energy profile.

$$\mathbf{F_i} = -\frac{\delta U}{\delta \mathbf{r_i}} \tag{2.20}$$

Newton's second law of motion relates the calculated force to the acceleration of a particle of a given mass (Eq. 2.1). With this new force we can rearrange this equation to obtain a value for the atom's acceleration (Eq. 2.22), then calculate the new velocities at $\mathbf{v_1}$ using the old velocities (Eq. 2.23). Finally, from this new velocity one can calculate the new atom positions at time t_2, using the old positions (Eq. 2.24 and 2.25) and evolve the simulation in time for a predefined number of

iterations.

$$\therefore \mathbf{a_0} = \frac{\mathbf{F_i}}{m_i} = \frac{\delta U}{\delta \mathbf{r_i}} m^{-1} \tag{2.21}$$

$$\mathbf{a_0} = \frac{\delta \mathbf{v}}{\delta t} = \frac{\mathbf{v_1} - \mathbf{v_0}}{\delta t} \tag{2.22}$$

$$\therefore \mathbf{v_1} = (\mathbf{a_0}\, \delta t) + \mathbf{v_0} \tag{2.23}$$

$$\mathbf{v_1} = \frac{\delta \mathbf{r}}{\delta t} = \frac{\mathbf{r_1} - \mathbf{r_0}}{\delta t} \tag{2.24}$$

$$\therefore \mathbf{r_2} = (\mathbf{v_1}\, \delta t) + \mathbf{r_1} \tag{2.25}$$

2.4.1 Time integration algorithms

In practice the trajectory of the atoms are not calculated directly from Newton's equation of motion due to the lack of an analytical solution, because the 3D potential energy surface is very complicated. Rather, in order to calculate the force (*i.e.* the gradient), an efficient time integration algorithm such as the Verlet or leap-frog algorithm is used. The leap-frog[205] algorithm is described by Eq. 2.26–2.27. It's given this name because the positions (r) are obtained at time t while its velocities ($\mathbf{v}$) are determined at time t - $\frac{1}{2}\delta t$. Then, it updates $\mathbf{r}$ and $\mathbf{v}$ using the forces determined by the positions at time t:

$$\mathbf{v}_{(\mathbf{t}+\frac{\mathbf{1}}{\mathbf{2}}\delta \mathbf{t})} = \mathbf{v}_{(\mathbf{t}-\frac{\mathbf{1}}{\mathbf{2}}\delta \mathbf{t})} + \frac{\delta t}{m}\, \mathbf{F_t} \tag{2.26}$$

$$\mathbf{r}_{(\mathbf{t}+\delta \mathbf{t})} = \mathbf{r_t} + \delta t\, \mathbf{v}_{(\mathbf{t}+\frac{\mathbf{1}}{\mathbf{2}}\delta \mathbf{t})} \tag{2.27}$$

Each of these schemes are approximations (using the Taylor series expansion) that may result in errors over time such as energy drifts. Its crucial for the algorithms to minimise these and to preserve energy, in order to accurately represent the system and its forces. Due to the half-step calculations, the leap-frog algorithm is inherently more accurate than the Verlet method because the kinetic energy and temperature of the system would be calculated more frequently given the same same step size. This is a good example to highlight how truncations errors can be intrinsic to the algorithms used.

In order to minimize these errors, small time steps of 1–2 fs can be used, which capture adequate sampling of the fastest vibrational frequency. It is important to understand that the size of the time step limits the length of the CPU time, because the processes that one may want to study could occur under microseconds,

and so could require up to one million steps or iterations. In addition, these algorithms are also prone to rounding errors that are associated with the finite number of digits used in the computations. Although these errors are unavoidable they can be kept at a minimum by using double precision which is widely used in workstations today.

2.4.2 Constant temperature MD

Thermostats are coupled to the system in order to modulate the average temperature of the systems. The temperature is allowed to fluctuate about the average, and the thermostats function by by adding or removing energy from the system outside of the boundaries. Some of the most popular thermostats that are used in MD simulations are the Velocity rescaling[206], Andersen[207], Berendsen[208] and the Nosé-Hoover[209] thermostat, all of which help to reduce the energy drifts incurred by the calculations of the total energy over time.

Berendsen thermostat

The Berendsen algorithm is described by Eq. 2.28 and it weakly couples the system to the external heat bath at temperature T_0. It works by scaling the velocities of atoms gradually in proportion to the deviation of the average system temperature to T_0.

$$\frac{\delta T}{\delta t} = \frac{T_0 - T}{\tau} \tag{2.28}$$

As a result, a slow correction is applied to the system temperature (T), which makes this scheme suitable for equilibration. As a result the deviation decays exponentially with the coupling constant, *i.e.* the coupling strength (τ).

Nosé-Hoover thermostat

Although the Berendsen thermostat is an efficient method for relaxing a system, it is not considered suitable for representing a canonical ensemble because it also suppresses kinetic fluctuations. As a result the thermostat is not ideal for the purpose of calculating properties like the heat capacities. Once equilibrium has been reached it is important to probe the correct canonical ensemble and so the Nosé-Hoover[209] algorithm is more appropriate for this purpose because it is an extension of the Lagrangian approach to classical mechanics. Instead of constraining

the kinetic energy of the system, the Nosé-Hoover thermostat acts to keep the energy of the system close to the desired value. In order to achieve this it introduces a virtual thermal reservoir at position $\mathbf{r}$ and a friction term in the equations of motion. The friction force is proportional to the product of each atom velocity and a frictional parameter (ξ) — a dynamic property with its own virtual momentum ($\mathbf{p_i}$), virtual mass (m_i) and equation of motion (Eq. 2.30), for which the time derivative is calculated from the difference between the T and the T_0. The Newtonian equations therefore have the additional terms in Eq. 2.29, where Q is the coupling constant.

$$\frac{\delta^2 \mathbf{r_i}}{\delta t^2} = \frac{\mathbf{F_i}}{m_i} - \frac{\mathbf{p}\xi}{Q}\frac{\delta \mathbf{r_i}}{\delta t} \tag{2.29}$$

$$\frac{d\mathbf{p}\xi}{dt} = T - T_0 \tag{2.30}$$

Recall that T is proportional to the kinetic energy.

2.4.3 Constant pressure MD

Pressure coupling of an external barostat is added to the system in order to make it reminiscent of a physical experiment. The physical pressure is typically altered by adjusting the volume of the box analogous to the effects of a pressure piston. The most common thermostats used are the Berendsen[208] and Parinello-Rahaman[210] barostats. During the volume adjustments, the barostats also rescale the coordinates of the atoms which make up the systems so that they remain at the same relative distance from each other. Isotropic pressure coupling describes a uniform volume change, while semi-isotropic and anisotropic describe non-uniform scaling in a plane or separately in x, y and z directions respectively.

Berendsen barostat

Similar to its thermostat counterpart, the Berendsen barostat is also weakly coupled to the system and rescales both the box size and atom coordinates at every step towards a target pressure, P_0 (Eq. 2.31).

$$\frac{\delta P}{\delta t} = \frac{P_0 - P}{\tau_P} \tag{2.31}$$

Parinello-Rahman barostat

The Parinello-Rahman barostat is different in that it allows for a pressure and tem-

perature feedback mechanism. Similar to the Nosé-Hoover thermostat, it appropriates the Lagrangian treatments and leads to more appropriate NPT ensemble. The box vectors are represented by the matrix $\boldsymbol{b}$ and its equations of motion are given by Eq. 2.32.

$$\frac{\delta \mathbf{b}^2}{\delta t^2} = V\mathbf{W}^{-1}\mathbf{b}'^{-1}(P - P_0) \tag{2.32}$$

$$\frac{\delta^2 \mathbf{r_i}}{\delta t^2} = \frac{\mathbf{F_i}}{m_i} - M\frac{\delta \mathbf{r_i}}{\delta t} \tag{2.33}$$

Where V is the volume of the box and $\boldsymbol{W}$ is the matrix parameter, which determines how the simulation box can be deformed (Eq. 2.34). It includes the isothermal compressibilities of the bulk system (β), the largest box matrix element (L), the pressure time constant (τ_P) and determines the coupling strength ($\boldsymbol{M}$) (Eq. 2.35).

$$(\mathbf{W}^{-1})_{\mathbf{ij}} = \frac{4\pi^2 \beta_{ij}}{3\tau_P^2} \tag{2.34}$$

$$\mathbf{M} = \mathbf{b}^{-1}\big[\mathbf{b}\frac{\delta \mathbf{b}'}{\delta t} + \frac{\delta \mathbf{b}}{\delta t}\mathbf{b}'\big]\mathbf{b}'^{-1} \tag{2.35}$$

Just as with the Nosé-Hoover thermostat the equations of motion for the particles are also changed as a result (Eq. 2.33).

2.4.4 Bond constraints

Bond constraints are applied in order to maintain them within certain lengths. Different types of constraints algorithms exists for linear bond geometries of which SHAKE[211] and LINear Constraint Solver (LINCS)[212] algorithms are the most commonly used. These typically exclude certain intramolecular motions and so they offer much larger time steps which results in more efficient computation times. This is particularly useful when modelling covalent bonds containing hydrogen, which are too important to neglect but produce high frequency vibrational motions. In order to apply constraints to non-linear geometries such as those found in 3-site water models, a more suitable protocol like the SETTLE[213] algorithm is typically applied.

2.4.5 Periodic boundary conditions

In finite size systems it is important to remove undesirable surface artefacts, which would ordinarily arise from simulating close to the box edge or at the vacuum interface. Periodic boundary conditions (PBC) are rules used to treat a simulation cell containing a few number of particles, so that it reproduces properties of a bulk system. These conditions are achieved by surrounding the origin cell with copies of itself and its contents. As every copy perfectly mimics the original cell, if a particle were to exit through one side (and into a neighbouring cell), a copy of the original particle would also re-enter the original cell simultaneously, but from the opposite side. PBC conditions means that each particle is able to experience forces from atoms within the origin cell and its neighbouring cells. For simplicity, the minimum image convention is applied and a cut-off (smaller than half the smallest box vector) is applied so that a particle in the origin cell does not interact with its own image as though it were part of its solvation shell. It also states that each particle can only interact with 1 image of another particle at a given time, and it must always be the closest copy. A schematic of a PBC set up is shown in Fig. 2.6.

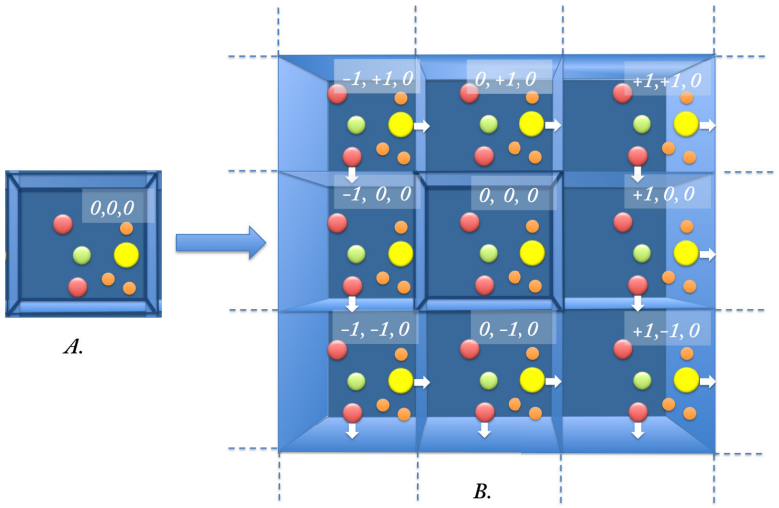

Figure 2.6: Schematic of a 2D cross section of periodic boundary conditions.

Chapter 3

Mixing and validation of OPLS-AA and TIP4P/Ice forcefields for simulations of ice growth in the presence of additives

3.1 Introduction

Modelling is now used to solve an incredibly wide range of problems from protein folding to adsorption and even crystal growth. The consequence is that vast amounts of forcefields for molecules have developed independently from one another. As some of these communities haven't been in collaboration in order to do so, this makes mixing forcefields an issue. It's therefore advised to check and quantify their compatibility before using these models and forcefields combined to address our simulation questions.

Many forcefields are developed to work with particular water models to obtain a proper balance between solvents and solute interactions. The OPLS-AA (Optimized Potential for Liquid Simulations - All Atoms) forcefield[194], was originally developed with 4-Point-Transferable-Intermolecular-Potential (TIP4P)[152] water and has been reported to work slightly better with this model than with TIP3P[152] and SPC[194] (simple point charge). It would therefore make it a preferential choice to a selected range of water models[214]. Similarly, the CHARMM[190,191] and AMBER[192] forcefields was developed with TIP3P. However practically many simulations still use

other water models because of their various advantages and disadvantages which are thoroughly documented in literature[152,200,203].
For instance, the TIP4P/Ice water model is a modified version of the TIP4P water model, which was designed to adequately simulate freezing and captures the solid phase diagram of water[152,203,204,215,216]. Reports by Vega, Absacal, Weisser and others[217] have repeatedly shown that unlike earlier water models (SPC, SPC/E[218], TIP3P, TIP4P, TIP4P/2005), TIP4P/Ice[204] does not significantly underestimate the melting temperature T_m, and has the closest value to experimental results at around 272.2 K[204,219,220] (compared to 190.5 K[204,220,221], 215 K[204,217,220,221], 145.6 K[200,220,221],
232 K[204,217,219–224] and 252.1 K[217,219,220] respectively)[199,215,225]. Although later models like TIP6P[226] have improved on this ability[204,219,221–223], its additional sites makes it almost twice as computationally expensive[204]. Understandably, these temperatures vary in literature as a result of using different computational methods and protocols. Additionally the 4-Point water models have been shown to predict the correct stable stable ice phase (Ice 1h), for which other models mistakenly predict other forms e.g. Ice II.[204,215,219,221,224,227]

In this study we aim to investigate the compatibility of the TIP4P/Ice water model with the OPLS-AA forcefield. These simulations are important for our investigations of ice growth in the presence and absence of additives like salts, antifreezes and synthetic macromolecules. Combining the OPLS-AA and TIP4P/Ice forcefields is particularly interesting to our studies as they were originally designed to improve the modelling and simulation of pure fluid systems. It is therefore important to quantify how well this and other water models perform with the OPLS-AA forcefield. In order to achieve an accurate description of our systems, we first employ the standard tests which check that the water models reproduce or resemble the well-documented dynamic and structural properties of water[214,228]. Primarily the investigation explores the dependence of the water properties on three temperatures and three cut-offs. Next we use the same tests to investigate how water behaves in the presence of salt ions (NaCl) and ethanol, a small organic molecule with known antifreeze activity.

The remainder of the chapter is is organised as follows. In section 3.2 we discuss the the computational methodology. In section 3.4.1 we compare the properties of all the different water models at ambient conditions to one another and to experimental results. These properties include the radial distribution functions, diffusivity, densities, hydrogen bonding, orientational order parameter and the phase transition kinetics. Since each of these models are optimised to fit different physical

properties of water, they are expected to behave differently. However comparisons are also made with reported theoretical values, which serve as valuable benchmarks. Next in section 3.4.2 we evaluate the effect of three temperatures (235 K, 298.15 K and 348 K) on the properties of the TIP3P, TIP4P and TIP4P/Ice water models. These simulation are relevant to systems which require the use of non-ambient temperatures such as the supercooling of water.

Fourth we investigated the effects of three commonly employed cut-offs (0.85 nm, 1.00 nm and 1.5 nm) for the aforementioned models. In order to understand the importance of investigating the effect of cut-offs, let's take the example of simulating proteins, polymers and alcohols which are typically done using 1.0–1.5 nm cut-offs in a box of solvent. A recently published paper on the re-parametrized OPLS-AA forcefield recommended similar cut-offs with molecules like propan-1-ol and other hydrocarbons.[229,230]. In contrast the TIP4P/Ice water was parametrised using 0.85 nm cut-offs and so simulating a system which require both models could prove difficult[204]. Which cut-off do we choose? Should we compromise between the two? Depending on the focus of the research, an informed compromise needs to be made which allows an accurate or reasonable description of both models. This is a difficult topic which only testing can give us the answer and this chapter serves as a contribution to the wealth of work already done in this area.

The fifth and sixth sections of the chapter focus on simulations of the water models in the presence of varying concentrations of salt (0.1–0.43 M) and ethanol (10%–100%). The TIP4P/Ice water model was not parametrized to interact with any additives, while the OPLS-AA forcefield has been re-parametrized for use with organic liquids like alkanes as well as aqueous solvents. It is important to demonstrate that the integrity of the reported properties of water are still maintained and that the experimental properties of the new mixtures can be reproduce within reason. Finally the last section of this chapter summarises the kinetics of the melting and freezing for TIP4P/Ice. It also reports the effects of cut-offs (and temperature) on the melting and freezing points as well as their rates.

3.2 Methods

3.2.1 Forcefield parameters

We use five different water models, SPC/E, TIP3P, TIP4P, TIP4P/Ice and TIP5P[199], to describe the atomistic interactions and molecular dynamics of water. In each of these models, only the oxygen atom is considered to be a Lennard-Jones (LJ) interaction site and partial charges are distributed on atomic sites as well as virtual sites

(Table 3.1). The 4-point and 5-point water models have massless dummy atoms, which we label M for simplicity. These sites are treated specially and their positions are calculated from the position of other sites[219]. While, the OPLS-AA salt ions (Na^+ and Cl^-) and rigid ethanol parameters were taken from Jorgensen *et al* paper[231] and GROMOS FF[232,233] respectively.

Model	**SPC/E**	**TIP3P**	**TIP4P**	**TIP4P/Ice**	**TIP5P**
r(OH), Å	1.00	0.9572	0.9572	0.9572	0.9572
HOH, θ	109.47	104.52	104.52	104.52	104.52
r(OM), Å	-	-	0.15	0.1577	0.70
q(O)	−0.8476	−0.834	-	-	-
q(H)	+0.4238	+0.417	+0.52	+0.5897	+0.241
q(M)	-	-	−1.04	−1.1794	−0.241
Description	3-Point	3-Point	4-Point	4-Point	5-Point

Table 3.1: Atomic charges (q), bond angles (θ) and bond distances (Å) for various water models .

3.2.2 Simulation parameters

Pure liquid water simulations

The forcefield's compatibility with various water models were validated by simulating a pure water system at ambient (298.15 K and 1 bar) and periodic boundary conditions. For these simulations 4,008 water molecules are placed in a cubic simulation box of approx. 4.95 nm^3. The simulations are performed in the NPT ensemble using the GROMACS simulation package[232,233] and the OPLS-AA forcefield. In all simulations the Leapfrog algorithm was was used to solve the equations of motion, and the SETTLE[213] algorithm was applied to constrain the bond length and angles of the water models in order to allow a larger integration time step of 2 fs. Lennard-Jones (LJ) potentials were cut-off at 0.85 nm and the particle-mesh Ewald (PME) algorithm[197,198] was employed which meant that electrostatics could be treated accurately. The real part of the Coulombic potential was also truncated at 0.85 nm while the width of the mesh was 0.16 nm and a cubic order polynomial was used. The Nosé-Hoover thermostat[209,234] was used alongside the Parinello-Rahman Barostat[210] to maintain isothermic-isobaric conditions. The relaxation times for the thermostat and barostat were 0.2 ps and 2 ps respectively. Isotropic conditions were maintained in this simulation, using the compressibility of water at 4.5×10^{-5} bar^{-1}. Unless stated otherwise, the temperature and cut-offs were main-

tained at 298.15 K and 0.85 nm respectively.

Each simulation lasted 3 ns and the first 1 ns of each run was discarded as equilibration. The remaining 2 ns was used for analysis. This range was selected by monitoring the conversion of the O-O RDFs of water over time (typically achieved by 0.9 ns, using short consecutive time blocks of 0.3 ns e.g. t_0=0–0.3 ns, t_1=0.3-0.6 ns ... t_{10}=2.7-3.0 ns).

Saline solution simulations

In order to validate the compatibility of the forcefields with small molecules like salts, and to compare the the simulations with the pure water systems, similar conditions as above were employed. The only exception was that water molecules were systematically and randomly replaced with Na and Cl ions, in order to achieve the specified concentration outlined in Table 3.2.

Conc. (M)	**0.10**	**0.14**	**0.21**	**0.28**	**0.35**	**0.43**
Water	3,994	3,988	3,978	3,968	3,956	3,946
Na	7	10	15	20	26	31
Cl	7	10	15	20	26	31

Table 3.2: The number of water molecules and ions in the saline solutions. Overall, the systems still remain neutral.

Water/ethanol mixtures

A single ethanol molecule was energy minimised using the steepest decent algorithm for 20,000 steps. Then a box of water was made and solvated with multiple ethanol molecules as specified in Table 3.3. To avoid unrealistic initial forces in the simulation, the system was energy minimized two more times under the same prior conditions before the final production run (once with flexible bonds on the ethanol and once with constrained bonds). During this 3 ns simulation, all of ethanol's hydrogen bonds were enforced using LINCS algorithm [212]. Although we use twice as many molecules in the system, the following protocol serves as comparison to the results from Wensink *et al* [12].

M	**10**	**20**	**30**	**40**	**50**	**60**	**70**	**80**	**90**	**100**
Wat	1,800	1,600	1,400	1,200	1,000	800	600	400	200	0
Eth	78	156	234	312	392	470	548	616	704	782
X	0.042	0.088	0.143	0.206	0.281	0.370	0.477	0.610	0.779	1.000

Table 3.3: The percentage mass (M) and mole (X) fraction of ethanol (Eth) in the solution and the number of water (Wat) and ethanol molecules in the mixtures.

Free Energy of Solvation of Ethanol

A single energy minimised ethanol molecule was arranged in a cubic box approximately 2.4 nm^3 and was solvated by 310 water molecules. The system was energy minimized again and equilibrated for 3 ns at the same conditions employed for the ethanol-water mixtures. Finally the production run was conducted using the leap-frog stochastic dynamics integrator, using lambda values from 0 to 1 with 0.1 intervals. The first 1 ns of the simulation was discarded as equilibration and the last 2 ns were evaluated using the Bennett Acceptance Ratio[235] (BAR) method.

The BAR is an algorithm which is used to estimate the free energy difference between two different states (A and B) and so it requires configurational data from both states. The BAR works under the principal there is a pathway connecting the states and likewise for the energy associated with them. Assuming that A and B have common configurational space, the free energy difference between the two states, ΔG, can be calculated by sampling both ensembles (Eq. 3.1).

$$\Delta G = G_B - G_A \tag{3.1}$$

In many cases the two end states have little overlap in phase space, so we define a series of intermediates using a coupling parameter or variable known as lambda (λ). Lambda describes the non-physical transformation from A ($\lambda = 0$) to B ($\lambda = 1$) at user-defined intervals e.g. $\delta\lambda = 0.1$. The sum of the potential energies (U) associated these intermediate states is equivalent to the overall free energy change during the transition from the initial state, A, to the end state, B. A schematic of the free energy of solvation is shown in Fig. 3.1, where interactions between the water and the ethanol molecule is linearly and gradually de-coupled.

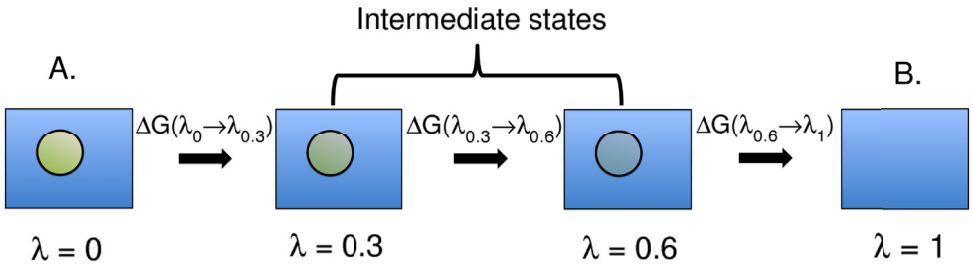

Figure 3.1: A schematic of the free energy of solvation. The ethanol molecule is represented by the green ball and the solvent is shown in blue.

Bennett showed that the free energy difference of a substep ($\Delta G(\lambda_l \rightarrow \lambda_{l+1})$) can be described by Eq. 3.2 provided that the unknown constant, C, can be found iteratively based on the condition in Eq. 3.3.

$$\Delta G(\lambda_l \rightarrow \lambda_{l+1}) = -k_B T ln \frac{n_{\lambda_{l+1}}}{n_{\lambda_l}} + C \tag{3.2}$$

$$\sum\nolimits_1 f(U_{\lambda_l} - U_{\lambda_{l+1}} + C) = \sum\nolimits_0 f(U_{\lambda_{l+1}} - U_{\lambda_l} - C) \tag{3.3}$$

where f is the Fermi function, n_{λ_l} is the coordinate frames for the initial state used to calculate the free energy difference between substeps, and $n_{\lambda_{l+1}}$ represents the coordinates of the final state.

Since the free energy of a system is a state variable, only the end states matter and so the free energy difference can be calculated in this manner. It is worth noting that the Helmholtz free energy difference is determined in NVT conditions, while the Gibbs free energy is obtained in NPT conditions such as our own. Other algorithms can be used to calculate the free energy such as Exponential Averaging[236] (EXP) and Thermodynamic Intergration[237] (TI) methods, however these methods use an ensemble average from a single state. As a result these methods are are significantly more biased than the BAR method.[238]

Freezing and melting simulations

These simulations are used to determine the melting and freezing kinetics of the TIP4P/Ice water model. It is used to check that this particular model still maintains its good representation of the water phase diagram in conjunction with the OPLS-AA forcefield. For these simulations we followed a similar protocol to that of

Weiss *et al* [19] and Fernández *et al* [219].

Essentially the simulation parameters are identical to the liquid simulation unless stated otherwise. A 2.9×3.1×2.7 nm box of hexagonal ice (768 water molecules) is equilibrated in an NVT simulation at 10 K. The simulation lasts 100 ps, using the Nosé-Hoover thermostat to maintain the temperature. The reason for this is that any bad initial contacts are given the chance to resolve themselves, while the bulk of the ice crystal remains frozen at sub-freezing temperatures. In comparison to a single interface, this set up allows a more realistic environment where the ice seed is surrounded by significant amounts of water. Next the equilibrated ice is solvated so that it is sandwiched between two water layers of similar size (763 molecules each). It is oriented in such a way that the fastest growing ice plane (the $11\bar{2}0$ face or the secondary prism plane [219]) is exposed to the liquid water, creating an interface at either side. This initial configuration is known as a two-phase coexistence or the direct coexistence method because both sides of the ice crystal are in direct contact with the liquid water [219]. This approach is important as the nucleation of ice is an activated process [219,239] and often requires a seed, so merely simulating pure liquid water below the freezing temperature usually produces supercooled water instead of ice. This has only once been successfully achieved following a one year NVT simulation by Matsumoto *et al* [240]. Additionally the presence of this interface also removes the phenomena of bulk solid superheating, which is a erroneous computational occurrence and an experimental impossibility. [219]

The new system contains 2,294 molecules and a second NVT run with 10,000 kJ mol^{-1} position restraints placed on the oxygen atoms that belong to the ice. These restraints mean that the atoms are only allowed to change their positions, provided that the atoms have the specified amount of energy, or more. This time the temperature is maintained at 283.15 K. It allows the water to equilibrate around the ice and the same conditions are conducted for a short consecutive NPT run using 10,000 kJ mol^{-1} and 100 kJ mol^{-1} respectively.

Once the NPT equilibration runs are complete, the restraints are removed and NPT production runs are conducted at different temperatures until melting or freezing is observed. In these simulations a 1 fs timestep was employed in order to accurately capture the shorter time scales reported for melting at high temperatures. During the NPT (equilibration and production) simulations, the box is allowed to fluctuate independently in all directions. This allows the system to freely freeze or melt, and the box shape can adjust accordingly. To accomplish this in GROMACS with Parinello-Rahman barostat, the compressibilities are specified and issued in such a way that it helps to scale the strength (or speed) of the pressure coupling and

the box deformation. The compressibility of the x- and y-planes are both set to the compressibility of real ice ($1.0\times10^{-5}\,\mathrm{bar}^{-1}$), while the z-direction is perpendicular to the ice/water interface so it remains set to the higher compressibility of real water. The angles are kept orthogonal and unlike the original Weiss simulations, the LJ potential was truncated using 0.85 nm cut-offs. To compare the effects of cut-offs, this same protocol was also repeated for the 1 nm cut-off.

Prior to evaluating the results of the simulation, it was necessary to demonstrate that the system had reached equilibrium. This process is monitored by the convergence of the total energy. The melting process is identified by an increase in the total energy and freezing by a decrease in the total energy. Once this process is complete, a plateau is observed. Additionally, just before the plateau a characteristic spike to the baseline serves as an initial indicator that a few of the interface layers remain to be processed and so melting or freezing is especially fast. Similar to Weiss *et al* [19], we acknowledge that the direct monitoring of the potential energy would also have been sufficient to monitor the melting and freezing of the system, however in order to allow direct comparisons we decided to follow the approach reported by Fernández *et al* [219].

3.3 Analysis methods

3.3.1 Radial distribution function

The radial distribution function (RDF) is also known as a pair correlation function and is described by Eq. 3.4. This analysis was conducted using an analysis tool in the GROMACS package. It provides the average probability of finding atom B radially packed around atom A as a function of distance (r). The results are averaged over the equilibrium trajectory and so it provides an ensemble- and time-average picture of the local environment around atom A. For this calculation, i and j are different atoms in group B, which has N_A number of atoms and likewise for group A. The $\langle\rho_B\rangle$ is the local particle density of B averaged over all spheres around particles A with radius equivalent to half the box length.

$$g_{AB}(r) = \frac{1}{\langle\rho_B\rangle}\frac{1}{N_A}\sum_{(i\in A)}^{N_A}\sum_{(j\in B)}^{N_B}\frac{\delta(r_{ij}-r)}{4\pi r^2} \tag{3.4}$$

3.3.2 Hydrogen bonding

There are several methods for extracting the hydrogen bonding in computational

simulations. The degree of hydrogen bonding in water is often estimated by calculating the coordination number of O-H RDFs, or by using an analysis script with a geometric criteria. We chose to use the latter for which GROMACS provides a suitable analysis tool. The criteria for a hydrogen bond is defined as when a donor-acceptor (e.g. oxygen and hydrogen) bond distance is less than 0.35 nm and the O-O bond angles are simultaneously less than 30 degrees. This cut-off was applied although subtle variations are present between models in their minima of the O-O RDFs. We do so in order to remain consistent in our approach for comparing the water models under the same specifications.

3.3.3 Diffusion coefficients

The diffusion coefficients (D) of select molecules were calculated from the Einstein relation which is shown in Eq. 3.5. Calculations were performed on linear fittings to the average mean-squared displacement, MSD, ($\langle |r_{t+\tau} - r_t|^2 \rangle$) of atom positions ($r$) at time t. MSD values are initially obtained by using a range timesteps (τ) and D is readily taken from the gradient of the plot.

$$D = \frac{\langle |r_{t+\tau} - r_t|^2 \rangle}{6t} \tag{3.5}$$

3.3.4 Orientational order parameter

An important description of the structure of liquid water and ice is provided by the orientational order parameter, Q_4 which is calculated by [137]:

$$Q_4 = 1 - \frac{3}{8} \sum_{(j=1)}^{3} \sum_{(k=j+1)}^{4} \left(\cos \theta_{jik} + \frac{1}{3} \right)^2 \tag{3.6}$$

For each water (i), the nearest four oxygen atoms are selected and the angle (θ_{jik}) between three oxygen atoms: i and two of these neighbouring oxygen atoms, j and k are determined. With a criteria of four neighbouring oxygen atoms, there are six possible combinations which involve i at the center, and these are all summed. The 3/8 constant is used to normalise the distribution within the range of 0 to 1. If the average $Q_4 = 1$, the arrangement of water molecules is perfectly tetrahedral because the cosine of θ_{jik} becomes equivalent to -1/3. For a random distribution (such as an ideal gas) the average $Q_4 = 0$, however limits for individual molecules have previously reported between -3 and 1 [137]. The same calculation can be performed for varying numbers of neighbours, and the normalisation constant must be adjusted accordingly: 3/4 for 3 neighbours (Q_3), 9/4 for 2 neighbours

(Q_2). A schematic of this calculation is shown in Fig. 3.2.

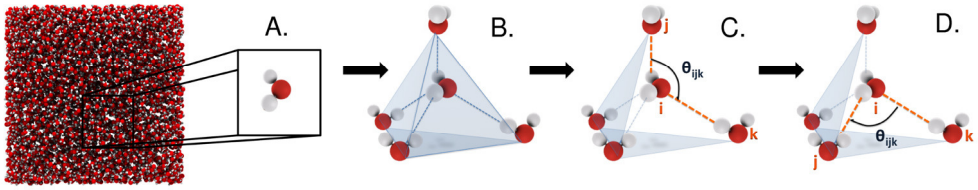

Figure 3.2: Schematic of the Q_4 calculation. Key: A. The reference water molecule is chosen. B. Its four nearest neighbours are identified. C. The first angle is calculated between the reference molecule and two of its neighbours. D. This is repeated for the next combination of neighbours with the reference atom at the centre. There are six possible combinations and the sum of these six angles are fed into Eq. 3.6

After equilibration the average number of hydrogen bonds, densities and diffusion coefficients for liquid simulations were calculated. In each instance, block averages were obtained by averaging over four blocks of 0.5 ns from the trajectory.

3.4 Results

3.4.1 All water models

We start by comparing the calculated properties of the different water models in order to confirm the validity of our OPLS-AA system for reproducing well tested properties of some older water models. We also use the same conditions to produce results for the less tested TIP4P/Ice water model. This benchmarks TIP4P/Ice in comparison to other water molecules when all other simulation parameters are kept identical.

The O-O, O-H and H-H radial distribution functions (RDFs) of all the simulated water models and experiment are shown in Fig.3.3. Work from Soper *et al* [11] was chosen as an experimental source because their spectral data are widely used and referenced in theoretical studies of water structure, particularly the oxygen-oxygen (O-O) RDF [241]. The reason for this is that it has often been used for the development and refinement of structural properties of water models. [242,243]

The most characteristic features of the O-O RDF are the position and heights of the first two peaks. With the exception of TIP3P all models predict the contours of these peaks well, and those of the other two RDFs. For the O-O RDFs, these models have a first peak at 0.275 nm but the height varies from 0.277 (TIP3P)

to 0.325 (TIP4P/Ice). The closest model to this first peak is TIP3P while the remaining models overestimate it, particularly TIP4P/Ice. In contrast the second peak is absent in TIP3P and visibly broader at around 0.45 nm for the other water models. Its height varies from 0.110 (TIP4P) to 0.119 (TIP4P/Ice). While the other water models flatten out, both TIP4P/Ice and TIP5P are the most accurate at tailing last few shells more closely, exhibiting the long range ordering shown in the experiment. In this section, all models demonstrate a loss of structure with each successive hydration shell, comparable to theoretical literature[204,244–246] and experiment. As reported in the original TIP4P/Ice paper, although the model is not intended for the liquid state it is able to adequately reproduce the liquid water structure.

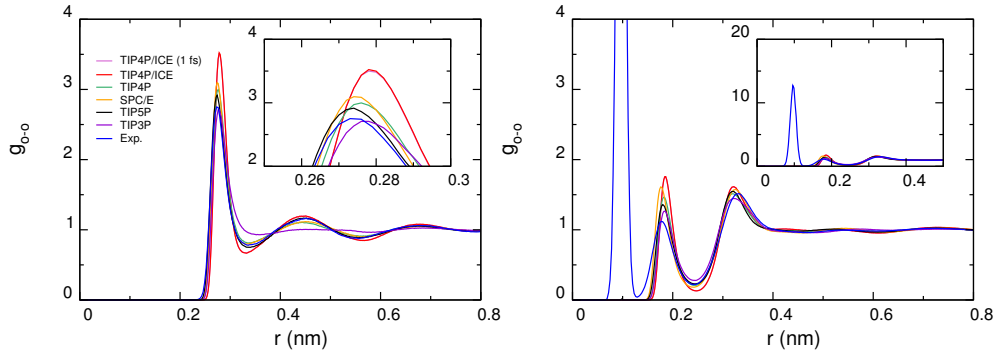

(a) Oxygen-Oxygen

(b) Oxygen-Hydrogen

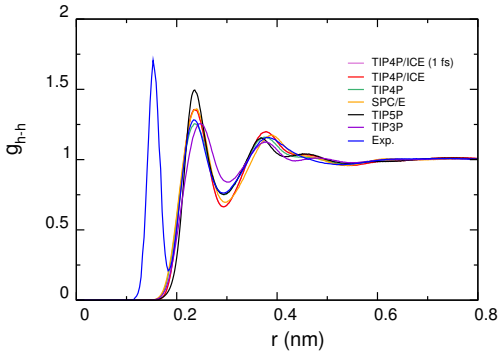

(c) Hydrogen-Hydrogen

Figure 3.3: RDFs of all water models and experiment[11] at 298 K and 0.85 nm cut-offs. There are no noticeable structural differences between using 1 fs and 2 fs timesteps for the TIP4P/Ice water model. Insets in (a) show and (b) highlight the differences between water models and depict the full RDF profile respectively.

Diffusion coefficients, D, were calculated from the mean square displacements (MSD) of the whole water molecule using the Einstein relation[247]. Their values are estimated from the gradient of the linear part of the MSD plot (D=MSD/6) and are tabulated for various water models in Table 3.4. Experimentally at 298.15 K

the diffusion constant of liquid water is $2.3 \times 10^{-5}\,\mathrm{cm^2\,s^{-1}}$ [248,249]. Of the water models reported here, the models that give diffusion coefficients closest to experiments are SPC/E and TIP5P. The TIP4P/Ice model is approximately half this value at $1.19 \times 10^{-5}\,\mathrm{cm^2\,s^{-1}}$, whilst TIP3P and TIP4P both severely overestimate it. The proposed diffusion coefficients of the models are as follow: SPC/E (2.49),[199,201,218,250] TIP3P (5.06±0.09),[152] TIP4P (3.29±0.05)[152], TIP4P/Ice (1.12±0.05)[19] and TIP5P (2.62±0.04)[199] in units of $10^{-5}\,\mathrm{cm^2\,s^{-1}}$. The lengths of simulation boxes in the cited work ranged from ∼3-4 nm^3. Although the calculated Ds in this work were systematically higher compared to literature, it is possible that the larger D values may be a consequence of a system size effect where D increases with the box dimensions due to fewer long-range interactions between periodic images. The problems for calculating D over short time scales and small to moderate system sizes have previously been addressed.[173,230,251,252]

Property	**Model**					
	SPC/E	**TIP3P**	**TIP4P**	**TIP4P/Ice**	**TIP5P**	**Expt.**
D, $10^{-5}\,\mathrm{cm^2\,s^{-1}}$	2.63	5.74	3.57	1.19	2.80	2.30
	(0.035)	(0.100)	(0.032)	(0.023)	(0.089)	(-)
ρ, $\mathrm{kg\,m^{-3}}$	998.56	985.06	993.19	992.20	983.64	997.05
	(0.19)	(0.07)	(0.22)	(0.12)	(0.37)	(-)
N_H	3.60	3.35	3.55	3.75	3.33	2-4

Table 3.4: Diffusion coefficient (D), density (ρ), the average number of hydrogen bonds per molecule (N_H) and associated standard deviations.

The results for hydrogen bonding are also tabulated in Table 3.4. Studies of hydrogen bonding in different water models have extensively been investigated and it has previously been reported that SPC/E, TIP3P, TIP4P and TIP5P have 2.46–3.59[253,254], 3.5[152,250], 2.36–4.0[243,250,253–255] and 2.08–3.7[199,253,255,256] hydrogen bonds per water molecule respectively. Our results are very similar to theoretical findings and the estimated experimental number broadly ranges from 2–4[246,255] at room temperatures which is suitably approximated by each model, including TIP4P/Ice. To our knowledge, hydrogen bonding for liquid TIP4P/Ice water has not previously been reported. It is apparent that TIP4P/Ice has the largest number of hydrogen bonds per molecule and this accounts for the overestimation of 28% seen in the first shell of its oxygen RDFs. The same rational can be used to explain its significantly slow diffusion coefficients.

The density of water at 298.15 K is $997.05\,\mathrm{kg\,m^{-3}}$ [23,257] and this prop-

erty is well represented by 3 water models: SPC/E, TIP4P and TIP4P/Ice. With the exception of SPC/E all models still provide underestimations, and surprisingly TIP5P provided one of the worst matches to the experimental value despite being parametrized to fit to the density properties of water[199]. For each models, the densities are widely recounted in literature and are typically quoted within the range reported here.[152,245,246,250]

A comparison of the orientational order parameter was made for all the water models at 298.15 K. The results are presented in Fig. 3.4 and we can see that TIP4P/Ice and TIP5P, have the highest degree of tetrahedral arrangements with maxima at $Q_4 = 0.81$, while the rest have maxima at lower values (0.72 for SPC/E and TIP4P, and 0.48 for TIP3P). This compliments our previous findings (Fig.3.3) that TIP4P/Ice is predisposed to a more well defined tetrahedral arrangement, even as a liquid, while the reverse it true for TIP3P. As expected the Q_4 distribution is bimodal for most models marked by a low Q_4 peak at $\sim$0.5 (for liquid-like) and a high Q_4 peak described earlier (for ice-like orientations).[137] However in our study the shoulder at 0.5 is faint for TIP4P/Ice and near unimodal for TIP3P. These profiles are more characteristic of lower and higher temperatures respectively[137,258]. Previously correlations between the bimodal features of Q_4 distributions have been drawn to the highly debated polymorphism of water,[137,259,260] which are typically seen at higher pressures and in supercooled systems, neither of which are the case here. Although these features are unusual, our results for TIP4P/Ice and TIP3P are the only two water models which rightly reflect this at ambient conditions. The high ordering present in TIP4P/Ice is most likely what makes the water model predisposed to a better representation of the phase diagram of water.

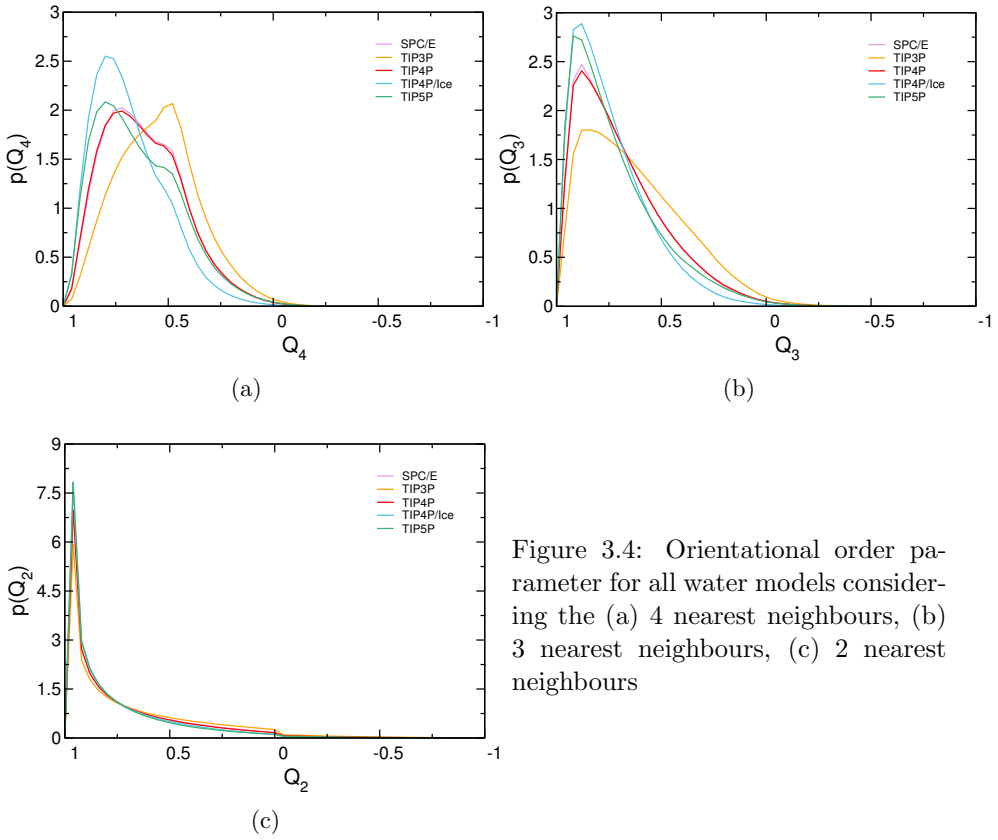

Figure 3.4: Orientational order parameter for all water models considering the (a) 4 nearest neighbours, (b) 3 nearest neighbours, (c) 2 nearest neighbours

In order to make this analysis suitable to other solutions where steric interference from solutes may prevent the approach of four neighbouring water molecules, we include analysis for 3 neighbours, 2 neighbours. Irrespective of the number of neighbours, TIP4P/Ice and TIP5P demonstrate much higher levels of tetrahedrality while the TIP4P and SPC/E water models display common features which almost overlap[261]. The effect of reducing the number of neighbours means that less waters are simultaneously involved in attaining the ideal tetrahedral criteria and so we see a greater ability to adopt this orientation, as reflected by the shift from low Q peaks in Q_4 to higher values in Q_2. It is also clear that the disparity between the models are drastically reduced with the transition from Q_4 to Q_3 and finally the Q_2 parameter. Under similar conditions fewer neighbours (e.g. the Q_2) may be used along side the Q_4 parameter to asses the ordering effects of larger antifreeze molecules which cannot sterically accommodate four neighbouring water molecules. Snapshots of an isolated TIP4P/Ice water molecule is shown at 298 K with its neighbours in order to illustrate what the Q_4=1 and Q_4=0.5 shoulder correspond to in solution (Fig. 3.5).

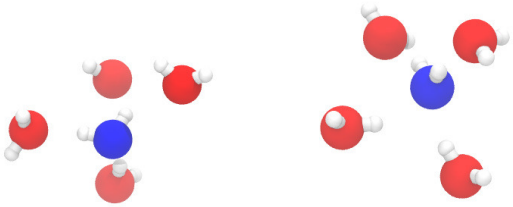

(a) (b)

Figure 3.5: TIP4P/Ice water oxygens which exhibit Q_4 values (a) at 0.5 and (b) at 0.81 are shown in blue, and their 4 closest neighbours at 298 K

In summary, TIP4P/Ice has a greater degree of H-bonding than other water models (albeit the closest to the experiments), as a result of greater charges on the oxygen and hydrogen atoms. This feature of the TIP4P/Ice water model causes reduces its D value to approximately half the expected value and induces an overestimated degree of tetrahedral order in neighbouring water molecules, particularly at short range distances. It is possible that this feature is what makes the TIP4P/Ice water model predisposed to freezing into the correct isoform of ice at 273.15 K and so it is important to study the model at other temperatures as well.

3.4.2 Effects of temperatures on TIP4P and TIP4P/Ice

Here we investigate the effects of temperature on the structure and dynamics of the TIP4P/Ice water model. The results will be used to assess the credibility of mixing forcefields under non-ambient conditions and the implications of varying cut-offs will be addressed in a later section. From here on, simulations in solution also focuses on TIP4P, a similar water model which the OPLS-AA forcefield was parametrized to work with.

All RDFs for TIP4P and TIP4P/Ice show that short and long range ordering is lost with increasing temperatures because more kinetic energy is available for water molecules to break out of their confined shells. As a result, the height and sharpness of each peak decreases with higher temperatures and the troughs become increasingly shallow. Similar observations have been reported for TIP4P and other water models in independent studies[199,252].

A 113 K increase in temperature from 235 K to 348 K corresponds to a 36 % drop in the first peak of the TIP4P/Ice O-O RDF. For TIP4P this value is much smaller at 31 %, and is to be expected since TIP4P/Ice exhibits the strongest peaks and troughs between the two (and in comparison to the other water models). At 235 K the faint but visible residual ordering can still be seen up 0.85 nm which is absent from the two higher temperatures. These stop at $\sim$ 0.68 nm and are shown in Fig. 3.7 and Fig. 3.6. The same qualitative trend is visible for the O-H and H-H RDFs and no significant shifts in any RDF peaks are apparent.

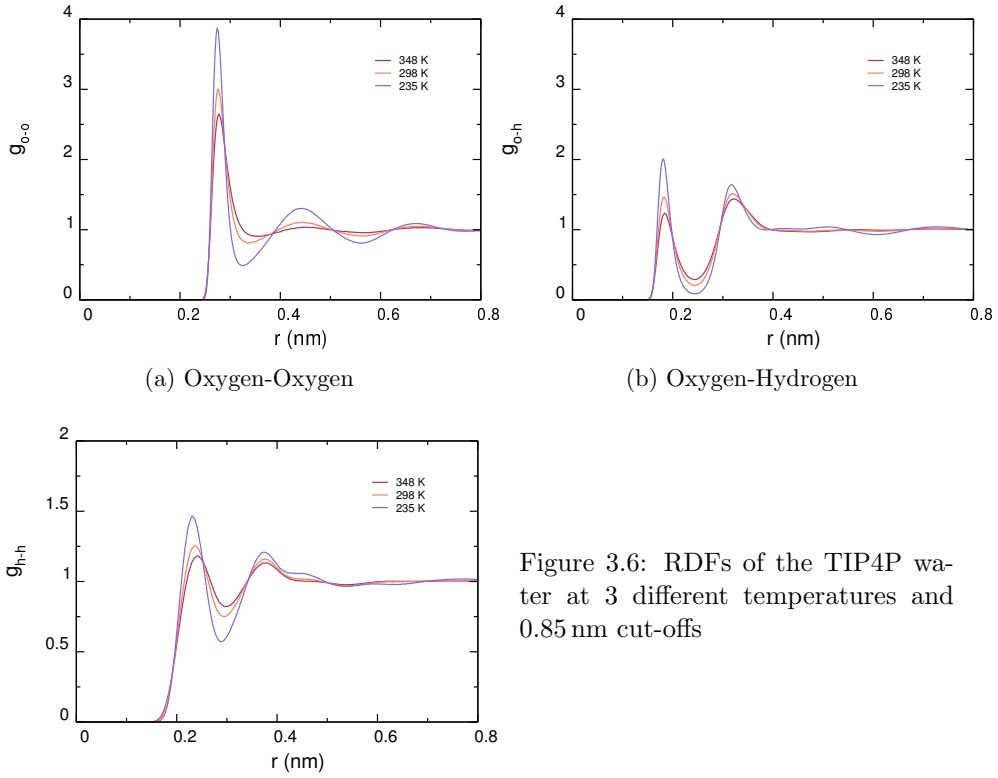

(a) Oxygen-Oxygen

(b) Oxygen-Hydrogen

(c) Hydrogen-Hydrogen

Figure 3.6: RDFs of the TIP4P water at 3 different temperatures and 0.85 nm cut-offs

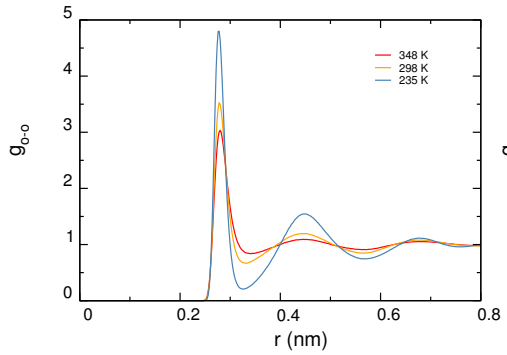

(a) Oxygen-Oxygen

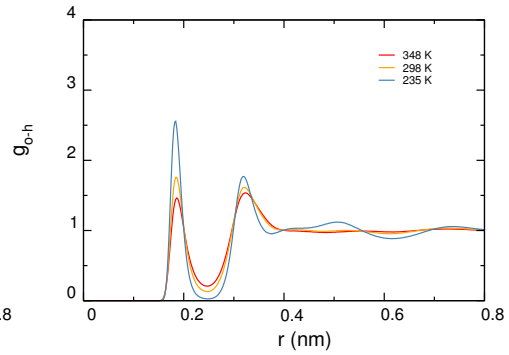

(b) Oxygen-Hydrogen

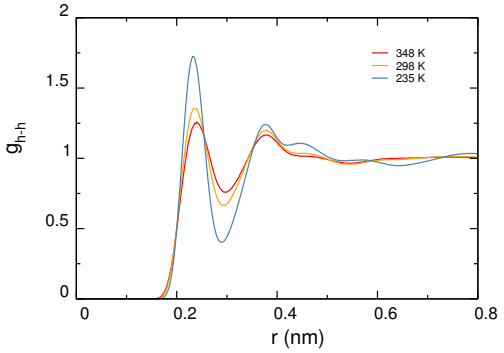

(c) Hydrogen-Hydrogen

Figure 3.7: RDFs of the TIP4P/Ice water at 3 different temperatures and 0.85 nm cut-offs

The effects of temperature and cut-offs on the diffusion coefficients are shown in Table 3.5. At varying temperatures it is important that TIP4P/Ice diffusion coefficients can be reproduced close to experimental values seeing as these values have large impacts on the rate of ice growth at ice/water interface. Experimental diffusion coefficients were taken from various reports[248,249,262–266] and an average was calculated for each temperature. With the exception of 235 K, we found that TIP4P/Ice consistently has half the diffusion coefficient values expected experimentally. Although the models cannot reproduce the exact diffusion constants, we are able to demonstrate that they relay the same qualitative trends seen experimentally. Moreover similar values have previously been calculated[267]. Overall TIP4P/Ice produces coefficients closest to the experimental values at lower temperatures (235 K and 298 K), while results for the TIP4P water model is the most suitable coefficient at 348 K.

T (K)	Cut-off (nm)	TIP3P	TIP4P	TIP4P/Ice	Expt.
235	0.85	1.58 (0.037)	0.46 (0.021)	0.015 (0.002)	0.187 (-)
235	1.00	1.63 (0.058)	0.45 (0.011)	0.015 (0.002)	
235	1.50	1.63 (0.0467)	0.45 (0.012)	0.016 (0.002)	
298	0.85	5.74 (0.100)	3.57 (0.032)	1.19 (0.023)	2.395 (-)
298	1.00	5.69 (0.109)	3.63 (0.052)	1.16 (0.014)	
298	1.50	5.66 (0.089)	3.63 (0.017)	1.20 (0.024)	
348	0.85	10.40 (0.097)	8.12 (0.197)	3.64 (0.070)	6.254 (-)
348	1.00	10.26 (0.186)	7.87 (0.083)	3.57 (0.054)	
348	1.50	10.35 (0.068)	8.07 (0.220)	3.55 (0.047)	

Table 3.5: Diffusion coefficient, D ($10^{-5}\,\mathrm{cm^2\,s^{-1}}$) for various water models at 3 different temperatures and cut-offs.

In Table 3.6 we present the hydrogen bonding per molecule as a function of temperature for 3 water models. As expected we found that the hydrogen bonding network was promoted with lower temperatures, similar to observations of the RDFs. Such observations are not unfamiliar[250] because higher temperatures the water molecules are able to move more freely and so disrupt the local hydrogen bonding network of the system.

T (K)	Cut-off (nm)	TIP3P	TIP4P	TIP4P/Ice
235	0.85	3.67	3.84	3.96
235	1.00	3.67	3.84	3.96
235	1.50	3.67	3.84	3.96
298	0.85	3.35	3.55	3.75
298	1.00	3.35	3.55	3.76
298	1.50	3.35	3.55	3.76
348	0.85	3.08	3.29	3.56
348	1.00	3.08	3.29	3.56
348	1.50	3.08	3.29	3.56

Table 3.6: Average number hydrogen bonds per molecule (N_H), for various water models at 3 different temperatures and cut-offs .

The densities of 3 water models are tabulated in Table 3.7. Each water model's density increases with the temperature in line with experiment. At 298 K

and 348 K the density of water is 997.05 kg m^{-3} [23,257] and 974.90 kg m^{-3} [23] respectively. At 235 K the simulated liquid water is sustained within a supercooled state which can only be achieved experimentally in pure water and in the absence of nucleation sites. Under experimental conditions this is difficult to achieve and so no comparisons are made to experimental densities at this temperature. The decline in density between 298 K and 348 K corresponds to a 2.2% drop. In the order of decreasing accuracy, the same calculation for TIP4P/Ice yields 1.21%, 3.80% for TIP4P and 5.07% for TIP3P. It is also known that the density of water increases non-monotonically with temperature, however this is not illustrated as we only investigate 3 temperatures [252]

T (K)	Cut-off (nm)	TIP3P	TIP4P	TIP4P/Ice
235	0.85	1029.36 (0.36)	1001.99 (0.12)	946.65 (1.77)
235	1.00	1029.77 (0.54)	1002.72 (1.05)	945.91 (2.55)
235	1.50	1029.78 (0.17)	1002.29 (1.00)	945.71 (2.85)
298	0.85	985.06 (0.07)	993.19 (0.22)	992.20 (0.40)
298	1.00	986.13 (0.35)	994.34 (0.15)	992.73 (0.31)
298	1.50	986.22 (0.35)	994.18 (0.26)	992.64 (0.12)
348	0.85	935.16 (0.40)	955.45 (0.27)	980.14 (0.26)
348	1.00	936.79 (0.12)	956.56 (0.19)	981.18 (0.37)
348	1.50	937.26 (0.28)	956.41 (0.46)	981.13 (0.17)

Table 3.7: Densities (ρ, kg m^{-3}) for for various water models at 3 different temperatures and cut-offs .

Figure 3.8 depict the distribution of Q_4 order parameters as a function of temperature and different cut-offs. As the temperature changed, the distributions for the orientational order showed similar traits for all the water models. From low to high temperatures a shift in Q_4 from high to low values indicates a clear decrease in tetrahedral order [137,261]. The highest peaks can be found for the 235 K system at 0.72, 0.84 and 0.88 for TIP3P, TIP4P and TIP4P/Ice respectively. In the case of the 4-point water models, the increase in temperature is earmarked by a transition from a unimodal distribution to a bimodal peak which suggests 2 dominant orientations of waters. The presence of the strengthening second shoulder is caused by a transition between tetrahedral and non-tetrahedral environments. The Q_4 peaks at 0.48 increased and an intermediary maxima is formed with an increase in the temperature, while the maxima at 0.84 or 0.88 vanishes. The shoulder peaks for TIP4P and TIP4P/Ice are found at 0.72 and 0.8 respectively while for TIP3P this transi-

tion is much sharper and non-existent before 0.48. Its absence and presence of a strong shoulder even at low temperatures indicates that the model is biased towards random arrangements while the reverse could be said for TIP4P/Ice which boasts of a higher degree of tetrahedral arrangements irrespective of temperature. The point at which these three temperatures cross indicates a cut-off value by which to identify ice-like water molecules. This point was most easily identified for TIP3P and TIP4P/Ice as 0.59 and 0.76 because the three distributions intersect at around the same point. For TIP4P we identified this cut-off at 0.68, however more temperature profiles may be required for confirmation.

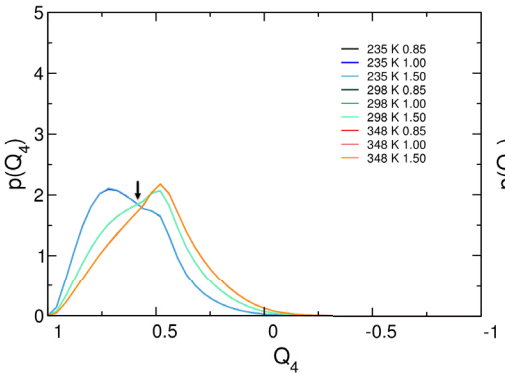

(a) TIP3P

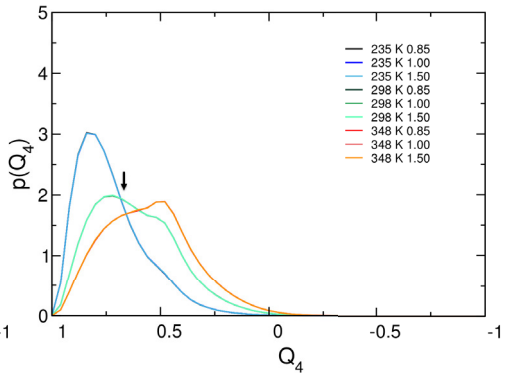

(b) TIP4P

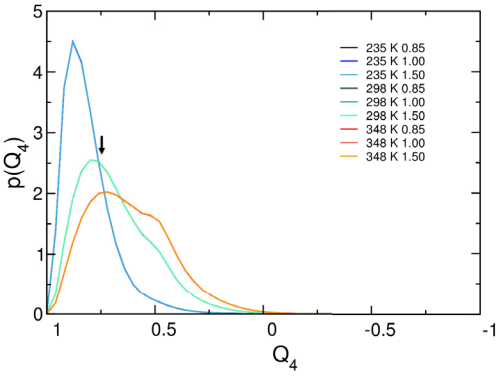

(c) TIP4P/Ice

Figure 3.8: Orientational order parameter for TIP3P, TIP4P and TIP4P/ice at 3 different temperatures and cut-offs. Black arrows mark intersections that divide ice-like and fluid regions in each water model. Each cut-off finely overlaps.

3.4.3 The effects of dilute salt concentrations on TIP4P/Ice and TIP4P

Often simulations are conducted with small solutes like salts in order to mimic

biological systems or saline conditions. In order to investigate the effects of small charged particles on the mixing of the OPLS-AA forcefield with TIP4P/Ice we introduce sodium and chlorine into the system. The RDFs of the saline solutions are summarised in Fig. 3.9–3.12. In this section we primarily focus on systems with 0.85 nm cut-offs (although most observations are also applicable to 1.00 nm cut-offs). From here on we chose to limit the studies of TIP4P/Ice with additives to just these two cut-offs because future work will carry forward from these studies as they are the less computationally expensive options. Consistent with the pure water systems, the RDFs for TIP4P/Ice reveal a more structured solution than for TIP4P. The models' salt-water RDFs, illustrates that increasing the salt concentration induces a subtle decrease in the intensities of the first and second shells. The position of the peaks in all water models are in good agreement with experimental data for these RDFs. For instance peaks are found at 0.266–0.244 nm[268–271] for sodium-oxygen (Na-O) RDFs. The main peaks for the chlorine-oxygen (Cl-O) RDFs and the chlorine-hydrogen (Cl-H) RDFs are also visible at 0.29–0.327 nm[272,273] and 0.225 nm[272] respectively.
Noticeably with higher concentrations there isn't a significant shift in peaks, but rather a change in the heights which reflects that the introduction of such small salt concentrations doesn't have a marked affect in the water ordering. This is expected because there are sufficient water molecules available to solvate the hydration shell of each ion. As a result neighbouring salt molecules do not particularly compete for solvation and so the distribution of their respective shells (and that of the waters') are not unusually disturbed.

The results of Na-Cl RDFs are also included in the same figures and their noisy outlines confirms that the concentration of the solutions are very small. In comparison to the water-water RDFs, there are far fewer salt ions available for the calculation and the averaging of the distribution plot. These traits and the following are apparent for both water models. The Na-Cl RDFs have 2 clear peaks; the first is 0.28 nm which corresponds to the distance between the ionic pair, while the second peak at 0.45 nm corresponds to an ion pair separated by solvents. These results also agree with previous reported observation in similar simulations[268,274,275].

It is important to note that the Na-Cl RDF profiles are markedly taller for the TIP4P water model at 0.85 nm. This feature can be attributed to the larger negative charges used in the TIP4P/Ice water model so results in stronger interactions with the ions instead. The ion-water RDFs are good measures to describe how strongly bound water molecules are to the ion and and can be used to calculate the coordination numbers[268].The calculated coordination numbers for our simulations

are displayed in Table. 3.8. For sodium we deduced values from the Na-O RDFs and we obtain values between 5 and 6 from integrating the area under the first peak (from zero to the first minimum). The position of the first minimum was taken at around 0.33 nm and 0.39 nm for Na-O and Cl-O respectively for both TIP4P and TIP4P/Ice. Experimental hydration numbers typically vary between 4–6 [276–280] for Na^+ but most simulations frequently predict a value of 6 [279–282]. While for Cl^- an estimated average of 6 to 7 [269,281–283] water molecules are found in the first hydration shell (also consistent with our findings).

It is important to note that the range for accepted coordination numbers vary due to the use of different experimental techniques and at times varying concentrations. In spite of this leeway the TIP4P system consistently overestimates the coordination numbers for Cl^- anions, while predictions for TIP4P/Ice constantly fall within the accepted experimental range. We find, in agreement to the theoretical studies [283], both models have coordination numbers which decline with increasing concentrations. This present work does not reveal stark contrasts between the structuring of TIP4P or TIP4P/Ice water in saline solutions, aside from the aforementioned and an artefact induced by changing the cut-offs which is discussed much later. We conclude that TIP4P/Ice water model performs just as good as TIP4P, if not better in saline concentrations at 0.85 nm.

Conc. (M)	Cut-off	TIP4P	TIP4P/Ice
Na^+ ions			
0.10	0.85	5.75 (0.112)	5.84 (0.084)
0.10	1.00	5.77 (0.094)	5.63 (0.144)
0.14	0.85	5.65 (0.064)	5.82 (0.063)
0.14	1.00	5.63 (0.195)	5.77 (0.086)
0.21	0.85	5.52 (0.178)	5.72 (0.079)
0.21	1.00	5.65 (0.039)	5.82 (0.055)
0.28	0.85	5.48 (0.105)	5.73 (0.061)
0.28	1.00	5.52 (0.046)	5.63 (0.062)
0.35	0.85	5.40 (0.065)	5.60 (0.076)
0.35	1.00	5.48 (0.043)	5.64 (0.075)
0.43	0.85	5.38 (0.107)	5.60 (0.073)
0.43	1.00	5.32 (0.036)	5.69 (0.070)
Cl^- ions			
0.10	0.85	7.39 (0.029)	6.86 (0.024)
0.10	1.00	7.37 (0.038)	6.80 (0.046)
0.14	0.85	7.34 (0.025)	6.83 (0.023)
0.14	1.00	7.34 (0.066)	6.86 (0.035)
0.21	0.85	7.30 (0.068)	6.84 (0.036)
0.21	1.00	7.34 (0.025)	6.86 (0.016)
0.28	0.85	7.30 (0.040)	6.84 (0.025)
0.28	1.00	7.31 (0.019)	6.83 (0.025)
0.35	0.85	7.24 (0.026)	6.83 (0.033)
0.35	1.00	7.31 (0.017)	6.84 (0.025)
0.43	0.85	7.23 (0.089)	6.82 (0.039)
0.43	1.00	7.25 (0.020)	6.82 (0.039)

Table 3.8: The coordination number of Na^+ and Cl^- ions in the saline solutions.

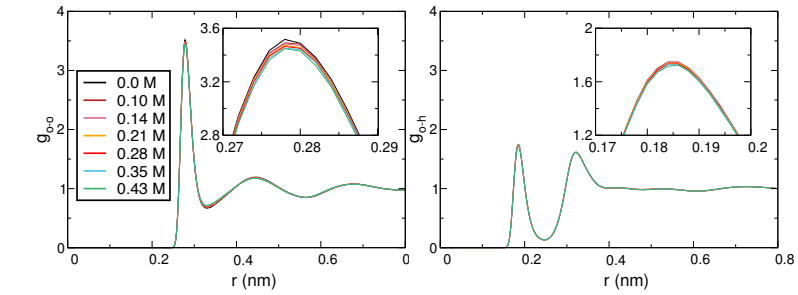

(a) Oxygen-Oxygen

(b) Oxygen-Hydrogen

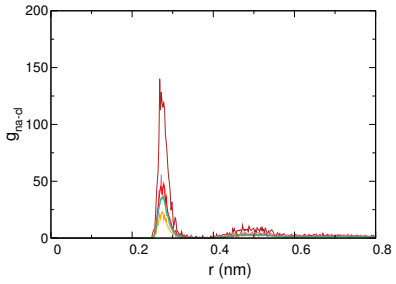

(c) Sodium-Chlorine

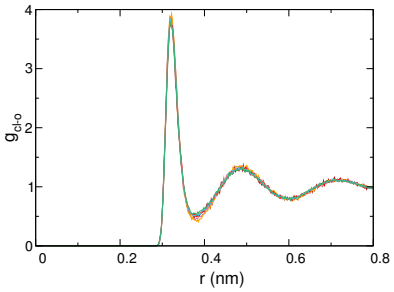

(d) Chlorine-Oxygen

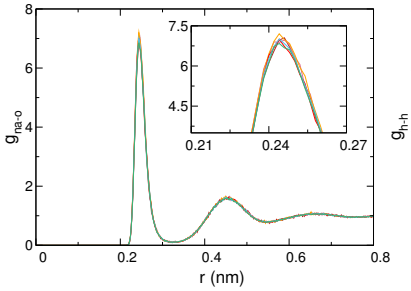

(e) Sodium-Oxygen

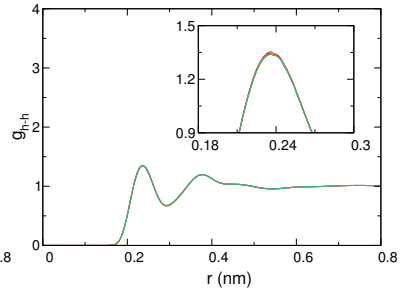

(f) Hydrogen-Hydrogen

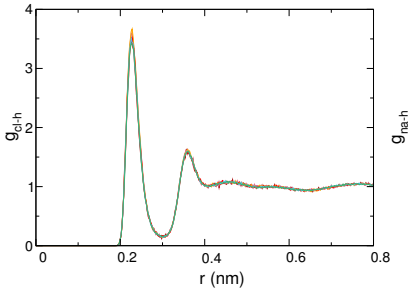

(g) Chlorine-Hydrogen

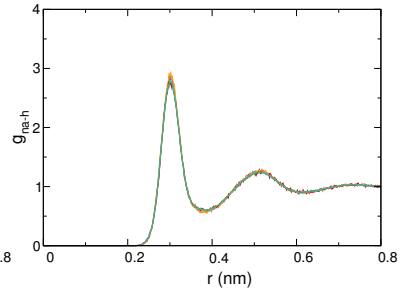

(h) Sodium-Hydrogen

Figure 3.9: RDFs for different salt concentrations at 298 K with the TIP4P/Ice water model at 1 nm cut-off.

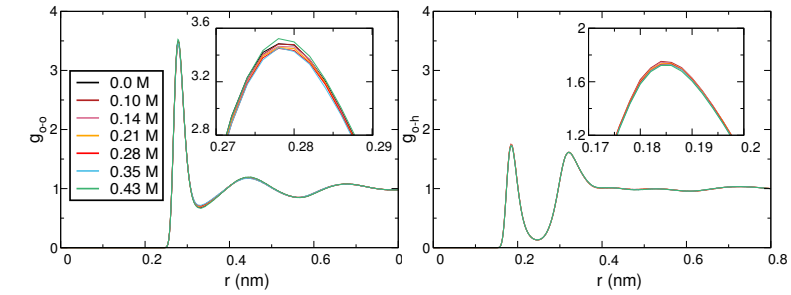

(a) Oxygen-Oxygen

(b) Oxygen-Hydrogen

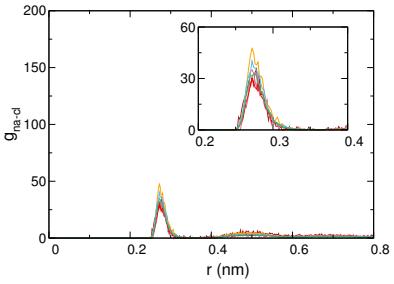

(c) Sodium-Chlorine

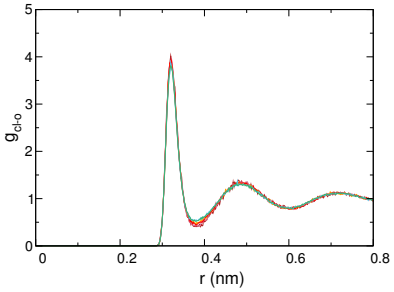

(d) Chlorine-Oxygen

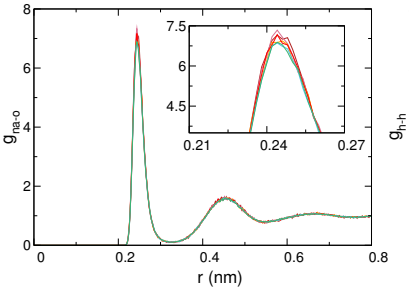

(e) Sodium-Oxygen

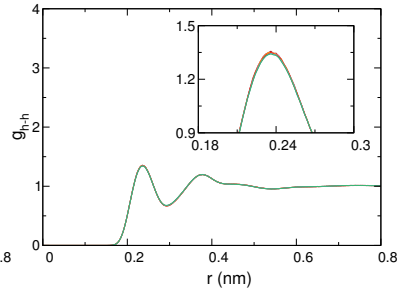

(f) Hydrogen-Hydrogen

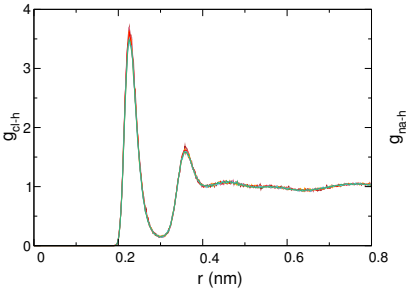

(g) Chlorine-Hydrogen

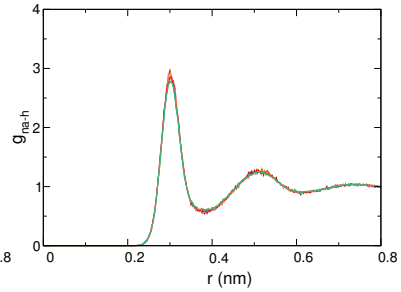

(h) Sodium-Hydrogen

Figure 3.10: RDFs for different salt concentrations at 298 K with the TIP4P/Ice water model at 0.85 nm cut-off.

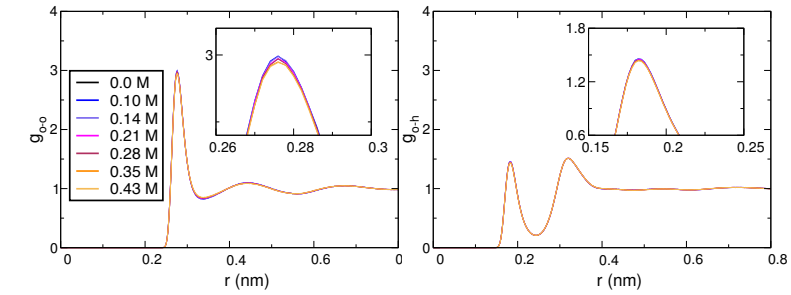

(a) Oxygen-Oxygen (b) Oxygen-Hydrogen

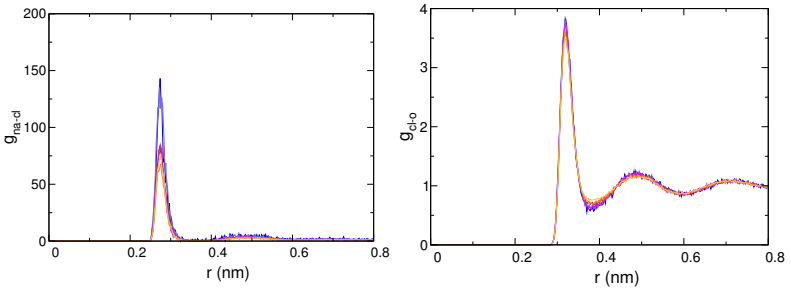

(c) Sodium-Chlorine (d) Chlorine-Oxygen

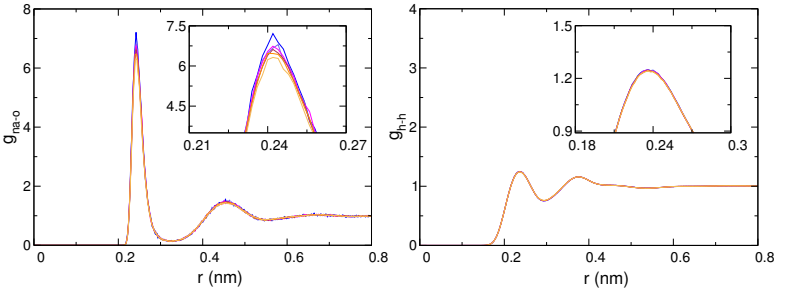

(e) Sodium-Oxygen (f) Hydrogen-Hydrogen

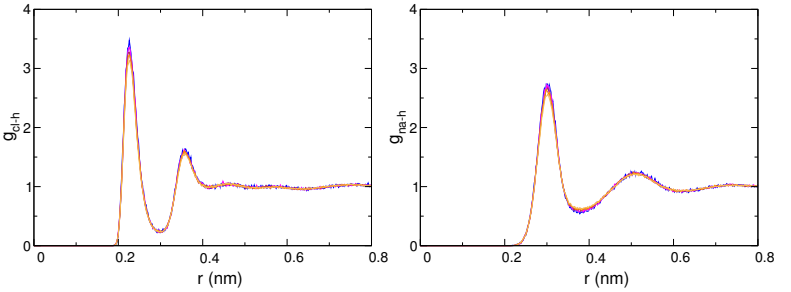

(g) Chlorine-Hydrogen (h) Sodium-Hydrogen

Figure 3.11: RDFs for different salt concentrations at 298 K with the TIP4P water model at 1 nm cut-off.

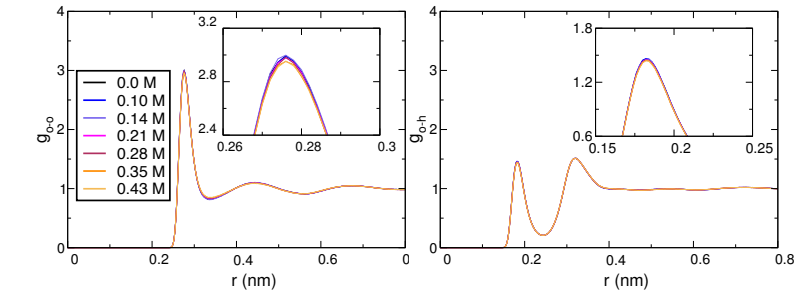

(a) Oxygen-Oxygen (b) Oxygen-Hydrogen

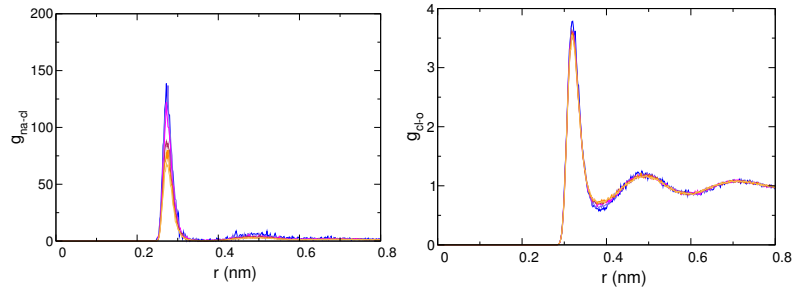

(c) Sodium-Chlorine (d) Chlorine-Oxygen

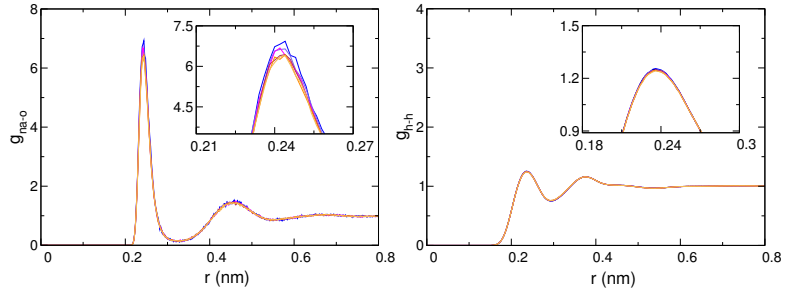

(e) Sodium-Oxygen (f) Hydrogen-Hydrogen

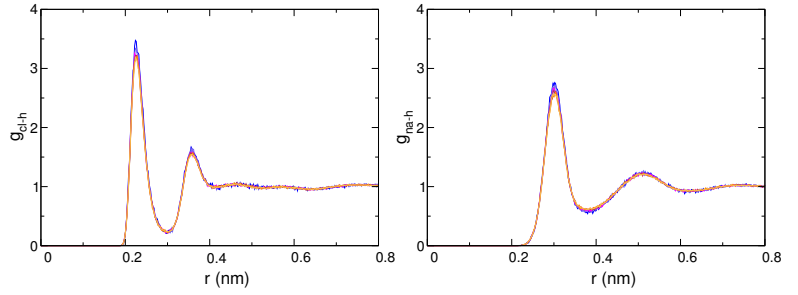

(g) Chlorine-Hydrogen (h) Sodium-Hydrogen

Figure 3.12: RDFs for different salt concentrations at 298 K with the TIP4P water model at 0.85 nm cut-off.

The diffusion coefficients for the saline solutions are depicted in Fig. 3.13. In these dilute solutions as the concentrations increase we see fluctuations of the diffusion coefficients, however on average the values do not substantially change past 0.21 M for the TIP4P/Ice water models. The same cannot be said for the TIP4P water model, where the diffusion coefficients for both ions of the 0.85 nm simulation appears to increase. At 298 K, NaCl is considered a "structure making" salt because it interacts strongly with water molecules and helps to maintain or build the hydrogen bonding network of water, reducing their mobility[284]. It is therefore expected that the diffusion coefficients of constituents would continue to decrease with increase concentration however previous work have also shown that at dilute concentrations the diffusion constants do not follow this trend perfectly.[274] As with the pure water systems, the diffusion coefficients of the TIP4P system is unsurprisingly higher than that of the TIP4P/Ice. Recent reports by Kim *et al* [284] have found that the self-diffusion of TIP4P, TIP3P and SPC/E water in 1 M–4 M solutions can be suppressed in the presence of NaCl relative to that of neat water (i.e. $D/D_{H_20} < 1$). Extrapolation of their results indicate that at 0.5 M, $D/D_{H_20} \approx 0.975$ in experiments and ∼0.95 in TIP4P water. Here we show that our simulations successfully reproduce the qualitative trends observed experimentally using the TIP4P systems (with D/D_{H_20}=0.95 at both cut-offs). Although the same could not be said for TIP4P/Ice which remained fairly constant, D/D_{H_20}= 0.93 and 0.98 at 0.85 nm and 1.00 nm cut-offs respectively, which is still in line with relative reductions in the diffusion coefficient.

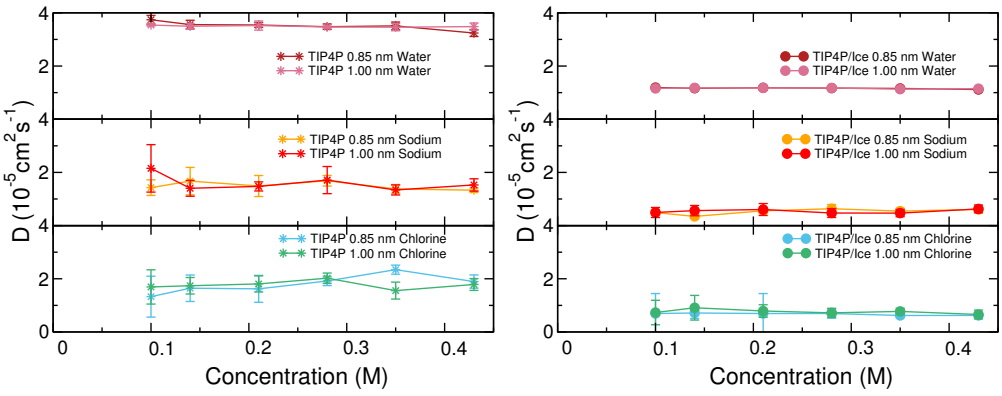

(a) TIP4P (b) TIP4P/Ice

Figure 3.13: The self-diffusion coefficients for different salt concentrations at 298 K and a 1.00 nm cut-off.

The number of hydrogen bonds per water molecule is calculated for the saline solutions in Table 3.9. Its shows a small decline in hydrogen bonds with increasing concentrations, which is a consequence of fewer water molecules and increasingly frequent occupations in salt-water interactions (see RDFs). For TIP4P and TIP4P/Ice water models a drop of 0.56 and 0.53% are seen in the hydrogen bonds from pure water to 0.1M respectively.

Conc. (M)	**Cut-off**	**TIP4P**	**TIP4P/Ice**
0.10	0.85	3.53	3.73
0.10	1.00	3.53	3.73
0.14	0.85	3.52	3.72
0.14	1.00	3.52	3.72
0.21	0.85	3.50	3.71
0.21	1.00	3.50	3.71
0.28	0.85	3.49	3.69
0.28	1.00	3.49	3.69
0.35	0.85	3.47	3.67
0.35	1.00	3.47	3.67
0.43	0.85	3.46	3.66
0.43	1.00	3.46	3.66

Table 3.9: The number of hydrogen bonds per water molecule (N_H) in the saline solutions.

Fig. 3.14 shows the Q_4 distributions for saline solutions. In comparison to the pure water systems and the effects of changing temperature, there are no substantial differences between the water ordering and the higher concentrations of salt for TIP4P. For the most part this is also the case for TIP4P/Ice water model. However at 0.43 M we begin to see a clearer decline in the tetrahedral arrangement which indicates a higher model sensitivity with the addition of small molecules. Although this disruption can be attributed to the tetrahedral bias of TIP4P/Ice, the model presents a 8% drop in the ice-like region of water in 0.43 M compared to its pure systems, while TIP4P only declines by 6%.

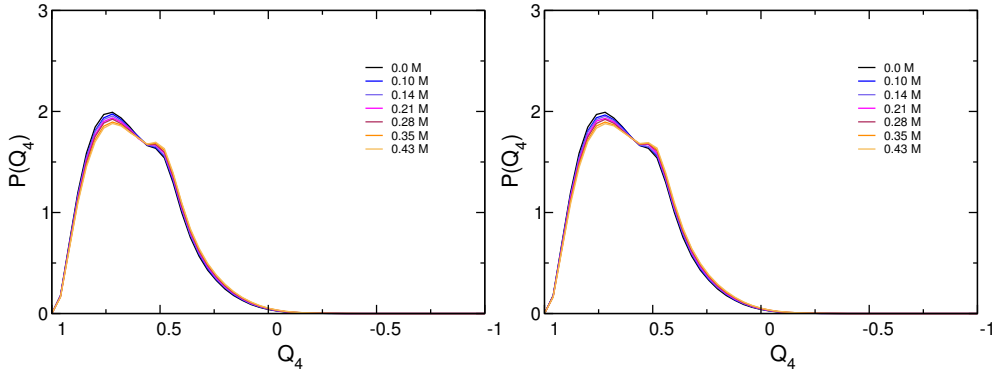

(a) TIP4P 0.85 nm (b) TIP4P 1.00 nm

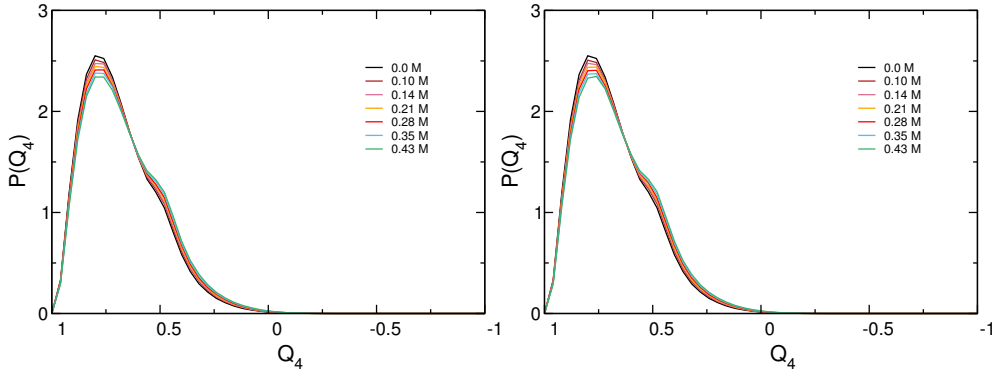

(c) TIP4P/Ice 0.85 nm (d) TIP4P/Ice 1.00 nm

Figure 3.14: Orientational order parameter for TIP4P and TIP4P/ice at 298 K, from low salt concentrations (dark colours) to high concentrations (light colours).

3.4.4 The effect of ethanol concentrations on TIP4P/Ice and TIP4P

In this section we continue to assess the compatibility of the TIP4P/Ice water model with the OPLS-AA FF using ethanol, which is an organic molecule that the OPLS-AA FF has been parametrized to work with, unlike the smaller NaCl ions. The ethanol molecules are of special interest to us because its basic chemical structure closely resembles the PVA oligomers, which we wish to study in the next chapter. The RDFs for various ethanol concentrations are shown for TIP4P and TIP4P/Ice in Fig. 3.15–3.16 and the atomic labels for ethanol are subscripted with a capital *E*. For instance ethanol oxygen atoms are assigned O_E. In this report of TIP4P/Ice and TIP4P ethanol-water mixtures, the local structure appears similar

to experimental and computational results[229]. For example, the expected peaks of the O_E-H_E RDFs are confirmed at 0.18–0.19 nm and 0.34 nm. While O_E-H and H_E-O have characteristic peaks between 0.17–0.18 nm and 0.3–0.33 nm. As with previous simulations, the systems with TIP4P/Ice water consistently display much higher local short range ordering. Otherwise no appreciable difference is found between the structures of the two water models. In both systems, the amplitudes of the first peaks grows visibly larger than that of the corresponding peaks in pure water as the ethanol concentration increases, however the position of the first peak doesn't move. The same could be said for all RDFs with second shoulders, except (O-O, O_E-O). In these exceptions the heights of the second peak is largely conserved until high (greater than 90% ethanol) concentrations are attained, causing a shift in the neighbouring shells to the right. Overall, these observations suggest that the addition of ethanol extensively enhances hydrogen bonding network of the water molecules surrounding it, which is confirmed later.

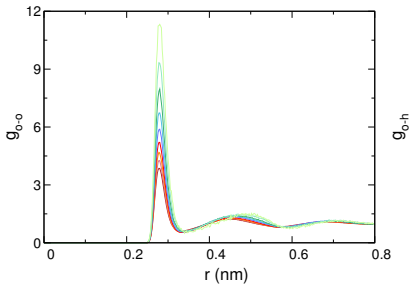

(a) Water Oxygen-Oxygen

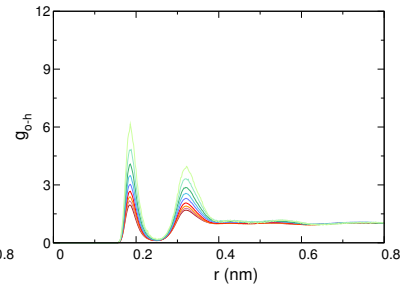

(b) Water Oxygen-Hydrogen

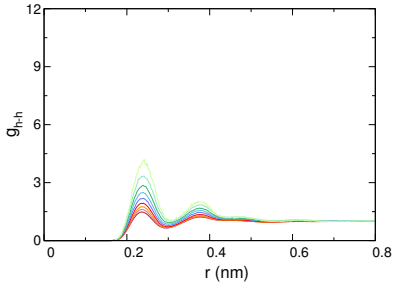

(c) Water Hydrogen-Hydrogen

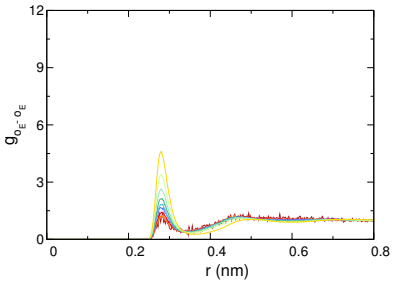

(d) Ethanol Oxygen-Oxygen

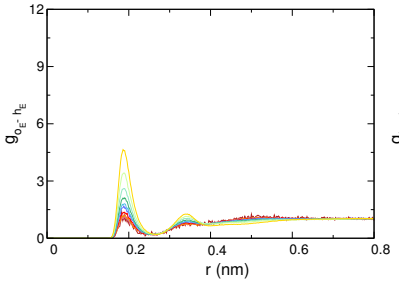

(e) Ethanol Oxygen-Hydrogen

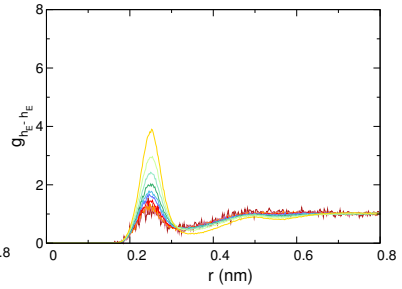

(f) Ethanol Hydrogen-Hydrogen

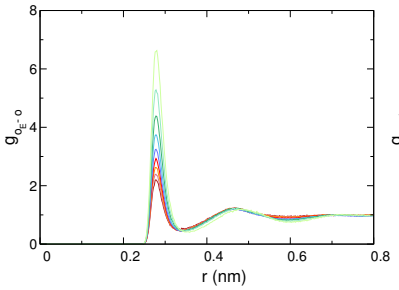

(g) Eth. Oxygen-Wat. Oxygen

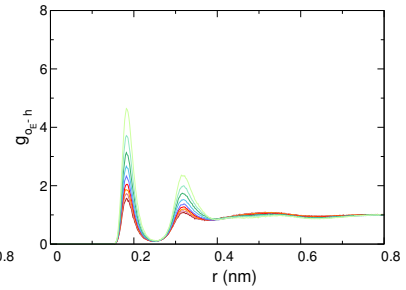

(h) Eth. Oxygen-Wat. Hydrogen

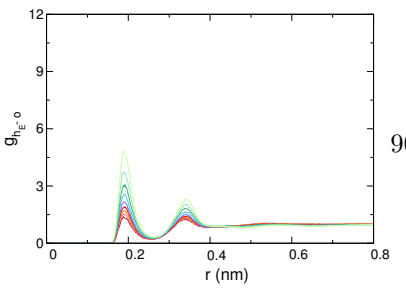

(i) Eth. Hydrogen-Wat. Oxygen

Figure 3.15: RDFs for different ethanol concentrations (10–100%) at 298 K with the TIP4P/Ice water model at 1.00 nm cut-off. Transition from dark red to blue, green and then yellow reflect low to high concentrations

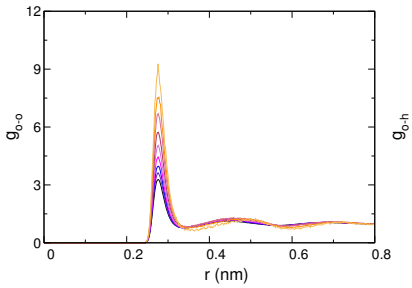

(a) Water Oxygen-Oxygen

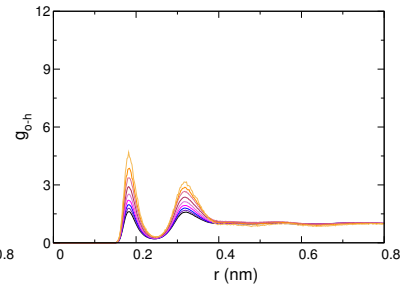

(b) Water Oxygen-Hydrogen

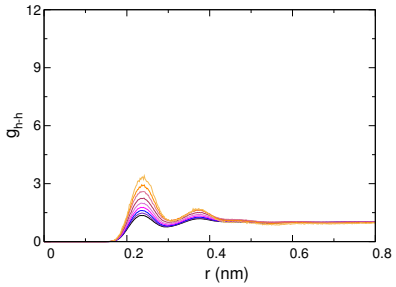

(c) Water Hydrogen-Hydrogen

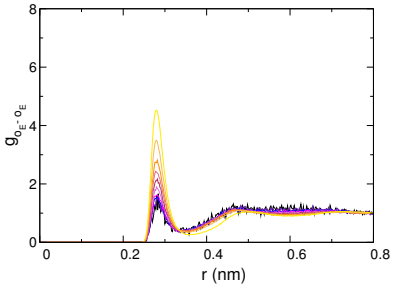

(d) Ethanol Oxygen-Oxygen

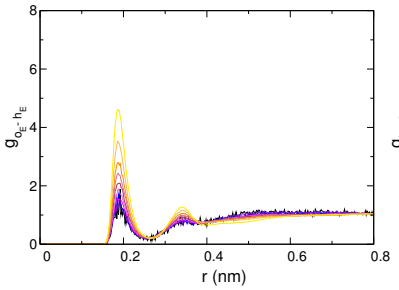

(e) Ethanol Oxygen-Hydrogen

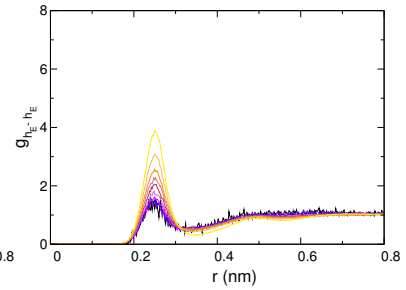

(f) Ethanol Hydrogen-Hydrogen

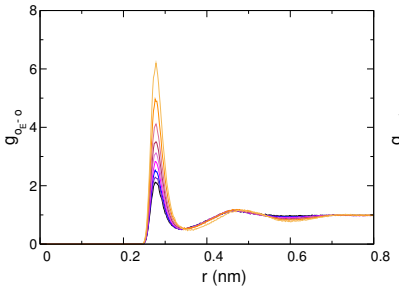

(g) Eth. Oxygen-Wat. Oxygen

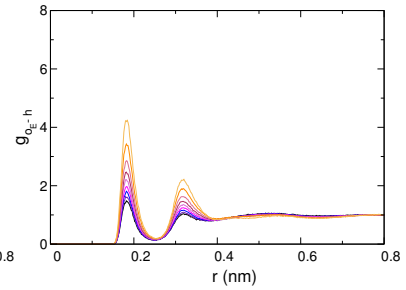

(h) Eth. Oxygen-Wat. Hydrogen

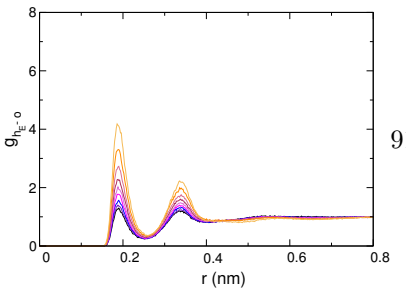

(i) Eth. Hydrogen-Wat. Oxygen

Figure 3.16: RDFs for different ethanol concentrations (10–100%) at 298 K with the TIP4P water model at 1.00 nm. Transition from purple, orange and then yellow reflect low to high concentrations

A wide range of diffusion coefficients were also obtained for an assortment of ethanol concentrations. Figure 3.17 shows the self diffusion coefficients for both water and for ethanol. We see that the model chosen to represent ethanol in these simulations do well to this respect and for both TIP4P and TIP4P/Ice systems the coefficients are fairly close to experimental values. The ethanol diffusion coefficient for the TIP4P water systems is closest to the experimental values at almost every concentration however it fails to predict a similar contour and transition seen between concentrations. In contrast however, TIP4P/Ice system mimics the contours of the experimental diffusion rates for both water and ethanol, although it remains somewhat shifted. TIP4P does not provide an accurate prediction of the experimental profile of water's self diffusion in the mixture. At best TIP4P/Ice is able to reproduce the experimental minimum close to 70% which is not achieved with TIP4P in our simulations nor in the cited literature[12,13]. Wensink *et al* began with several different parameters from our own systems. They used a Berendsen thermostat, a 1.1 nm cut-off and the SHAKE constraints algorithm but still wind up with the same results, which strongly suggests that these trends are not artefacts. We can therefore conclude that combining the TIP4P/Ice and OPLS-AA forcefields may present a better choice than a combination with the TIP4P water model.

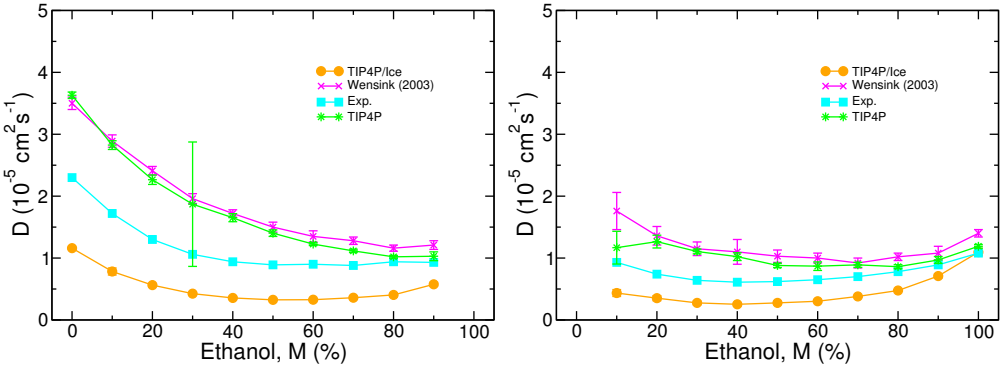

(a) Water (b) Ethanol

Figure 3.17: The self-diffusion coefficients for (a) water and (b) ethanol in ethanol/water mixtures at 298 K and a 1.00 nm cut-off. Results from Wensink *et al* [12] (TIP4P model) and experimental values[13–15] are also included.

Figure 3.18 reveals the results for N_H in ethanol-water binary mixtures. For both water and ethanol, these plots highlights the total N_H that the species participate in. The results are normalised for the number of species present, and so the units are effectively number of hydrogen bonds per species. Contributions from

species-species and water-ethanol interactions are also shown.

As the ethanol concentrations rise, we observed an increase in the total N_H per water (N_{HW}) and a decrease is seen in the total N_H per ethanol (N_{HE}). In pure ethanol, the average N_{HE} has been reported as 1.85–1.92 and our solutions produce 1.83, which is in close agreement.[16,285–287] A simple calculation is made in order to determine an ideal average N_H per molecule ($N_{H(W+E)}$) for the mixture at 70%. Consider that pure liquid TIP4P/Ice water has a value of 3.76 N_{HW}, $N_{H(W+E)}$ would therefore yield a value of 2.41 (i.e. (0.7× 1.83) + (0.3× 3.76)). The same calculation for TIP4P yields a lower average of 2.35. At 70% the actual $N_{(HW)}$ for TIP4P/Ice was 4.81 and N_{HE} was 3.49 yielding a higher average than expected at 3.88.

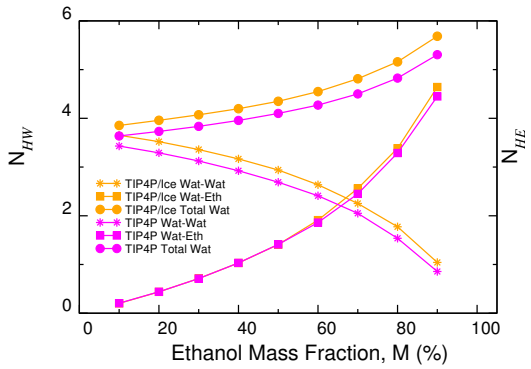

(a) Water

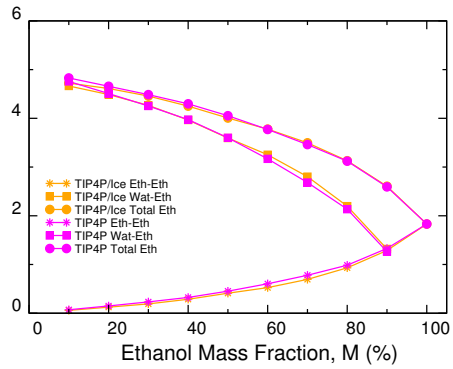

(b) Ethanol

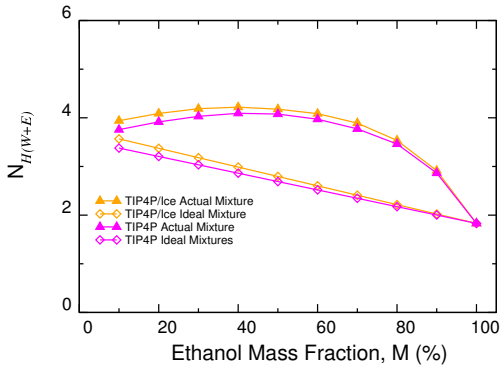

(c) Mixture

Figure 3.18: The number of hydrogen bonds, (N_H) (a) per water, (b) per ethanol and (c) per molecule in the ethanol/water simulations.

As a whole, Fig. 3.18c demonstrates that in the mixtures, the average hydrogen bonds per molecule grow with concentration reaching a maximum of ∼4 at 60%, and then decreases to ∼2. The maximum observed for TIP4P and TIP4P/Ice are 4.09 and 4.22 respectively. These maxima are achieved at a much lower concen-

tration than the 70% experimental benchmark however the profile is consistent with observations in numerous other computational studies[16] and experimental investigations[234,288,289] on the hydrogen bonding in alcohol-water binary mixtures. In the region of 0–20% the hydrogen bonding structure of water is reinforced by the addition of small amounts of ethanol, induced by the formation of more water-ethanol hydrogen bonds. While in the range of 70% and onwards the water structures is disrupted by the increasing alcohol concentrations. It is important to note that significant variations in these profiles exist depending on the methods used to investigate the hydrogen bonding[234,288,290].

Additionally, other binary ethanol-water studies report that at low alcohol concentrations, the binary mixture predominantly have 3 hydrogen bonds per molecule, whereas in the alcohol rich mixtures it is reduced to 2. Unlike the experiments our results proposes a higher average value at low concentrations which is further from the predictions of ideal mixing.[285,291]. This is to be expected as both water models overestimate the hydrogen bonding of water, however this notion is validated by our hydrogen bonding and ignites an interest in the water ordering.

Per ethanol molecule, as the concentration increases we can see that the number of water-ethanol interactions declines due to fewer water molecules present and as a result of the sterics associated with adding more ethanol molecules. Unsurprisingly, the resulting sterics shield the centring ethanol from surrounding water molecules and so the ethanol-ethanol interactions gradually increases as reflected by the growing number of hydrogen bonds. At most concentrations the water-ethanol interaction dominates ethanol's total hydrogen bonding per molecule, particularly at lower concentrations. Similar trends have been seen before for methanol, ethylene glycol and glycine in TIP3P water under a different forcefield.[292]. These observations are also corroborated by RDF marginally closer distance of approach found in O_E-O_E compared to O_E-O. In contrast the number of hydrogen bonds per water molecule decreases with ethanol concentration as they are successively replaced with ethanol. Experimentally the maximum number of hydrogen bonds for water should be found at around 20%[234,289,290] however this limit is not present in the simulation studies due to the models' predisposition to overestimate hydrogen bonding and so the water-ethanol interactions rapidly incline.

The densities of the ethanol-water mixtures are depicted in Fig. 3.19, and so are the number densities across the box of the 50% ethanol system. It is clear that the density decreases with the addition of ethanol to the system (Fig. 3.19a). The TIP4P water models closely overlap the experimental trail, while TIP4P/Ice overestimates the densities between the wide region of 30–80%. These features are

largely due to close packing of molecules which may have consequences for our work with polymer simulations. It appears that mixing the OPLS-AA FF and TIP4P/Ice may confine future simulations of poly(vinyl alcohol) to either low or high concentration solution studies in order to provide reliable estimates of the system density. Fig. 3.20 are snapshots of the system at the end of the simulation, which also confirm the disparities in density.

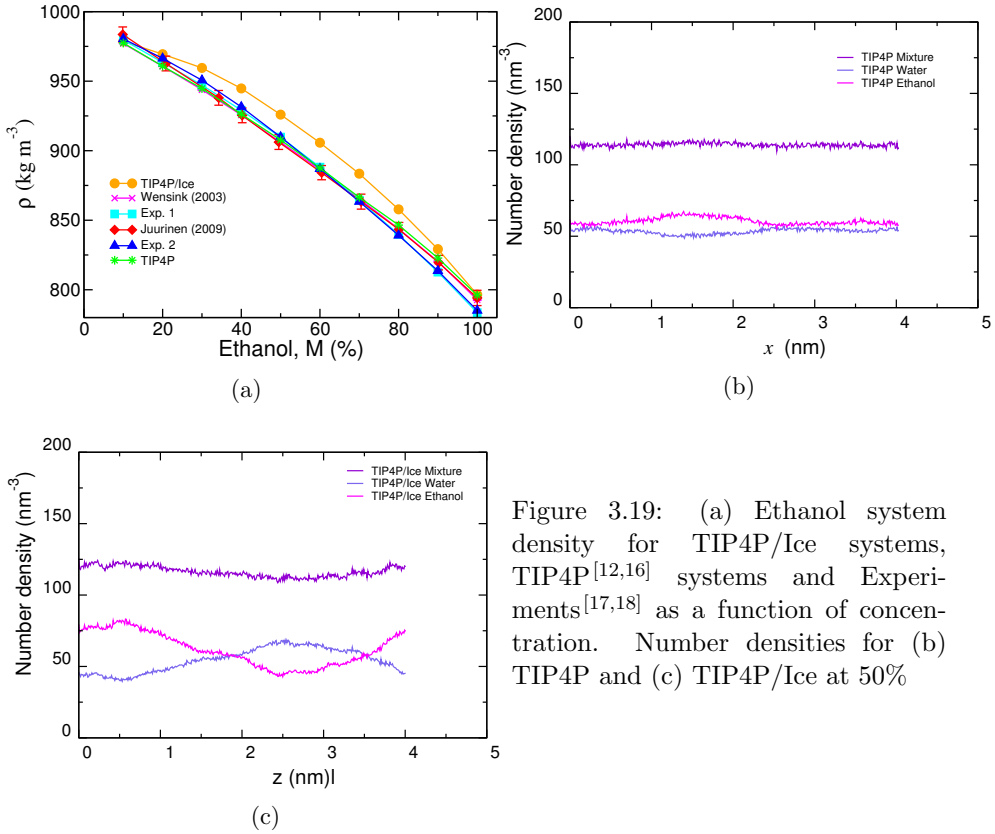

(a) (b)

(c)

Figure 3.19: (a) Ethanol system density for TIP4P/Ice systems, TIP4P [12,16] systems and Experiments [17,18] as a function of concentration. Number densities for (b) TIP4P and (c) TIP4P/Ice at 50%

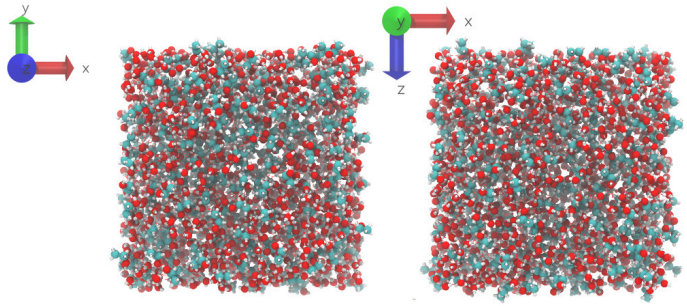

(a)

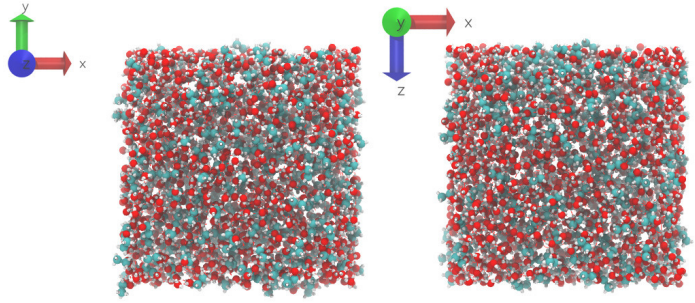

(b)

Figure 3.20: (a) Snapshot of packing density for 50% ethanol-water binary mixtures with (b) TIP4P and (c) TIP4P/Ice at the end of 3 ns trajectory. The element colours are: carbon (cyan), oxygen (red) and hydrogen (white).

Fig. 3.21 shows the distribution of the Q_4 parameter as a function of water concentration (%) in the ethanol solutions. In both cases the degree of tetrahedrailty declines with the introduction of ethanol molecules, similar to the effect of increasing the temperature. In line with previous observations, the ethanol molecules disrupt the hydrogen bonding network in the pure water system. The impact on the structuring of the waters is much greater than the effect of salt or temperature, particularly in TIP4P/Ice. The shoulders at 0.29–0.41 and -0.12 appear after 70% which indicates that another structuring may become prevalent with the introduction a certain level of hydrophobic molecules in the system. It is possible that the third shoulder indicates a random and non-specific clustering of water molecules, which is in line with the hallmarks of the hydrophobic effect.

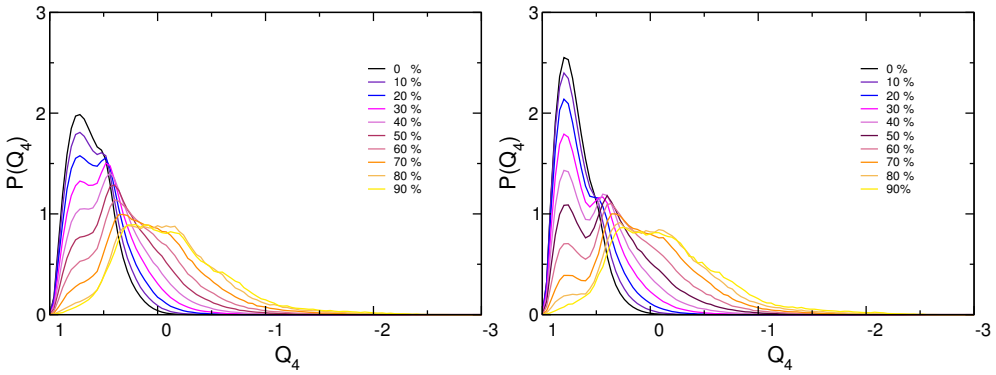

(a) TIP4P (b) TIP4P/Ice

Figure 3.21: The tetrahedral order parameter for (a) TIP4P and (b) TIP4P/Ice.

Free energy of solvation of ethanol was also calculated for TIP3P, TIP4P and TIP4P/Ice water models and the results were found to be -18.86 kJ mol^{-3} ($\pm$ 0.16), -19.71 kJ mol^{-3} ($\pm$ 0.30) and -20.37 kJ mol^{-3} ($\pm$ 0.30) respectively. These are similar to experimental value (-20.9 kJ mol)[293] and is best reproduced by TIP4P/Ice.

3.4.5 The effect of cut-offs on TIP4P and TIP4P/Ice

In this section we review the earlier data and report on the effects of using different sized cut-offs. For all TIP4P/Ice RDFs the three cut-offs (0.85–1.50 nm) overlap finely and this is true at every sampled temperature (235 K, 298 K and 348 K). The oxygen-oxygen RDFs is depicted in Fig. 3.22 and demonstrates that changing the cut-off within this range has negligible effects on the structure of the TIP4P/Ice water. This is also the case for the TIP4P water model which has also noted elsewhere[152].

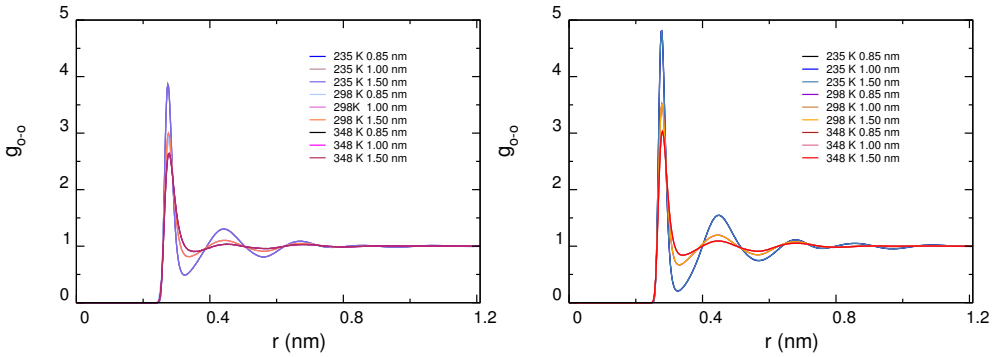

(a) TIP4P pure water box

(b) TIP4P/Ice pure water box

Figure 3.22: Oxygen-Oxygen RDFs for both water models at 3 temperatures and three cut-offs. The results of all three cut-offs overlap finely.

Similar approaches have previously been addressed, comparing popular water models for use in various forcefields[189,214] or the effect of changing a computational parameter[243]. The same could be said for simple pure water box systems[226,276,294,295], however to our knowledge none of these studies have focused on TIP4P/Ice. The results by Yonetani *et al* [294,296] summarised that with the exception of 1.5 nm, increasing the cut-offs from 0.9–1.8 nm for a pure TIP3P water system introduces undesirable artefacts in the orientational behaviour of water molecules over a 2 ns trajectory. These artefacts become apparent at 1.4 nm, and eventually manifests itself to an extent that an unphysical layer formation is observed. Although other water models were also investigated at smaller cut-off ranges, the study focused on TIP3P water model which is notorious for poorly representing the structural properties of liquid water[200,201]. They found that the artefact was dependent on the system size from 2,201 to 3,316 and 4,736 water molecules. With 2,201 waters the artefacts was present with 0.14, 0.16 and 0.18 nm cut-offs. However, with the larger system this artefact was only seen at 0.18 nm. Moreover they found that the potential energy decreases and the density increases with the higher cut-offs, suggesting a cut-off dependence of the thermodynamic and structural properties of these water models. These artefacts were also visible in other water models, however they were found to be much lower. Similar conclusions have been deduced for simulation of 1.0 M aqueous NaCl solutions between 0.9–1.6 nm cut-offs[297]. This study focused on the SPC water model and revealed that the cut-off approximation can severely affect the ion-ion radial distribution function at distances equivalent to the cut-off length.

We found that for TIP4P/Ice there were some artificial attributes associated with the structuring of Na-Cl in solution, resulting in more pronounced peaks and troughs as a result of a larger interaction sphere (see Fig. 3.9c). Aside from the effects of greater negative charges placed on the dummy atom, it is not clear why these same attributes were not detected with TIP4P, and are particularly true of the 0.10 M concentration.

For the observations of ionic simulations we see the following. Due to the noise visible in the Cl-Cl and the Na-Na plots, we assessed both water models for the artefact reported by Auffinger[297] using the Na-Cl RDFs. Our findings show that at both 0.85 nm and 1.00 nm, the tell-tale minima at the cut-off lengths were absent for all the concentrations. We did not conduct these simulation for larger cut-offs and are unaware if this is still the case for a system with a 1.5 nm cut-off. Rather what we do see is that reading from the graphs directly is much clearer to see the effect of concentrations with the 1.00 nm cut-off simulations than with the 0.85 nm cut-offs, particularly with respect to the Na-Cl and O-O RDFs. Except for the Na-Cl RDFs, there aren't substantial differences between the two cut-offs. For TIP4P/Ice water model, the Na-Cl RDFs of the longer cut-offs are considerably taller. For instance at 0.1 M solution it's almost 25% taller at 1.00 nm cut-off than it is at 0.85 nm. These changes cannot be attributed to larger sphere of interaction between the ions, since the same changes are not visible with the other water model.

Additionally we see that the water models do have small but different effects with the introduction of cut-offs. Generally in the TIP4P systems, the hydration number increases for both ionic species with an increase in the cut-offs. However, TIP4P/Ice shows conflicting results with decreases for Na and increases for Cl. Nevertheless as the concentration is increased the standard deviation between the two cut-offs decreases for TIP4P/Ice (from 0.057 to 0 for Cl hydration) and so may be negligible at much higher concentrations. In contrast no clear pattern can be deduced for the TIP4P water model.

The cut-offs have negligible effects on the diffusion coefficients of pure water system. Reductions in the diffusion coefficients were observed between 0.85 nm and 1.5 nm cut-offs for the 3 water models at higher temperatures (Table 3.5). However these reductions are much smaller for TIP4P/Ice, particularly at 348 K, where the largest deviation is present. The onset of these deviations begins much earlier with TIP3P at 298 K and demonstrates a lower tolerance towards changes in the cut-offs. It is clear from Table 3.9 that the hydrogen bonding is unaffected by changes in the cut-offs employed and so it is not surprising that this is reflected in the RDFs. This is true for pure water systems and those with low concentrations of salt (Table 3.6

and 3.9)

On average, at 298 K and 348 K the actual densities of water are best reproduced by the 4-point water models. At 298 K the closest representative of density is consistently attained at the 1.00 nm cut-off for all models, while at 348 K it appears to be different for each model (1.5 for TIP3P, 1.00 for TIP4P and 0.85 for TIP4P/Ice). Between the cut-offs we calculate the standard deviations for the density of the models and discover that the differences between cut-offs are minor. We see that with TIP3P the variation between the three cut-offs increases with temperature from 0.24 to 0.65 and 1.10 $\mathrm{kg\,m^{-3}}$. This linear dependence on the temperature is absent for the 4-point water models, however by averaging these three values we can calculate the average standard deviation between cut-offs at different temperatures. We see that TIP4P/Ice has the smallest variation at 0.46 $\mathrm{kg\,m^{-3}}$ and TIP3P has the largest with 0.66 $\mathrm{kg\,m^{-3}}$, which means that the effect of changing the cut-offs on the density is smallest for TIP4P/Ice and greatest for TIP3P.

It has previously been remarked upon that the use of a cut-off radius leads to higher densities which displaces the temperature of maximum density at 1 bar to lower temperatures[155,204,295,298,299]. In 2006 work by van der Spoel *et al* [295] previously reported the effect of two different cut-off treatments (0.9 and 1.2 nm) on the effect of the density, energy, dynamics and dielectric properties. This work was done on SPC, SPC/E, TIP3P and TIP4P water models however no report was made for TIP4P/Ice. These were done for two systems of 216 and 820 molecules, treating the long range electrostatic interaction with the reaction field approach. Their work serves as a good comparison to our work, however we have worked with larger systems of 4008 water molecules, longer simulation times (three times), and did not alter the OPLS-AA forcefield.

In our simulations, increasing the cut-offs at 235 K decreases the density of TIP4P/Ice and at the higher temperatures (298 K and 348 K) the densities increase (with an anomalous peak at 1.00 nm). This is not a linear trend and more points are needed to establish a more complete density profile. The aforementioned reports indicate that from 0.9 to 1.2 nm cut-offs, the density of the largest system increases for all water model at 298 K, regardless of the size of the reaction field used (1 and 78.5 $\mathrm{kJ\,mol^{-1}}$). Results for TIP3P are completely consistent with these observations, while it is much more difficult to draw a fine conclusion with the 4 point water models.

Again, no differences can be seen for the tetrahedral ordering as a result of changing the cut-offs rather the results for all finely overlap, as we see with the RDFs. This is evident in the absence (Fig. 3.8) and presence of small ions (Fig. 3.14)

and such features are very important in studying the induced effects of the structuring by small polymeric, antifreeze molecules around the ice quasi-liquid layer. It is important that we observed no artefacts and so far the results are promising under these conditions. As with the liquid solutions, the melting points of the water models as a function of the cut-offs have previously been discussed by many [226]. The effects of cut-off are primarily discussed in the section which follows (§ 3.4.6).

3.4.6 Melting and freezing

The melting points of the water models have previously been mentioned in this report and by many others [204,217,219,226] however we are primarily interested in the use of TIP4P/Ice for melting/freezing under reported conditions, [19,219] as well as our own. Understandably these melting and freezing temperatures vary slightly in literature with respects to the methods used to simulate or calculate the melting and freezing points. Nevertheless the results are in reasonable agreement with the experimental melting point of ice (272.2 K) at 269 K. A range from 266–278 K have previously been found as the melting points for the TIP4P/Ice model and our simulations comfortably fall within this range for both cut-offs. [19,204,217,219]

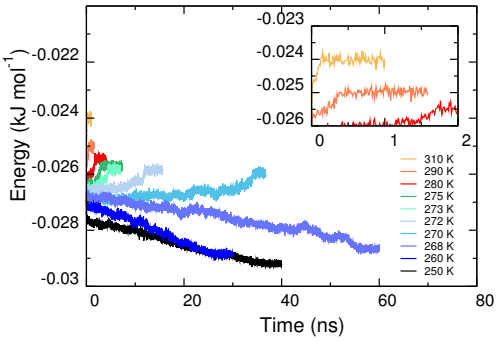

Figure 3.23: The total energy per water molecule from 250 K–310 K for 1 nm cut-off simulations.

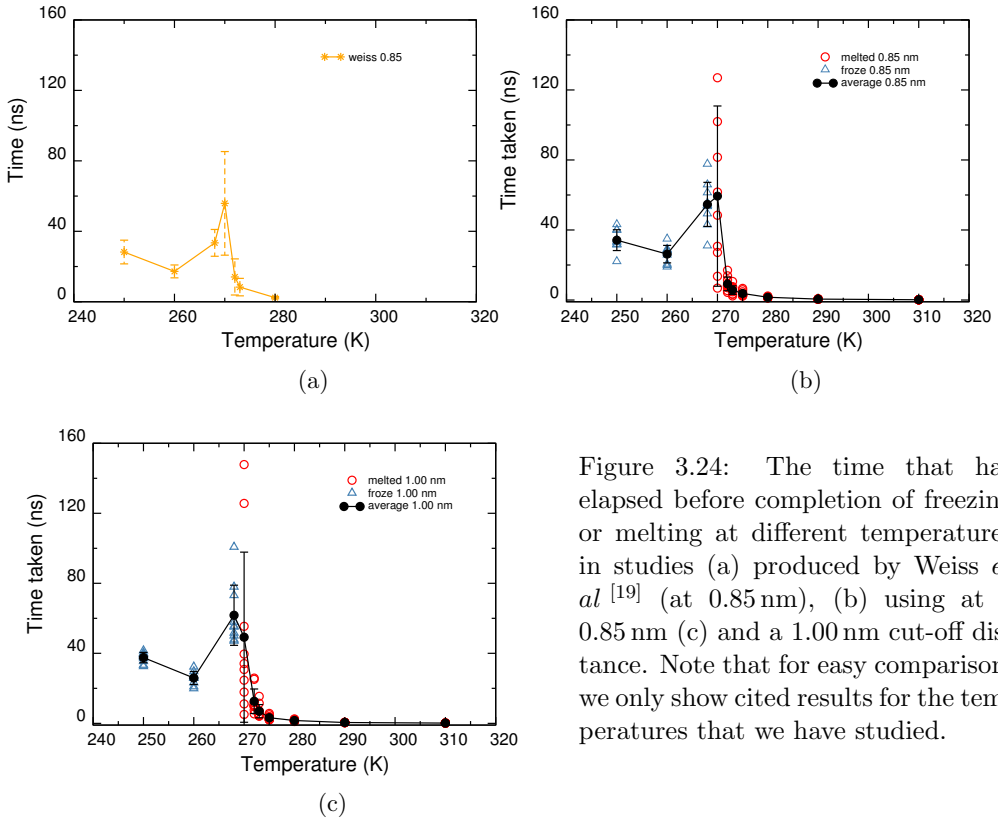

Figure 3.24: The time that has elapsed before completion of freezing or melting at different temperatures in studies (a) produced by Weiss *et al* [19] (at 0.85 nm), (b) using at a 0.85 nm (c) and a 1.00 nm cut-off distance. Note that for easy comparison, we only show cited results for the temperatures that we have studied.

Figure 3.23 depicts the total energy as function of time at different temperatures (230–310 K) for the 1 nm the cut-off simulation, and it shows that at and above 270 K the TIP4P/Ice completely melts. Below 270 K the system completely freezes. The time taken for completion of freezing or melting of our own simulations is displayed in Fig. 3.24b and 3.24c for 0.85 nm and 1.00 nm cut-offs respectively. For comparison we include the the results produced by Weiss *et al* [19] (Fig. 3.24a). They determined that the melting point of TIP4P/Ice was approximately 270 K because at this temperature they observed complete melting as well as complete freezing of the simulation between ∼32–93 ns and ∼7–14 ns, respectively. We however did not find a temperature at which both complete melting and freezing could be observed. Rather we deduced 269 K to be the melting temperature for both cut-offs, since melting is observed above that and freezing below it. These temperatures are in good agreement with the expected T_m for the TIP4P/Ice water model and once again illustrate that the mixing of the two forcefields can still reproduce reliable thermodynamic data. Fernandez *et al* [219] studied the effects of system size and different

computational modelling techniques on the T_m [and freezing rates] of TIP4P/Ice using the direct coexistence protocol. They found that it is not uncommon to see small disparities in the values due to as a result of using different methods and found only a 4 K variation in using MD simulations rather than free energy calculations and a 2 K variation in doubling the system size. We observe only a 1 K difference between the work produced by Weiss *et al* [19] and our own, although they used a 0.85 nm cut-off distance, semi-isotropic pressure coupling, a system almost half the size of our own and 40% ice composition (compared to our 67%).

The contours of these plots illustrate that at lower temperatures the freezing process typically takes much longer, as a result of depleting kinetic energy (needed to diffuse and reorient), and having approximately twice as many water layers to process than for melting. This is particularly true close to the melting point where we see a sudden spike in time required. Such observations are in line with theoretical findings[19,126]. For the shorter cut-off the apex of the graph is marked by melting simulations while for the larger cut-off it is marked by the freezing simulations. Neither is incorrect and this feature can be explained by drawing parallels to the finite-size effects in freezing simulations. Liquid regions in smaller systems are more influenced by periodicity introduced by using 3D PBC and so exhibit some artificial ordering. This reflects in higher growth rates and larger T_m[19,164,219]. In our studies, the first point of melting appears at 270 K using a shorter cut-off and this increases to a higher temperature (272 K) using the 1 nm cut-off. Using a greater cut-off radius provides more opportunities for the water molecules to interact with its neighbours, and the crystalline phase can induce further ordering into the liquid phase.

As mentioned earlier, the Q_4 parameter is often used to determine the regions of hexagonal ice-like arrangements in liquid water[137,258,261], and proves useful in the assessment of the growth of an interfaces in ice/water simulations[300]. This parameter is quite advantageous, seeing that hexagonal ice represents the limiting case of a well ordered tetrahedral network of hydrogen bonds in water. Figure 3.25 depicts the average orientational order parameter for different temperatures over time. As for the total energy plots, an inflection into a plateau signifies the completion of the melting or freezing process. The plot illustrate that the liquid water from the melting simulations can adopt a range of Q_4 orientations (0.68–0.76 at 310–270 K) whereas the ice simulations, on completion of freezing are limited to a much more narrow range of Q_4 values (0.94–0.95). Earlier, in section 3.4.2 we determined that liquid water that has been supercooled to 235 K can even obtain a values as high as $Q_4 = 0.88$. As a result, it is better to use these Q_4 values obtained

from the ice simulations as the cut-off to distinguish between ice like and liquid like water, rather than identifying intersections in Q_4 distributions from a large range of the solution studies of pure water conducted at a range of temperatures. Using the ice growth simulations at 268–260 K we propose a cut-off criteria of Q_4= 0.94. This method eliminates the need to repeat many simulations in solution, as is custom, and the uncertainty that accompanies the use of a smaller range of simulations.

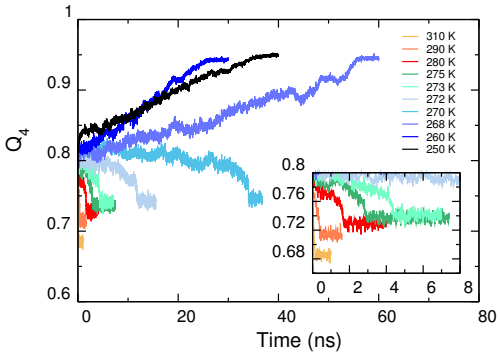

Figure 3.25: Orientational order parameter for different temperatures.

Figure 3.26 depicts the distribution of the x/y averaged density as a function of distance in the z direction. The entire sample was partitioned along the z direction into bins of 0.2 Å wide. The density profile in the last column corresponds to liquid while the second column corresponds to a fully frozen system. The centre of the density profile in **??** is the middle of the ice region within the starting configuration (approx. 4 nm into the z direction). The density profiles show characteristic long spikes where water is present and almost zero values in-between which reflected a highly ordered and regularly spaced structures at the center of the box. In contrast the density of the liquid sections undergo random fluctuations and so peaks are consistently present at regions before ∼2.5 nm and after ∼5.5 nm. Additionally the troughs between the spikes do not approach zero at all. Notice that taking the average of the ice region and the liquid water region separately still shows that the density of liquid water is higher than the density of ice and unsurprisingly, upon melting the box shrinks slightly. Ordinarily the structure and dynamics of the interfacial water is reduced compared to those of other surrounding bulk environments, often an intermediate between the two. This structural change at the interface is evident in our density profiles, ∼ 0.5 nm from either bulk environments, which somewhat lower than the expected 1.00–1.5 nm [26], however it suffices to say that the QLL will gradually form over simulation time as a function of temperature.

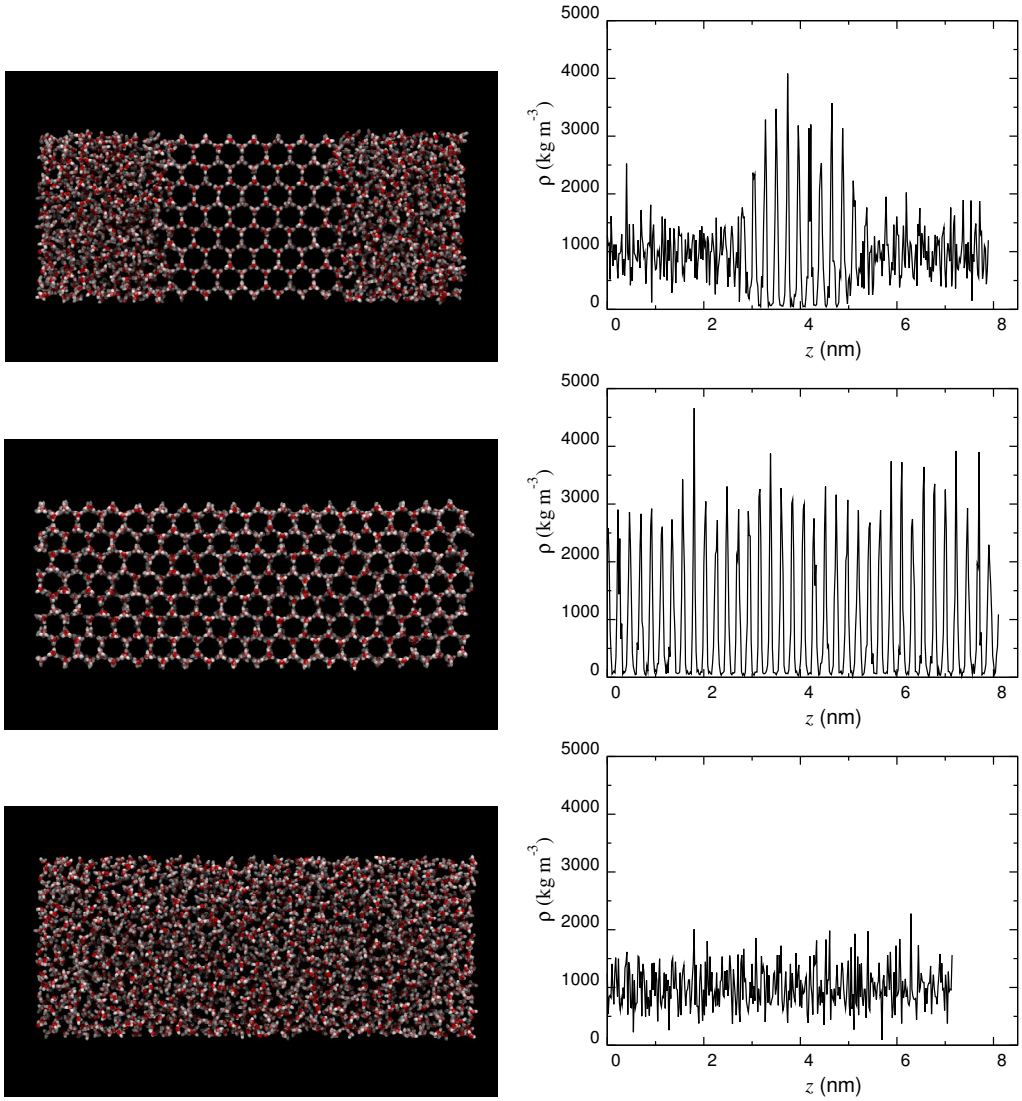

Figure 3.26: Snapshots of the ice/water system are shown on the left hand side and the corresponding density profile are shown on the right hand side. The density is averaged in the x/y direction as a function the z-box position. From top to bottom; the starting position of the system contains an ice slab sandwiched between liquid water, a completely frozen system after simulations at 250 K and a completely melted system after simulations 300 K. Oxygen atoms are shown in red and hydrogen atoms in white.

3.5 Conclusion

In this chapter, we have compared the different water models describing the liquid properties of water. Our results show that the density, structuring, hydrogen bonding and diffusiveness are fairly insensitive to the choice of the cut-offs between 0.85 nm, 1.00 nm and 1.5 nm. Moreover TIP4P/Ice and the other water models have been able to reproduce physical properties of water to similar previous reports of these models and in many cases similar to experimental results. To our knowledge this is the first time that in a molecular dynamics simulation that a variation of all water models have been compared and explored under the exact same conditions, over a systematics series of varying simulation conditions which includes later models like TIP5P and TIP4P/Ice.

The TIP4P/Ice appears suitable for use with the OPLS-AA forcefield and the use of larger cut-offs does not particularly impede the properties of water in the presence or absence of additives. However we foresee that for larger concentrations of NaCl, one should be cautious as the effects of cut-offs may induce problematic structuring features with small ionic additives like salts. The variations in properties like hydrogen bonding, RDFs, density and many features arise between different water models because of differences in molecular geometry and intermolecular potentials[258]. From our assessment it is evident that the TIP4P/Ice water model was parametrized to be much more ordered than the other water models and is biased towards tetrahedral orientations even in liquid phase. The relatively strong and long range ordering of TIP4P/Ice water is crucial to what makes it particularly suitable for ice growth studies. Its indifference to cut-offs, over the range tested here, makes it reliable for investigations using the OPLS-AA forcefield and in studies of ice growth with additives like salts, ethanol and larger macromolecules such as antifreeze polymers.

Chapter 4

MD simulations of antifreeze active and antifreeze inactive polymers in solution

4.1 Introduction

The solution properties of the antifreeze active and inactive polymers may provide information about the prerequisites for the antifreeze activities of PVA and why PEG remains inactive. MD simulation studies in solution can help to clarify which specific interactions the polymers partake in, and how these or other properties may change in the presence of the ice crystal. Studying these systems is also useful for addressing other aspects such as the importance of hydrophobic groups and the possibility of lattice matching or water ordering which may be required for significant interactions with ice. First we aimed to validate the PVA and PEG models by comparing them to polymer theory and previous published modelling results. Next, we also investigated single polymer chains in solution in order to observe the effects of polymer type, oligomer size and temperature on the structure and dynamics of PVA and PEG. We aimed to identify differences in the two polymers that may account for their antifreeze properties, and to determine if any properties are switched on at a particular chain length or if they can be triggered by a new, colder environment. The respective chemical formulas of PVA and PEG are: X(-$CH_2CH(OH)$-)$_N$-Y and X(-CH_2CH_2-O-)$_N$-Y where $\boldsymbol{N}$ is the number of repeat units, while X and Y can be end groups of different types. In this study we have chosen X=Y=H because it omits experimental end groups which vary as a result of different synthetic approaches. The selected range of polymers and their degrees of polymerisations (N= 5, 10, 19, 30

and 56) studied here were chosen for direct comparisons to recent splat experiments conducted by Congdon *et al* [7]. The significance of these chain lengths is that IRI activities seemed to switch on between N= 10 and 19, while the addition of further repeat units had less of a significant effect (See § 1.3.4 and Fig. 4.1). [7]

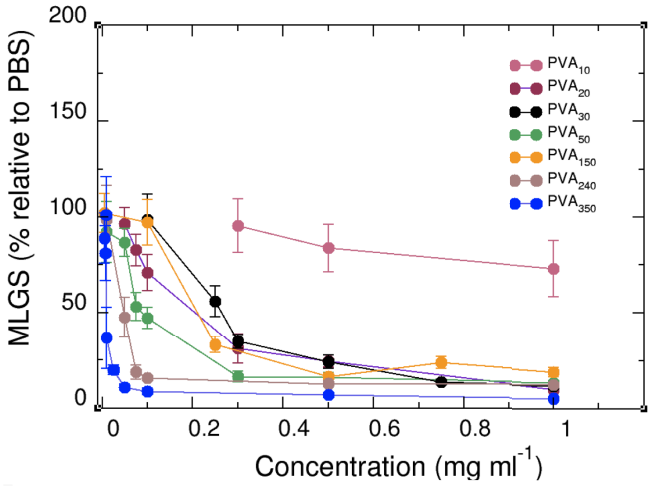

Figure 4.1: IRI activity of PVA polymers in PBS solution. Error bars represented standard deviations (stdevs) between repeats. Taken from Ref. 7.

4.2 Methods

4.2.1 Forcefield parameters

In the previous chapter we demonstrated the compatibility of the OPLS-AA forcefield with the TIP4P/Ice water model which has not previously been done. Following this demonstration we used the OPLS-AA forcefield to model the polymers in water, in room temperature (298 K) and in a cold temperature (260 K). Simulations were also conducted in cold temperatures because splat experiments [7] were typically performed at temperatures between 265–267 K. In some other experiments such as the microfluidic flow systems [86] and the capillary techniques [54,301] even lower temperatures may be used. It is therefore important to perform simulations in experimentally relevant conditions in order to fully understand the mechanism of PVA and other antifreeze active macromolecules. [302]

The TIP4P/Ice water model was chosen to represent water.

4.2.2 Simulation parameters

All simulations were performed using the GROMACS (v4.5.4) simulation package and can be described in the following stages. A simulation box of $9.10 \times 10.34 \times 10.75$ nm was placed around a single equilibrated polymer and the system was solvated via random placement of 33,207 TIP4P/Ice waters into free spaces. This equilibration procedure is crucial and outlined in the next section. It is important to ensure complete equilibration because polymer activities may rely greatly on their conformations as well as composition. When a system has equilibrated various properties will fluctuate around a stable average including structural properties. It is important to realise that once a system has reached equilibrium the quality of the conformational sampling is also important. The convergence of the system was therefore monitored using the radius of gyration over time. This approach is a routine, non-intensive calculation and is a appropriate way to measure polymer compactness over time. During the NPT simulation the temperature was maintained at 298 K using the Nosé-Hoover thermostat and the system was coupled to the thermostat every 0.2 ps. The pressure was held at 1 bar using the Parinello-Rahman barostat and a 2 ps coupling constant. Short range LJ and Coulombic interactions were cut-off at 1.00 nm, and long range electrostatics were controlled using using the PME protocol. These include the application of a 0.16 nm grid and a cubic interpolation. LINCS constraints were applied to all bonds involving hydrogen and periodic boundary conditions were used to remove surface effects and simulate a bulk environment. The lengths of interest were 5, 10, 19, 30 and 56 repeats units. Three simulations were conducted for each chain length and in sum 15 simulations were conducted for each polymer at 298 K. The last configurations from these runs were used to create initial configurations for simulations at 260 K. A subsequent 3 ns productions simulation was run at this temperature and aside for adjustments to the output frequency, the same simulation parameters were applied. The results of these simulations were used to validate the polymer models and to assess their physical properties before introduction to the ice environments.

4.2.3 Initial configuration and equilibration

Coordinates for the range of selected oligomers were generated to produce linear architectures and this was achieved using a C-program written in-house. The atom type assignments for our polymers are shown in Fig. 4.2 and Table 4.1. These atom types are standard choices for ethers and alcohols. Starting configurations for each linear polymer was built isotactic in structure. In order to remove unreasonable or

close contacts between given atoms, each polymer was subjected to a 20,000 step energy minimisation using the steepest descent algorithm. The new structures were placed in a cubic box accommodating their full length with an additional border of 3 nm in all box directions. Next the system was solvated with TIP4P/Ice water and subjected to a second energy minimisation, with periodic boundary conditions. Each system was equilibrated for 30 ns with short NPT simulations using the same conditions described above. This was performed in order to allow the polymers to collapse into their preferred conformations in solution and the process was monitored using the radius of gyration. A good convergence was reflected by a stable plateau. If convergence was incomplete the polymer was re-boxed, re-solvated and the system was prepared for a second 30 ns simulation. This stage was repeated until convergence was observed and the results are shown in Fig. 4.3. Our choice of polymers were taken from the work produced by Congdon *et al* [7] in 2013 however we chose to study a single chain and omit polymer concentration effects which are outside the scope of the present study but may be useful avenues for future work.

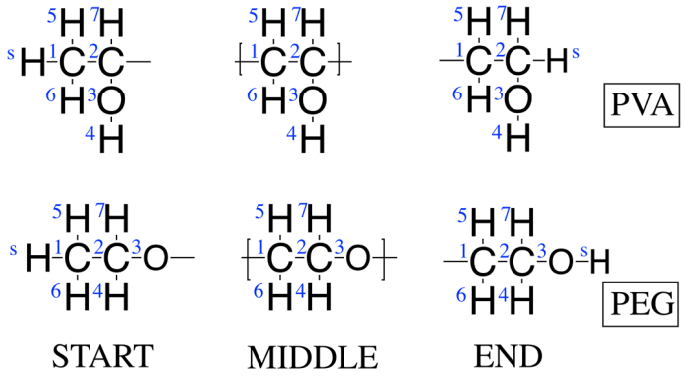

Figure 4.2: Numbering for atom type assignments of the terminal groups and repeat monomers used for PVA and PEG polymers.

	PVA			PEG		
Label	**Start**	**Middle**	**End**	**Start**	**Middle**	**End**
1	OPLS135	OPLS136	OPLS136	OPLS135	OPLS182	OPLS182
2	OPLS158	OPLS158	OPLS157	OPLS182	OPLS182	OPLS157
3	OPLS154	OPLS154	OPLS154	OPLS180	OPLS180	OPLS154
4	OPLS155	OPLS155	OPLS155	OPLS185	OPLS185	OPLS140
5	OPLS140	OPLS140	OPLS140	OPLS140	OPLS185	OPLS185
6	OPLS140	OPLS140	OPLS140	OPLS140	OPLS185	OPLS185
7	OPLS140	OPLS140	OPLS140	OPLS185	OPLS185	OPLS140
S	OPLS140	-	OPLS140	OPLS140	-	OPLS155

Table 4.1: Atom type assignment of the terminal groups and repeat monomers used (4.6a) for PVA and (4.6b) PEG polymers in the OPLS-AA forcefield. The labels correspond to atoms in Fig. 4.2 and are standard choices for modelling ethers and alcohols.

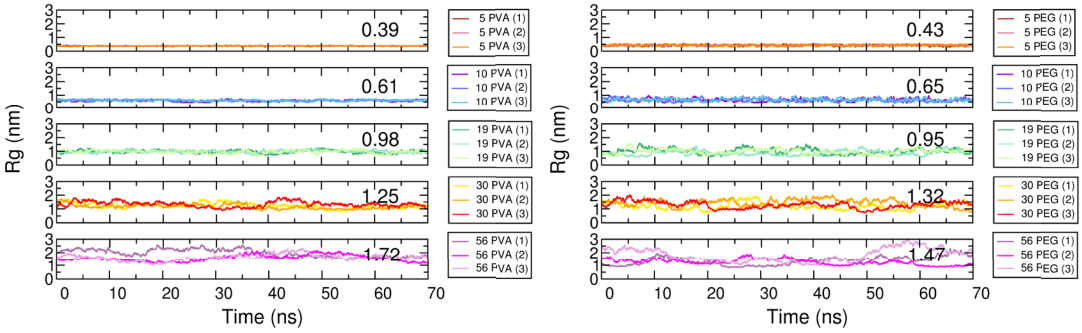

(a) (b)

Figure 4.3: The average R_g for (a) PVA and (b) PEG as a function of trajectory time at 298 K. Each repeat is shown and averages are shown in black. The plots are are stable and provide evidence that proper equilibration has taken place.

4.2.4 Analysis methods

Previous analysis

H-bond analysis and the orientational order (Q_4) of water were both calculated as described in § 3.3. In this current section the Q_4 calculation also includes the

polymeric oxygen in order to account for the possible incorporation of the polymeric structure into a tetrahedrally ordered water structure.

Radius of gyration

The radius of gyration (R_g) was calculated using Eq. 1.1 which was introduced in § 1.2.3.

Solvent accessible surface area

The solvent accessible surface area of the polymers were calculated using a GROMACS analysis tool and hydrophobic residues are classified according to their partial charges. Values of ± 0.2 were used represent hydrophobic residues and a 0.14 nm water-sized probe was used to trace the contours of the polymers in order to determine the area. A schematic is shown in Fig. 4.4

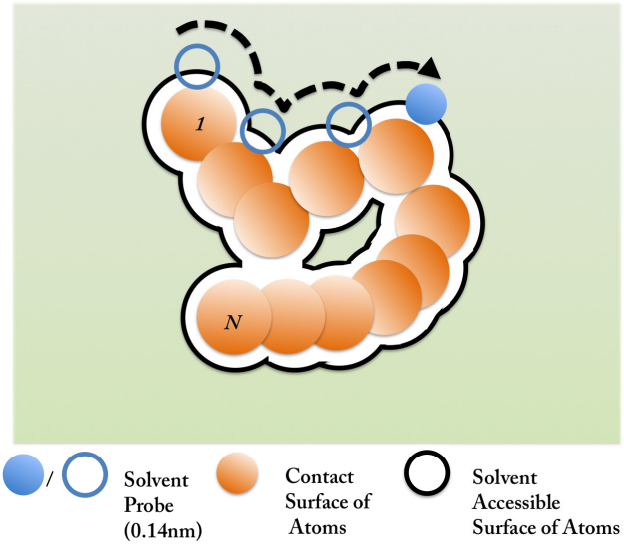

Figure 4.4: A schematic of the solvent accessible surface area of a polymer.

Root-mean-square fluctuation

The root-mean-square fluctuation of the polymer atoms was computed using another GROMACS tool and is described by Eq. 4.1. It represents the deviation of atoms from their average position and the averages are calculated over time. The r_t represents the position of the atom at time t and $\langle r \rangle$ is the average value.

$$RMSF = \sqrt{\frac{1}{N}\sum_{t=1}^{N}(r_i - \langle r \rangle)^2} \tag{4.1}$$

Hydration numbers

Hydration numbers are the number of water molecules with atoms that fall within 0.35 nm of the whole polymer. These calculation was performed using a TCL script and the results provides a quantitative description of the size of the polymer's hydration. In this thesis the results were typically presented as distributions and were normalized for the size of the polymers.

4.3 Results

4.3.1 Macromolecules shape and size

The average radius of gyration (R_g) was calculated for all oligomers and are shown in Fig. 4.5. The results are also shown alongside a distribution of values explored by each oligomer over a full trajectory (Fig. 4.7). Due to the relationship between molecular weight and the R_g , Fig. 4.5 is presented on a double logarithmic scale, which means that the Flory exponent can be extracted from the gradient of the graph. We found that the R_g for our oligomers obtained a power law dependence with chain lengths, which is in good agreement with theory ($R_g \propto \mathrm{Mw}^{0.588}$), experiments[303,304] and other modelling studies.[57,172–174] Our PEG oligomers obtained a Flory exponent of 0.53 ± 0.051, while PVA had one of 0.63 ± 0.027. Dynamic light scattering was used on aqueous solutions of PEG and determined an exponent of 0.50[303], while PVA obtained a value of 0.54[304]. Rossinsky *et al* [57] previously investigated pure PVA oligomer melts within a similar range of chain lengths and determined an exponent of 0.65. Similarly, Lee *et al* calculated values of 0.52 for poly(ethylene oxide)[173] and Hezaveh *et al* [173] obtained a value of 0.59 using the OPLS forcefield. These calculations provide an insight into the relative shapes or sizes of the polymers in solution. The better the solvent, the more likely they are to adopt a random coil conformation, and the greater the Flory exponent. In contrast, polymers in poorer solvents are typically more compact and globular in conformation, so they yield values that are much closer to 0.3. Therefore we conclude that both polymers are extended as random coils in water, as expected.

It is important to note that unlike the polymers in experiments our oligomers

are rather small and monodisperse, while a solution of polymers are typically several hundreds of units long and polydisperse. For instance Congdon *et al* studied the ice recrystallisation inhibition (IRI) of PVA with polydispersity indices between 1.18–1.45.[7] In light of this we acknowledge that these values may be somewhat overestimated, similar to findings from the aforementioned modelling studies.[57,172–174]

The distributions of R_g reveal that larger oligomers and PEG explore a wider range of conformations while smaller oligomers and PVA sample a narrower range. In response to the cold temperature, these distributions continue to narrow (Fig. 4.6) and the Flory exponent of PVA oligomers declines by 0.1 which indicate that they became less soluble in water, almost to the same extent as PEG at 298 K (Fig. 4.5), while the solubility of PEG remained approximately the same at both temperatures. At this present time we cannot tell whether or not this is part of the mechanism but with further study it may prove to be an important feature for antifreeze activity.

It is worth remembering that the simulation of long polymers presents a challenge to ergodic sampling, and that the use of cold temperatures can exasperate this further. The distributions of R_g at 260 K indicate that there may be some incomplete sampling of conformational space by larger chain lengths. However, recall that the ergodicity of the system is improved provided that sufficiently long simulation times are used ($\sim$70 ns) and that convergence has been reached, both of which are true (see § 2.1.1).

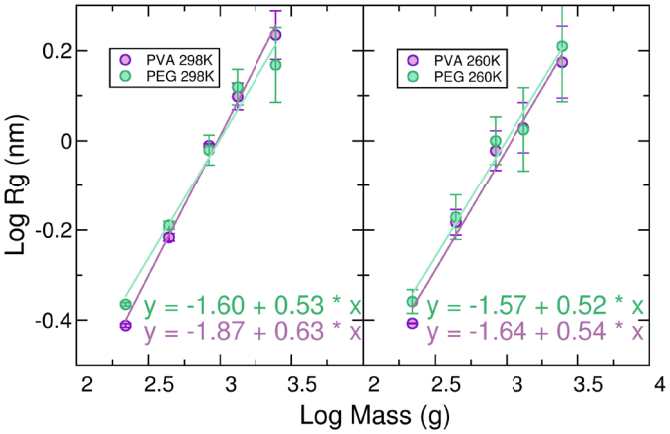

Figure 4.5: Linear fit to log R_g vs. log molecular weight at 298 K and 260 K. Error bars are stdevs between repeats.

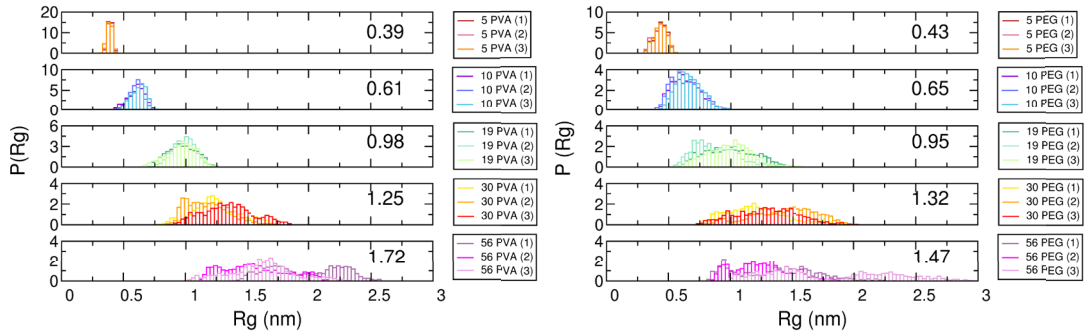

(a) (b)

Figure 4.6: The probability distributions of the R_g for (a) PVA and (b) PEG oligomers at 298 K. There are three different histograms for each oligomer, which refer to the repeat runs.

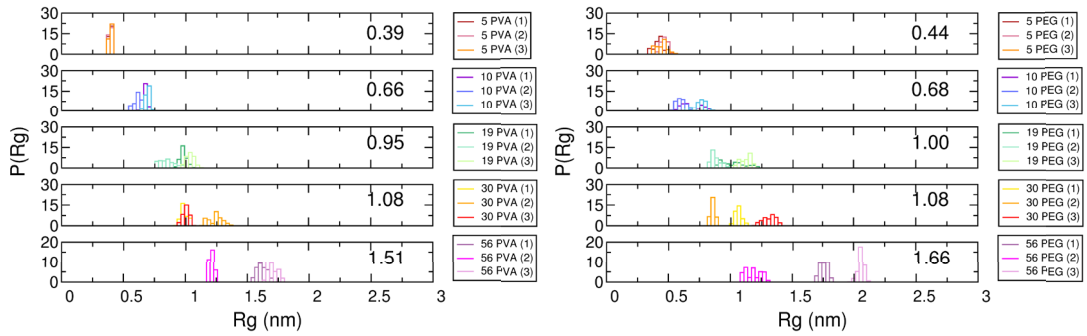

(a) (b)

Figure 4.7: The probability distributions of the R_g for (a) PVA (b) and PEG oligomers at 260 K. There are three different histograms for each oligomer, which refer to the repeat runs.

4.3.2 Water ordering or disordering properties

Through perturbation

One of the hypotheses mentioned earlier is the possibility that AF(G)Ps and their mimics function by ordering or disordering surrounding water in order to inhibit growth of ice on the ice/water interface.[75,147–149,154] This is one of the most im-

portant issues we aim to clarify during ice crystal growth as well as in solution. If these oligomers are capable of distorting the bulk or hydrating water significantly, one would expect to observe some of this activity in solution and at room temperature. In order to achieve this we characterised the water around the polymer by calculating the radial distribution functions (RDFs) of water oxygens (O) to the polymeric oxygens (O_X), the hydration number and the orientational order of hydrating waters.

Fig. 4.8 shows the RDF results for each oligomer and highlights the probability of finding a water oxygen close to the polymeric oxygen. We find that these RDFs exhibit characteristic peaks for PVA at 0.28 nm (strong), 0.47 nm, 0.66 nm, 0.87 nm and 1.07 nm (weak), as well as for PEG at 0.28 nm, 0.48 nm (strong), 0.83 nm and 1.13 nm (weak). These positions agree with those reported by other similar studies and the shapes of the RDFs are comparable to theirs.[57,181–184] The probability of finding a water oxygen close to the polymer oxygen is highest at 0.28 nm, which is characteristic of hydrogen bonding between the two species, and declines on approach to the bulk water, which is further away from the polymer. It is apparent that PVA has multiple peaks, all of which are more pronounced and narrower than corresponding PEG polymers and indicates well defined hydration shells, with strongly confined water molecules. It is also describes the longer-range ordering induced by interactions with PVA, which is unsurprising because PVA has two atoms which are capable of hydrogen bonding with surrounding water molecules, while PEG only has one.

The RDFs for PEG have markedly taller peaks for the second shell than the first one, which hints at another type of interaction being prioritized for short range interaction with the oligomers. As a result there is also a higher probability that water will be found some distance away. One such example could be a preference for polymer-polymer interactions or some form of hydrophobic solvation. For both types of polymers the height of the peaks are reduced somewhat with increasing chain length. We attribute this to the ability of longer polymers to fold and temporarily mask or bury its own oxygen groups from waters around it.

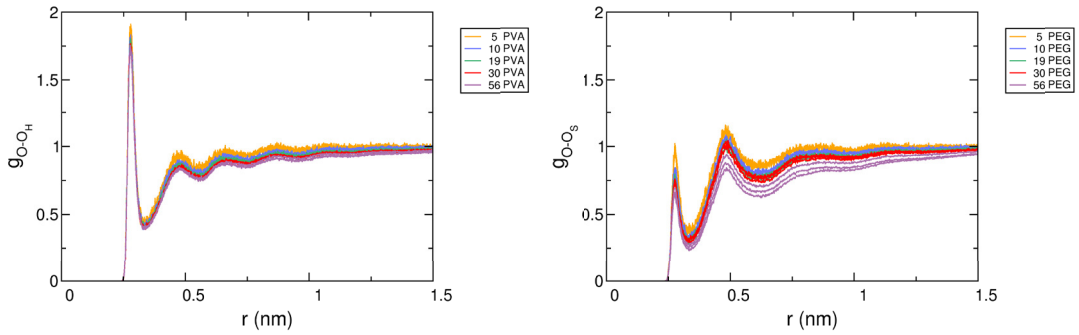

(a) (b)

Figure 4.8: RDF between water oxygen and polymer oxygen atoms at 298 K. Three repeats are included for each chain length.

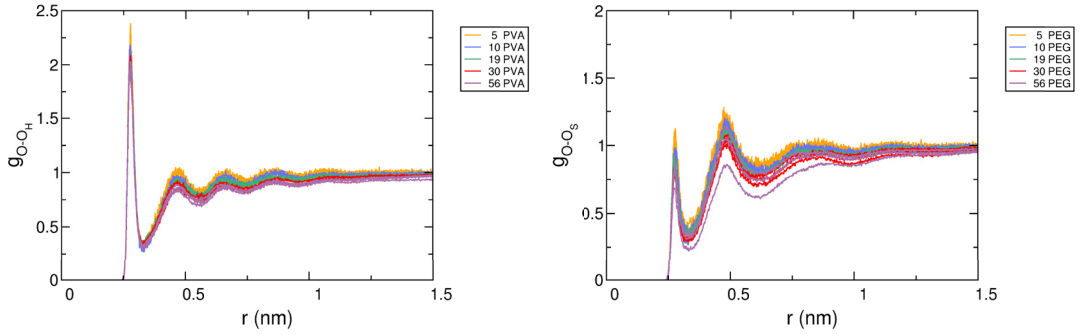

(a) (b)

Figure 4.9: RDF between water oxygen and polymer oxygen atoms at 260 K. Three repeats are included for each chain length.

Because it is possible for the polymers to influence the structure of surrounding water molecules via hydrogen bonding or through hydrophobic interactions or both, we plot the RDF for water oxygens with polymeric carbons in Fig. 4.10. The relative importance of these interactions can also be evaluated through several other types of analysis; the solvent accessible surface areas, the hydrogen bonding as well as the RDF of both hydrophilic and hydrophobic groups in water. The O-C_S RDFs for PEG reveal peaks at 0.38 nm which merges with a weak shoulders at 0.50 nm, and again for the next two weak peaks at 0.65 nm and 0.76 nm. In contrast, PVA

oligomers have well separated peaks at 0.37 nm, 0.51 nm and 0.79 nm, all of which are lower in height than for PEG. A comparison of the two RDFs for PEG oligomers (O-O_S and O-C_S) indicates that water oxygens can approach more closely to the oxygen atoms (0.28 nm) than the carbon atoms (0.38 nm), however the relative heights of the peaks may be indicative of a particular type of hydrophobic interaction. This is further emphasised by the taller second shoulder in the O-O_S RDFs, which confirm that the water oxygens are likely to be dispelled some distance away from the polymeric oxygen as a result of the hydrophobic repulsion. A similar comparison of the two RDFs of PVA reveals that waters largely reside at a distance of 0.28 nm and preferentially interact with its polymeric oxygen. Consequently, we can suggest that the PEG polymer largely interacts with solvent via hydrophobic interactions, while PVA does so via hydrophilic interactions provided by its hydroxyl side groups. These attributes remain true at cold temperatures, and the RDF peaks and troughs are simply more pronounced as a result of reduced thermal energy available for molecules to move outside of their respective shells.

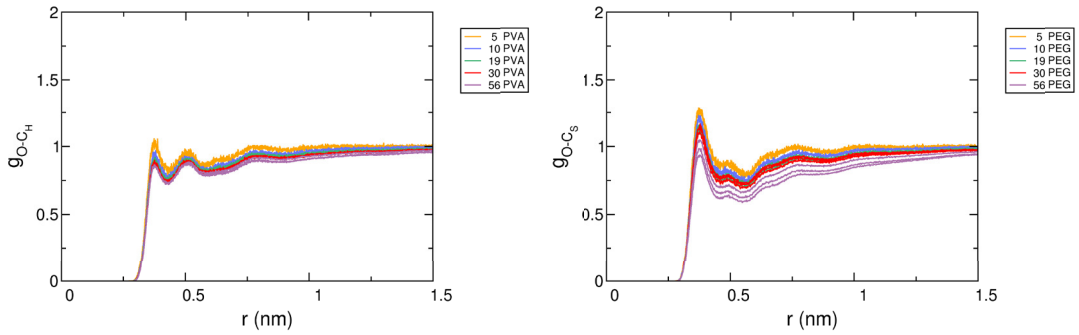

(a) (b)

Figure 4.10: RDF between water oxygen and polymer carbon atoms at 298 K.

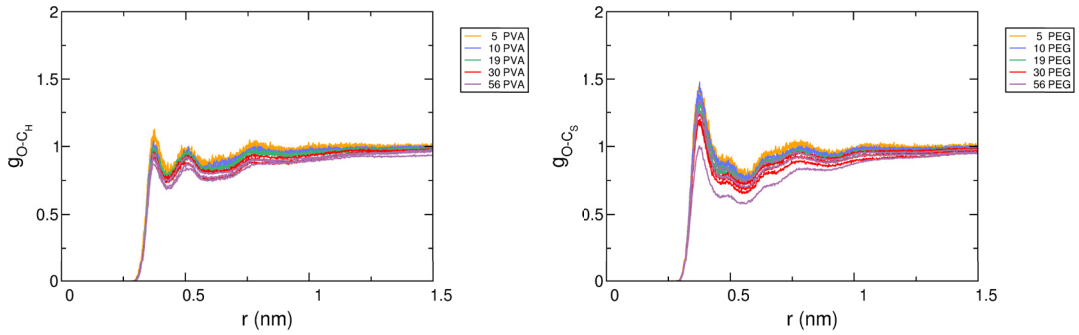

(a) (b)

Figure 4.11: RDF between water oxygen and polymer carbon atoms at 260 K.

Through hydration indices

A histogram of hydration numbers is shown in Fig. 4.12 for both types of oligomers. Carbohydrates have previously been used to demonstrate the importance of hydration in IRI activity.[6,305] In order to consider this, we investigate the hydration numbers of oligomers within a 0.35 nm cut-off distance. The longer the polymer, the wider the distribution because more conformations are accessible and so the hydrating water will also be altered just as much. We find a much narrower distribution for PVA. Throughout the trajectory the 5-mers of both polymer encounter approximately the same number of waters with the same frequency. With polymers

larger than five units long, we find that PEG consistently has a larger hydration number than PVA. This too is reflected in the broader RDFs in Fig. 4.8 and is surprising as it indicates that more hydrophilic groups does not necessarily translate into larger hydration sphere, but could mean the reverse.

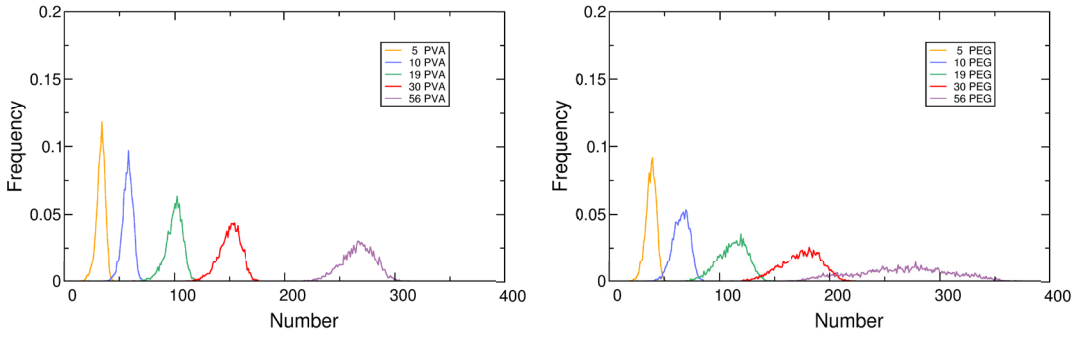

(a) (b)

Figure 4.12: Probability density showing the average hydration number of the *whole* polymer at 298 K.

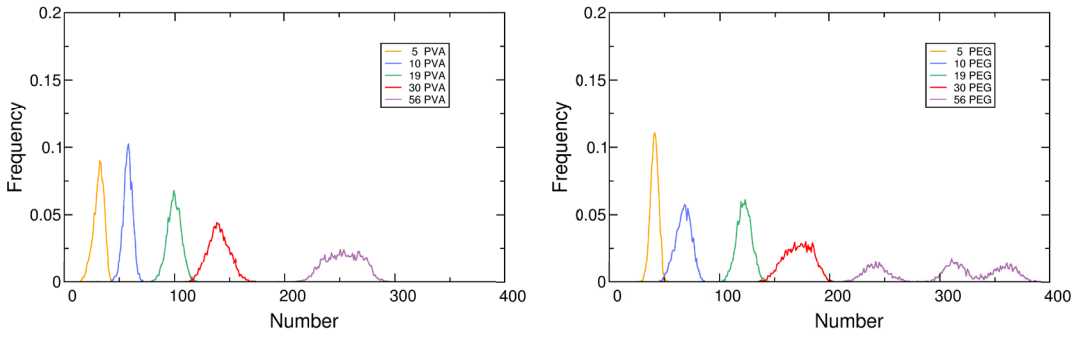

(a) (b)

Figure 4.13: Probability density showing the average hydration number of the *whole* polymer at 260 K.

Through tetrahedral ordering

In Fig. 4.14 and Fig. 4.15 we plot the tetrahedral orientation of water and polymeric oxygens. We find a characteristic peak at 0.80 and a subtle shoulder at ∼0.5 for

ordered and disordered regions respectively. In pure water, the transition from 298 K to 260 K caused an increase in tetrahedrality from 0.80 to 0.84, and in population from 2.55 to 3.32 (by approx. 30%). At both temperatures, we do not observe any remarkable tetrahedral ordering or disordering of the water oxygens within 0.35 nm of the polymeric oxygens, by either of the polymers nor as a function of chain length. A comparison of PVA and PEG polymers did reveal a weak 0.04 shift for the PEG simulations to disordered regions. No such shifts were observed for any of the PVA systems. Rather PVA exhibits a minuscule decline in heights of the ordered peaks. This is reflected in the fact that the same transition from 0.80 (at 298 K) to 0.84 (at 260 K) in the presence of PVA_{5-56} increased the population of the ordered region by just 25–28% and by 24–30% in the presence of PEG_{5-56}. Generally, these disordering changes for both types of polymers are accompanied by a growing shoulder at $\sim$0.5, but it is important to stress that these changes are very faint.

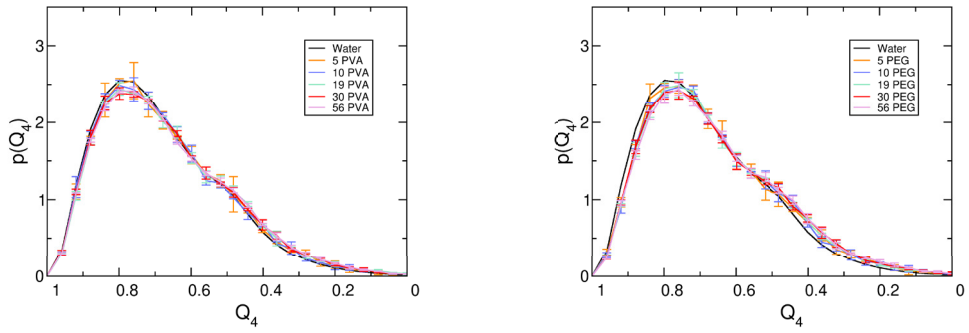

(a) (b)

Figure 4.14: Probability density distribution of the tetrahedral order parameter of interfacial water at 298 K. Interfacial water molecules lie within a 0.35 nm radius from the polymer oxygen atoms. For each oxygen, the Q_4 is calculated using its four nearest neighbours. Error bars are stdevs between repeats.

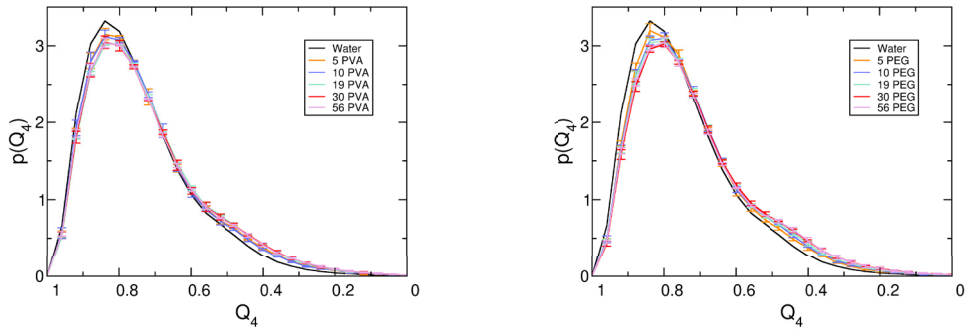

(a) (b)

Figure 4.15: Probability density distribution of the tetrahedral order parameter of interfacial water at 260 K. Interfacial water molecules lie within a 0.35 nm radius from the polymer oxygen atoms. For each oxygen, the Q_4 is calculated using its four nearest neighbours. Error bars are stdevs between repeats.

In order to account for the steric interferences from whole polymer the Q_2 and Q_3 values were also calculated for simulations at 298 K. The distributions from these calculations are shown in Fig. 4.16 and Fig. 4.17 respectively. The Q_2 and Q_3 analyses are useful because steric obstruction from the polymers could prevent the approach of four neighbouring water molecules, while they may still be able to ac-

commodate clusters of two or three neighbours. As a result these distributions could prove to be better representations of the orientational order of surrounding water molecules than the Q_4 distributions. The results reveal that the use of fewer water molecules increases the likelihood that the oxygen atoms will simultaneously occupy the angles required to form tetrahedral arrangements. As a result the shoulders at 0.5 is reduced and any bimodal features are lost for Q_2 and Q_3 distributions of all polymers.

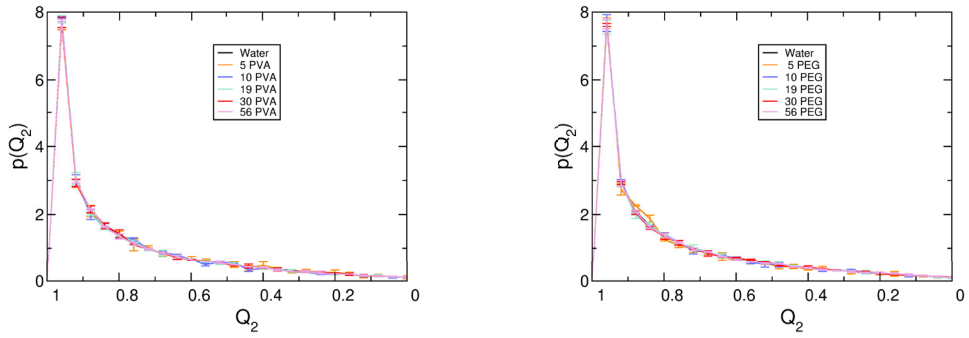

(a) (b)

Figure 4.16: Probability density distribution of the tetrahedral order parameter of interfacial water at 298 K. Interfacial water molecules lie within a 0.35 nm radius from the polymer oxygen atoms. For each oxygen, the Q_2 is calculated using its two nearest neighbours. Error bars are stdevs between repeats.

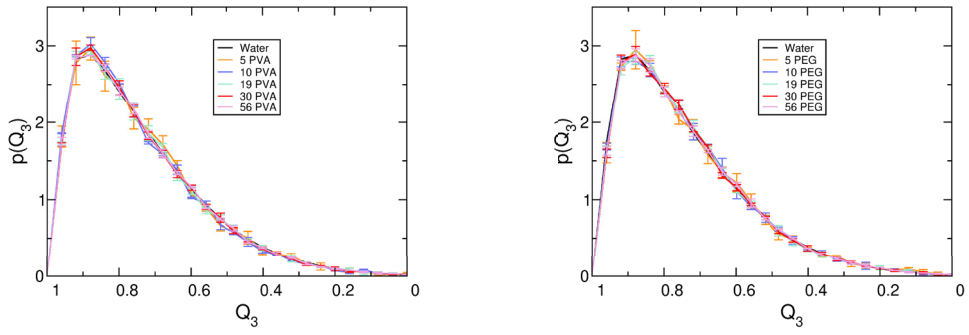

(a) (b)

Figure 4.17: Probability density distribution of the tetrahedral order parameter of interfacial water at 298 K. Interfacial water molecules lie within a 0.35 nm radius from the polymer oxygen atoms. For each oxygen, the Q_3 is calculated using its three nearest neighbours. Error bars are stdevs between repeats.

Compared to pure water, the results obtained for the Q_2 and Q_3 distributions are not remarkably different to the polymeric systems, yet again. The Q_4 results for PVA suggest a slight decrease in tetrahedrality, while in Q_3 there appears to be some small amounts of ordering, and no marked difference in the Q_2 analysis. For PEG, the results obtained for Q_4 suggests a small disordering effect, and no marked

difference for both the Q_2 and Q_3 distributions.

In order to determine which of these distributions provides the most accurate description of the system, the average number of oxygen molecules which surround the polymeric oxygen atoms were also recorded. The results are shown in Fig. 4.18 and it reveals that each PVA oxygen atom is normally surrounded by 3 oxygen atoms, which can belong to either a water molecule or another polymeric oxygen. The results from the Q_3 parameters therefore provide the most suitable description of PVA at 298 K and 260 K. The same is also true for PEG oligomers, however there are occasions where the oligomers are equally as likely to have 2 oxygen atoms close to the polymeric oxygen. Regardless of the temperature, this never occurs for PVA so only the Q_3 distributions were calculated for the polymeric systems at 260 K, and the results are shown for PVA in Fig. 4.20. At the lower temperature, there is still no significant ordering or disordering by the PVA or PEG oligomers compared to pure water. This suggests that the tetrahedral ordering of surrounding liquid water may not be as important as first expected.

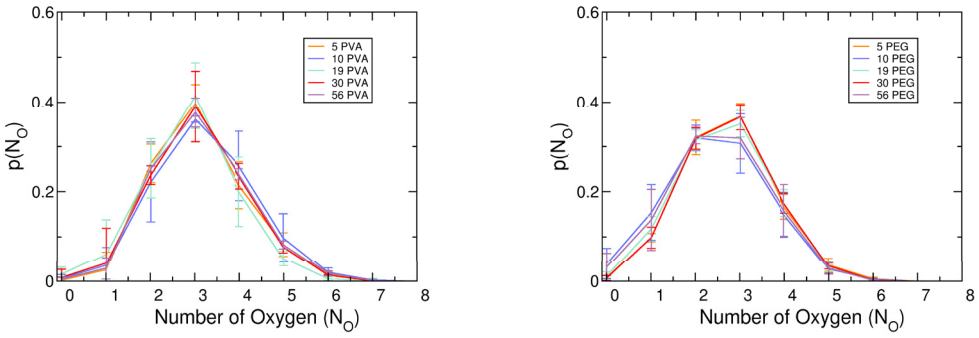

(a) (b)

Figure 4.18: Probability density distribution of the number of oxygens which approach the polymeric oxygen at 298 K. Error bars are stdevs between repeats.

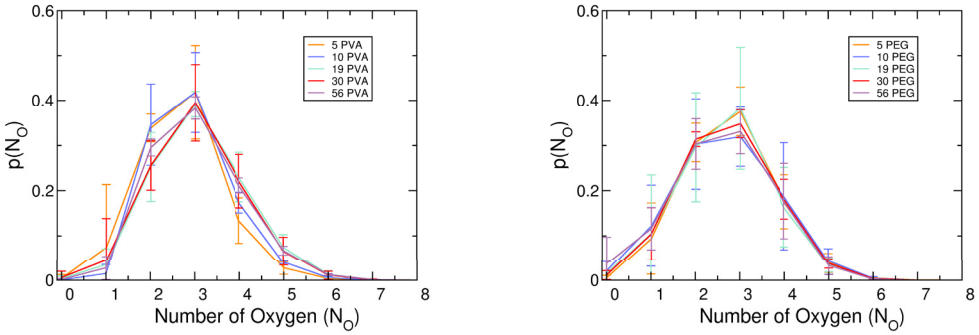

(a) (b)

Figure 4.19: Probability density distribution of the number of oxygens which approach the polymeric oxygen at 260 K. Error bars are stdevs between repeats.

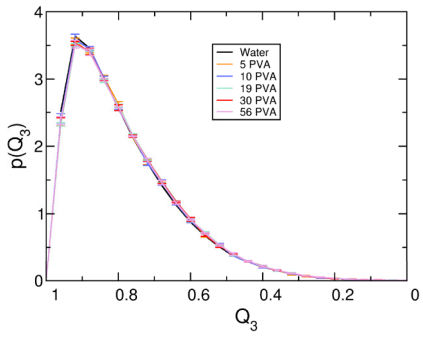

Figure 4.20: Probability density distribution of the tetrahedral order parameter of interfacial water at 260 K for PVA oligomers. Interfacial water molecules lie within a 0.35 nm radius from the polymer oxygen atoms. For each oxygen, the Q_3 is calculated using its three nearest neighbours. Error bars are stdevs between repeats.

4.3.3 Lattice matching properties

Another interesting theory we explore is the concept of specificity and the ability of the PVA polymer to compliment the ice lattice spacing (see § 1.3.1, § 1.3.3– 1.3.4 and § 1.4.2 for the importance of lattice matching in IRI). So we calculated the RDFs between the polymeric oxygens and the results are shown in Fig. 4.21 and Fig. 4.22. For PVA, we obtain large peaks at 0.30 nm, 0.46 nm and smaller ones at 0.62 nm, 0.73 nm and 0.81 nm. In total 3 distances could be found between PVA oxygens which compliment the lattice spacing on ice with deviations of just 0.01–0.02 nm, which is an excellent fit. There are two characteristic distances, depending on the conformation of the polymer. For each oxygen atom, these two peaks are typically populated due to adjacent oxygen atoms. The one with the highest probability is 0.46 nm and perfectly matches the 0.45 nm oxygen spacing on the prism planes. The fourth and fifth populated peaks at 0.73 nm and 0.81 nm are formed by non-adjacent oxygens on the polymer backbone and these also coincide with oxygen separations of other planes of ice. The basal plane is characterised by spacings of 0.83 nm while oxygens on the other prism plane are distanced by 0.74 nm. In stark contrast, PEG only has two well defined peaks at 0.31 nm and 0.40 nm; neither of which match the oxygen separation distances reported for any of the ice planes. These distances are also highly populated by adjacent oxygen atoms. We can therefore conclude that the lattice matching may simply be due to separation distances between the pen-

dant hydrophilic groups. This feature is a direct consequence of molecular structure, although molecular flexibility may also enhance it or play some part. Therefore the design of an ideal antifreeze macromolecule should consider the separation distances between adjacent, hydrophilic pendant groups, as they may play an important feature in the mechanism of IRI. Again, we report that with increasing chain length the peaks become increasingly broader and shorter. Peaks for oxygen separation also begin to form and merge at further distances because of an increased flexibility experienced by longer chain lengths (see below).

We also report the RDFs for hydroxyl hydrogen atoms of the PVA oligomer. In order for these hydrogen atoms to interact with the ice lattice, it also needs to be in the correct orientation. Results are shown in Fig. 4.23 and we find that the H-H spacing supports the idea of lattice matching. It is important to note that this analysis does not take into account the direction of the hydrogen bond relative to the oxygen atom.

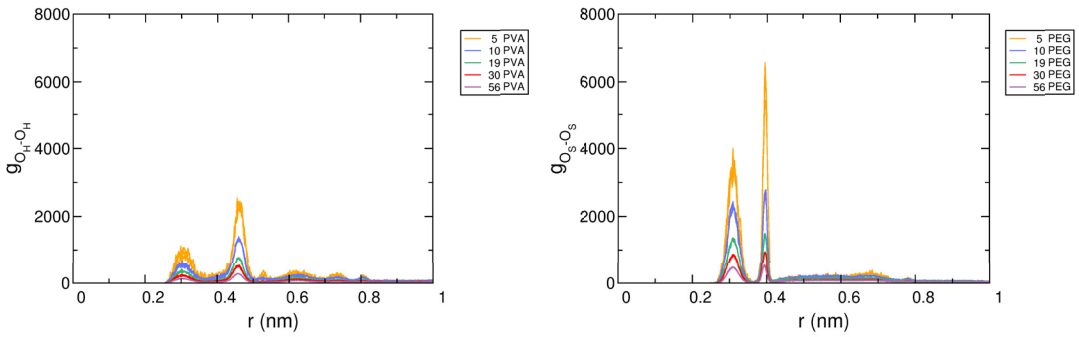

(a) (b)

Figure 4.21: RDF between oxygen atoms in oligomers at 298 K.

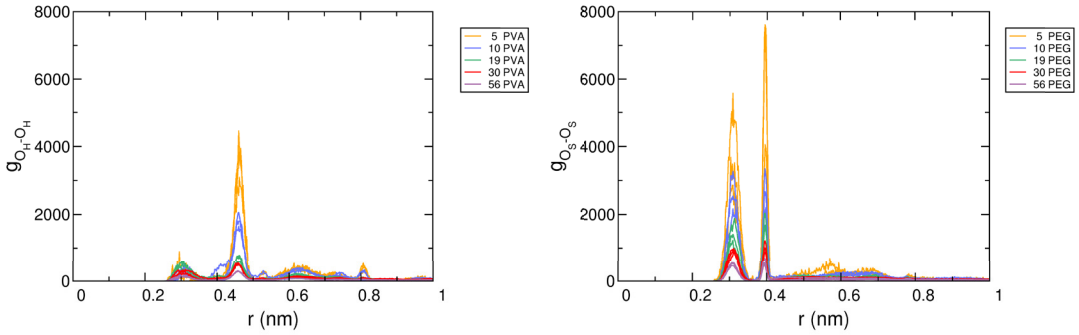

(a) (b)

Figure 4.22: RDF between oxygen atoms in oligomers at 260 K.

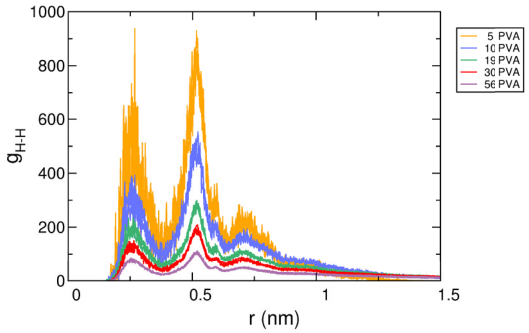

Figure 4.23: RDF between hydroxyl hydrogen atoms in PVA oligomers at 298 K.

4.3.4 Solvent accessibility

One other hypothesis that we tested in the solution studies is the importance of hydrophobicity and solvent accessible areas (SASA). Fig. 4.24 shows the total SASA of the polymers alongside their corresponding distributions. We find that PVA and PEG have approximately the same total SASA (TSASA) at each chain length and it increases linearly with size. Fig. 4.25 shows what proportion of TSASA that is hydrophobic and it shows that PVA oligomers are generally less hydrophobic than PEG. For PVA, as the chain length increases we observe a decrease in percentage hydrophobic SASA, and a corresponding increase in the exposure of hydrophilic groups. As the hydrophobic SASA (ASASA) decreases for PVA it plateaus reaching a threshold at approximately 40% (and 60% for hydrophilic SASA) once the chain length is 19 units long or more. The reverse trend is observed for PEG, which also approaches a limit of 90% for hydrophobic residues and 10% for hydrophilic SASA (PSASA) at 19 units long. These opposing differences in surface exposure may be important to the IRI activities of PVA and the lack of it in PEG, particularly as the 19-mer has been shown to be the point at which the IRI activity is switched on. Further still, the overlap of values for hydrophobicity corresponds with the chain lengths of PVA at which IRI activity has been switched on. At these chain lengths the percentage IRI activities reported by Congdon *et al* [7] also overlap. They report that 1mg ml^{-1} solution of PVA_{10} yields an IRI activity of ∼80%, while the remaining polymers (PVA_{19-351}) all overlap at ∼20% using the same concentration.

At 260 K the average TSASA of PEG oligomers increases in solution compared to values obtained at room temperature, and the percentage of TSASA that is hydrophobic increased by only 0.21–0.30% (Fig. 4.24). This increase is not reflected

in the log-log R_g of PEG and so hints at a small change in shape rather than size (Fig. 4.5). In stark contrast the predominantly hydrophilic PVA oligomers contract in colder environments and the small proportion of ASASA shrunk as well (by 0.3–0.75%). These changes are also corroborated by a general decrease in the log-log R_g. These observations support the ideas that the hydrophobic faces or regions of amphiphilic macromolecules become preferentially exposed to cold environments, which consist of moderate levels of tetrahedrally ordered water. Recent modelling studies on the sfAFP, which is also an amphiphilic protein, has confirmed that it has a hydrophobic ice binding face. The authors, Todde *et al* [166], reported a small, but similar size contraction in the TSASA as the temperature is decreased or is placed in the presence of an ice crystal. A 21 K drop in temperature from 298 K to 277 K produced an 4.08% decrease in TSASA, and although the ASASA declined (from 23.4 to 22.9 nm^2) as a result, the proportion of ASASA increased from 52.9% (at 298 K) to 53.8% (at 277 K) and 55.7% (in the presence of ice). All the while, at the expense of the PSASA. These three examples and other similar studies[306] combined suggests that the variations in hydrophobicity at 298 K may facilitate the contraction or expansion of the TSASA in cold water.

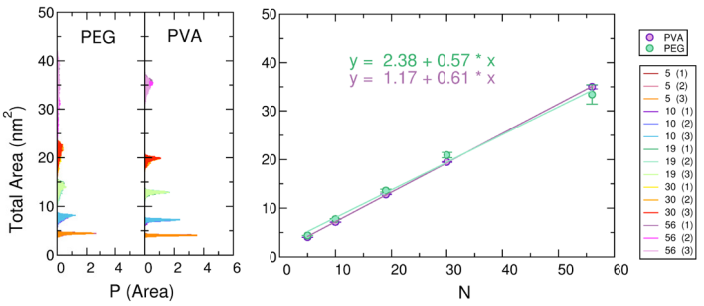

(a)

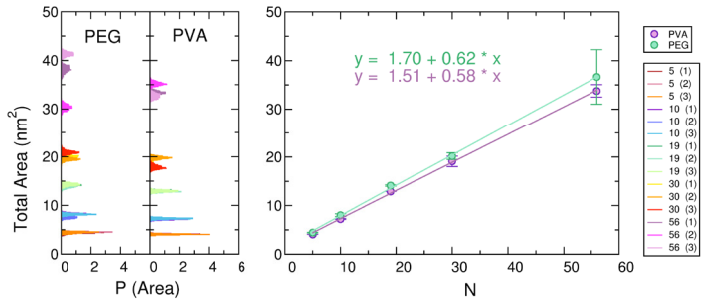

(b)

Figure 4.24: Distribution of the TSASA and plots of the average TSASA for each oligomer (a) at 298 K and (b) at 260 K. Error bars are stdevs between repeats.

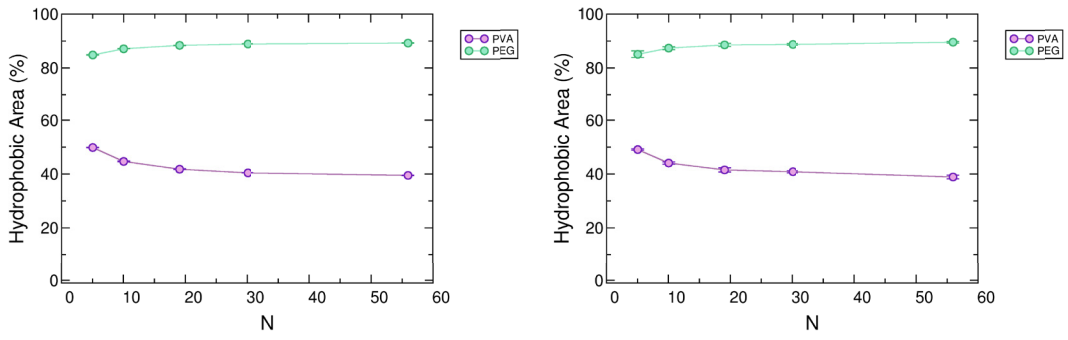

Figure 4.25: Proportion of the ASASA in TSASA (in %) for each given oligomer at (a) 298 K and (b) 260 K. Error bars are stdevs between repeats.

Fig. 4.26 shows a snapshot of the polymers in solution at the end of the simulations in warm water. Aside from the smaller oligomers (PVA_{5-10} and PEG_5), none of the faces are particularly linear because they begin to kink and fold as the polymers increase in size. In both polymers, these bends occur at the oxygen atoms for PEG or at carbon atoms carrying the hydroxyl groups for PVA. It is clear that PVA oligomers have hydroxyl groups that protrude out of the backbone to create an array of hydrophilic SASA. The PVA oligomers also appear to twist or kink in order to expose sections of 3–4 clustered hydrophilic groups and as a result produce some small regions that are flat. As the PVA chain length increases to N= 56, these clusters increase and the hydrophobic groups begin to collapse at the centre with hydroxyl groups visibly decorating the outer region. These regions could be the sites that interact with the ice and so would form ice binding regions of PVA. PEG cannot behave in this fashion as the oxygen atoms are inserted into the polymer backbone.

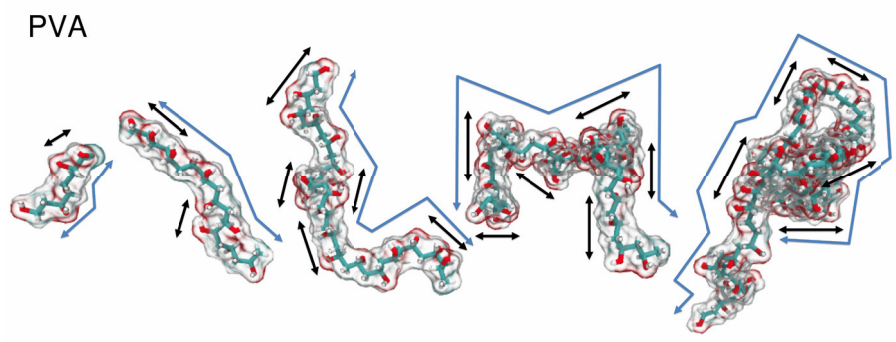

(a)

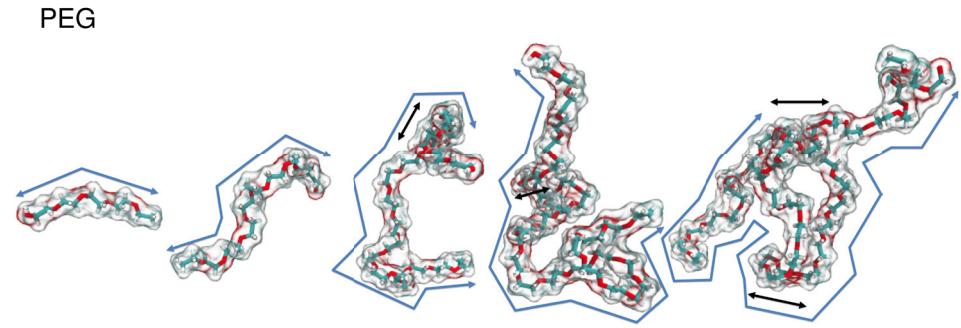

(b)

Figure 4.26: Snapshots of the polymers inside a box of 33,207 water molecules, at the end of a 70 ns simulation and at 298 K. From left to right: N= 5, 10, 19, 30, 56. The SASA are shown by surf representation and displayed as a translucent material. Red highlights hydrophilic groups while the rest is hydrophobic. The chemical structures of the polymers are shown in detail at the center using dynamic bonds representations. Red represents oxygen, blue is carbon and white is hydrogen. Black arrows highlight clusters of polymeric oxygens and blue arrows highlight the contours of the oligomers.

4.3.5 Hydrogen bonding

To further assess the influence of the polymer on the surrounding water, we calculated the average number of H-bonds of solvent water molecules. Fig. 4.27 shows the average number of H-bonds per water molecule (N_H) over the whole system, and for water molecules that reside within the first solvation shell of the polymers. The waters within this shell were found at a distance of 0–0.35 nm from the polymer and were determined from the minima in the RDFs between water oxygens and the

polymeric oxygens.

The bulk water in PVA and PEG systems both produce values between 3.76–3.75, neither of which are substantially different to 3.75 obtained in the pure water systems using the TIP4P/Ice water model. This means that on average, bulk water still H-bonds with itself as it would normally. The same holds true for both warm and cold temperatures; at 260 K, the average number of solvent H-bonds increases to 3.88–3.89 for pure water systems and polymeric systems.

Irrespective of the polymer type or size, water molecules that are close to the polymer participate in fewer solvent-solvent N_H compared to the bulk water. Waters within 0.35 nm of PVA interact more with the hydrophilic surface of the polymer and so have smaller N_H value than PEG. Although PEG can only participate in H-bonding with the solvent, PVA is better able to H-bond with itself as well as the water molecules. Due to these competing interactions, it is not surprising that the H-bonding analysis revealed that the HBN of water is affected more by the PVA polymer.

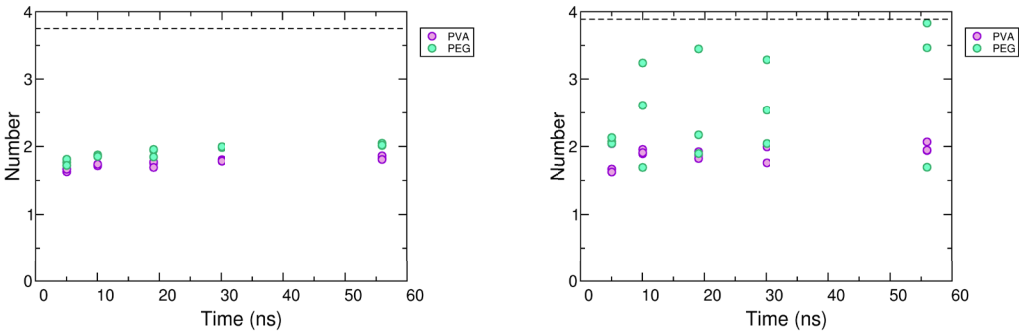

(a) (b)

Figure 4.27: The number of solvent-solvent hydrogen bonds for water molecules that reside within 0.35 nm of the polymers at (a) 298 K and (b) 260 K. All three repeats are shown for each chain length. The dotted lines represent the N_H value for the bulk water at each temperature.

As mentioned earlier in the thesis, the inhibition of ice growth by antifreeze macromolecules was shown to involve some H-bonds and it was first believed that the antifreeze mechanism was dominated by H-bonding interactions[4,143,146] (see §1.3.1). As shown in Fig. 4.25, the hydrophilicity is higher in PVA oligomers which means that there are more hydrophilic groups available for H-bonding than in PEG,

however these hydroxyl groups may also have propensity to form polymer-polymer H-bonds. Thus, we also examine the intramolecular H-bonds formed by the polymer, and the number formed between the polymers and water. The results are shown in Fig. 4.28 and Fig. 4.29 respectively. PVA has two atoms capable of hydrogen bonding; one donor (O) and the other is an acceptor (H). While PVA forms intramolecular H-bonds, PEG cannot do this because it does not have a H-bond donor. Any H-bonds that PEG makes in these simulations are due to the terminal -OH groups, which are absent in experiments.

In the PVA systems, the number of polymer-solvent H-bonds range from 21.60–224.71 and for every increment in N that is added, an additional number of 3.98 H-bonds are formed, which is greater than for PEG (1.44). At 260 K these values only increase slightly to 4.04 and 1.50 respectively. As a result, one would expect PEG to interact more with water than PVA because it does not H-bond with itself, however we find that this is not the case. PVA has more H-bonds with itself than PEG, which one may need to consider as a contributing factor when we observe the potential interactions with an ice face. Once the ice crystal is introduced there will be a trade-off between PVA interacting with itself and with the ice, and so it is important to be aware that these H-bonds exist as they may affect how this polymer binds or interacts with the the ice/water interface. The H-bonds within PVA may also explain the narrower R_g for PVA because the PVA-PVA H-bonds may stabilise a folded structure and restrict the oligomer to fewer conformations. The reverse is true for PEG because it is not able to have as many H-bonds.

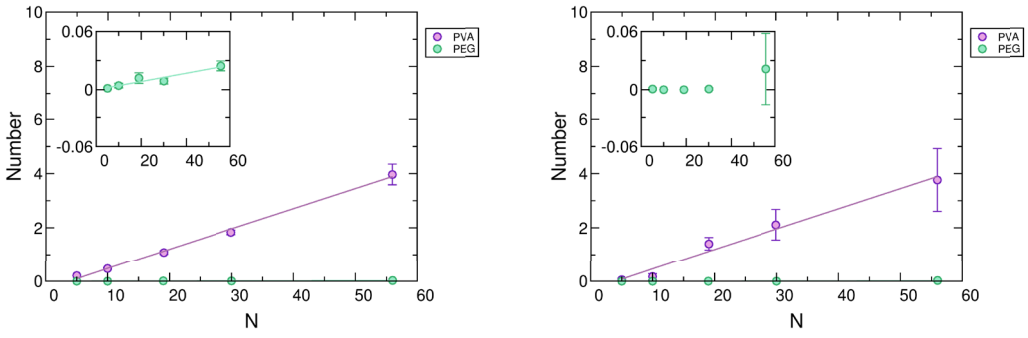

(a) (b)

Figure 4.28: The number of intramolecular H-bonds in PVA and PEG oligomers at (a) 298 K and (b) at 260 K. In colder simulations a non-linear relationship exists between the number of intramolecular H-bonds and the chain length of PEG oligomers. Insets show zoomed plots for PEG. Error bars are stdevs between repeats.

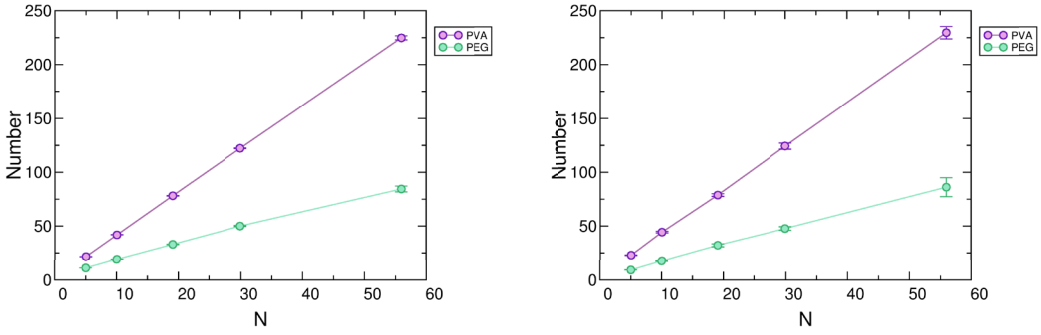

(a) (b)

Figure 4.29: The number of intermolecular H-bonds between PVA or PEG oligomers and TIP4P/Ice water (a) at 298 K and (b) at 260 K. Error bars are stdevs between repeats.

At 298 K the number of polymer-polymer bonds for PVA oligomers ranged from 0.20–3.98 and decreased slightly to 0.05–3.77 at 260 K. At both temperatures, oligomers smaller than than N= 19 have values less than 1, which may be significant for switching on antifreeze activity. Especially as PEG, which is antifreeze inactive, consistently has values below that threshold at both temperatures (0.00–0.02 at

298 K and 260 K). Similar analysis was conducted on the sfAFP at 277 K and 298 K. It was found that the within error, there was negligible difference between the number of sfAFP-sfAFP H-bonds at the two temperatures.[166] However the number of H-bonds range from 40–45, which is substantially greater than the values reported for our oligomers.[166] H-bond analysis of other AFPs also produce much higher levels of protein-protein H-bonds and indicate that the proteins and PVA may rely on H-bonds to different extents, and may therefore have different mechanisms. Notice that in this study we applied a simple geometric criteria for hydrogen bonding by using 0.35 nm and an angle cut-off of 30° deviation from and ideal Donor-Hydrogen-Acceptor angle of 180°. We acknowledge that the H-bonding criteria used may vary from study to study. As a result it means that direct comparisons to AF(G)P studies cannot always be made, particularly as our antifreeze macromolecules are not similar at all in size nor in the number of water molecules used, forcefields used, or the types of water models selected.[116,166,186,307]It was demonstrated in Ch. 3 that the level of H-bonding in a system is very much dependent on the water potential used to model the interactions of the water solvent. To our knowledge TIP4P/Ice has not previously been used in AFP/water studies nor in AFP/water/Ice studies. They have however been used for the investigation of AFPs with the TIP4P/Ice/Methane clathrate studies produced by Bagherzadeh *et al* [308] in 2015.

4.3.6 Polymer flexibility

To determine the structural deviations of atoms within the oligomers, the root mean square fluctuation (RMSF) of each atom was measured for all simulations (Fig. 4.30). The RMSF highlights which sections moved throughout the simulation trajectory and how much. Three repeats of each oligomers are also shown in each plot and help to illustrate the likelihood that certain regions of the polymers will move. The RMSFs of atoms indicates that the termini of PVA and PEG oligomers are generally more flexible than the centre of the polymers. In both PVA and PEG the regions of lowest flexibility are typically half the amount of the maximum values. For example in PVA_{56} the terminal ends exhibit RMSF values of 1.0 nm while the regions of lowest flexibility reach 0.5 nm.

The main difference between the two types of polymers is that PEG oligomers have greater RMSF values on average, however PVA is more rigid. PVA also appears to have segments of approximately 50–100 atoms long, whereas the PEG typically has smaller segments of about 25–100 units. The flexible region in PVA seem to have comparable movement to the flexible regions in PEG as the polymers increase in size. These differences are most clearly seen in comparing PVA_{56} and PEG_{56}.

These regions of pronounced flexibility and inflexibility reveal that the PVA_{56} polymers maintain two hinges or kinks with approx. three dedicated areas that flap about. As the chain length decreases the flexibility of the oligomers also declines. PVA oligomers that are smaller than 19 units long do not have sufficient number of atoms for these flexible and more rigid regions to appear.

The atoms which moved the most in PEG oligomers are hydrogen atoms and all other atoms moved less. Frequent, but small kinks or segments occur at the oxygen atoms that lie in the PEG backbone. Alongside the effects of fewer intramolecular H-bonds, these segmental movements encourages PEG oligomers to create more conformations than PVA, discussed earlier. However for PVA the hydrogen and oxygen atoms moved the most, while carbon atoms moved the least. With regards to the ice lattice matching theory these movements would be ideal because it allows IRI active PVA oligomers to compensate for any small deviations from the ice-lattice spacing so that the atoms could orient accordingly for binding.

Fig. 4.30c–4.30d shows the same RMSF analysis for PVA and PEG oligomers in supercooled water at 260 K. Unsurprisingly we find that the flexibility for all polymers declined dramatically in colder solutions, due to less available thermal energy. If present at all in PVA, small segmented regions of flexibility and inflexibility in extend for shorter periods and do not vary much from the baseline, unlike the studies at 298 K. Some additional features we find at reduced temperatures are that the average baselines for PVA_5 and PVA_{10} is lower than 0.1 nm, while larger PVA oligomers are at least 0.13 nm for PVA_{19-56}). These larger values are comparable to results reported for AFPs. For example, RMSF analysis of the 6.5 kDa snowflea AFP (sfAFP) was recently conducted by Todde *et al* [166] at 298 K and 277 K in a box of 1000 TIP4P waters, and trajectory of 100 ns. They found that aside from the C-terminals, which had the highest RMSF values, the sfAFP backbone had two distinct regions of high flexibility (approx. 0.25 nm and 0.5 nm) at room temperature and an average baseline value of 0.1 nm.[166] These values are consistent with reports in literature[307] and they also report a similar trend in flexibility as a function of temperature. It is noteworthy that sfAFP is an insect AFP and therefore has a high TH, which is absent in PVA however what both molecules have in common is they are both IRI potent[309]. It is also important to note that PEG does not display either of these properties.

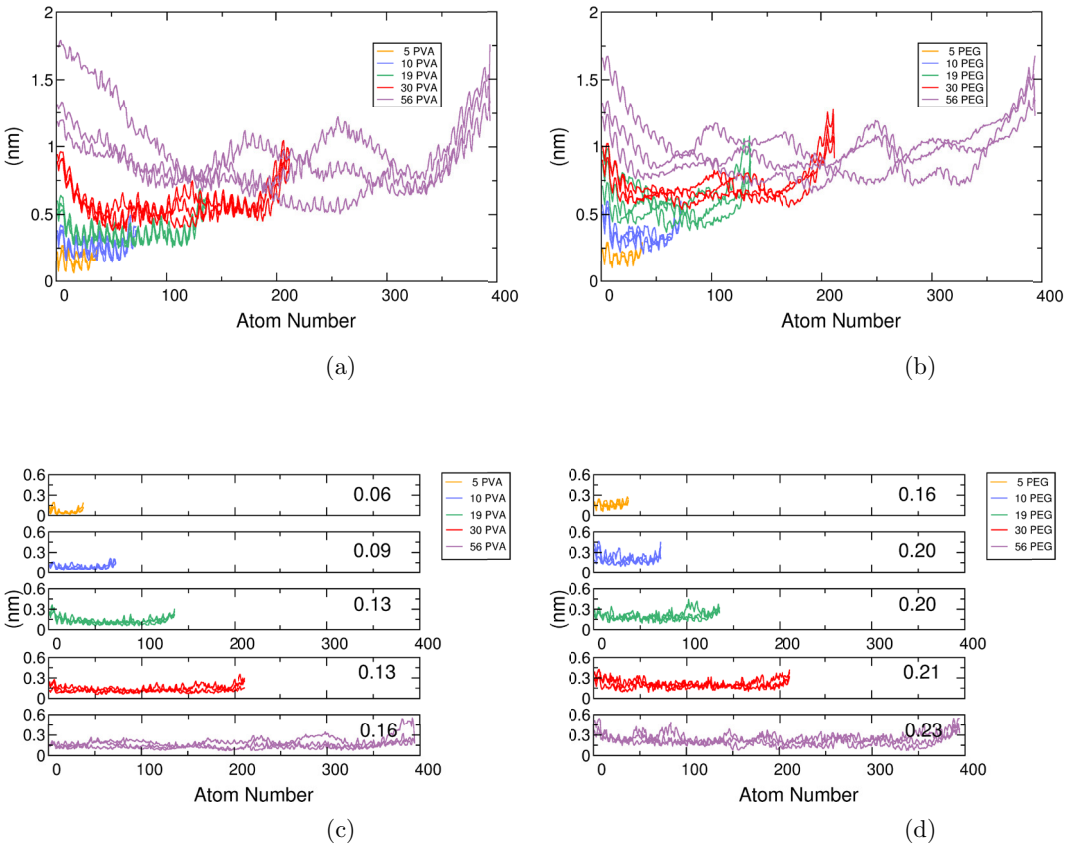

Figure 4.30: The relative fluctuation of each atom on the oligomer with respect to starting positions at 298 K (top panel) and 260 K (bottom pannel). PVA oligomers preserve long stretches of important regions of low and high fluctuations at 298 K which is lost at 260 K. PEG is more flexible than PVA and also becomes rigid with a decline in temperature. Nb. The two temperature plots are plotted differently for clarity because the data for 260 K overlap and likewise at 298 K.

4.4 Discussion

Thus far the results from our solution studies, especially the O-O RDF separation distances support some form of complimentary ice matching mechanism in PVA. The oxygen-oxygen RDFs distances suggest that PVA can indeed lattice match and could potentially become incorporated into the ice lattice effortlessly because PVA already adopts the appropriate conformations in solution at room temperature. It

will be interesting to see if these distances, or any other RDF distributions change during the ice/polymer simulations.

After exploring the concept of specificity and ice lattice matching in solution we find that the Q_4 results suggests that PEG and PVA polymers have no significant effect on the tetrahedral ordering of surrounding water molecules at 298 K. In addition the hydration numbers for PEG are consistently higher than for PVA. Combined, there is no evidence for substantial ordering (or disordering) of surrounding water molecules into coherent tetrahedral arrangements or structures within a 0.35 nm radius from PVA oxygen atoms. Thus the hypothesis that synthetic PVA oligomer disrupt the the ice/water interface via its own clathrate is unsupported by its activity in solution at 298 K. This also remains true for studies conducted at 260 K, where water molecules are supercooled enough to crudely represent an unfrozen ice-like region

It has become clear that the two polymers behave very differently in solution. PEG exhibits greater reliance on its hydrophobic interactions to interact with nearby waters while PVA forms more H-bonds with water. For instance there are also many indications that PVA adopts and maintains a narrow range of more rigid, random coil conformations. Analysis which support these conclusions include the R_g, RDFs (O-O_H, O-H_H, O-C_H), the hydration numbers and RMSF calculations. Hydrogen bond analysis reveals the presence of a small number of H-bonds which may stabilise the internal structure of PVA. In contrast PEG cannot act in this way and so is able to vary a lot in conformation. It is possible that a restricted or restrained structure may be important for lattice matching interaction with ice. The collapse of the PVA oligomer with increasing chain length allows the clustering of neighbouring groups into small segments, which may bind to ice or which may be important for ice binding. The RMSF analysis showed that IRI potent PVA oligomers have regions of greater rigidity than PEG and regions of comparable flexibility to PEG. The ability to form regions of high and low flexibility provides an allowed range of movement that may be important for the IRI mechanism. For instance the polymers' ability to bend or fold may be relevant features for alignment in lattice matching, regulation of the hydration sphere, or it may be crucial for selective exposure of specific faces in order to encourage select interactions as reported by Tam *et al* .[116] Alternatively the mechanical motion of folding or flapping could disrupt the local ice crystal growth for an extended period of time, until adjacent regions are surrounded and the polymer is submerged in the ice lattice. The importance of folds, kinks, pivots and bends is apparent across the literature for AFPs[145,150,154,166,307,309,310] and for the simulations of glycopeptides[116,186]. In

these referenced works, characteristic folding properties have also previously been reported for IRI potent molecules whilst the features are lacking in the IRI inactive molecules.

Although one can say that the PEG has a greater number of waters around it, the PVA is better able to influence its water than PEG due to to its greater hydrogen bonding network and a delicate balance of exposed hydrophilic and hydrophobic regions. For the IRI potent PVA_{19-56}, we determined a 60:40 ratio of hydrophilic:hydrophobic SASA.

The presence of an ice interface ordinarily induces a gradient of ordered water, and so cold water alone is not wholly encompassing and a suitable representation of the *whole* QLL. We hypothesise that the ability of PVA to influence surrounding water molecules may have greater implications for specific regions of the gradient, which have not been illustrated here. It is likely that large PVA oligomers could achieve this by disordering waters in the QLL that lie close to ice because these waters are weakly ordered by the ice/water interface. Waters in the QLL that lie further away from the ice will be even more weakly held in place and so these waters are better represented by the cold water studies. Due to their increased mobility, those waters may not be particularly influenced by the presence of the PVA oligomers.

Granting that the solution studies did not find substantial amounts of disordering or ordering of surrounding water molecules, we cannot rule out the possibility that PVA may significantly disorder waters in specific regions of the QLL. Particularly, as there is evidence to suggest that both types of polymers in warm and and cold temperatures hint at a decline in the $Q_4 = 1$ positions rather than an increase, and lattice matching would prove useful for such a mechanism.

Unlike the AF(G)Ps, our simulation studies of PVA in warm and cold water do not appear to have a single clear and definite hydrophilic or hydrophobic faces to interact with ice or water and this suggests that they function through a very different mechanism. As the temperature drops from 298 K to 260 K, the TSASA of PVA decreases and the polymer becomes more rigid. One possibility is that the PVA may strongly govern an albeit smaller cluster of hydrating waters when the polymer resides in the QLL regions that are closer to the bulk ice.

4.5 Conclusion

We have established that the OPLS-AA forcefield and TIP4P/Ice water model are

suitable for the simulations of PVA and PEG at 298 K and 260 K in solution. Thus far we find several distinguishing features between PVA and PEG which may be important for IRI activity in warm and cold simulation studies. Our hypothesis from these MD simulations are that the PVA polymer interacts directly with the ice interface or with layers of the QLL very close to the ice lattice. They may do so via their hydrogen bonds, as evidenced by their strong lattice matching features and hydrogen bond analysis. PVA appears to confine water close to itself. Narrow and well defined successive shells, and the Q_4 parameter indicate that despite these confined regions, the waters are somewhat reduced in tetrahedral order but no different to PEG. Overall, PVA presents more of a hydrophilic surface whereas PEG presents more of a hydrophobic surface. We suggest that these are more important for IRI activity. When comparing the results of warm simulations to the cold ones we find that there is no real difference except for the rigidity, compactness and hydrophobicity of the polymers. These vary between the two polymers and there is evidence to suggest that the balance of properties like rigid/flexible regions, and of hydrophobic/hydrophilic groups is important for switching on IRI activity at 19 units long. At 19 units long, when the antifreeze activity is switched on[7], we find that 40% of PVA's solvent accessible surface area is hydrophobic and this may represent a cut-off for the design of other polymers. Without a library of IRI active, synthetic polymers, it is difficult to say with certainty if the percentage hydrophobicity is important for IRI activity, or if the values themselves are most relevant. Largely because PVA and PEG have similar TSASA values, while other polymers may vary enough in TSASA to confirm if the reported trend exists. Early simulation studies of AF(G)P in solution found that the MD study revealed hinges or twists in the helical structure of the polymer using different water models.[145,150,154] The same was found for later and recently improved modelling studies on analogues.[166,307,309] We too find that the IRI active PVA can produce hinge like regions that may be useful for aligning with different faces of ice. The hydroxyl groups on PVA are positioned so that they are able to reorient to interact with the ice. Whereas in PEG the oxygen atoms are restricted to positions in the polymer backbone. Using trajectory snapshots, we have revealed that regions of the PVA and PEG oligomers seem relatively flat, however only PVA has lattice matching groups that stick out more to interact with ice. Although the PVA oligomers twist to form arrays of hydroxyl groups, and in spite of their isotactic structure these arrays are not restricted to largely one side of the polymer. Unlike AF(G)Ps, the known IRI active PVA oligomers do not appear to be divided into a largely hydrophilic and hydrophobic face, it is apparent that the two types of macromolecules may function in a different manner.

Chapter 5

The effect of poly(vinyl alcohol) and poly(ethylene glycol) polymers on ice crystal growth rates

5.1 Introduction

Earlier in this thesis, we studied PVA and PEG polymers in solution and found some properties of interest that are chain length dependent, in a similar fashion to IRI potency. These properties are the RMSF and the hydrophobicity of the polymers. In this chapter, we aim is to use MD simulations to identify the effects of polymer chains on the $11\bar{2}0$ plane of ice during the freezing and melting process, because this is the fastest plane to grow. To effectively model this system we previously studied the ice growth in the absence of any additives and investigated the effects of 2 different cut-offs, and mixing the TIP4P/Ice water model with the OPLS-AA FF (§ 3). Here, we build on this work and continue to use the direct coexistence methods, which places an ice lattice in contact with water in order to produce two ice/water interfaces with an immersed oligomer.

Our previous ice growth simulations have demonstrated that the direct coexistence method is reliable and can be used to successfully reproduce the melting point of water. For this reason it is also custom in the literature to use direct coexistence methods, and in doing so will make our results comparable to recent studies, which probe the effects of AFPs on growth of ice crystals[148,156,158–160,166–168]. This is especially important because, to the best of our knowledge, this work presents the

first MD simulation of such systems for large, synthetic polymers.

In order to probe the effects of each polymer on the ice growth, we monitored changes to the melting point, ice growth/melting rates and water structure. We chose to study ice growth instead of nucleation for several reasons. As mentioned earlier, PVA has been shown to inhibit the ice nucleation as well as growth[117] even in the presence of nucleators like bacterial proteins[118] and silver iodide[30]. Interestingly studies of the ice nucleator, silver iodide, revealed that inhibition of nucleation was also possible by other known antifreeze active macromolecules such as AFP (TH active) and poly(vinyl pyrolidone) (PVP) (TH inactive). Surprisingly, inhibition was also achieved using antifreeze inactive polymers, poly(ethylene glycol) (PEG)[30]. So in order to investigate the mechanism for IRI activity, our MD simulations were designed to reflect our interest in ice crystal growth and its inhibition because PEG does not show any appreciable IRI activity.

These results are in line with observations by Gibson *et al* [3], that IRI activity is a consequence of slowed growth rather than nucleation. Congdon *et al* also showed that IRI activity of PVA switches on between N= 10 and 19[7]. To keep our studies in line with experimental observations, isotactic PVA_{10}, PVA_{19}, $PVA_{10\times2}$ and PEG_{10} oligomers were chosen for our studies in order to better understand the difference between IRI activity and inactivity, as well as scales of IRI potency that are introduced by greater chain lengths and concentrations.

An additional advantage of studying ice growth rather than ice nucleation, is that the latter is spontaneous process which requires the formation of a critical cluster or nuclei. This process is computationally demanding to observe because of the energetic cost of forming a new interface, and so it may not be possible to observe nucleation under the simulation time scales accessible to us for atomistic studies.

Some key hypothesis for the molecular mechanism of antifreeze activities of AF(G)Ps and their analogues were discussed earlier in § 1.3 and § 4. These were that the polymer could bind directly onto the ice, or induce some ice-like ordering of vicinal water molecules that it could complex with and uses these to latch onto a growing ice front. In the latter scenario, the ordered water molecules essentially act as a bridge between the polymer and ice crystal. Another hypothesis is that the polymers form a disordered region around itself by disrupting local interactions or dynamics of water molecules, and ultimately prevents the ice lattice from advancing any further. The challenge comes in deciphering which, if any, of these mechanisms are applicable and what types of interactions are responsible for these behaviours.

Based on the results from polymers in solution (see § 4), we found that the H-bonding, flexibility and lattice matching properties were characteristic features

that differentiated the antifreeze active PVA and antifreeze inactive PEG isomers. From those simulations, some key expectations for these particular studies are that we expect to see direct binding of the PVA onto the ice lattice or interacting more closely with well-ordered QLL regions nearer the ice surface. In addition to this, we expect that the steric interference from the two polymers would induce a disordering effect in ice, relative to the pure ice systems. This steric effect would be greater for PVA, which has a greater flexibility than PEG in solution and a longer range influence over its vicinal water molecules.

5.2 Methods

5.2.1 Forcefield parameters

The TIP4P/Ice water model was used alongside the the OPLS-AA forcefield as with § 3. The same forcefields were used for the polymers are reported in § 4.

5.2.2 Simulation parameters

Simulations were preformed using the Gromacs (v4.5.4) package. Once the equilibration was complete (see below), restraints on the ice were removed and the production runs were conducted at a range of 10 different temperatures (300 K, 290 K, 280 K, 275 K, 273 K, 272 K, 270 K, 268 K, 260 K and 250 K). A timestep of 1 fs was used and anisotropic pressure coupling was applied in order to permit independent fluctuations of the box in all directions during phase change. The compressibilities of the x- and y-planes were set to those of real ice ($1.0\times10^{-5}\,\mathrm{bar}^{-1}$), while the z-direction was set to the higher compressibility of real water ($4.5\times10^{-5}\,\mathrm{bar}^{-1}$). The Parinello-Rahman barostat[210] was used to maintain the pressure at 1 bar and the Nosé-Hoover thermostat[209,234] was used to control the temperature. All box angles were kept orthogonal and 1.00 nm cut-offs were applied to the short range Lennard Jones potentials and coulombic interactions. Long range electrostatics were controlled using the PME protocol[197,198] using a 0.16 nm grid and a cubic interpolation. LINCS constraints[212] were applied to all H-bonds and PBCs were used to mimic bulk conditions.

Pure water simulations were repeated ten times for each temperature, and nine repeats were made for the simulations conducted in the presence of a polymer. The progress of each simulations was monitored by plotting the convergence of the total energy against the trajectory time. A negative slope in the total energy is indicative of freezing and a positive slope depicts melting of the system.

5.2.3 Initial configuration and equilibration

A simulation box of hexagonal ice (768 water molecules), which was equilibrated in § 3, was multiplied by two in each direction to create a box of 6,144 water molecules which would represent the ice phase. The dimensions of the ice crystal were 5.8×6.2×5.5 nm. The box dimensions were 5.8×6.2×16.5 nm and the ice lattice was placed in the centre of the box. If included, the starting configurations of the polymers used were obtained from the final 70 ns trajectory from the solution studies (§ 3). The polymer was placed at $\sim$ 0.2 nm away from the secondary prism plane (the $11\bar{2}0$ face)[219] which is a plane of interest and is also reputed as the fastest growing plane. Next, the system was solvated in order to create an ice/water interface on either side, and interstitial waters were removed from the ice lattice. A total of 12,363 waters represented the fluid phase and a schematic of the simulation set up is shown in Fig. 5.1.

The same protocol as in § 3 was used to simulate the melting and freezing of these larger systems. The new system contained 18,507 molecules and an NVT and an NPT run were conducted in sequence. The conditions were maintained at 300 K and 1 bar with 10,000 KJ mol^{-1} restraints placed on the ice. This allowed the water to equilibrate around the ice, as well as the polymer if included. Finally an NPT run was continued as the temperature is dropped to 283.15 K and the whole system is allowed to equilibrate in cooled conditions. Equilibration was monitored using two properties; the total energy and the z-directional movement of the polymer's centre of mass. Once both of these features become stable then the production runs were started.

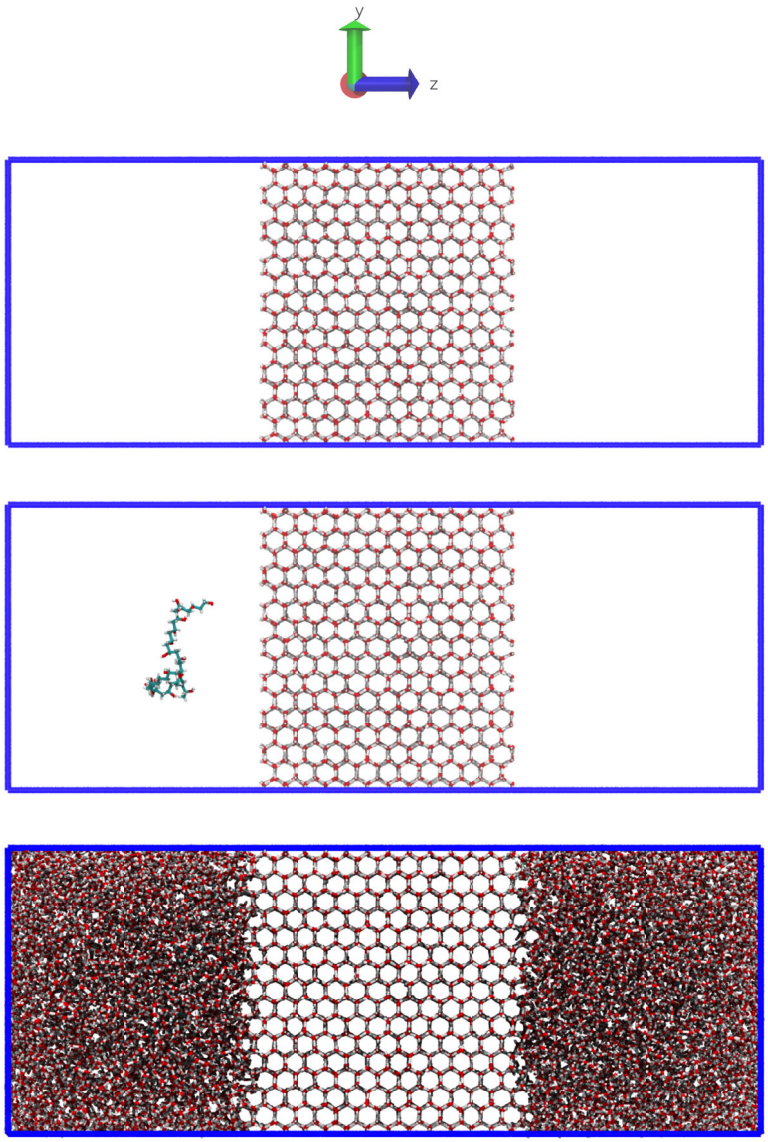

Figure 5.1: Schematic of the simulation system and the geometry of the ice and water positions in the yz- plane. In the top panel an ice crystal is placed in the simulation box. In the middle pannel the polymer is introduced at fixed distance from the ice crystal in the simulation box. In the bottom panel water is introduced to sandwich either side of the ice crystal and solvates the polymer. The growth or melting of the I_h $11\bar{2}0$ face occurs in the z-direction.

5.3 Results

5.3.1 Total energy profiles

Figs. 5.2–5.6 illustrate the evolution of the total energy over the duration of our simulation at 10 different temperatures, in the presence and absence of any polymers. As normal, the positive gradient represents melting while a negative slope represents freezing of the system. In the absence and presence of any additives we determined a melting point of 270 K because the system remained stable, and neither melting nor freezing was completely achieved during the 300 ns trajectory. This is only 1° greater than for the smaller systems in chapter 3 and close to the experimental value of 272.2 K. The T_m that we have obtained in this study is in excellent agreement with values reported for the TIP4P/Ice water model.[19,204,217,219,220]

The time taken for the system to completely freeze or melt was recorded for each system and the results are summarised in Fig. 5.7. As the temperatures declines, the time taken for the completion of the freezing or melting process increases and it becomes progressively computationally demanding to study these processes. The reduced thermal energy provides less kinetic energy for the water molecules to diffuse about, which is necessary to break away from the ice lattice or to reorient themselves accordingly in order to build the growing ice lattice. It is important to consider that the freezing simulations can take longer than 300 ns and so it is possible to miss important features that occur as a result of crucial interactions between the ice and the antifreeze molecules during the remaining 290 ns trajectory. Take for instance a two-stage adsorption process, which may be earmarked by an intermediate plateau instead of just the single and final one, which ordinarily represents the completion of the freezing or melting process.

In the presented total energy profiles, the IRI active and inactive polymers both occasionally exhibit intermediate states at 268 K that are non-existent in the pure water studies (Figs. 5.2–5.6). From here on these are referred to as metastable states because ice crystal growth has been paused. These states last longer for the antifreeze active polymers with the lengthiest metastable periods of 52 ns, 125 ns, 114 ns and 182 ns for PEG_{10}, PVA_{10}, PVA_{19} and $PVA_{10\times2}$ respectively. If these metastable features only occurred in one repeat then they are highlighted in dark blue, however if similar features (metastable/lack of metastability) have been identified elsewhere then they are highlighted in black. Notice that these plateaus which earmark the metastability not only last longer in IRI active polymers, but occur in other repeats of PVA_{19} and $PVA_{10\times2}$. In some trajectories they even occur multiple times for brief periods. Combined, these features indicate that larger and more PVA

polymers may stabilise the growing ice lattice. It also appears that the inhibition of ice could occur in stages or in a fashion similar to the successive coordination associated with multidentate ligands, which would be understandable for a lattice matching process.

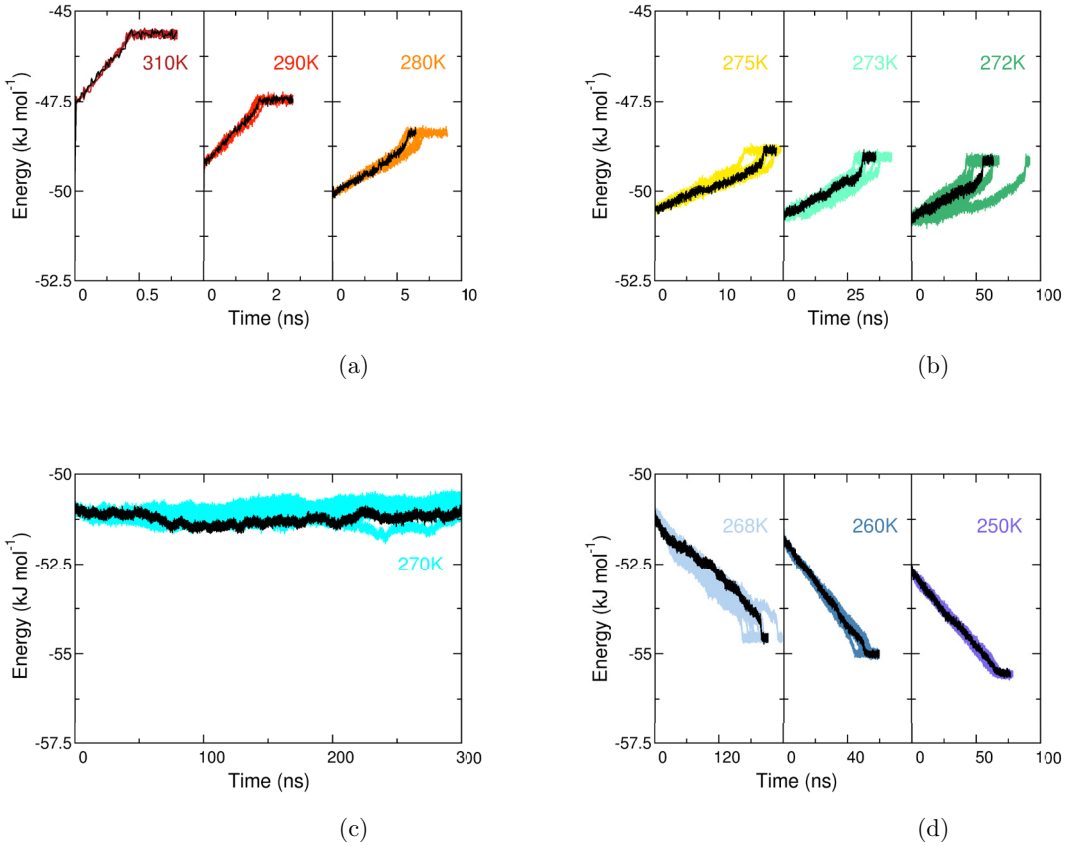

Figure 5.2: The evolution of the total energy per water molecule as a function of temperature. Complete melting is observed above 270 K (red, yellow, orange and green) and complete freezing occurs at temperatures below 270 K (blue). The T_m of TIP4P/Ice is identified as 270 K (cyan). Results for all ten repeats are included in each graph and a single representative is highlighted in black for clarity.

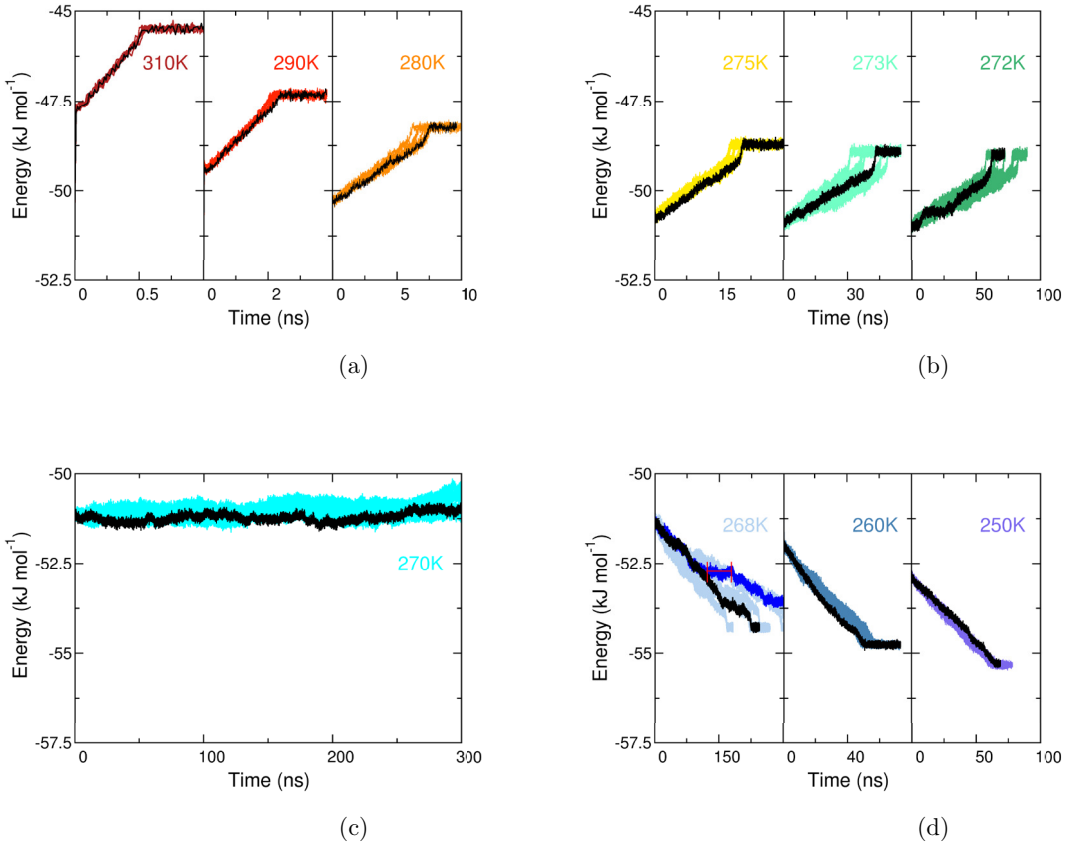

Figure 5.3: The evolution of the total energy per water molecule as a function of temperature for PEG_{10}. Same colour key as in Fig. 5.2.

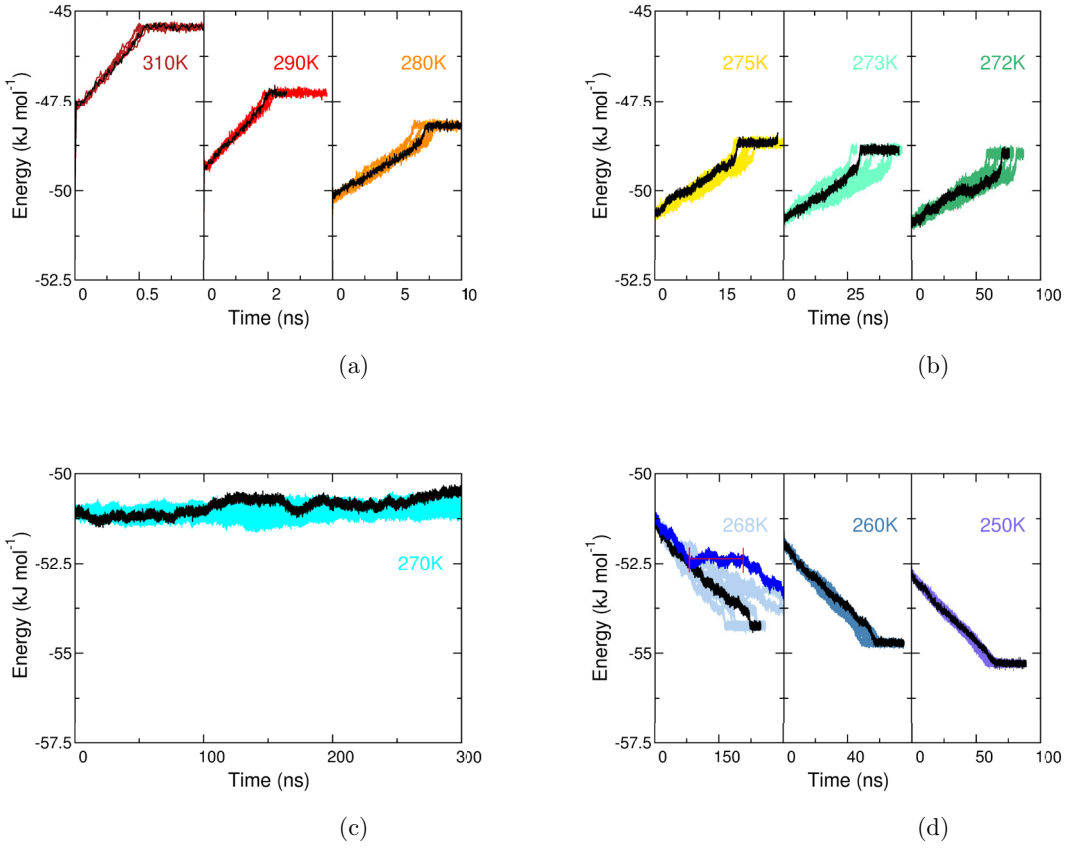

Figure 5.4: The evolution of the total energy per water molecule as a function of temperature for PVA_{10}. Same colour key as in Fig. 5.2.

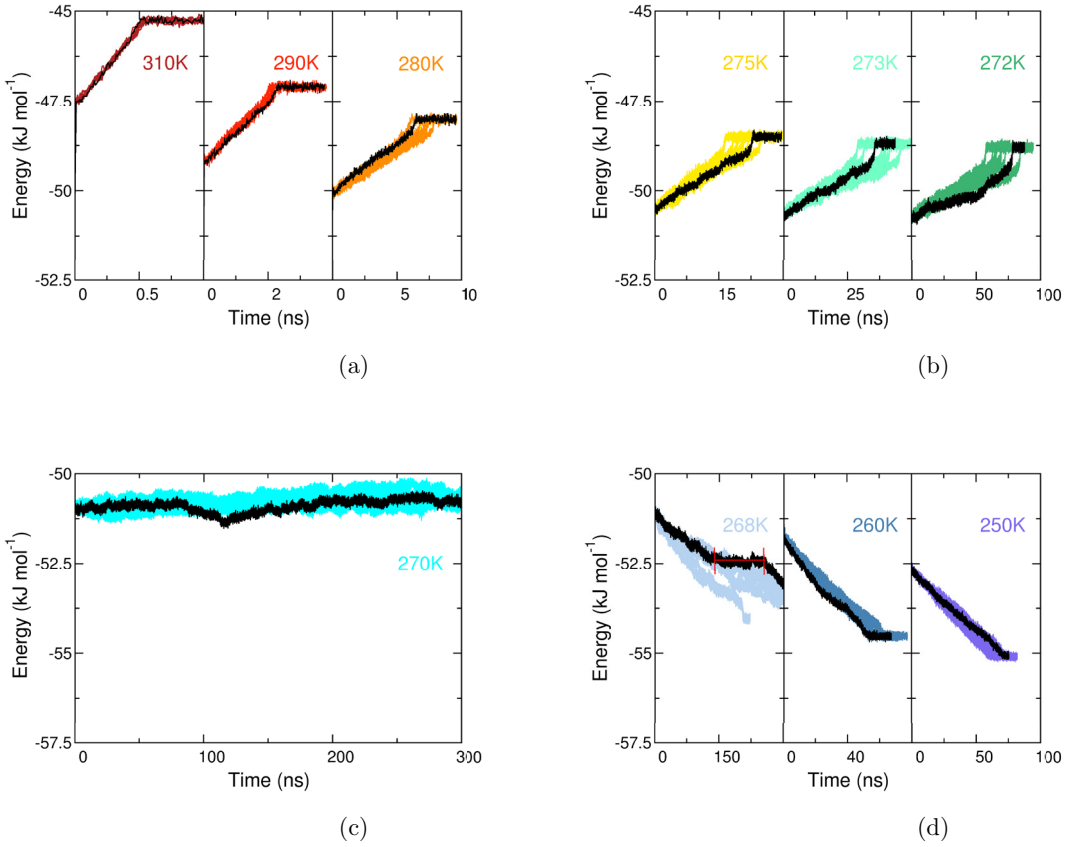

Figure 5.5: The evolution of the total energy per water molecule as a function of temperature for PVA_{19}. Same colour key as in Fig. 5.2.

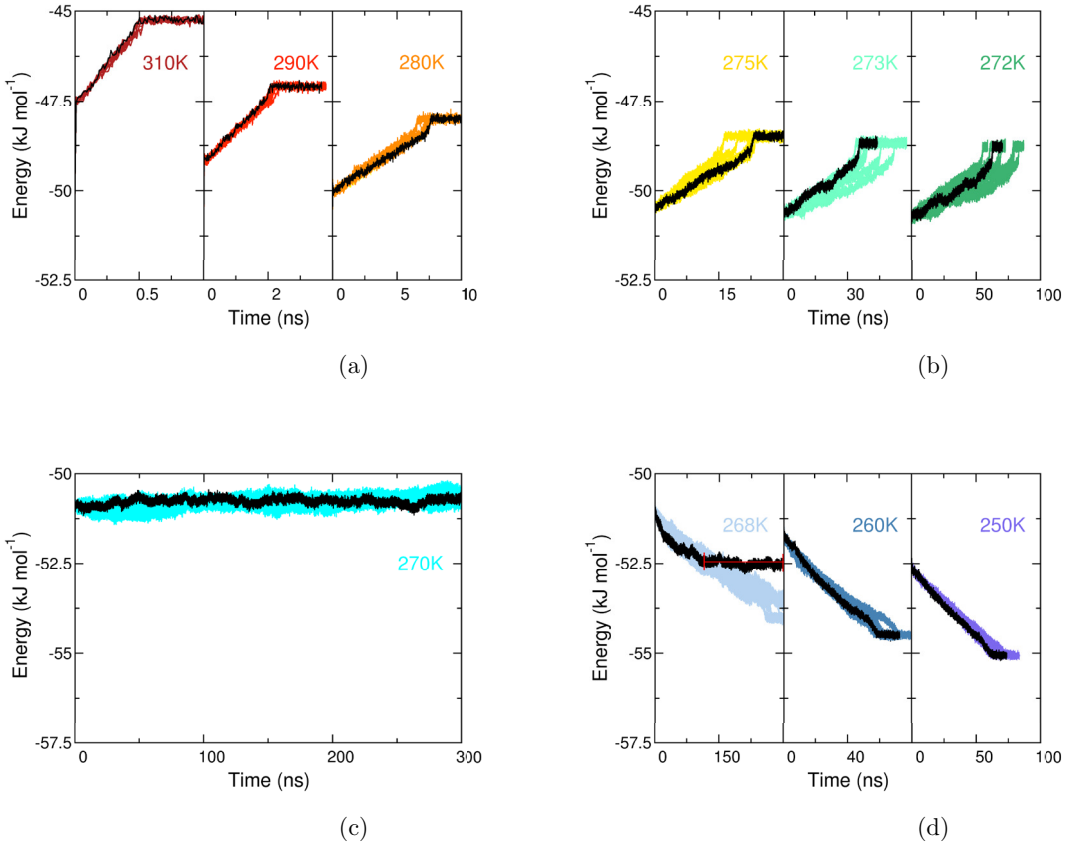

Figure 5.6: The evolution of the total energy per water molecule as a function of temperature for $PVA_{10\times2}$. Same colour key as in Fig. 5.2.

5.3.2 Growth/melt kinetics

The time taken for the system to completely freeze or melt was recorded in the presence of each polymer and the results are shown in Fig. 5.7 and Table 5.1. As with the pure water systems the time taken for the freezing, and for melting at temperatures closest to the T_m took the longest time. In the presence of polymers, the systems which experienced the greatest delay relative to pure water systems were conducted at 275–260 K, whereas at higher temperatures (310–280 K) the delays were much smaller and there was generally no real difference between any of the types of polymers.

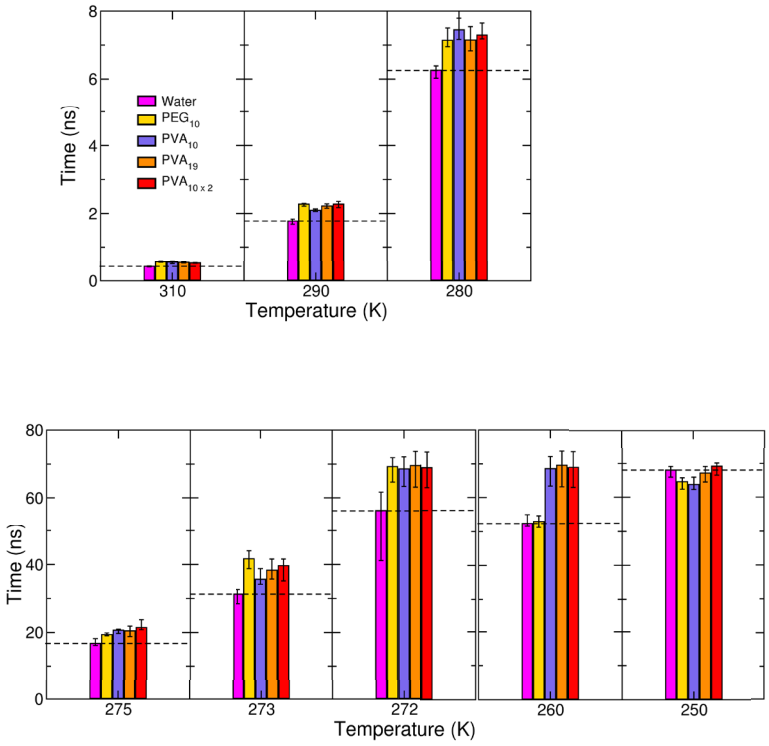

Figure 5.7: The timescales reached in MD simulations for freezing and melting processes in the absence and presence of PVA or PEG oligomers. Error bars represented stdevs. between repeats.

A clear difference between the IRI active and inactive polymers appears at three temperatures in particular; 250 K, 260 K and 268 K. Firstly, at 260 K there is

no significant difference between the time taken for the pure water samples to freeze on their own, and in the presence of PEG_{10}. Both systems take ∼52–53 ns whereas the addition of PVA_{10}, PVA_{19} and $PVA_{10\times2}$ delay the simulation by roughly same amount to ∼69–70 ns.

As the temperature is dropped even further to 250 K the weakly IRI active and non-active oligomers — PVA_{10} and PEG_{10} respectively — freeze prematurely. For PVA_{10}, these results are reminiscent of explosive growth rates that have previously been reported for AF(G)Ps outside of their TH range or range of antifreeze activity. Recall that PVA only has a TH of 0.024–0.037 K [3,52,111,112], while PEG is TH inactive and so we do not expect to capture any freezing depression in any of these simulation studies, just their IRI properties. Interestingly, the more potent IRI inhibitors (PVA_{19} and $PVA_{10\times2}$) take the same amount of time as for pure water systems to completely freeze, or slightly more. At the same temperature, Vrbka and Jungwirth [123] found that a 0.15 M brine solution yielded a 20% delay in freezing time to 300 ns, when compared to pure water that ordinarily froze after 250 ns. Similarly, Kuiper *et al* [168] reported that a single TH active (TH= 6 K) [85] swbAFP at 255 K delayed the freezing time by 67% from 150 ns in pure TIP4P water to 250 ns. The results from these modelling studies suggest that the polymers function in a manner different to both salts and swbAFP.

At 268 K we found that the pure water system typically achieved complete freezing for all 10 simulations under an average of 185.82 ns (±27.8 ns stdev). The presence of polymers did not change the melting point of 270 K, however fewer simulations at 268 K were completed within 300 ns in the presence of both PVA and PEG. These finding are tabulated in Table 5.1.

Seven of nine simulations were completed with PEG_{10}, and even fewer were

	Water	**PEG_{10}**	**PVA_{10}**	**PVA_{19}**	**$PVA_{10\times2}$**
Completed [a]	10/10	7/9	6/9	2/9	4/9
Average, ns [b]	185.82	213.95	204.96	206.90	274.45
Stdev, ns [c]	(27.28)	(32.45)	(30.30)	(1.11)	(11.81)

Table 5.1: [a]The number of simulations which completely froze within 300 ns are recorded. [b]The average time taken for complete freezing at 268 K from the simulations which did completely freeze. [c]Stdevs. between average times taken from completed simulations.

completed in the presence of PVA (between two–six) in correlation with increasing IRI activity. This suggests that PVA oligomers are capable of considerably delaying the time taken for freezing simulations only, provided that the temperature is close

to the melting temperature, however the freezing point remains unchanged because there is still a visible downward slope in the total energy profiles, that is typically captured within the timescale of the whole simulation. These findings are somewhat reflected in the time taken for the repeats which completely froze at 268 K; where remarkable slowed growth was observed in the presence of all polymers, and in particular the $PVA_{10\times2}$ samples. Between the polymers the additional times required ranged from 19.14–88.63 ns at just 2 K below the melting temperature (T_m-2 K), whereas milder changes were observed at other temperatures. Take for instance at 272 K, (T_m+2K) where no discernible difference in the time taken for melting was observed between PVA and PEG, nor between chain lengths or concentrations. Overall the number of completed simulations suggest that neither PVA nor PEG exhibit any significant TH, which is in agreement with experiments.[111]

Another feature which is consistent with literature is that the fluctuations around the average energy drift is greatest at temperatures closest to the T_m (275–268 K).[38] This is also reflected in the standard deviations of times taken between repeats in Fig. 5.7 and these arise due to the heightened competing effects between the addition and removal of water molecules from the ice/water interface within this temperature range.

During the ice growth simulations, the ice/water interfaces grow in the z-direction to fill out the regions that sandwich the ice crystal. The overall distance travelled is 11 nm in the this direction, whilst melting of the ice crystal only requires half the distance. The ice growth rates translates to distance travelled divided by the time taken. Thus pure water simulations at 268 K, 260 K and 250 K yield growth rates of 0.06 ± 0.011 nm ns^{-1}, 0.21 ± 0.011 nm ns^{-1} and 0.16 ± 0.003 nm ns^{-1} respectively. These are comparable to the maximum growth rates of 0.11 nm ns^{-1} reported by Pruppacher[38,39] at ∼255 K. Similarly, Furukawa *et al* recently reported growth rates of the basal face at 268 K as 0.27 ± 0.12 nm ns^{-1} [157] and prismatic face as 0.40 ± 0.18 nm ns^{-1}, using the TIP6P[311] water model.[164] While Kusalik and Rozmanov reported the growth rates at the secondary prismatic planes at 250 K and 260 K at 0.04 ± 0.018 nm ns^{-1} and 0.54 ± 0.034 nm ns^{-1} respectively.[164] These too are in the same order of magnitude as our own results, although different forcefields were used. Comparisons of our growth rates to empirical formulas listed in chapter 1 were not extensively explored here because they describe tip velocities of free standing crystals, which are largely determined from studies of the basal plane.[38–45] Rather we investigate the growth rate of a planar face.

It is worth mentioning that the ice growth rates do not increase with the degree of undercooling as in experiments, however this behaviour is not com-

pletely unexpected. It is frequently reported that the ice crystal growth rates determined from simulated systems are much faster than those determined by experiments.[19,126,157,159,164,311] This is also true for the TIP4P/Ice water model even though we have repeatedly demonstrated that the self-diffusion coefficient of this model is exceptionally slow compared to experiments and other water models (See § 3 and 6).[19] This trend in growth rates is largely due to the swift removal of latent heat by the thermostats used in our simulations and the use of PBCs. Ordinarily latent heat would be removed more slowly by thermal diffusion from the ice/water interface and onto the bulk phases, and this process plays a determining role on whether the ice crystal will grow or melt. Thermostats, however, work by rescaling the velocities of the molecules of the system in order to maintain an average pre-defined temperature, and so any deviations from this — even if it is induced by latent heat — is quickly dealt with. At temperatures close to the T_m, the growth velocity is low due to a weak thermodynamic driving force because the chemical potential for the water molecules in the liquid and solid phases are close. Although the driving force increases with the a drop in temperature, the water molecules have slower self-diffusion rates and this becomes a rate-limiting step. As a result of these two competing factors, the maximum growth rate is observed at 260 K instead of 255 K. A more extensive discussion of this behaviour can be found in a paper by Weiss *et al* [19].

5.3.3 Rate of water addition

Measurements of the time taken for a system to freeze indicates the overall impact of the IRI polymers on the total ice growth of the crystal, similar to splat assay experiments. However the gradient of the total energy profiles represent the rate at which the water molecules accumulate at the ice front in order to advance the growing ice crystal. Although the IRI active polymers may slow the overall rate of ice growth because of these plateaus, analysis of the gradients will provide some insight as to whether the polymer slow the rate of the water addition to this front compared to the pure water system. Or if they just temporarily suspend the accumulation of water onto the ice front. The rates obtained for the addition of water at 260 K is summarised in Table 5.2 and is expressed in terms of energy per water molecule per unit time. At 260 K, all the polymers slow the rate of water addition onto the ice relative to the pure water systems. The greatest effect is seen in the presence of more IRI potent oligomers.

The same analysis was performed on samples at 268 K, mainly for samples with plateaus and the results are summarised in Table. 5.3. Pure water systems

	Water	**PEG$_{10}$**	**PVA$_{10}$**	**PVA$_{19}$**	**PVA$_{10\times2}$**
Gradient	1.05	0.90	0.88	0.83	0.76
Stdev.	(0.07)	(0.07)	(0.08)	(0.06)	(0.07)

Table 5.2: The plateau at the end of the total energy profiles is removed and the rate of addition is taken from the gradient of the remaining data. The average rate of water addition to the ice crystal during the simulations conducted at 260 K in kJ mol^{-1} ns^{-1} for each water molecule. Averages are obtained over the repeat simulations and stdevs. are shown in brackets.

obtained a value of 0.27 ($\pm$ 0.03) at 268 K and we find that once again, the presence of polymer reduces the overall rate of water addition, disregarding the plateaus. This is certainly the case for all polymers during the first stages of freezing just before the metastable period, and the fastest initial rates are obtained for the IRI active polymers. For some polymers freezing resumes in a second stage. In those instances and in the presence of PVA, the rate of water addition returns to its initial rate unaffected, or close to the rate of pure water. Interestingly, we do not see the same behaviour in the presence of PEG, which slow the rate of water addition even further.

Stage	**PEG$_{10}$**	**PVA$_{10}$**	**PVA$_{19}$**	**PVA$_{10\times2}$**
Initial	0.22	0.01	0.17	0.01
Final	0.13	0.01	0.26	-

Table 5.3: The plateau at the centre of the total energy profiles is removed and the rate of addition is taken from the initial and final gradients of the remaining data. The average rate of water addition to the ice crystal during the simulations conducted at 268 K in kJ mol^{-1} ns^{-1} for each water molecule. This data was collected from only one repeat in each system. Pure water systems obtained a gradient of 0.27 ($\pm$ 0.03) at 268 K and do not have a metastable state.

5.3.4 Polymer residence regions

Fig. 5.8–5.10 shows the number density of water oxygens in homogeneous systems and in the heterogenous systems at the midpoint (30 ns or 150 ns), and towards the end (60 ns or 300 ns) of the simulations. These results are only shown for a single repeat and the analysis reveals that between 250–270 K, the pure water systems typically have a QLL of 0.85–0.95 nm at the midpoint of the trajectory. The thickness of the QLL layer was determined using the 10–90 rule[312], which states that

the thickness of an interface can be estimated by the length over which an order parameter such as density changes from 10% to 90% of the bulk solid whilst moving from the bulk liquid phase into the solid phase. This range is slightly lower than the expected 1.0–1.5 nm.[26]

The density profiles can also provide some useful snapshots of the regions that the polymers reside in. It is important because this may provide some insight into the activity of IRI active polymers. For instance, if there is a preference to slow freezing at the QLL or once it is partially incorporated into the ice lattice. Fig. 5.9–5.10 show that at the midpoint of the freezing processes, the oligomers typically reside within the icy regions at low temperatures (250 K), the QLL regions at 260 K and the liquid regions at temperatures approaching the T_m (268 K and 270 K). Aside from two exceptions, the oligomers normally become overgrown at the same positions they were found in at the midpoint of the simulations.
These exceptions only occur at temperatures near the T_m, which incidentally exhibit some metastability of the ice crystals because PVA appears to have an affinity for the icy regions. For instance at 268 K systems PEG travels ahead of the growing ice front whereas PVA travels from the liquid region in towards the icy regions. Both polymers appear equally mobile because they both travel the same distance ($\sim$1 nm) but in opposite directions. The second exception occurs at 270 K where more kinetic energy is available. At this relatively elevated temperature, the PEG oligomers behaves accordingly and moves $\sim$5 nm, while PVA remains the same distance from the centre of the ice lattice.

These observations are not artefacts, but real features that are independent of the starting position of the polymers because each polymer was placed in the QLL, at the same distance away from the ice lattice. The apparent affinity for ice-like regions explains the observation that larger PVA oligomers and systems with more PVA molecules eventually reside deeper in the ice than the other polymers at the end of freezing simulations, which were conducted at 250 K and 260 K. At 268 K, the slowed freezing rates induce a partial incorporation of the polymer into the ice lattice under the same timescale, and in turn provides the opportunity for the oligomers to extend across into the two phases for a prolonged period of time.

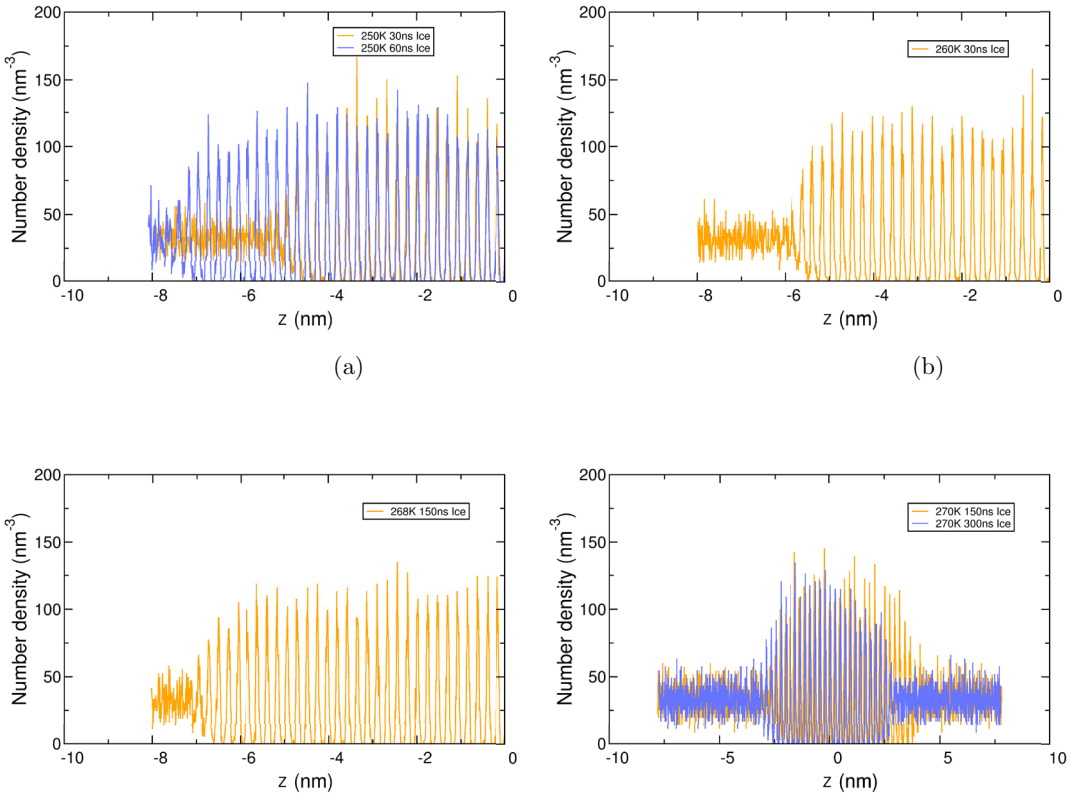

Figure 5.8: The density profile of oxygens in the pure water systems at the middle (orange) of the trajectory and end of the simulations (blue), used for comparisons with the polymeric systems. At 270 K and 268 K the middle point is 150 ns and 300 ns. At 260 K and 250 K these points are at 30 ns and 60 ns respectively.

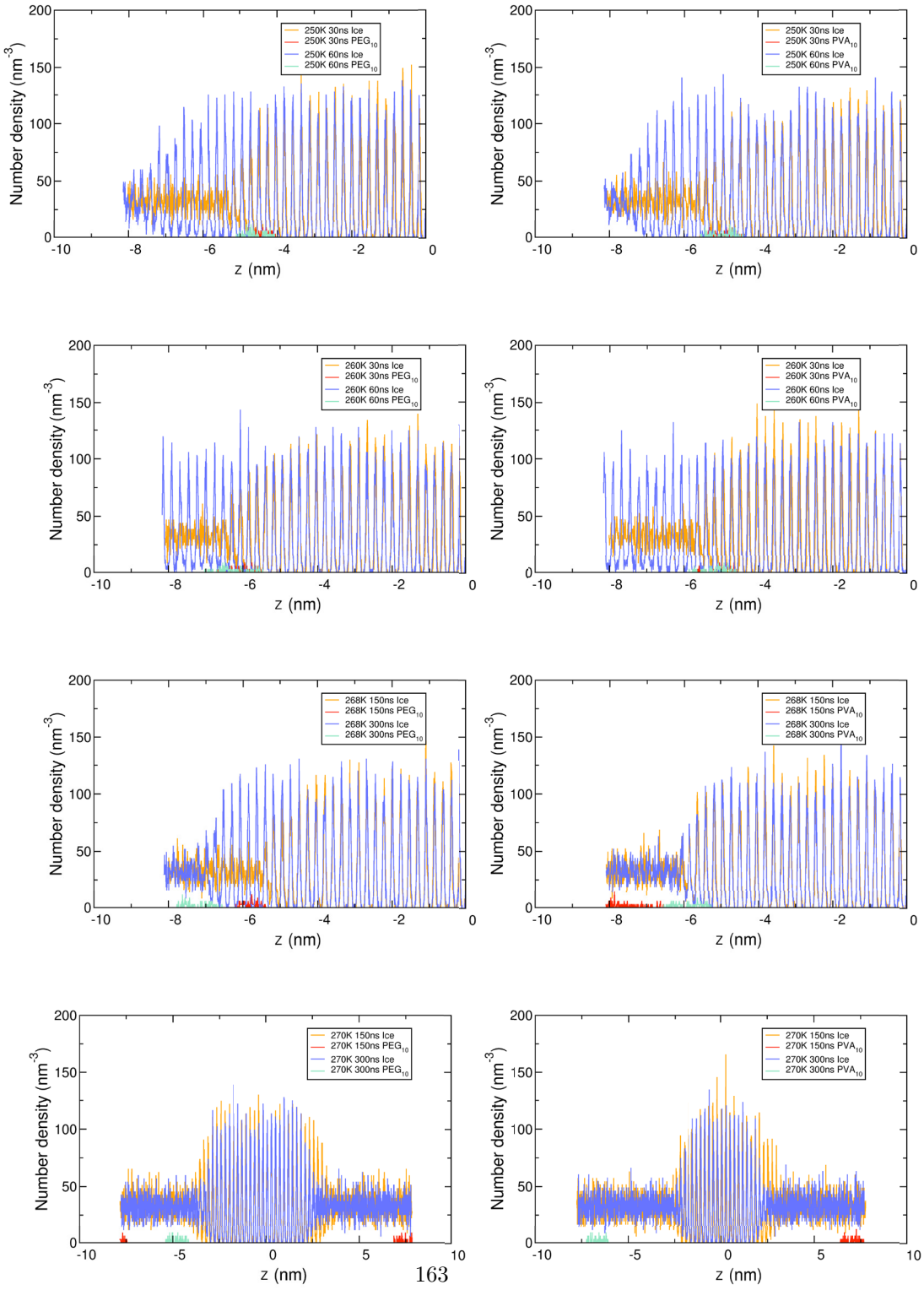

Figure 5.9: The density profile of the PEG_{10} (left) and PVA_{10} (right) systems at the middle (orange and red) of the trajectory and end of the simulations (blue and green)

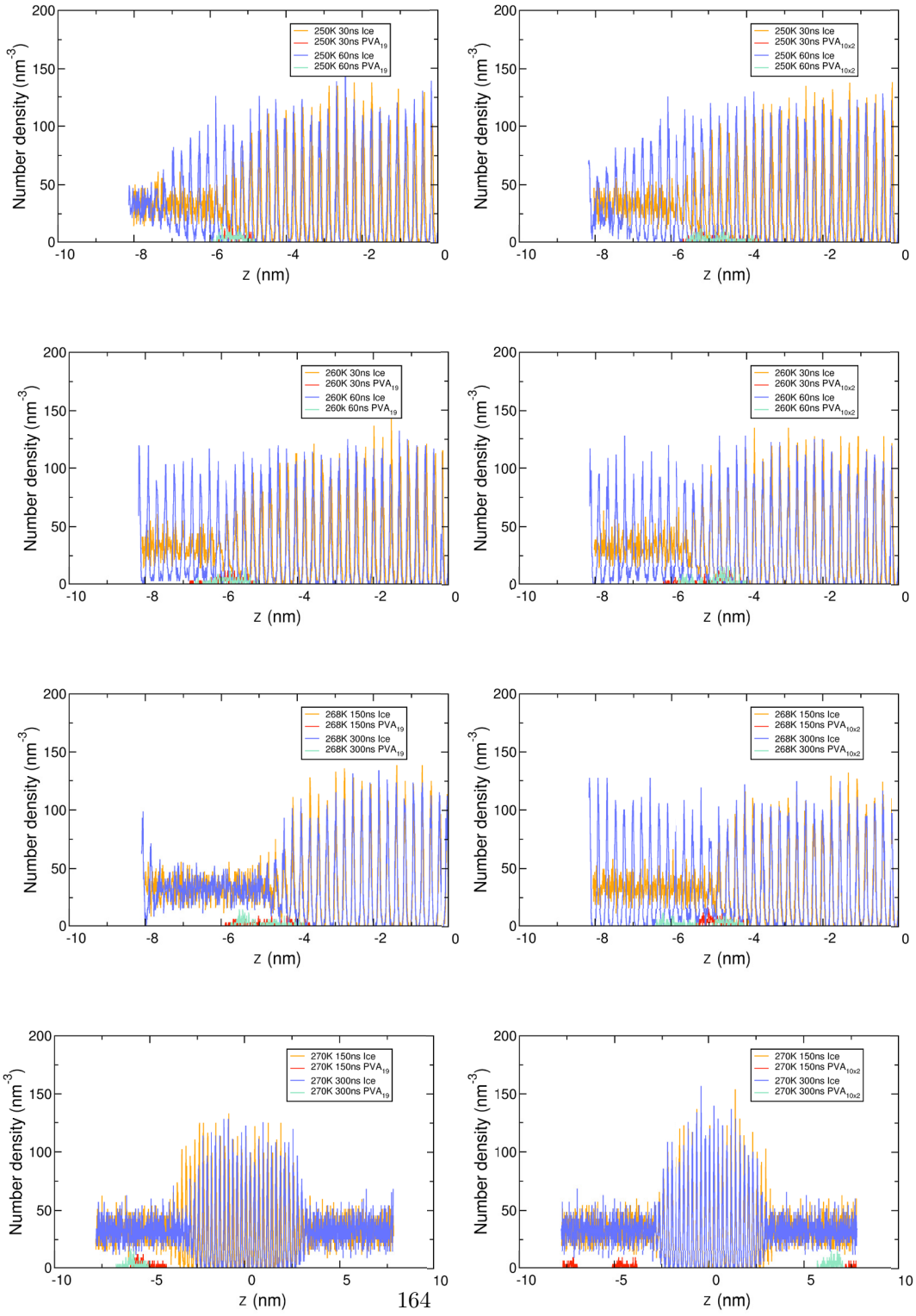

Figure 5.10: The density profile of the PVA_{19} systems (left) and $PVA_{10\times2}$ (right). Same colour key as in Fig. 5.9

5.3.5 Ice growth around polymers

The TH properties of AF(G)Ps have long been attributed to the Gibbs-Thomson effect; the local curvature of the ice in the regions adjacent to the adsorbed protein. Fig. 5.11 show snapshots of the simulation box with polymers at the ice/water interface at 150 ns and at 268 K. These snapshots partially support these findings and reveal that the curvature of the ice/water interface is faint in all our modelled systems.

At 268 K, PVA_{10} temporarily exhibits short-lived (<75 ns), curved ice growth around the polymer at 150 ns, which is the only snapshot to also coincide with the metastable state of ice for this system. Similarly, the metastable states for $PVA_{10\times2}$ at 268 K is partly explained by the existence of a small curved ice front which presumably slows the growth rate of ice at 225 ns. This curvature is formed by the adsorption of one polymer onto the ice. Notably this feature is weak in PVA_{19} system although it exhibits a metastable state greater than PVA_{10} and the reasons for this are discussed later. Notice that, we also provide snapshots of the pure water system for comparisons at 268 K because they serve as important benchmarks for understanding how much curvature is really introduced by the antifreeze macromolecules. Doing this is important, considering that recent modelling studies that have shown the prismatic planes are especially rough and uneven compared to other planes of ice[9,124], however these visual comparisons are often omitted in these types of studies.

Overall the results are not surprising as none of the polymers are known to display significant TH activity, and is consistent with our interpretations of the results thus far. The curvature induced by TH is proportional to the degree of supercooling and can be described by the Gibbs-Thompson equation (Eq. 5.1)[160,168].

$$R = \frac{A_g V \gamma T_m}{\Delta T \Delta H} \tag{5.1}$$

Assuming a spherical growth of the ice crystal between the periodic images of the oligomers on the ice/water interface, R represents the radius, T_m is the melting point (270 K), ΔT the freezing depression ($T - T_m$), V is the molar volume of the solid phase ($m^3 mol^{-1}$), ΔH is the molar latent heat of fusion ($5.4 \times 10^3 J\,mol^{-1}$)[204,313] and γ is the interfacial free energy ($30.8 \times 10^{-3} J\,mol^{-2}$)[313]. V is calculated as the molecular weight of water ($0.018\,kg\,mol^{-1}$) divided by the density of ice at T_m ($906\,Kg\,m^3$)[204,313]. In the case of ice embryos A_g=1 for cylindrical geometries, which are characteristic at temperatures less than ΔT=-5 K (see § 1.2.1). If our

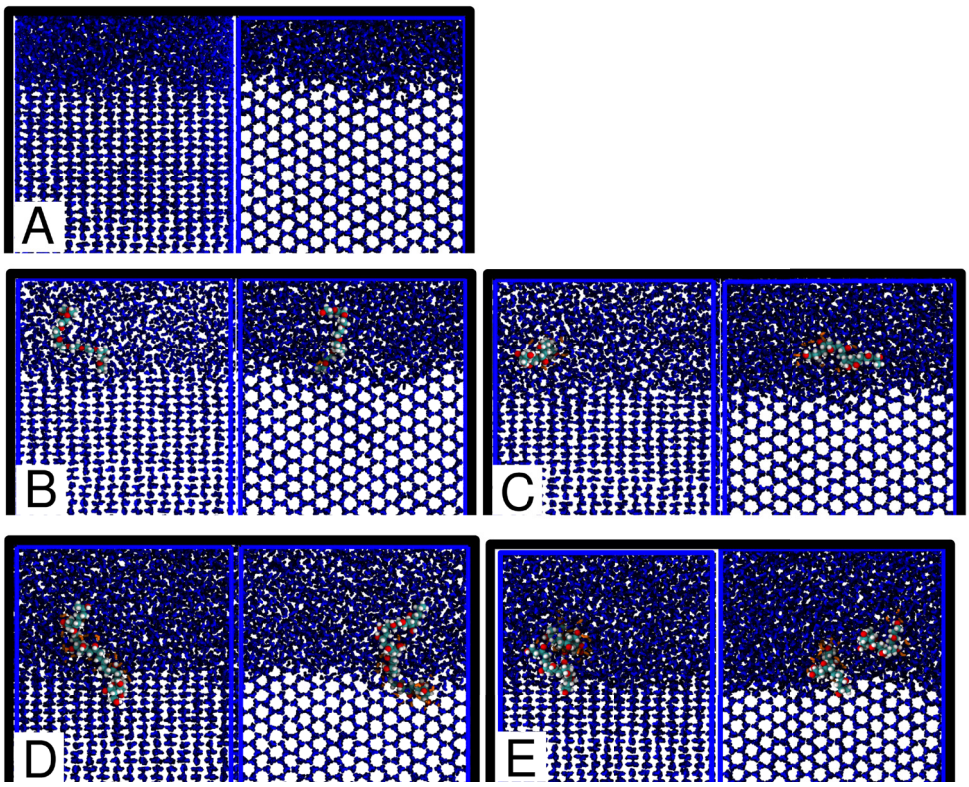

Figure 5.11: Snapshots of the systems freezing at 268 K for A. pure water, B. PEG_{10}, C. PVA_{10}, D. PVA_{19} and E. $PVA_{10\times2}$. Dark blue molecules represent water molecules and the polymers are shown using a space-filling model. For clarity, only cross-sections of the polymeric systems are shown, using the polymer centre of mass as a reference point for the inclusion or exclusion of water molecules. Any water molecules which are included in the cross-section and fall within the 0.35 nm cut-off from the polymer oxygens atoms are highlighted in orange. In each panel, both the *xz*- (left) and *yz*- (right) perspectives of the ice/water interfaces are shown.

polymers were highly TH active, at lower temperatures we would also expect a critical cylindrical radius of 3.06 nm and and 1.53 nm at 260 K and 250 K respectively. At 260 K this can be approximated as 7 hexagons on the yz-plane and 14 lattice oxygens in the xz-plane however, we do not observe such large curvatures rising from the baselines in either of these temperatures for any of the systems.

Recently Furukawa *et al* [158–160] and Kuiper *et al* [168] have both conducted novel simulations which demonstrate the involvement of the Gibbs-Thomson effect in the mechanism of AFPs. They modelled AFPs adsorbed onto a mobile ice/water interface at 10 K and 5 K below the melting point of two different water models (TIP6P and TIP4P) respectively, and they found marked convex curvature on either side of the AFPs. Kuiper *et al* found that the TH active sbwAFP achieved an ideal curvature with a radius of 4.6 nm, using a similar water model and undercooling.[168] In addition to this, the sbwAFP managed to sustain the curvature for much longer timescales (up to 100 ns). These differences confirm that the curvature is indeed mainly a consequence of TH activity, and not IRI. Especially as the issue of latent heat removal, which was discussed earlier, may encourage the tendency for a larger R values in simulations.[159]

Lattice matching and polymer motion

Fig. 5.12–5.15 show a series of zoomed in snapshots of oligomers at the ice/water interface at 30 ns intervals using two different planes. The snapshots reveal that oxygen atoms in the PEG and PVA oligomers can match the oxygen arrangement on the ice lattice. Although the studies of the polymers in solution revealed that there are no distinct hydrophobic and hydrophilic faces in either PVA or PEG, there is a clear preference for the PVA to incorporate into the ice lattice vacancy sites using an oxygen atom or a hydroxyl hydrogen atom. While PEG approaches with its oxygen atom, which lies within the polymer backbone. In doing so, the oligomers become partially incorporated into the ice lattice and prevent the interface from advancing.

During the course of the simulations PEG_{10} repeatedly incorporates into the ice lattice and detaches, which supports the density profiles that PEG_{10} largely remains in front of the growing ice lattice (Fig. 5.12). In contrast the PVA oligomers generally remained attached for longer to the ice lattice because PVA has more atoms that are capable of H-bonding with the surrounding water molecules.

Metastable states of the ice crystal growth at 268 K for the systems containing the more IRI potent oligomers, PVA_{19} and $PVA_{10\times2}$, were not earmarked

by the expected local curvature which suggest that other factors may be responsible for the polymer's IRI activities. Fig. 5.14 reveal how the PVA_{19} oligomer remains partly incorporated into the growing. The first point of contact between the polymer and the ice lattice occurs prior to these snapshots. During which, the incorporated section of the polymer is approximately 3 units long and the whole chain is linear. The polymer arranges itself so that its oxygen atoms sit within the free sites on the ice lattice which would normally have become occupied by oxygen atoms from incoming liquid water in the QLL. By folding upwards onto itself to form a hinge, a ∼3–6 unit long tail is formed that is kept away from the growing ice lattice, and it sways from side to side. The slowed growth of the interface resumes as the kink ceases to fold back onto the bound PVA regions, causing the tail to align with and venture towards the ice. Possible implications for this mechanical motion is that it scatters surrounding water molecules and disrupts the build-up of the ice front during the metastable period. Fig. 5.16 shows a different perspective of the PVA_{19} polymer in order to illustrate this feature.

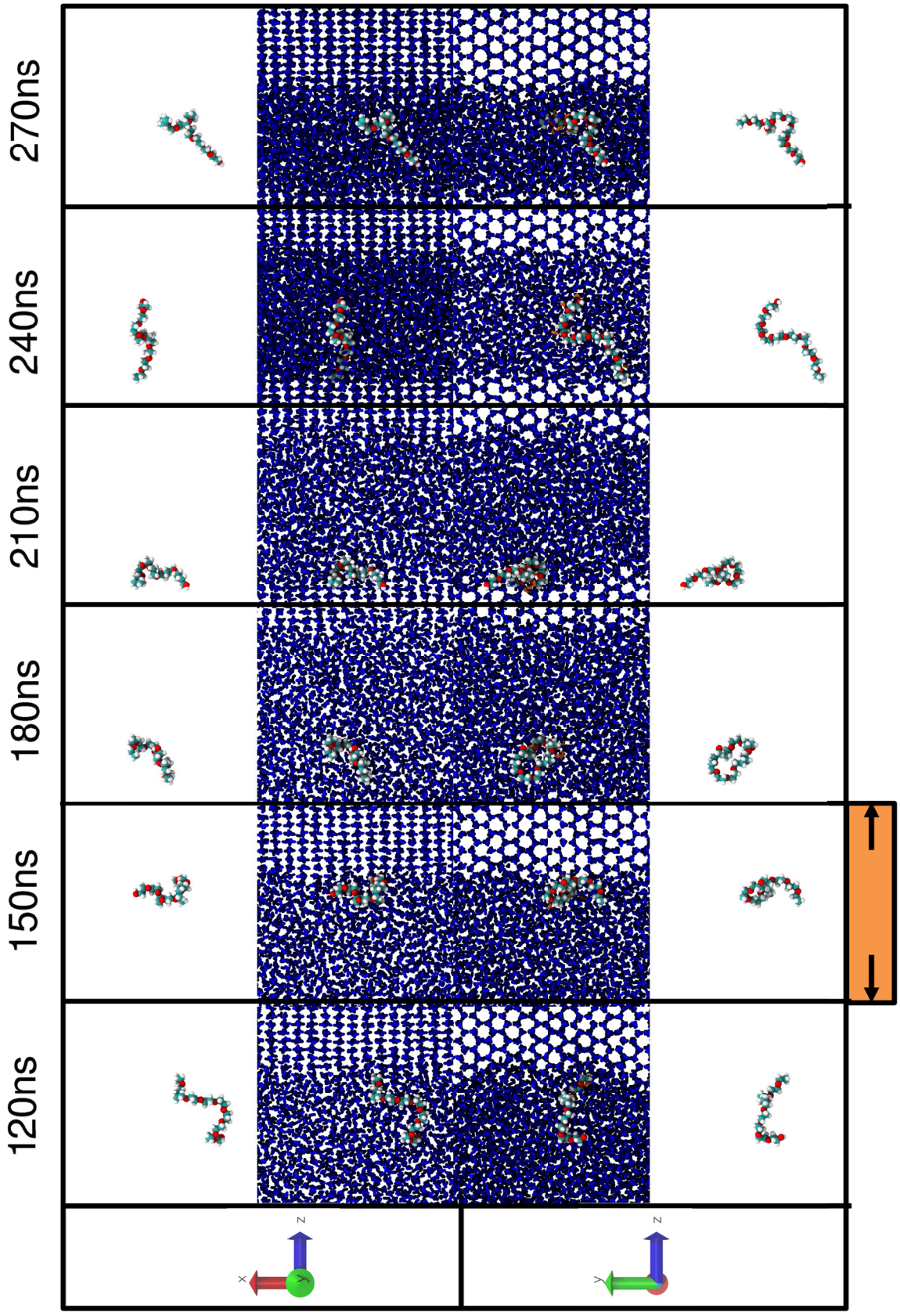

Figure 5.12: Snapshots of the evolution of freezing at 268 K for PEG_{10}. Same key as in Fig. 5.11. Time frames which conincide with the metastable states are highlighted by the orange bar. At each time, snapshots of the polymer are also shown in the *xz*- and *yz*- perspectives, without any water molecules.

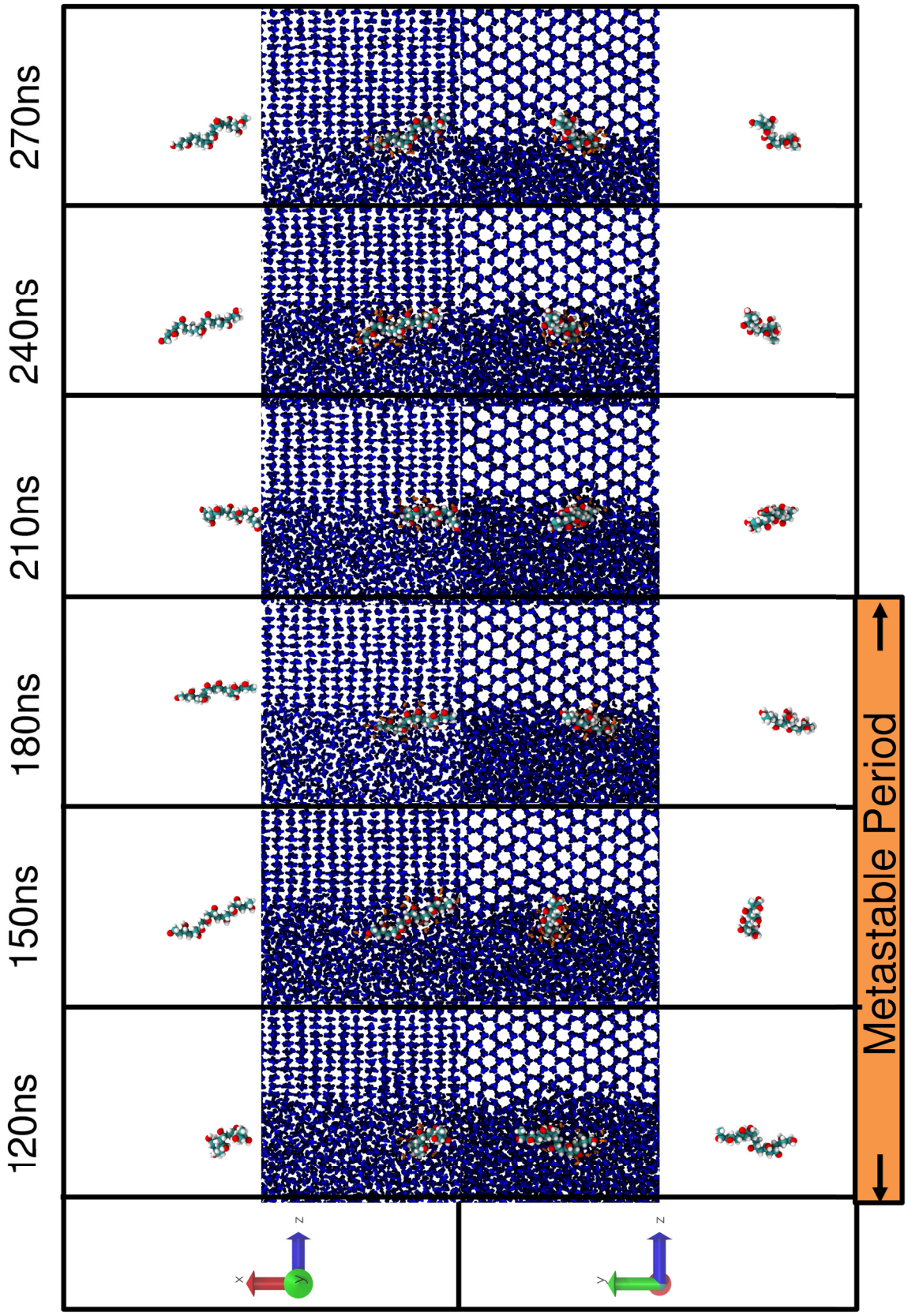

Figure 5.13: Snapshots of the evolution of freezing at 268 K for PVA_{10}. Same key as in Fig. 5.12.

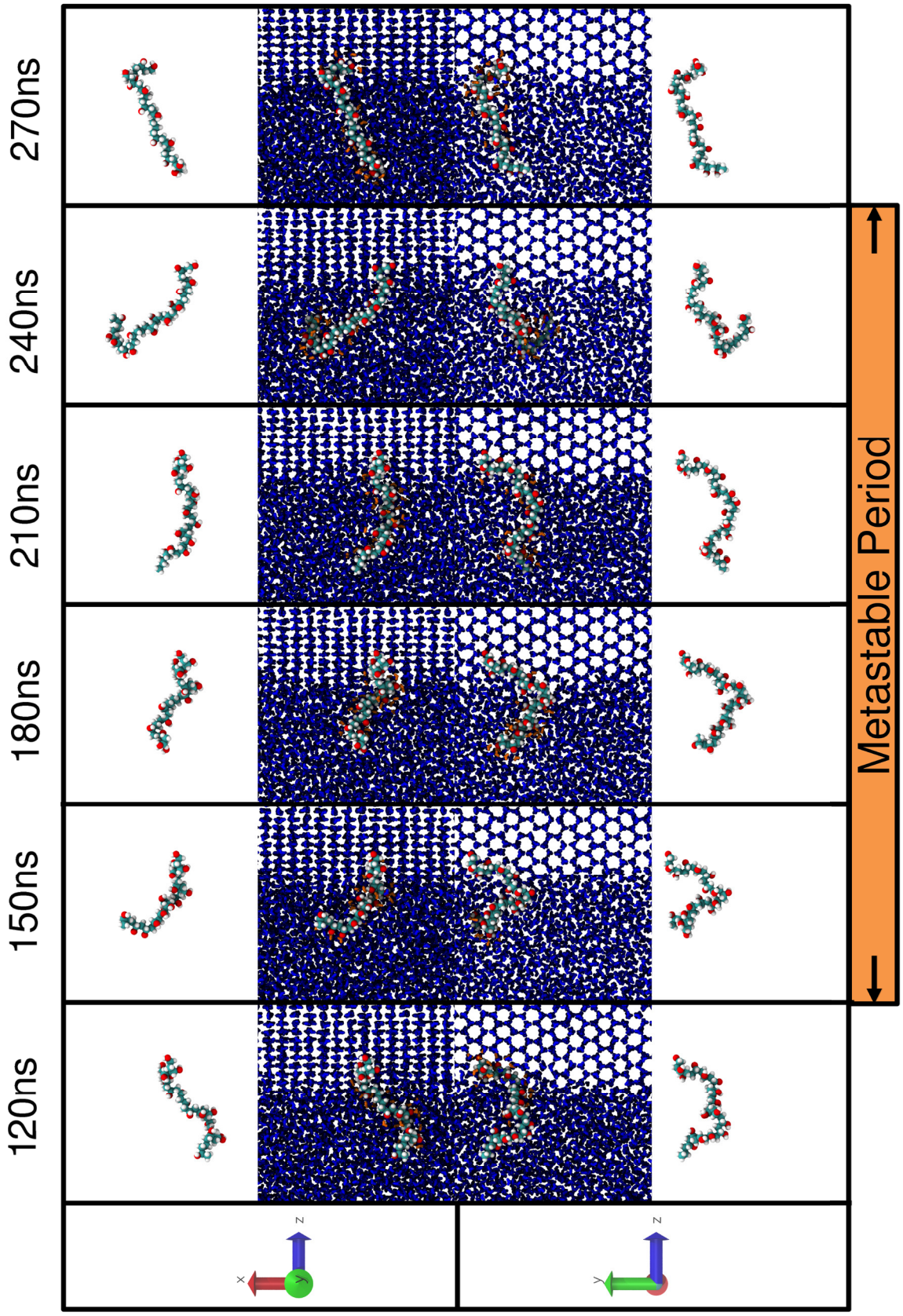

Figure 5.14: Snapshots of the evolution of freezing at 268 K for PVA_{19}. Same key as in Fig. 5.12.

In order to investigate the importance of flexibility in the IRI activity of PVA and PEG oligomers, the RMSF was calculated for simulations at 268 K and the results are shown in Fig. 5.17. The flexibility of polymers are lowest in the solution studies conducted at 260 K and are greatest at 298 K. In the presence of ice, during the metastable period at 268 K, the RMSF of the polymers resemble the warm solutions more closely than the colder temperatures. For PVA_{19}, the contours of the RMSF profile at 268 K is different to both warm and cold profiles in that it presents a "W"-shape. This feature is absent in all other polymers and is consistent with the notion that the flexibility of PVA_{19} could allow it to behave like a microscopic stirrer, once it becomes partially incorporated into the ice lattice. Similar features have been observed for AFPs[145,150,154,308,310], IRI active AFP analogues[116,166,307,309] and polyols[314] in simulation studies but have not been explored as a feature that are relevant to antifreeze activity.

Although the RMSF analysis is not a comprehensive study of the role that flexibility plays in the IRI activity of synthetic polymers, it is a reasonable method to draw out differences between the two types of polymers. If these properties differentiate greatly between the two types of polymers then flexibility may be important and could contribute towards their respective IRI activities. If this happens to be the case, new methods could be used to explore the importance of flexibility at the ice/water interface such as modeling rigid IRI active polymers in both coiled and uncoiled configurations.

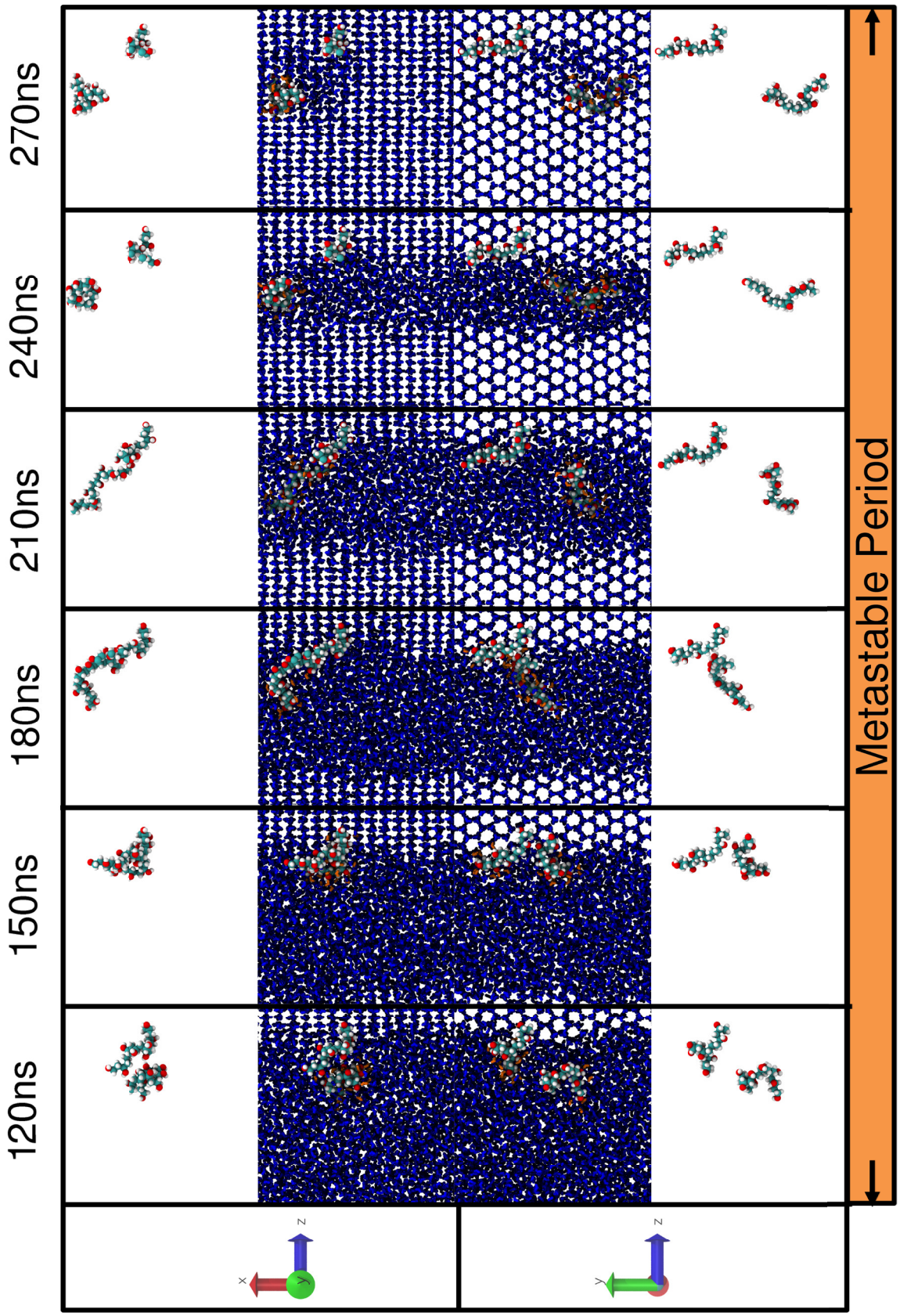

Figure 5.15: Snapshots of the evolution of freezing at 268 K for $PVA_{10\times2}$. Same key as in Fig. 5.12.

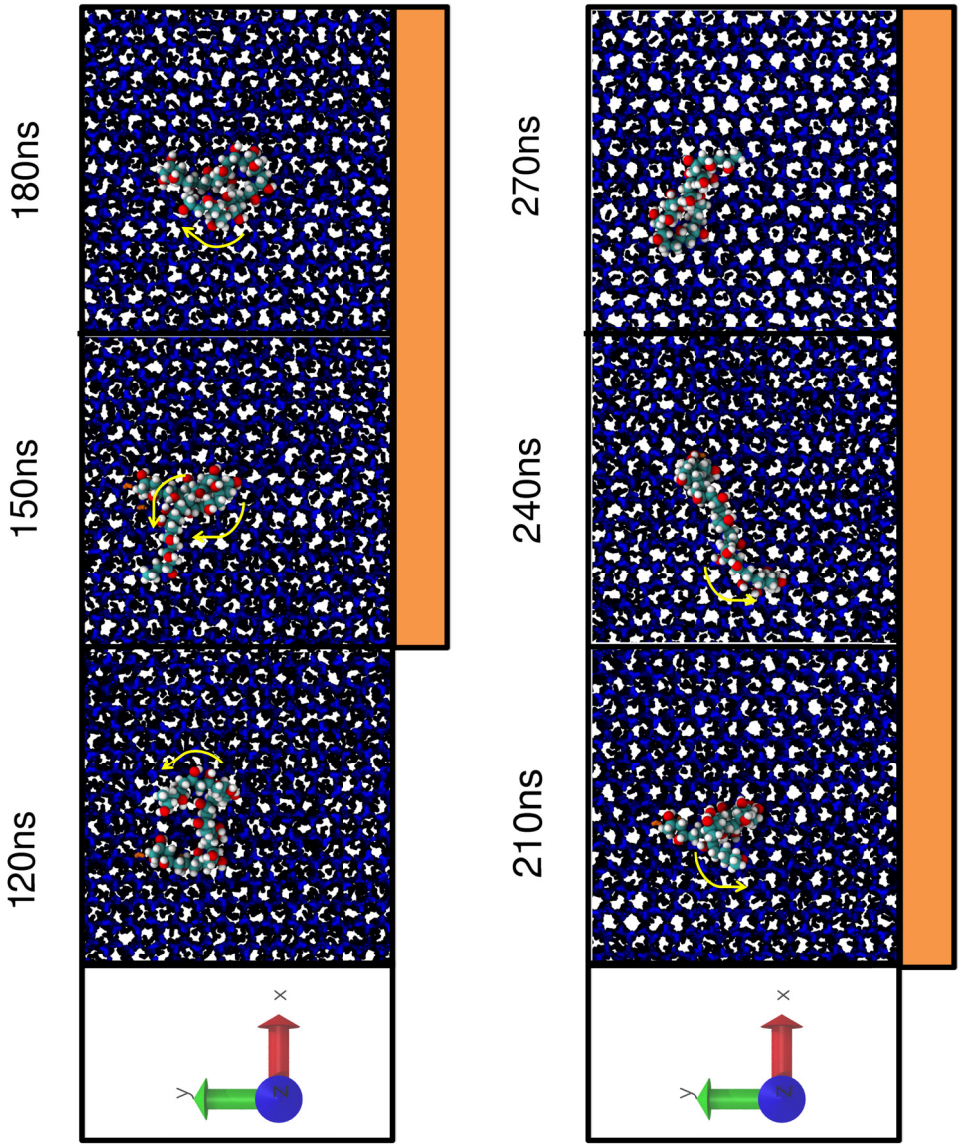

Figure 5.16: Snapshots of the evolution of freezing at 268 K for PVA_{19} in the *xy*-plane. Same key as in Fig. 5.12. Yellow arrows represent the movement of the tail regions.

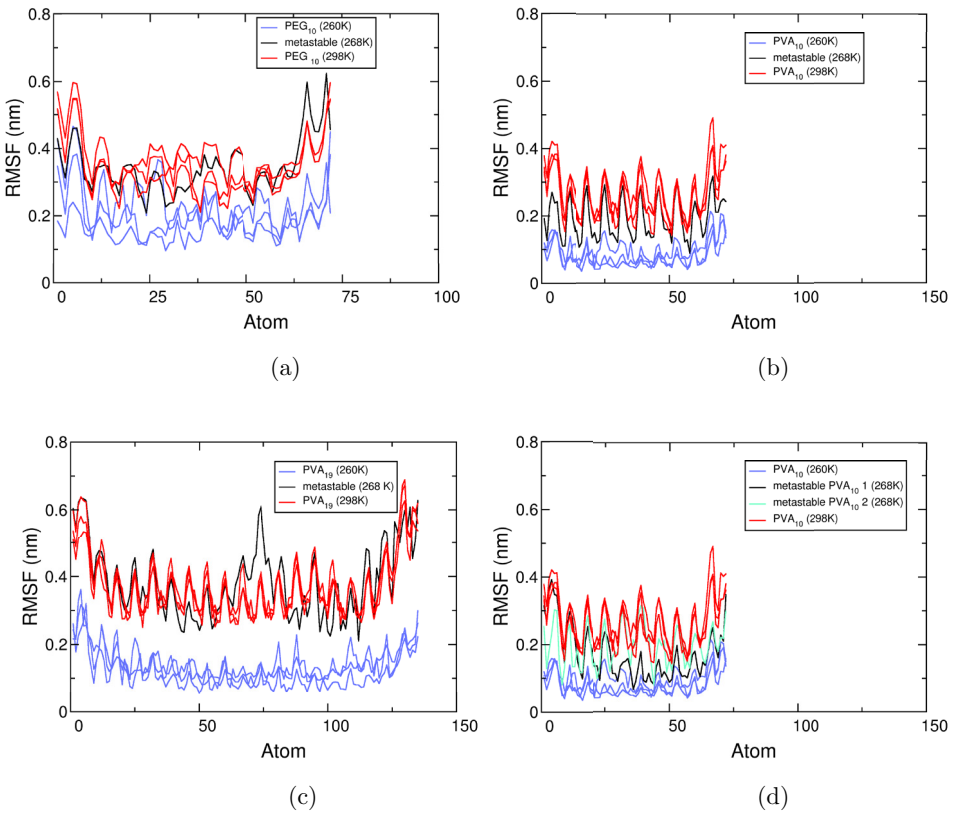

Figure 5.17: The RMSF plots for (a) PEG_{10}, (b) PVA_{10}, (c) PVA_{19} and (d) $PVA_{10\times2}$. Results are shown for three repeats in the solution at 298 K and 260 K, and for one repeat during the metastable period in the ice growth simulations at 268 K.

In order to quantify the lattice matching properties of the polymers in the presence of the ice crystal, RDFs were calculated at 260 K using polymeric oxygen pairs because complete freezing was captured in every simulation at this temperature. The results are depicted in Fig. 5.18 and are calculated over the last 3 ns after the system froze. PVA oligomers still have major peaks at 0.30 nm, 0.46 nm and minor peaks 0.62 nm, 0.73 nm and 0.81 nm, as with the RDFs from solution studies (See § 4). Three of these oxygen separation distances still coincide with separation distances between oxygen atoms on the ice lattice; 0.46 nm, 0.73 nm and 0.81 nm. Earlier we found that PEG oligomers did not have any distances that matched the ice lattice, however this changed as the PEG_{10} oligomer were

overgrown by the ice. Two new peaks emerge at 0.45 nm and 0.60 nm (compared to the merged region at 0.6–0.8 nm obtained in solution (see Fig. 4.22). PEG obtains a lattice matching peak at 0.45 nm, however it is still small compared to the IRI active polymers. Without the hydroxyl group we find that it typically takes much longer for the PEG to adsorb to the ice lattice, and pause the growth of ice. In repeats without the metastable states PEG_{10} temporarily attaches and then falls off the lattice site. As this happens the ice front advances, eventually cornering PEG_{10} at the end of the box and the system freezes over. PEG_{10} only successfully re-attaches in two out of nine simulations.

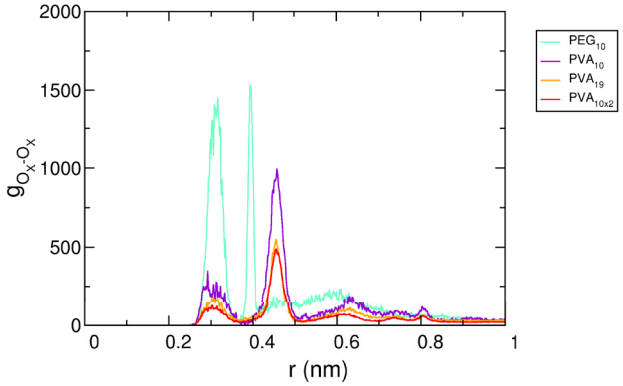

Figure 5.18: Averaged RDF between oxygen atoms in oligomers at 260 K. For each oligomer, the RDF profile was obtained from the last 3 ns of the frozen simulation trajectories and averaged over the nine repeats.

Ice recognition

Another question is how does the IRI active polymers come to recognize the ice crystal from pure water? Thus far the analysis indicates that the IRI active oligomers do not necessarily recognise the ice. Density profiles of select repeats indicate that the polymers remain in largely the same position over time, which leaves the onus on the ice front to advance towards the polymer in solution (Fig. 5.9–5.10). One may pose the question "how does one know if an interface does in fact grows towards the polymers, and if so which one?" The only way to be certain is to re-design the experiment so that a single interface is used. This question is posed because it is possible that the use of PBC effects make it difficult to isolate which interface the polymers actually impede. However in this study total energy profiles make it

apparent that the crystal growth rates are definitely slowed by the polymers, and in the absence of any polymer additives the visual inspection of the trajectory reveals that both interfaces typically grow at approximately the same rate but in opposite directions. It is therefore viable to use the current set-up to investigate the IRI activities of the polymers studied in this thesis. By re-designing the experiment, one removes the added complication that the interfaces can grow in the "wrong direction" due to PBC effects. Moreover the total energy profiles will only represent the single interface that the polymers interact with.

As mentioned earlier, studies using different water models have shown that the prismatic planes are rougher than other planes due to differences in the way that they grow. Basal planes, grow smoothly via layer-by-layers whilst prismatic planes grow in a more disorganised fashion.[125,126] Recent simulations studies of brine solution in contact with an I_c crystal at 15 K undercooling found that the rough regions on the prismatic planes are prone to trapping ions, and as a result metastable states were also achieved until all ions were paired.[124] This behaviour is not at all unusual, and similar observations have also been made for simulations of CO_2 adsorption onto ice[315] and other small peptides[187]. Similarly, from the 268 K simulations we can see that once the PVA_{19} polymer folds to interact with itself, effectively pairing up segments, the ice continues to grow slowly.

To characterise this further, we monitored the SASA of the polymers over time at 260 K and the results are shown in Fig. 5.19 and Table 5.4. This temperature was chosen for three reasons. Firstly, a complete phase change was always observed for every system at this temperature and so the polymers' responses to ice growth could easily be compared. Secondly, differences observed between the IRI active and inactive polymers were one of the most pronounced with respect to delayed freezing times, and this feature was consistent across repeats. Lastly, the results at this temperature can be compared to solution studies taken at the same temperature in chapter 4.

Table 5.4 shows the average TSASA and percentage ASASA for the oligomers which were obtained from the ice growth simulations at 260 K. It also shows the results obtained in chapter 4 from solution studies at 298 K and 260 K. It is possible to tell that the ice has been recognized by an oligomer if there is a change in the SASA or another property of the oligomer in the presence of ice. These changes may coincide with the onset of freezing at the start, or at the end of the simulation once the oligomers are frozen over.

Both PVA and PEG polymers exhibit roughly same average percentage hydrophobicity in the ice growth simulation, as they do in water. Since PEG_{10} has

a higher percentage ASASA than the PVA oligomers, an increase in the HBN of water molecules surrounding the oligomer causes it to contract in order to minimize interactions with the solvent. This is denoted by a decrease in TSASA, and an example of this is shown in Fig. 5.19. In the highlighted repeats for PEG_{10} the drop in the SASA occurs at 13.81 ns and corresponds to the point at which the PEG_{10} oligomers becomes incorporated into the ice lattice. This response does not appear in the PVA systems due to the lower proportion of ASASA. This suggests that PVA oligomers assimilate more easily into the ice lattice than PEG.

Polymer	**298 K**	**260 K**	**Ice/water system**	**ASASA (nm^2)**
PEG_{10}	87.13 (0.03)	87.34 (0.56)	87.14 (0.50)	7.59 (0.52)
PVA_{10}	44.68 (0.13)	44.08 (0.42)	44.43 (0.54)	7.20 (0.07)
PVA_{19}	41.80 (0.11)	41.50 (0.75)	41.80 (0.45)	12.89 (0.17)
$PVA_{10\times2}$	-	-	44.51 (0.46)	14.37 (0.07)

Table 5.4: The average percentage ASASA in TSASA in water at 298 K and 260 K, and in the ice growth simulations at 260 K. The average ASASA for the ice growth studies and stdevs between repeats are also shown in brackets.

5.4 Discussion

It is the first time that studies of synthetic antifreeze macromolecules, PVA and PEG, have been conducted in a dynamic ice/water interface in order to determine their TH and IRI activities. In literature, studies of other antifreeze macromolecules often subject liquid water and the ice lattice to full or partial constraints.[143,168] These studies also frequently dock the antifreeze macromolecules onto the ice lattice and may even restrain the macromolecules in position.[143] We previously discussed the importance of simulating the AFPs in more realistic environments and the implications that these may have (§ 1.4.2). A more critical discussion on the effects of simulating AFPs outside of their natural temperatures can be found in work produced by Kar *et al* [302], and the importance of dynamic interfaces have also recently been commented on by others[160,168].

The results from this study support Knight *et al* 's[4] model for the mechanism of antifreeze action. The IRI active PVA polymers have polar groups which compliment the spacing of atoms in the ice lattice. This ability to lattice-match allows them to H-bond with the atoms belonging to the ice crystal, and then to incorporate into the growing structure (Fig. 1.7). The consequent immobilization

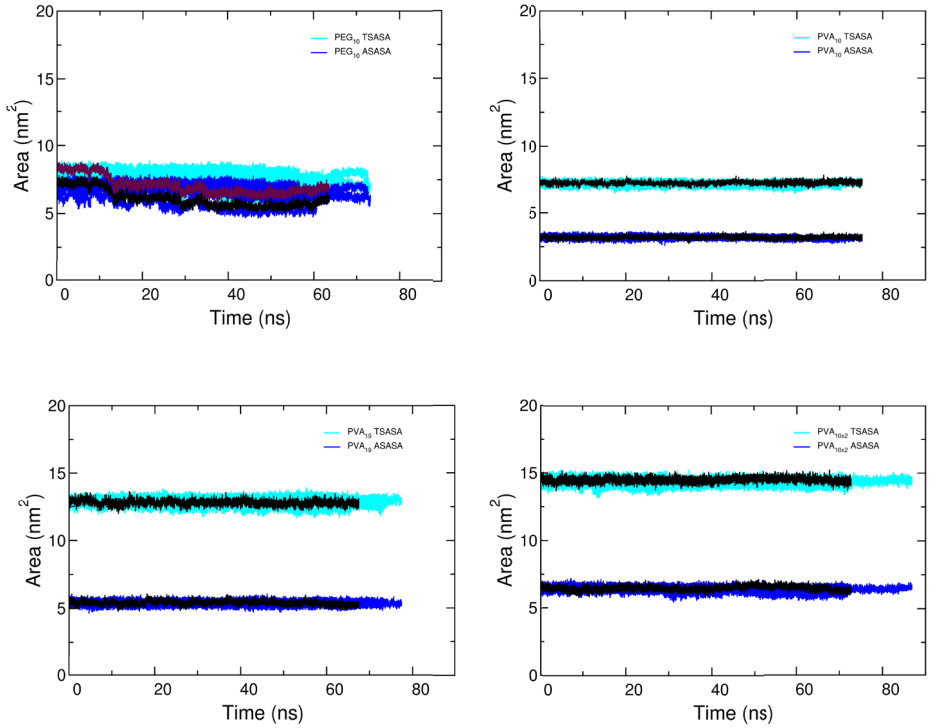

Figure 5.19: The SASA for PVA and PEG ice/water systems at 260 K. Same colour key as in Fig. 5.2, except for PEG_{10} where the representative repeat for TSASA is highlighted in maroon for clarity.

of the PVA polymers onto the ice, temporarily pauses the ice crystal's growth. In contrast to this, PEG polymers do not have the ability to do and so rarely adsorb on to the ice lattice which means that they less frequently pause the growth of ice.

In order to identify these features which differentiate IRI and non-IRI active polymer, we conducted long ice growth simulations at a range of temperatures below the T_m of the system. Until recently, lengthy timescales such as those reported in this study and by others[168] were considered computationally expensive. In order to circumvent this, various studies run shorter simulations (*e.g.* 5–10 ns) and infer a phase change from the initial gradients of their total energy profiles.[166,167] Although this method is accurate and computationally efficient for pure water systems, this may not be the case for *in silico* studies of the mechanism of AFPs or their analogues. We have demonstrated that freezing simulations in the presence of antifreeze molecules can significantly delay the time taken for the system to completely freeze (>300 ns), at least for systems with similar sizes to our own. It is important to consider that the use of short trajectories means it is possible to miss important features that occur as a result of crucial interactions between the ice and the antifreeze molecules during the remaining 290 ns trajectory. Take for instance a two-stage adsorption process, which may be earmarked by an intermediate plateau instead of just the single and final one, which ordinarily represents the completion of the freezing or melting process.

5.5 Conclusion

It is the first time that studies of synthetic antifreeze macromolecules, PVA and PEG, have been conducted in a dynamic ice/water interface in order to determine their TH and IRI activities. In this section, we have studied the effects of PVA and PEG oligomers in a range of 10 temperatures from 310 K–250 K in the presence of an ice crystal. We have found that in agreement with experiments the ice growth rates are slowed as a result of their presence, particularly for IRI active compounds[3,7]. They do so by stabilising the ice crystal at temperatures close to the Tm, although significant TH properties were not observed in the study. Stabilisation of the ice crystal was identified whilst monitoring the convergence of the crystal growth or melting process using the total energy of the system and was earmarked by temporary a plateau.

Analysis of the SASA of oligomers at 260 K suggests that it may be possible for PEG_{10} undergo a response to and hence a recognition process of the ice while

PVA does not. Both PVA_{10} and PEG_{10} have similar TSASA values, and so the responsiveness of SASA can be attributed to difference in hydrophobicity. Density profiles of the oligomers highlight that PVA was pinned much more deeply into the ice lattice than PEG, and at times without being completely overgrown (Fig. 5.14). There was a clear correlation with increasing IRI activity for systems with more hydrophilic groups, which was reflected in the slowed growth of ice by PVA oligomers. Whereas PEG_{10} did not alter the timescales of freezing to the same extent. This behaviour is not unexpected because our solution studies showed that PVA hydroxyl groups already adopt lattice-matching spacing in solution in both warm and cold temperatures (§ 4). It is clear that as both polymers become incorporated into the ice crystal lattice, the polymeric oxygens occupy the sites which would ordinarily be taken by free water molecules. Due to PVA's better complimentary fit to the ice lattice and hydroxyl groups, it frequently immobilizes at the ice surface and pauses the growth of the ice crystal while PEG does not. The full or partial incorporation of polymeric oxygens introduced some small amounts of curvature during the freezing simulation as a response to periodic images of the oligomers. However none of these were large enough to be classed as a the Gibbs-Thomson effect despite using a relatively large ice/water interface compared to similar studies in literature[158–160,168]. Instances of PVA's partial incorporation requires some degree of complementation, flexibility and hydrophobicity.

Chapter 6

The antifreeze activity of poly(hydroxyproline): A molecular dynamics simulation study

6.1 Introduction

Poly-l-hydroxyproline (PHYP) has been shown to exhibit high degrees of IRI activity[52] and nearly non-existent TH at low concentrations ($<$1mg ml^{-1}) and low degrees of polymerization.[48,52,316] For instance, Gibson *et al* conducted splat assays on a series of polymers, including PVA_{88} and $PHYP_{44}$. They reported that a 3.5 mmol L^{-1} solution of $PHYP_{44}$ caused a $\sim$34% reduction in the MLGS. These IRI activities were comparable to those a 5.0 mmol L^{-1} solution of PVA_{88}, even though the two polymers have completely different secondary structures. PHYP has a PPII helical structure, which is particularly interesting because of its similarity to the secondary structure of low molecular weight AF(G)Ps[120,121], while PVA is largely unstructured in solution.[52]

In another study, Corcilius *et al* [316] compared the IRI activities of a 7 mM solution of glycosylated peptides. They found that the unglycosylated hydroxyproline-based peptides were the most IRI potent and comparable to a 5.5μM solution of native AFGP-8.

These properties makes PHYP a desirable antifreeze for the cold storage of biological tissues, partly because the absence of TH also means that the polymers do not exhibit significant ice shaping properties, which can mechanically damage cells.

They therefore serve as strong candidates as alternatives to biological antifreezes and even to synthetic mimics such as PVA.
A brief overview of MD simulations of proline-based polymers, such as hydroxyproline in solution is covered in §1.4.3. Kim *et al* [187] recently studied the effects of tetrapeptides on the growth of the secondary prismatic face of a small I_h crystal at 260 K. They found that the peptides were able to retard the crystallization process but only once they approached the ice/water interface. The peptide containing proline (Gly-Pro-Ala-Gly) was most effective at retarding the ice crystal growth rates by a factor of 2.5–5. They propose that the bulky proline residue prevents the peptide and vicinal water molecules from incorporating into the ice lattice. They also observe that the peptides align in the direction of crystal growth and approach the ice lattice with the C termini 80% of the time. A total of 1920 water molecules were used to model the system, of which 40% was ice. Their work only focused on small peptides, while we studied the longer chains of $PHYP_{19}$, because experiments have shown that longer peptides may be more effective antifreeze agents.

In this chapter, we model the growth and melting of an ice crystal in the presence of a single $PHYP_{19}$ molecule, in order to gain a better understanding of its IRI activities at a molecular level. To the best of our knowledge the study of PHYP at the ice/water interface has not been previously been published elsewhere. This study uses atomistic MD simulations to study the interactions between the polymers and water molecules which make up the dynamic ice/water system. The interaction potentials for the polymers was obtained from the AMBER03 FF [144].
This remainder of the chapter is organized as follows: The first section is a brief forcefield validation to confirm that the AMBER03 FF is suitable for use with the TIP4P/Ice water model. This section characterises the $PHYP_{19}$ polymers in solution and the final section studies the polymers in the ice/water system over a range of eight temperatures. In the last two sections we aim to determine some features which make PHYP IRI active and throughout this chapter, an occasional reference will also be made to previous chapters for comparison to PVA and PEG polymers. Assuming the the two polymers function in a similar fashion, the attributes which PHYP and PVA have in common can be used to guide the design of novel antifreeze polymers.

6.2 Methods

6.2.1 Forcefield parameters

The AMBER03 FF[144] was chosen for the simulations instead of the OPLS-AA FF because the structure of PHYP more closely resembles a protein than an alkyl chain that the OPLS-AA FF was designed for. Although the CHARMM[145] and GROMOS forcefields are also suitable potentials for representing proteins, the AMBER03 forcefield was chosen because it is a good forcefield to represent hydroxyproline. The AMBER FF has also often been used to evaluate the properties of proline based molecules such as hydroxyproline, largely in order to determine its role in the rigidity and structure of collagen helices.[169,171] The validation of these studies showed that the AMBER worked well.

Simulations of polymers in solution

The $PHYP_{19}$ oligomer was built into a PPII helical structure using the Avogadro[317] molecule editor package. The backbone dihedral angles were set to ϕ= 75° and ψ=145°, which is characteristic of this type of left-handed helix.[171] As with the PVA and PEG polymers in §4.2.2, the polymers were placed in a cubic box with PBC conditions and randomly solvated with 33,207 TIP4P/Ice water molecules. Then the system was subjected to a 20,000 step energy minimisation using the steepest descent algorithm and resulted in the new box dimensions of 9.1×10.3×10.8 nm.
The resulting structure was used as a starting point for three repeat NPT simulations at room temperature (298.15 K). The Nosé-Hoover thermostat[209,234] was was used to maintain the temperature and the pressure was kept at 1 bar using the Parinello-Rahman barostat[210] alongside a 2 ps coupling constant. As with the previous polymer studies, all the intermolecular interactions were turned off at 1 nm. This was achieved using a cut-off for short range LJ and Coulombic interactions, whilst long range electrostatic interactions were evaluated using the PME protocol[197,198]. The width of the mesh used for the Fourier part of the electrostatic interaction was 0.16 nm and a cubic interpolation was applied. LINCS constraints[212] were applied to all bonds involving hydrogen. A full 70 ns trajectory was obtained and the convergence of the systems were monitored using RMSD calculations, as is custom for the simulation of proteins in solution (Fig.6.2b).
Once again, the final structure from this simulation served as the starting point for the ice growth and melting simulations in the presence of the polymers. The set-up for this has already been discussed elsewhere (§ 5.2), however two things were different. Firstly the system size of the ice simulations had the dimensions

of 5.8×6.2×16.7 nm. Secondly, the simulations were conducted at a range of 9 temperatures: 300 K, 290 K, 280 K, 275 K, 272 K, 270 K, 268 K, 260 K and 250 K instead of ten. Everything else remained the same. The polymers were placed close to the QLL region of an ice crystal which was sandwiched between two liquid layers. In this study the prismatic planes of the ice lattice were in contact with the water once again and consisted of 12,363 free water molecules and 6,144 water molecules were used for the ice

Initial configuration and equilibration

The structure of the $PHYP_{19}$ oligomer is shown in Fig. 6.1 and the details of the atom type assignments used in the GROMACS package[232,233] are described in Table 6.1. Further details can be found in Ref. 169.

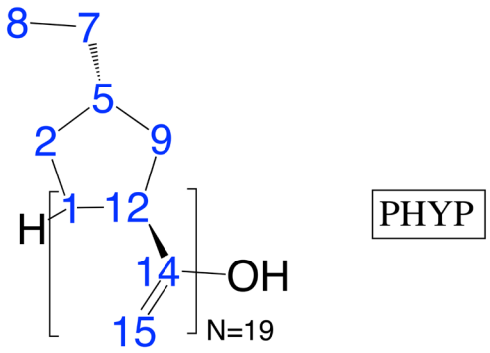

Figure 6.1: Numbering for atom type assignments of the repeat monomers used for the $PHYP_{19}$ polymers.

Label	Atom	Charge	Label	Atom	Charge
1	N	-0.2548	9	CB	0.0203
2	CD2	0.0595	10	HB1	0.0426
3	HD21	0.07	11	HB2	0.0426
4	HD22	0.07	12	CA	0.0047
5	CG	0.04	13	HA	0.077
6	HG	0.0416	14	C	0.5896
7	OD1	-0.6134	15	O	-0.5748
8	HD1	0.3851			

Table 6.1: Atom type assignment of the repeat monomers used for $PHYP_{19}$ in the AMBER03 forcefield. The labels correspond to atoms in Fig. 6.1.

6.3 Results

6.3.1 Poly(hydroxyproline) in solution

Stability and secondary structure

The R_g and the root mean square deviation (RMSD) of the polymer backbone was calculated relative to the starting structure and the results are shown in Fig. 6.2. The profiles of each repeat indicates that each of the repeats rapidly reach a plateau in less than 10 ns, and the results remain stable over a 70 ns trajectory at room temperature. The RMSD stabilises at 0.28±0.01 nm with relatively small fluctuations, and similarly the R_g of the polymers indicate that the polymers remain roughly the same size (1.53±0.00 nm) throughout the simulation.

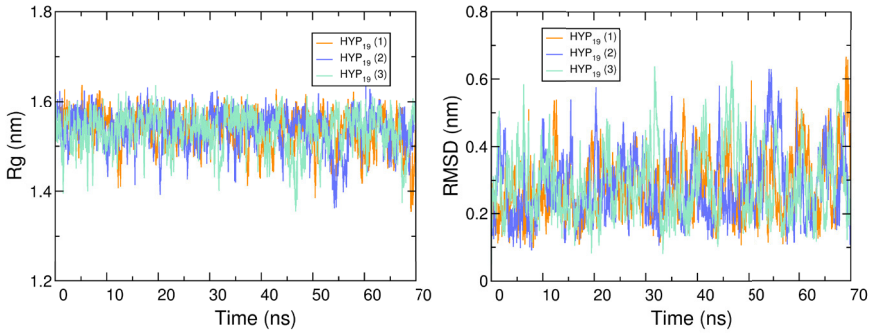

(a) (b)

Figure 6.2: The average (a) R_g and (b) RMSD of the $PHYP_{19}$ backbone at 298 K. The RMSD was calculated using the least squared fit to the polymer backbone and each repeat is shown. Both plots are are stable and provide evidence that proper equilibration has taken place.

Fig. 6.3 shows the distribution of the main chain dihedral angles of the $PHYP_{19}$ polymers. It is clear from the Ramachandran plots, that each of the three polymers achieve and also maintain the expected ϕ=-75° and ψ=145° dihedral angles that are associated with the PHYP polymers[171]. This ability to reproduce the experimental properties of the polypeptide once again reinforces the reliability of the results which are arise from mixing the AMBER03 and the TIP4P/Ice forcefields.

Flexibility

The flexibility of the polymer was assessed by calculating the RMSF over time. Calculations were performed using the starting frame as a reference structure and the results are shown in Fig. 6.4. The analysis was performed on the polymer backbone and whole chains. In each plot the time evolution of the RMSF indicated that significant fluctuations were typically found at the termini and at the centre of the polymer backbone. The greatest of these fluctuations appear at the termini of the polymers.

Aside from these regions, distinct fluctuations appear symmetrically in three parts of the polymers. Between atoms 20–34 the backbone exhibits higher flexibility with ∼0.3 nm while the atoms on either side, atoms 9–17 and 37–45 are much more rigid ∼0.1 nm. These key features are present in both plots because the pattern is the same, with or without side chain atoms included. The contours of the RMSF profile

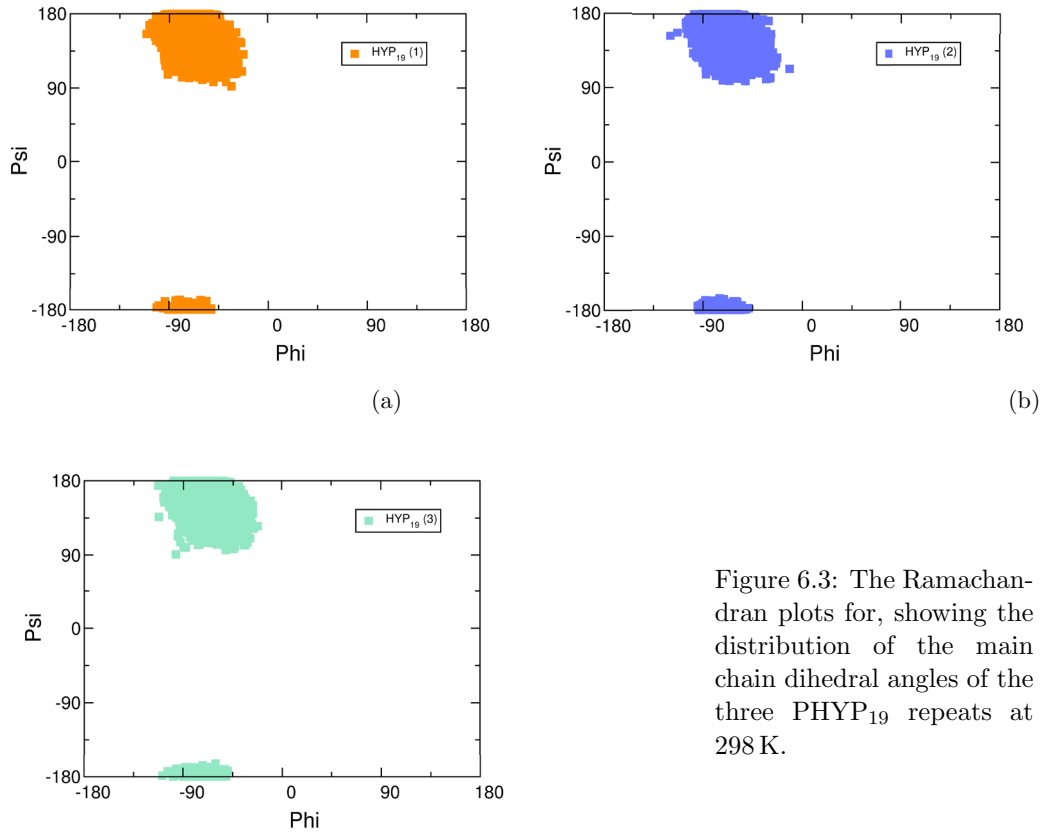

(a) (b)

(c)

Figure 6.3: The Ramachandran plots for, showing the distribution of the main chain dihedral angles of the three $PHYP_{19}$ repeats at 298 K.

suggests that the polymer is slightly bent. Fig. 6.5 shows a snapshots of a single polymer in solution and it confirms these observations.

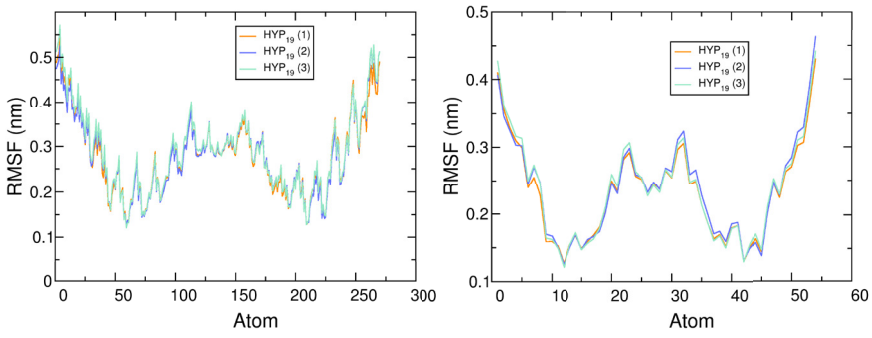

(a) (b)

Figure 6.4: The RMSF, showing the fluctuation of (a) the whole polymer chain, (b) the polymer backbone of the three $PHYP_{19}$ repeats at 298 K.

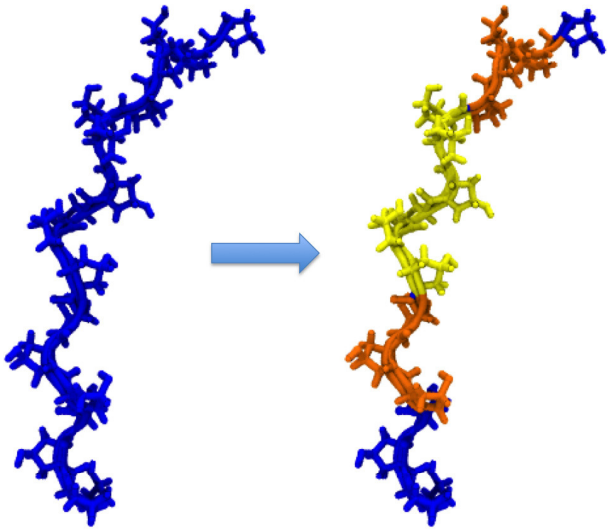

Figure 6.5: A snapshot of a single $PHYP_{19}$ chain in solution (left). The same image is duplicated on the right and regions of the protein are highlighted to identify the flexible and rigid regions in Fig. 6.4. Yellow and orange represents regions of higher (∼0.3 nm) and lower flexibility respectively (∼0.1 nm). The terminal ends are not coloured.

Solvent accessible surface area

The distribution and average TSASA was calculated for the polymers the results are shown in Fig. 6.6a and Fig. 6.6b respectively. The PHYP polymer obtained an average TSASA value of 22.09 nm^2, which is closer in value to those obtained earlier for the larger PVA_{30} (19.34 nm^2) and PEG_{30} (20.92 nm^2) at the same temperature (§ 4.3.4), than to the corresponding chain lengths (12.82 and 13.62 respectively). Of the two aforementioned polymers, the narrow distribution of the TSASA resembles the PVA polymer more closely than the PEG polymers. The ASASA value of 13.54 nm^2, means that the ASASA accounts for approximately 61%, which is greater than the 40% threshold for PVA and still lower than the 90% value for PEG.

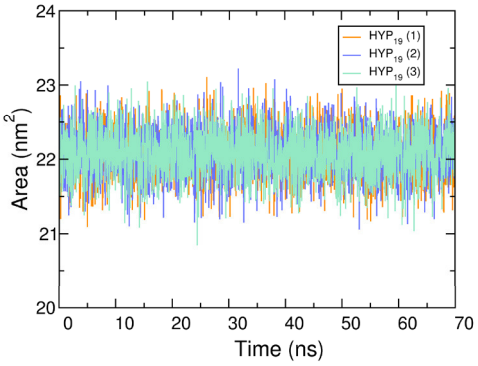

(a)

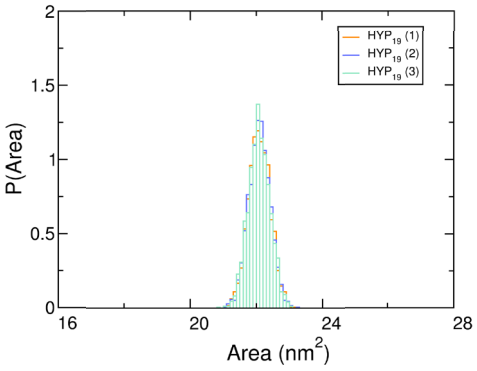

(b)

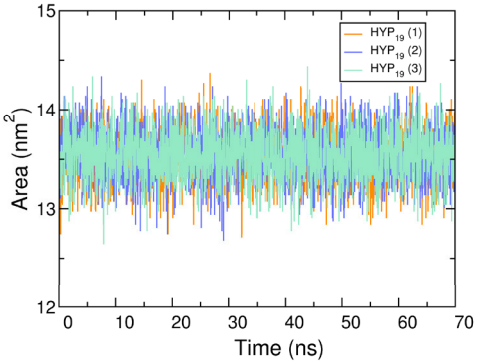

(c)

Figure 6.6: (a) The average TSASA, the (b) calculated distribution of TSASA, and (c) the average ASASA for the three $PHYP_{19}$ repeats at 298 K.

Hydrogen bonds

The importance of H-bonding was also investigated in this study. There are an average of 3.60 (±0.10) intramolecular H-bonds between the polymer residues over the whole trajectory. This value is comparable to the high PVA H-bonding for larger PVA_{30} and PVA_{56} oligomers, which was discussed in the previous chapters. These low numbers of H-bonds for the $PHYP_{19}$ indicates that there are no H-bonds stabilising the helix, which is not suprising. Experiments have shown that PPII helices are significant feature of disordered proteins.[171] The PPII helix is relatively open compared to other helical secondary structures such as the α-helix because the *trans* conformation of the PHYP polymers forces polar atoms further apart.
Compared to bulk water, the number of H-bonds between the water molecules within 3.5 nm of the polymer decreases from 3.76 to 0.92 (±0.01). This shows that the $PHYP_{19}$ polymers significantly disrupt the H-bonding network of the water molecules that surround it in order to maintain a HBN with itself and an average of 109.72 (±0.19) H-bonds with the water molecules.

Polymer-polymer RDFs

The RDFs of O-O, OD1-OD1 and N-N atom pairs was computed and the results are shown in Fig. 6.7a–6.7c respectively. Each distribution obtained pair separation distances which match the 0.45 nm oxygen-oxygen spacing on the prism plane of ice, primarily peaks at ∼0.91 nm and ∼1.80 nm. The RDF profiles for the hydroxyl oxygen atom, OD1 merged after just 0.90 nm due to a greater degree of bond rotation and flexibility available to these atoms. In contrast, both the carboxyl oxygen, O, and the nitrogen atoms, N, are more restricted to movement with the polymer backbone because they are directly incorporated into the proline ring or *via* an amide bond. This is reflected in the RDFs as long range order, because $PHYP_19$ maintains a well-defined, helical secondary structure and this also enforces a regular arrangement of these atoms. The lattice matching theory proposes that if these spacings coincide with oxygen or hydrogen atoms on the ice lattice, then the polymers may be able to H-bond with the ice lattice and inhibit further ice growth if these H-bonds are strong enough. Alternatively the atoms which are projected from the helix backbone could become incorporated into the ice and inhibit further growth.[82]

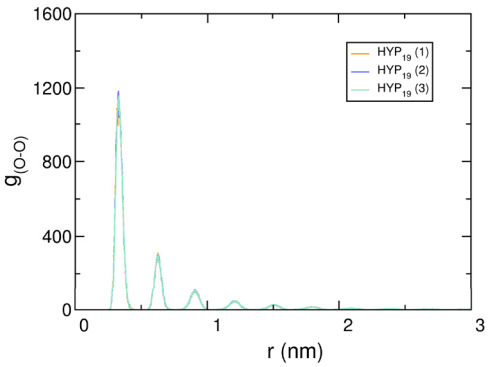

(a)

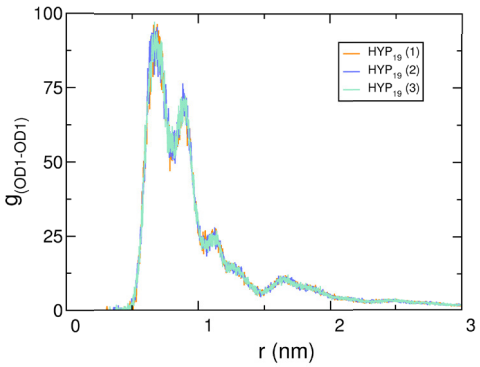

(b)

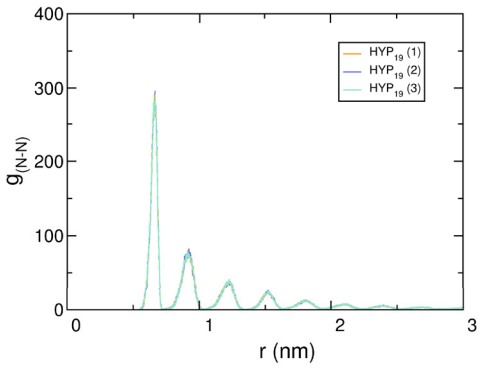

(c)

Figure 6.7: The (a) O-O, (b) OD1-OD1 and (c) N-N RDF functions for $PHYP_{19}$ at 298 K.

Water ordering around the polymer

Aside from direct adsorption unto the ice lattice, it is possible that the structuring of water around the polymer may influence the ability of ice crystals to grow in the presence of $PHYP_{19}$. In order to characterise this effect in solution, the Q_4 order parameter was calculated and Fig. 6.8 illustrates how vicinal water molecules orient around the polymer within a 0.35 nm radius of its hydrophilic groups. The high Q_4 peaks reflect a structured, ice-like arrangement while the low Q_4 peaks indicate an unstructured liquid environment. The formation of a new shoulder at $Q_4 = 0.5$ denotes a 25% decline in tetrahedral arrangement of the liquid water. This suggests that the polymers disrupt the local water-water HBN, which is consistent

with the dramatic decline in H-Bonds reported above, and with the results from recent simulation studies of proline in water.[170] The possible implications for this is that the polymer will disrupt the HBN of ice because ice has a greater HBN than liquid water. The number of water molecules around the whole polymer was counted using the method outlined in § 4.2.4. It is worth noting that $PHYP_{19}$ maintains a relatively large hydration shell, which consists of 904.56 (±5.61) water molecules around the whole polymer even compared to 56-mers of PVA and PEG (∼280).

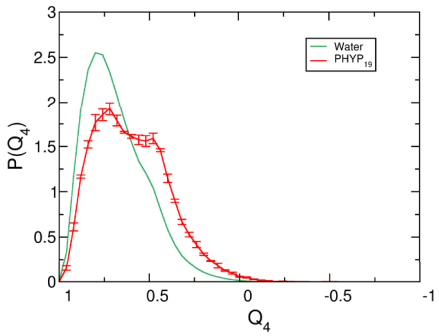

Figure 6.8: The effects of proline on the Q_4 distribution of water molecules within 3.5 nm of the O, OD1 and N atoms in $PHYP_{19}$.

6.3.2 Hydroxyproline at the ice/water interface

Total energy profiles

Prior to the introduction of the $PHYP_{19}$ polymer the TIP4P/Ice water model produced a melting point of 270 K for a large ice/water system (see Fig. 5.2 in § 5). In order to do determine the T_m in the presence of $PHYP_{19}$ we also employed the direct coexistence protocol and monitored the total energy of the system over time. The results are shown in Fig. 6.9. $PHYP_{19}$ reproduces the same T_m of 270 K because the total energy profile remains stable without an overall upward or downward drift.
Fig. 6.9d shows that the total energy profiles of the simulations conducted at 268 K have plateaus which last ∼ 60–150 ns. These features are absent in pure water growth studies and this suggests that the presence of the $PHYP_{19}$ temporarily pauses the growth of the ice crystal for extended periods of time, just like with PVA. As a result the polymers cause fewer simulations to completely freeze at 268 K within the 300 ns trajectory.

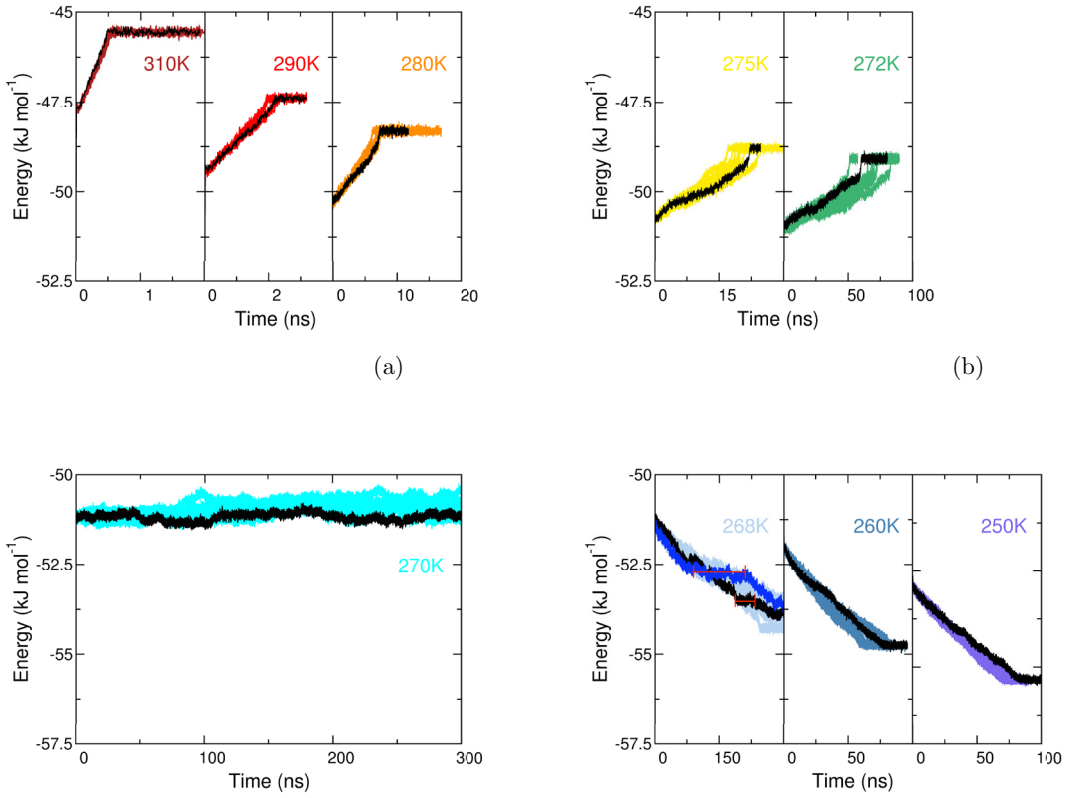

Figure 6.9: The evolution of the total energy per water molecule as a function of temperature for $PHYP_{19}$. Complete melting is observed above 270 K (red, yellow, orange and green) and complete freezing occurs at temperatures below 270 K (blue). The T_m of TIP4P/Ice is identified as 270 K (cyan). Results for all nine repeats are included in each graph and a single representative is highlighted in black for clarity. Red bars mark just two metastable states.

Growth/melt kinetics

Fig. 6.10 illustrates the time taken for each process to come to completion and it shows that $PHYP_{19}$ slows the overall growth of the ice crystal, as expected. At every temperature, in the presence of $PHYP_{19}$ the time required for each melting or freezing process is delayed compared to pure water systems.

With the exception of simulations at 250 K, the delay times are comparable to those reported for both PVA_{19} and $PVA_{10\times2}$ in the previous chapter. These results are in

good agreement to experiments conducted by Gibson *et al* [52] and Knight *et al* [48]. To the best of our knowledge, Gibson *et al* were the first to publish direct and quantitative comparisons between the IRI activities of PVA and PHYP polymers. They used the splat assay to assess the mean largest grain size of each polymer and found that the two polymers had comparable activities at dilute concentrations ($<$1mg ml^{-1}) for similar molecular weights. Similarly, Knight *et al* [48] also demonstrated this qualitatively.

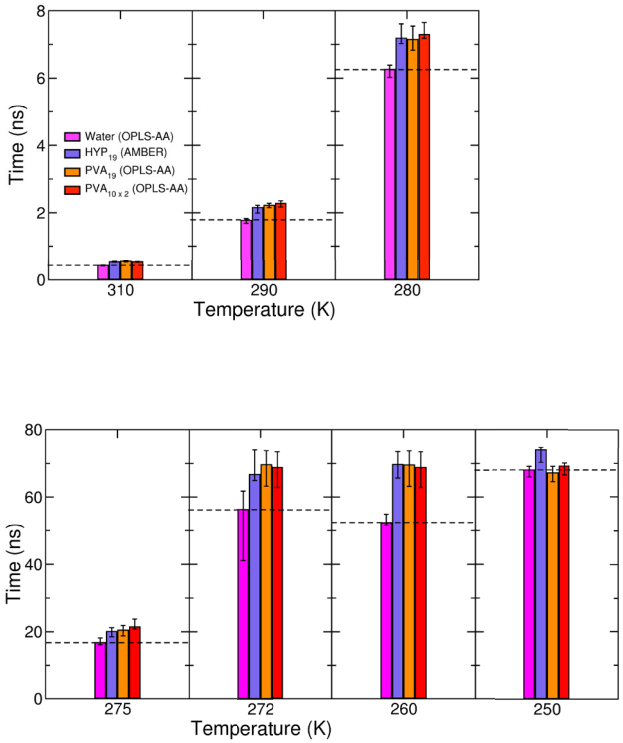

Figure 6.10: The timescales reached in MD simulations for freezing and melting processes in the absence and presence of $PHYP_{19}$. Results from the previous chapter are also reported for PVA, using the OPLS-AA forcefield for comparison. Error bars represented stdev between repeats.

Rate of water addition

At 250 K the polymer takes an additional 6 ns on average compared to pure water, however the system always completely froze and without any metastable states.

This is not the case at 268 K, where only three of nine simulations completely froze. In the instances where freezing was incomplete, the adsorption of the polymer at the ice/water interface induced short-lived metastable states, where the addition of liquid water molecules to the ice crystal was paused. The largest of these lasted between 40–150 ns and these are earmarked by plateaus in the total energy profiles (Fig. 6.9c). In order to determine if $PHYP_{19}$ affects the rates of water addition to the ice lattice, the gradient of the total energy profiles were recorded in Table 6.2. It shows that the rate of water addition is notably slowed at temperatures closer to the T_m. The rate reduced by 96% while at 250 K it only fell by 25%.

System	**Water**			**$PHYP_{19}$**		
Temperature	**250 K**	**260 K**	**268 K**	**250 K**	**260 K**	**268 K**
Gradient	0.04	1.05	0.27	0.03	0.04	0.01
Stdev.	(0.00)	(0.07)	(0.03)	(0.00)	(0.01)	-

Table 6.2: The plateau at the end of the total energy profiles is removed and the rate of addition is taken from the gradient of the remaining data. This table shows the average rate of water addition to the ice crystal during the simulations in $kJ\,mol^{-1}\,ns^{-1}$ for each water molecule. In the $PHYP_{19}$ systems, the value obtained at 268 K correspond to the gradients before and after the metastable periods. If averages are obtained over the repeat simulations, the stdevs. are shown in brackets.

Ice growth around poly(hydroxyproline)

Fig. 6.11 shows the snapshots of the freezing process at 268 K. Visual inspection of the trajectory with the longest metastable state at 268 K reveals that these states correspond to frames where $PHYP_{19}$ becomes attached to the ice lattice. During this period, parts of the polymer detach and reattach while at lower temperatures the polymers become completely overgrown. Unlike PVA_{19} regularly spaced hydrophilic groups on the $PHYP_{19}$ only permit temporary attachment onto the growing ice lattice *via* H-bonds. $PHYP_{19}$ is not incorporated into the ice lattice and the polymer spends most of trajectory in the QLL or front of the ice lattice as it grows. This suggest that the two polymers may function in different ways.

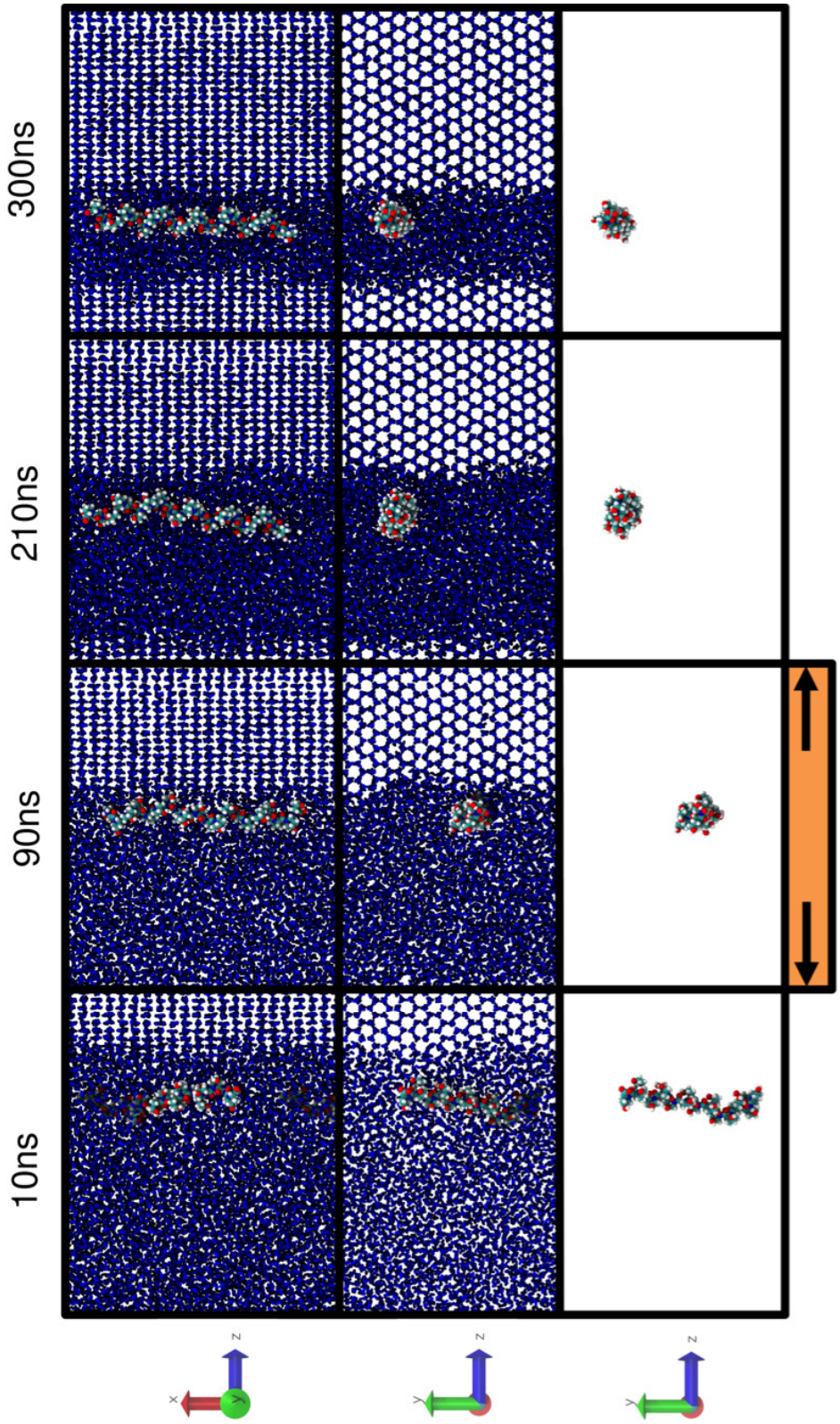

Figure 6.11: Evolution of freezing at 268 K in the presence of $PHYP_{19}$. Each frame is a cross-section and the polymer is shown using a space-fill model. Atom key: N (blue), O (red), C (cyan) and H (white). Water molecules are shown in blue using dynamic bonds and those which fall within 3.5 nm of the hydrophillic groups are coloured orange.

Fig. 6.13 also shows the snapshots of the polymers at the end of freezing simulations for select repeats at each temperature. They confirm that the bulk crystal largely possesses its regular structure and regions around the polymers are disordered. In order to quantify this disordering effect, the Q_4 analysis of the water molecules around the polymer was calculated at the end of the freezing simulation trajectory and in the largest plateau regions at 268 K (Fig. 6.12). The analysis quantitatively confirms that the polymer induces a slight local deformation of the crystal structure due to the steric interference or specific interaction with the surrounding water molecules. This is denoted by the formation of bimodal distribution and the dampening of the high Q_4 peak compared to pure water.

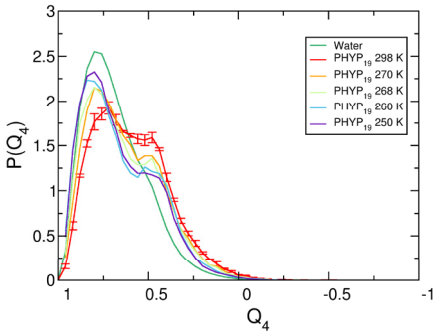

Figure 6.12: The Q_4 analysis of water molecules around the $PHYP_{19}$ oligomer in the ice/water simulations. All distribution were calculated over last 2 ns of the simulations. Results for pure water and $PHYP_{19}$ in solution are also included.

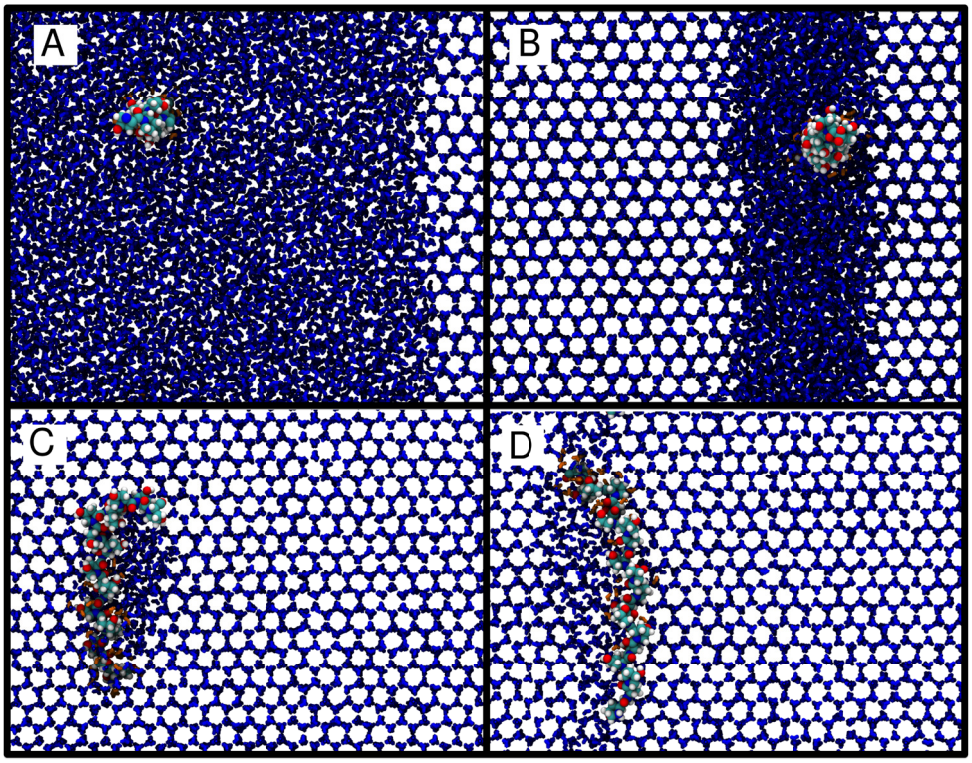

Figure 6.13: Snapshots of water molecules disordered around the polymer at the end of the simulations at A. 270 K, B. 268 K, C. 260 K and D. 250 K. Same key as in Fig 6.11.

In order to understand what interactions are responsible for the slowed rate of water addition to the ice lattice at 270–250 K, a H-bond analysis was conducted between the polymer and the water molecules, and the SASA was calculated for the polymers. The results are shown in Fig. 6.14–6.15 respectively. In agreement with the Q_4, analysis, the polymers increasingly H-bond with the water as they become attached to or incorporated into the ice lattice at greater undercoolings, and disrupt the extensive HBN of the growing ice lattice. This process has the greatest effects at 250 K and 260 K where the polymer is overgrown and the water-water HBN is typically at its greatest. The TSASA did not change drastically from 22.09 nm reported in the solution at 298 K (Fig. 6.6). A snapshot of the polymer is shown at the end of the solution studies at 298 K and the SASA is coloured according to ASASA and PSASA (Fig. 6.16). It is clear from Fig. 6.16 that $PHYP_{19}$ is not facially amphiphilic in solution, but rather the polar groups are regularly distributed across

the polymer backbone. This does not change in the ice/water interface because the regular arrangement, encourages the groups to complement the regularly spaced ice lattice, as demonstrated in Fig. 6.11.

IHE studies of overgrown AF(G)Ps reveal that the proteins become incorporated and pinned onto the ice lattice at certain planes. For instance, the shorthorn sculpin and the wfAFPs both become pinned at the (201) face of ice.[148,318] Variants of the adsorption inhibition model have been proposed such as the step-pinning model[53] and the mattress model[76,77].[78] These suggests that the TH activity AF(G)Ps are due to the strong, irreversible binding of AFPs onto the ice lattice which results in the local curvature of ice/water interface. At 260 K and 250 K, the expected radius of this curvature is 3.06 nm and 1.53 nm respectively (See §5.3.5 and Eq. 5.1). At 260 K this translates to 7 hexagons on the yz-plane and 14 lattice oxygens in the xz-plane. The small amounts of local curvature on either side of the polymer at each of these temperatures suggests that the Gibbs-Thomson effect is negligible and agrees with the experimental observation that $PHYP_{19}$ is only IRI active and not TH active.[48,52,316] Take for instance, the snapshot at 90 ns for 268 K simulations.

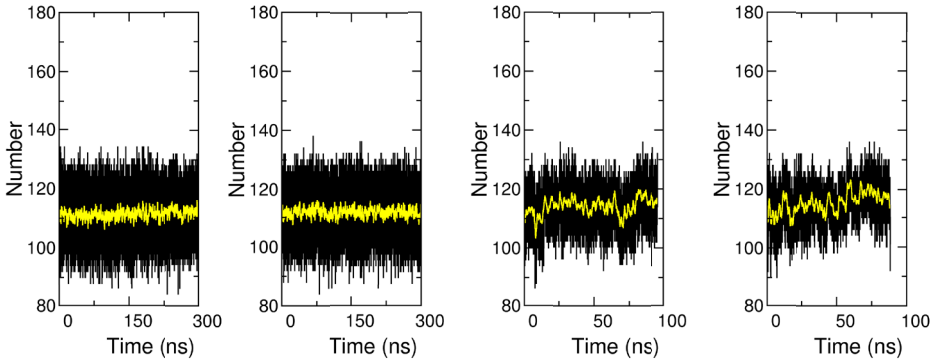

Figure 6.14: The number of polymer-solvent H-bonds at (a) 270 K, (b) 268 K, (c) 260 K, and (d) 250 K for $PHYP_{19}$ a single repeat. Running averages are shown in yellow for clarity.

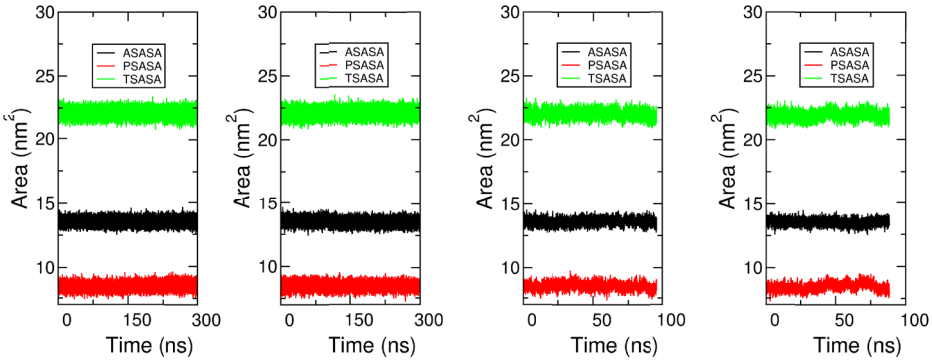

Figure 6.15: The SASA for $PHYP_{19}$ at (a) 270 K, (b) 268 K, (c) 260 K, and (d) 250 K for $PHYP_{19}$ a single repeat.

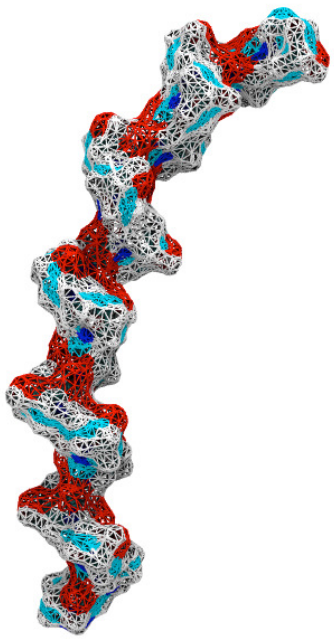

Figure 6.16: A snapshot of the SASA for the $PHYP_{19}$ at 298 K in solution. White regions are ASASA and other regions are part of the PSASA.

In order to understand if the flexibility of the polymers or their secondary structures are altered during the course of the freezing simulations, the RMSF of the protein and its distribution of dihedral angles were also calculated. The results for RMSF calculation are shown in Fig. 6.17a. The RMSF plot at 298 K indicates that the polymer is allowed to bend at the centre, and the chain structure consists of alternating rigid and semi-flexible segments (Fig. 6.4). At the ice/water interface the flexibility of the polymer is dampened compared to these solution studies, particularly at 250 K where these feature are lost. Some possible implications for this are that the polymer is less likely modify its hydration shell at said temperatures, while the bend at the centre of the helix is gradually regained at warmer temperatures.[116] Similar bends have previously been reported for helical AFPs[145,150,154,308,310], IRI active AFP analogues[116,166,307,309] and polyols[314] in simulation studies.

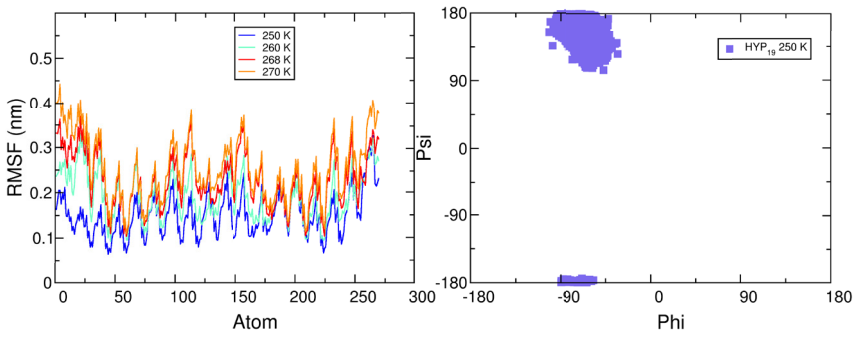

(a) (b)

Figure 6.17: (a) The RMSF of $PHYP_{19}$ at 250–270 K for a single repeat. (b) The Ramachandran plot of $PHYP_{19}$ at 250 K for a single repeat.

Ananthanarayanan *et al* [319] investigated the structural integrity of AFPs as a function of temperature using Circular Dichroism (CD). They found that AFPs (Type 1 and Type 4), which rely heavily on a helical secondary structure for their antifreeze activity remained more stable at lower temperatures close to the T_m than at room temperature. This is not normally the case for most proteins however the PPII helical structure of $PHYP_{19}$ was also retained throughout the simulations between 270–250 K. Fig. 6.17b shows the result for a simulation at 250 K.

6.4 Discussion

6.4.1 The solution properties of $PHYP_{19}$

A single $PHYP_{19}$ chain was studied in liquid water at room temperature. The secondary structure of $PHYP_{19}$ was conserved using the AMBER03 bimolecular forcefield and the TIP4P/Ice water model to model the system. The structure of the polymer is comparably more solvent exposed than the corresponding PVA_{19} and PEG_{19} oligomers in solution and has larger proportion of PSASA. As a result a large hydration shell is maintained around the $PHYP_{19}$ and a greater number of H-bonds are formed with the solvent.

It is worth noting that the RDFs of hydrophilic atoms in the polymer suggests that $PHYP_{19}$ could function through direct adsorption onto the ice lattice *via* a ice lattice matching mechanism. However the Q_4 analysis revealed that the $PHYP_{19}$ dramatically disrupts the orientation of water molecules at 298 K, which is substantially less structured than the arrangement of water molecules in ice or in the QLL. This suggest that the polymer does not function by structuring water molecules into ice-like arrangement around itself.[149]

6.4.2 Analysis of the mechanism of action for $PHYP_{19}$

Simulations of $PHYP_{19}$ at the ice/water interface have shown that the polymers work by slowing the rate of water addition to the growing ice lattice and that they are capable of pausing the growth of the ice crystal. Combined, this produces the slowed growth that can be translated into reduced ice recrystallization as seen in experiments.[3]

Snapshots at the end of the freezing simulations and Q_4 analysis of water molecules around $PHYP_{19}$ confirm that the polymers produce a thin amorphous layer around itself during the freezing process. This process slows the rate of water addition to the ice crystal, and this amorphous layer may be the consequence of having a large hydration shell, TSASA and percentage PSASA. In fact, experiments have previously demonstrated that the IRI activity of simple carbohydrates, AF(G)Ps and their mimics can be linked to the size of their hydration shell.[3,6,73,104,305,320] Largely because they preoccupy the surrounding water molecules from contributing to the QLL or the growing ice crystal.

The results from this study suggest that $PHYP_{19}$ does not function *via* a pre-water-ordering process[148] such as the anchored clathrate mechanism proposed by Garnham *et al* [149]. Although the RDF analyses at 298 K and simulations at 268 K demonstrated that $PHYP_{19}$ share some surface complementarity with ice, the poly-

mer only temporarily H-bonds with the ice lattice. Unlike PVA_{19}, they do not become incorporated into the ice lattice as suggested by Knight *et al* [4]. The presence of proline rings impedes this process, as well as the addition of nearby water molecules. Similar observations have also been made for the smaller proline-based peptides, while those without proline were more readily incorporated into the ice crystal lattice.[187] The fact that PVA does not substantially disrupt the HBN of liquid water in solution suggests that the two polymers may function in very different ways, where H-bonding to the ice lattice with complementary fit are important to both mechanisms.

6.5 Conclusion

Poly-l-hydroxyproline (PHYP) is a synthetic polymer, which is IRI active at dilute concentrations ($<1 \mathrm{mg\,ml^{-1}}$). In order to better understand the molecular mechanism behind the polymer, we conducted simulations of the polymer at the ice/water interface using the TIP4P/Ice and the AMBER03 FF.

The AMBER03 FF was chosen because it designed for use with proteins and so this forcefield served as a suitable choice for the simulation study. Extensive tests were first performed in order to determine the effects of mixing the TIP4P/Ice water model with the AMBER03 FF, and the effects of cut-offs, temperature and small additives were monitored. We have successfully shown that the TIP4P/Ice water model can be used to estimate the interaction between water molecules, in the presence of additives like salts, and reproduce the phase diagram of water. Preliminary simulation of $PHYP_{19}$ were used to characterise the polymer in solution at 298 K. These studies correctly predicted a disordering effect of the polymer at the ice/water interface during the growth of ice crystals at 250–268 K. On the basis of these simulations we predict that the $PHYP_{19}$ does not function *via* the anchored clathrate mechanism. We propose that they inhibit ice recrystallisation at the QLL/ice interface because they slow the rate of ice growth by disrupting the local arrangement of water molecules and they are able to pause the growth of ice by attaching to the surface of the growing ice crystals. The polymers are not incorporated into the ice lattice and subsequent withdrawal of $PHYP_{19}$ units away from the interface results in the resumption of growth.

To the best of our knowledge this is the first MD simulation study of $PHYP_{19}$ at the ice/water interface, and this work presents a contribution to the understanding of mechanism behind ice growth inhibition in the presence of synthetic AF(G)P mimics.

Chapter 7

Conclusions

It is clear from the solution studies (§4 and 6), as well as the ice/water simulation studies (§ 5 and 6), that polar atoms on the IRI active polymers present a close spatial match to the oxygen atoms on the prismatic plane of I_h, while PEG does not. This suggests that H-bonding and lattice matching plays an important role in the IRI mechanism at a molecular level.

In Chapters 5 and 6, we present results for the retardation of ice crystal growth by synthetic AF(G)P mimics at the ice/water interface. Our study helps to shed some light on the molecular mechanisms of two structurally different polymers, which perform similarly [48,52] but do not have the same mechanism of action. At 268 K, and even in room temperature, PHYP disrupts the HBN of vicinal ice-like water molecules, while the PVA partially assimilates into the growing ice lattice or liquid environment. These differences in antifreeze action are not particularly surprising considering the major structural differences between the two polymers.

The magnitude of crystal growth retardation increased with IRI activity, however it is worth noting that all polymers induced slowed growth of the ice crystals compared to pure water systems. The reasons for this is that the polymers sterically obstruct the ice/water interface as it advances towards the polymers. The polymers also impede the incorporation of water molecules into the ice crystal, effectively slowing the rate of water addition. [187]

The interaction of polar groups on the polymers with the ice lattice temporarily paused the ice crystal growth, described as a metastable period. It is clear that the immobilization of the IRI active and inactive polymers at the ice/water interface is therefore required for kinetic inhibition of crystal growth. There is a considerable variation in the frequency of immobilizaton and duration of metastable states between IRI active and inactive polymers. The frequency and duration of

these metastable states was clearly greater for the IRI active polymers, particularly for systems with a greater number of hydroxyl groups. We speculate that IRI active polymers like PVA and PHYP, which have at least one H-bond acceptor and donor atom, are able to form a large number H-bonds with the water molecule and so retain their positions, interacting with the ice lattice for longer, while PEG cannot. Due to the absence of bulky groups such the proline ring in PHYP, PVA was able to adsorb long enough to incorporate its hydroxyl groups into vacant lattice sites on the ice crystal, while PHYP could not.

The ability to identify the complementarity of polymers to the ice lattice in the solution and the orientational order of water molecules around polymers served as useful predictions for the kinetic inhibition of ice growth. However this work has has shown that several, lengthy ice growth simulations in the presence of polymers are better suited to screen for the IRI activities of polymers. Primarily as interactions between the polymers and the ice can be observed directly rather than being inferred from their behaviours in solution. Additionally, the total energy profiles can be used to measure the duration and the number of metastable states induced by a polymer.

It is important to reiterate that the use of solution studies for the screening of antifreeze polymers are still valuable. For instance, the antifreeze active polymers do not necessarily act in the same way in liquid water as they do in ice-like environments. The ability to characterise the properties of the polymers in solution means that we could identify if the polymers recognise the ice from liquid water. The characterisation of polymers in solution can also be used to classify a library of IRI active polymers based on their properties in solution. In the future, this will help us to identify other prerequisite features which can be used for the rational design of an ideal antifreeze polymer.

7.1 Limitations and Future Outlook

In order to aid the future direction of studies, it is important to acknowledge that all research suffers from limitations and a few of these are briefly outlined. First is the issue of using single polymer chains in solution or studying single ice crystals. For instance, the ice/water simulation studies focus on the microscopic growth rates since only a single I_h crystal is modelled with one face exposed to liquid water. In experiments such as splat assays and capillary-based assays, the IRI activity actually reflects an average effect of millions of polymers on a multitude of ice crystals. Each of which have various planes exposed to the surrounding solution.

In order to model systems like this more accurately, other planes of ice must also be studied and mesoscopic investigations of ice crystal growth is required.[187] This is particularly true for the study of IRI, because some polymers and AF(G)Ps have been shown to widen the amorphous regions between the ice crystals known as the grain boundary. Although this revised approach can produce a more statistically accurate representation of IRI activities, a costly trade-off is made with computing billions of interactions.[321,322] To put this into context, we used 84 processors per 48-hr slots with speeds of up to 22 ns/day to model a system of ∼19,000 molecules at 270 K. Assuming that the system becomes frozen after 300 ns, each complete simulation takes approximately 14 days to run using a 4-point water model. Consider that in order to determine a reliable T_m of the modelled system, ten different temperatures were studied with up to ten repeats each.

Secondly, future directions could explore also the importance of ions. To maintain physiological conditions, the IRI assays are typically conducted in the presence of salts. To replicate the real experimental conditions much more closely, the effects of salts in the ice/water simulation studies and solution studies should be investigated in the presence and absence of the IRI active and inactive oligomers. This would produce a more comprehensive understanding of what role the salts play and if the two structures may have an interactions that interplay for the mechanism to become that much more efficient. For example, greater roughening of the prism surface for instance. The interfacial curvature induced by polymers or salts could be measured using an algorithm such as the recently developed CHILL+[323,324], which combines a clustering algorithm and order parameters to identify the largest cluster of ice-like water molecules and water molecules within the interfacial region.

In light of PHYP and PVA's separate functions, a future direction of this study would be to screen a library of antifreeze polymers in order to determine a clear pattern of IRI activities. It is important that a library of different polymer chain lengths and secondary structures are studied, as this will reveal the various ways that different classes of polymers can retard the ice crystal growth.

Bibliography

[1] C. J. Capicciotti, M. Doshi, and R. N. Ben. Ice Recrystallization Inhibitors: From Biological Antifreezes to Small Molecules. In Peter Wilson, editor, *Recent Dev. Study Recryst.*, chapter 7, pages 177–224. InTech, Ottawa, feb 2013.

[2] H. Kawahara. *Characterizations of Functions of Biological Materials Having Controlling-Ability Against Ice Crystal Growth*. InTech, 2013.

[3] M. I. Gibson. Slowing the growth of ice with synthetic macromolecules: beyond antifreeze(glyco) proteins. *Polym. Chem.*, 1(8):1141, 2010.

[4] C. A. Knight, E. Driggers, and A. L. DeVries. Adsorption to ice of fish antifreeze glycopeptides 7 and 8. *Biophys. J.*, 64(1):252–259, jan 1993.

[5] M. Leclere, B. K. Kwok, L. K. Wu, D. S. Allan, and R. N. Ben. C-Linked Antifreeze Glycoprotein (C-AFGP) Analogues as Novel Cryoprotectants. *Bioconjug. Chem.*, 22(9):1804–1810, sep 2011.

[6] A. K. Balcerzak, C. J. Capicciotti, J. G. Briard, and R. N. Ben. Designing ice recrystallization inhibitors: from antifreeze (glyco)proteins to small molecules. *RSC Adv.*, 4(80):42682–42696, sep 2014.

[7] T. Congdon, R. Notman, and M. I. Gibson. Antifreeze (Glyco)protein Mimetic Behavior of Poly(vinyl alcohol): Detailed Structure Ice Recrystallization Inhibition Activity Study. *Biomacromolecules*, 14(5):1578–1586, may 2013.

[8] R. C. Deller, T. Congdon, M. A. Sahid, M. Morgan, M. Vatish, D. A. Mitchell, R. Notman, and M. I. Gibson. Ice recrystallisation inhibition by polyols: comparison of molecular and macromolecular inhibitors and role of hydrophobic units. *Biomater. Sci.*, 1(5):478, 2013.

[9] M. A. Carignano, P. B. Shepson, and I. Szleifer. Ions at the ice/vapor interface. *Chem. Phys. Lett.*, 436(1-3):99–103, feb 2007.

[10] H. Ode, M. Nakashima, S. Kitamura, W. Sugiura, and H. Sato. Molecular dynamics simulation in virus research. *Front. Microbiol.*, 3(JUL):1–9, 2012.

[11] A. K. Soper. The radial distribution functions of water and ice from 220 to 673 K and at pressures up to 400 MPa. *Chem. Phys.*, 258(2-3):121–137, aug 2000.

[12] E. J. W. Wensink, A. C. Hoffmann, P. J. van Maaren, and D. V. D. Spoel. Dynamic properties of water/alcohol mixtures studied by computer simulation. *J. Chem. Phys.*, 119(14):7308, 2003.

[13] W. S. Price, H. Ide, and Y. Arata. Solution Dynamics in Aqueous Monohydric Alcohol Systems. *J. Phys. Chem. A*, 107(24):4784–4789, jun 2003.

[14] A. J. Easteal and L. A. Woolf. Pressure and temperature dependence of tracer diffusion coefficients of methanol, ethanol, acetonitrile, and formamide in water. *J. Phys. Chem.*, 89(7):1066–1069, mar 1985.

[15] K. R. Harris, P. J. Newitt, and Z. J. Derlacki. Alcohol tracer diffusion, density, NMR and FTIR studies of aqueous ethanol and 2,2,2-trifluoroethanol solutions at 25C. *J. Chem. Soc. Faraday Trans.*, 94(14):1963–1970, jan 1998.

[16] I. Juurinen. Water-ethanol mixtures by molecular dynamics and x-ray Compton scattering, oct 2009.

[17] R. Perry, D. Green, and J. Maloney. *Perry's Chemical Engineers' Handbook*. Number 7th. Mcgraw-hil edition, 1997.

[18] E. Washburn. *International Critical Tables of Numerical Data, Physics, Chemistry and Technology*. New York, 1926.

[19] V. C. Weiss, M. Rullich, C. Köhler, and T. Frauenheim. Kinetic aspects of the thermostatted growth of ice from supercooled water in simulations. *J. Chem. Phys.*, 135(3):034701, jul 2011.

[20] NHS. NHS Organ Donation and Transplantation Activity Data: United Kingdom, 2015.

[21] R. C. Deller, M. Vatish, D. A. Mitchell, and M. I. Gibson. Synthetic polymers enable non-vitreous cellular cryopreservation by reducing ice crystal growth during thawing. *Nat. Commun.*, 5:3244, jan 2014.

[22] C. A. Knight, J. Hallett, and A. L. DeVries. Solute effects on ice recrystallization: An assessment technique. *Cryobiology*, 25(1):55–60, feb 1988.

[23] D R Lide. CRC Handbook of Chemistry and Physics, 1999.

[24] P. G. Debenedetti. *Metastable Liquids: Concepts and Principles*. Princeton University Press, 1996.

[25] N. H. Fletcher. *The Chemical Physics of Ice*. Cambridge University Press, Cambridge, 1970.

[26] O. A. Karim and A. D. J. Haymet. The ice/water interface: A molecular dynamics simulation study. *J. Chem. Phys.*, 89(11):6889, 1988.

[27] J. J. DeYoreo and P. G Vekilov. Principles of Crystal Nucleation and Growth. *Rev. Mineral. Geochemistry*, 54(1):57–93, jan 2003.

[28] C. N. Nanev. *Theory of Nucleation*. Elsevier, 2015.

[29] H. R. Pruppacher and J. D. Klett. *Microphysics of Clouds and Precipitation*, volume 18 of *Atmospheric and Oceanographic Sciences Library*. Springer Netherlands, Dordrecht, 2010.

[30] T. Inada, T. Koyama, F. Goto, and T. Seto. Inactivation of ice nucleating activity of silver iodide by antifreeze proteins and synthetic polymers. *J. Phys. Chem. B*, 116(18):5364–5371, may 2012.

[31] M. J. Shultz, P. J. Bisson, and A. Brumberg. Best Face Forward: Crystal-Face Competition at the IceWater Interface. *J. Phys. Chem. B*, 118(28):7972–7980, 2014.

[32] B. A. Garetz, J. Matic, and A. S. Myerson. Polarization Switching of Crystal Structure in the Nonphotochemical Light-Induced Nucleation of Supersaturated Aqueous Glycine Solutions. *Phys. Rev. Lett.*, 89(17):175501, oct 2002.

[33] T. Gonda and T. Yamazaki. Morphology of ice droxtals grown from supercooled water droplets. *J. Cryst. Growth*, 45:66–69, dec 1978.

[34] A. A. Chernov. *Modern Crystallography III*, volume 36 of *Springer Series in Solid-State Sciences*. Springer Berlin Heidelberg, Berlin, Heidelberg, 1984.

[35] A. S. Myerson and A. F. Izmailov. Handbook of Crystal Growth. In *Handb. Cryst. growth*, volume 1, chapter Crystal gr, pages 249–306. North-Holland, 1993.

[36] Y. Furukawa and H. Nada. *Anisotropy in microscopic structures of ice-water and ice-vapor interfaces and its relation to growth kinetics*. Elsevier, 1999.

[37] Y. Furukawa, M. Yamamoto, and T. Kuroda. Ellipsometric study of the transition layer on the surface of an ice crystal. *J. Cryst. Growth*, 82(4): 665–677, apr 1987.

[38] H. R. Pruppacher. Interpretation of Experimentally Determined Growth Rates of Ice Crystals in Supercooled Water. *J. Chem. Phys.*, 47(5):1807–1813, 1967.

[39] H. R. Pruppacher. Some relations between the structure of the ice-solution interface and the free growth rate of ice crystals in supercooled aqueous solutions. *J. Colloid Interface Sci.*, 25(2):285–294, oct 1967.

[40] J. Hallett. Experimental Studies of the Crystallization of Supercooled Water. *J. Atmos. Sci.*, 21(6):671–682, nov 1964.

[41] W. B. Hillig and D. Turnbull. Theory of Crystal Growth in Undercooled Pure Liquids. *J. Chem. Phys.*, 24(4):914, oct 1956.

[42] B. Lindinger, R. Mettin, R. Chow, and W. Lauterborn. Ice Crystallization Induced by Optical Breakdown. *Phys. Rev. Lett.*, 99(4):045701, jul 2007.

[43] C. S. Lindenmeyer. Growth Rate of Ice Dendrites in Aqueous Solutions. *J. Chem. Phys.*, 45(8):2807, may 1966.

[44] C. S. Lindenmeyer, G. T. Orrok, K. a. Jackson, and B. Chalmers. Rate of Growth of Ice Crystals in Supercooled Water. *J. Chem. Phys.*, 27(3):822, aug 1957.

[45] S. H. Tirmizi and W. N. Gill. Effect of natural convection on growth velocity and morphology of dendritic ice crystals. *J. Cryst. Growth*, 85(3):488–502, nov 1987.

[46] C. Budke and T. Koop. Ice Recrystallization Inhibition and Molecular Recognition of Ice Faces by Poly(vinyl alcohol). *ChemPhysChem*, 7(12):2601–2606, dec 2006.

[47] S. Ablett, C. J. Clarke, M. J. Izzard, and D. R. Martin. Relationship between ice recrystallisation rates and the glass transition in frozen sugar solutions. *J. Sci. Food. Agr.*, 82(15):1855–1859, dec 2002.

[48] C. A. Knight, D. Wen, and R. A. Laursen. Nonequilibrium antifreeze peptides and the recrystallization of ice. *Cryobiology*, 32(1):23–34, 1995.

[49] B. Sharma and R. Deswal. Antifreeze proteins in plants: an overview with an insight into the detection techniques including nanobiotechnology. *J. Proteins Proteomics*, 5(August):89–107, aug 2014.

[50] C. A. Schneider, W. S. Rasband, and K. W. Eliceiri. NIH Image to ImageJ: 25 years of image analysis. *Nat. Methods*, 9(7):671–675, jun 2012.

[51] D. E. Mitchell, M. Lilliman, S. G. Spain, and M. I. Gibson. Quantitative study on the antifreeze protein mimetic ice growth inhibition properties of poly(ampholytes) derived from vinyl-based polymers. *Biomater. Sci.*, 2(12): 1787–1795, sep 2014.

[52] M. I. Gibson, C. A. Barker, S. G. Spain, L. Albertin, and N. R. Cameron. Inhibition of Ice Crystal Growth by Synthetic Glycopolymers: Implications for the Rational Design of Antifreeze Glycoprotein Mimics. *Biomacromolecules*, 10(2):328–333, feb 2009.

[53] J. a. Raymond and a. L. DeVries. Adsorption inhibition as a mechanism of freezing resistance in polar fishes. *Proc. Natl. Acad. Sci.*, 74(6):2589–2593, jun 1977.

[54] S. O. Yu, A. Brown, A. J. Middleton, M. M. Tomczak, V. K. Walker, and P. L. Davies. Ice restructuring inhibition activities in antifreeze proteins with distinct differences in thermal hysteresis. *Cryobiology*, 61(3):327–334, dec 2010.

[55] T. N. Hansen and J. G. Baust. Differential scanning calorimetric analysis of antifreeze protein activity in the common mealworm, Tenebrio molitor. *Biochim. Biophys. Acta - Protein Struct. Mol. Enzymol.*, 957(2):217–221, nov 1988.

[56] F. Tanaka. *Polymer Physics: Applications to Molecular Association and Thermoreversible Gelation*. Cambridge University Press, 2011.

[57] E. Rossinsky, K. B. Tarmyshov, M. C. Böhm, and F. Müller-Plathe. Properties of Polyvinyl Alcohol Oligomers: A Molecular Dynamics Study. *Macromol. Theory Simulations*, 18(9):545–552, dec 2009.

[58] H. Schiessel. *Biophysics for Beginners: A Journey through the Cell Nucleus*. Pan Stanford Publishing, 2012.

[59] P. Atkins and J. D. Paula. *Atkins's Physical Chemistry, Volume 1.* W. H. Freeman, 8th edition, 2006.

[60] P. L. Davies and C. L. Hew. Biochemistry of fish antifreeze proteins. *FASEB J.*, 4(8):2460–2468, may 1990.

[61] a. L. DeVries and D. E. Wohlschlag. Freezing Resistance in Some Antarctic Fishes. *Science (80-.).*, 163(3871):1073–1075, 1969.

[62] A. L. Devries. Biological antifreeze agents in coldwater fishes. *Comp. Biochem. Physiol. Part A Physiol.*, 73(4):627–640, jan 1982.

[63] J. G. Duman, V. Bennett, T. Sformo, R. Hochstrasser, and B. M. Barnes. Antifreeze proteins in Alaskan insects and spiders. *J. Insect Physiol.*, 50(4): 259–266, 2004.

[64] P. F. Scholander, L. V. D. Dam, J. W. Kanwisher, H. T. Hammel, and M. S. Gordon. Supercooling and osmoregulation in arctic fish. *J. Cell. Comp. Physiol.*, 49(1):5–24, 1957.

[65] J. Barrett. Thermal hysteresis proteins. *Int. J. Biochem. Cell Biol.*, 33(2): 105–117, feb 2001.

[66] W. Gronwald, H. Chao, D. V. Reddy, P. L. Davies, B. D. Sykes, and F. D. Sönnichsen. NMR Characterization of Side Chain Flexibility and Backbone Structure in the Type I Antifreeze Protein at Near Freezing Temperatures . *Biochemistry*, 35(51):16698–16704, 1996.

[67] F. D. Sönnichsen, P. L. Davies, and B. D. Sykes. NMR structural studies on antifreeze proteins. *Biochem. Cell Biol.*, 76(2-3):284–93, 1998.

[68] M. M. Harding, L. G. Ward, and A. D. J. Haymet. Type I 'antifreeze' proteins. Structure-activity studies and mechanisms of ice growth inhibition. *Eur. J. Biochem.*, 264(3):653–665, 1999.

[69] W. C. Hon, M. Griffith, P. Chong, and D. S. C. Yang. Extraction and Isolation of Antifreeze Proteins from Winter Rye (Secale cereale L.) Leaves. *Plant Physiol.*, 104(3):971–980, mar 1994.

[70] L I Jin Yao and M a Ji. Revie w Recent Advances in Research of Antifreeze Proteins. *Zhongguo sheng wu hua xue yu fen zi sheng wu xue bao = Chinese J. Biochem. Mol. Biol.*, 08(2001):717–722, 2005.

[71] a. L. Devries. Glycoproteins as Biological Antifreeze Agents in Antarctic Fishes. *Science (80-.).*, 172(3988):1152–1155, 1971.

[72] M. M. Harding, P. I. Anderberg, and A. D. J. Haymet. 'Antifreeze' glycoproteins from polar fish. *Eur. J. Biochem.*, 270(7):1381–1392, apr 2003.

[73] J. Bang, J. Lee, R. Murugan, S. Lee, H. Do, H. Koh, H.-E. Shim, H.-C. Kim, and H. Kim. Antifreeze Peptides and Glycopeptides, and Their Derivatives: Potential Uses in Biotechnology. *Mar. Drugs*, 11(6):2013–2041, jun 2013.

[74] C. B. Marshall, G. L. Fletcher, and P. L. Davies. Hyperactive antifreeze protein in a fish. *Nature*, 429(6988):153–153, may 2004.

[75] K. A. Sharp. A peek at ice binding by antifreeze proteins. *Proc. Natl. Acad. Sci.*, 108(18):7281–7282, may 2011.

[76] C. A. Knight, A. L. DeVries, and L. D. Oolman. Fish antifreeze protein and the freezing and recrystallization of ice. *Nature*, 308(5956):295–296, jan 1984.

[77] C. A. Knight, C. C. Cheng, and A. L. DeVries. Adsorption of alpha-helical antifreeze peptides on specific ice crystal surface planes. *Biophys. J.*, 59(2): 409–418, feb 1991.

[78] D. G. Hall and A. Lips. Phenomenology and mechanism of antifreeze peptide activity. *Langmuir*, 15(6):1905–1912, mar 1999.

[79] A. L. Devries and Y. Lin. Structure of a peptide antifreeze and mechanism of adsorption to ice. *Biochim. Biophys. Acta - Protein Struct.*, 495(2):388–392, 1977.

[80] C. S. Strom, X. Y. Liu, and Z. Jia. Ice Surface Reconstruction as Antifreeze Protein-Induced Morphological Modification Mechanism. *J. Am. Chem. Soc.*, 127(1):428–440, jan 2005.

[81] H. Xu, S. Perumal, X. Zhao, N. Du, X.-Y. Liu, Z. Jia, and J. R. Lu. Interfacial Adsorption of Antifreeze Proteins: A Neutron Reflection Study. *Biophys. J.*, 94(11):4405–4413, jun 2008.

[82] Z. Jia and P. L. Davies. Antifreeze proteins: an unusual receptorligand interaction. *Trends Biochem. Sci.*, 27(2):101–106, feb 2002.

[83] Y. Celik, R. Drori, L. Graham, and Y.-F. Mok. Freezing and Melting Hysteresis Measurements in Solutions of Hyperactive Antifreeze Protein from an Antarctic Bacteria. In *Phys. Chem. Ice*, pages 403–409. 2012.

[84] C. A. Knight and A. L. Devries. Melting inhibition and superheating of ice by an antifreeze glycopeptide. *Science*, 245(1010):505–507, aug 1989.

[85] Y. Celik, L. A. Graham, Y.-F. Mok, M. Bar, P. L. Davies, and I. Braslavsky. Superheating of ice crystals in antifreeze protein solutions. *Proc. Natl. Acad. Sci. U. S. A.*, 107(12):5423–5428, mar 2010.

[86] Y. Celik, R. Drori, N. Pertaya-Braun, A. Altan, T. Barton, M. Bar-Dolev, A. Groisman, P. L. Davies, and I. Braslavsky. Microfluidic experiments reveal that antifreeze proteins bound to ice crystals suffice to prevent their growth. *Proc. Natl. Acad. Sci.*, 110(4):1309–1314, jan 2013.

[87] R. N. Ben. Antifreeze glycoproteins–preventing the growth of ice. *Chembiochem*, 2(3):161–6, mar 2001.

[88] R. A. Brown, Y. Yeh, T. S. Burcham, and R. E. Feeney. Direct evidence for antifreeze glycoprotein adsorption onto an ice surface. *Biopolymers*, 24(7): 1265–1270, jul 1985.

[89] R. E. Feeney, W. H. Fink, J. Hallet, K. Harrison, D.T. Osuga, J. P. Vesenka, and Y. Yeh. Investigations of the differential affinity of antifreeze glycoprotein for single crystals of ice. *J. Cryst. Growth*, 113(3-4):417–429, sep 1991.

[90] Y. Yeh and R. E. Feeney. Antifreeze Proteins: Structures and Mechanisms of Function. *Chem. Rev.*, 96(2):601–618, mar 1996.

[91] Y. Tachibana, G. L. Fletcher, N. Fujitani, S. Tsuda, K. Monde, and S.-I. Nishimura. Antifreeze Glycoproteins: Elucidation of the Structural Motifs That Are Essential for Antifreeze Activity. *Angew. Chemie Int. Ed.*, 43(7): 856–862, feb 2004.

[92] A. L. Devries, S. K. Komatsu, and R. E. Feeney. Chemical and Physical Properties of Freezing Glycoproteins from Antarctic Fishes Point-depressing. *J. Biol. Chem.*, 245(11):2901–2908, 1970.

[93] N. Du, G. W. Toh, and X. Y. Liu. Bioinspiration. In Xiang Yang Liu, editor, *Bioinspiration*, Biological and Medical Physics, Biomedical Engineering, chapter 2, pages 57–105. Springer New York, New York, NY, 2012.

[94] J. G. Duman and A. L. DeVries. Freezing behavior of aqueous solutions of glycoproteins from the blood of an Antarctic fish. *Cryobiology*, 9(5):469–472, oct 1972.

[95] Y. Lin, J. G. Duman, and A. L. DeVries. Studies on the structure and activity of low molecular weight glycoproteins from an antarctic fish. *Biochem. Biophys. Res. Commun.*, 46(1):87–92, jan 1972.

[96] J. A. Raymond and A. L. DeVries. Freezing behavior of fish blood glycoproteins with antifreeze properties. *Cryobiology*, 9(6):541–547, dec 1972.

[97] P. F. Scholander and J. E. Maggert. Supercooling and ice propagation in blood from arctic fishes. *Cryobiology*, 8(4):371–374, aug 1971.

[98] G. L. Fletcher, C. L. Hew, and P. L. Davies. Antifreeze Proteins Of Teleost Fishes. *Annu. Rev. Physiol.*, 63(1):359–390, mar 2001.

[99] H. Chao, S. R. Hodges, C. M. Kay, B. D. Sykes, C. M. Loewen, P. L. Davies, and F. D. Sönnichsen. A Diminished Role for Hydrogen Bonds in Antifreeze Protein Binding to Ice. *Biochemistry*, 36(48):14652–14660, dec 1997.

[100] J. Baardsnes and P. L. Davies. Contribution of hydrophobic residues to ice binding by fish type III antifreeze protein. *Biochim. Biophys. Acta - Proteins Proteomics*, 1601(1):49–54, nov 2002.

[101] D. Slaughter, G. L. Fletcher, V. S. Ananthanarayanan, and C. L. Hew. Antifreeze proteins from the sea raven, Hemitripterus americanus. Further evidence for diversity among fish polypeptide antifreezes. *J. Biol. Chem.*, 256(4): 2022–6, feb 1981.

[102] H. Kondo, Y. Hanada, H. Sugimoto, T. Hoshino, C. P. Garnham, P. L. Davies, and S. Tsuda. Ice-binding site of snow mold fungus antifreeze protein deviates from structural regularity and high conservation. *Proc. Natl. Acad. Sci.*, 109 (24):9360–9365, jun 2012.

[103] A. D. J. Haymet, L. G. Ward, M. M. Harding, and C. A. Knight. Valine substituted winter flounder 'antifreeze': Preservation of ice growth hysteresis. *FEBS Lett.*, 430(3):301–306, jul 1998.

[104] R. N. Ben, A. A. Eniade, and L. Hauer. Synthesis of a C-linked Antifreeze Glycoprotein (AFGP) Mimic: Probes for Investigating the Mechanism of Action. *Org. Lett.*, 1(11):1759–1762, 1999.

[105] K. B. Storey and J. M. Storey. Biochemical adaption for freezing tolerance in the wood frog,Rana sylvatica. *J. Comp. Physiol. B*, 155(1):29–36, 1984.

[106] C. Polge, A. U. Smith, and A. S. Parkes. Revival of spermatozoa after vitrification and dehydration at low temperatures. *Nature*, 164(4172):666, oct 1949.

[107] J. E. Lovelock and M. W. H. Bishop. Prevention of Freezing Damage to Living Cells by Dimethyl Sulphoxide. *Nature*, 183(4672):1394–1395, may 1959.

[108] K. Matsumura and S.-H. Hyon. Polyampholytes as low toxic efficient cryoprotective agents with antifreeze protein properties. *Biomaterials*, 30(27): 4842–4849, sep 2009.

[109] S. Deville, C. Viazzi, and C. Guizard. Ice-Structuring Mechanism for Zirconium Acetate. *Langmuir*, 28(42):14892–14898, oct 2012.

[110] S. Deville, C. Viazzi, J. Leloup, A. Lasalle, C. Guizard, E. Maire, J. Adrien, and L. Gremillard. Ice Shaping Properties, Similar to That of Antifreeze Proteins, of a Zirconium Acetate Complex. *PLoS One*, 6(10):e26474, jan 2011.

[111] T. Inada and S.-S. Lu. Thermal hysteresis caused by non-equilibrium antifreeze activity of poly(vinyl alcohol). *Chem. Phys. Lett.*, 394(4-6):361–365, aug 2004.

[112] T. Inada and P. R. Modak. Growth control of ice crystals by poly(vinyl alcohol) and antifreeze protein in ice slurries. *Chem. Eng. Sci.*, 61(10):3149–3158, may 2006.

[113] K. V. Ewart, Q. Lin, and C. L. Hew. Structure, function and evolution of antifreeze proteins. *Cell. Mol. Life Sci. C.*, 55(2):271–283, jan 1999.

[114] T. Inada and S.-S. Lu. Inhibition of Recrystallization of Ice Grains by Adsorption of Poly(Vinyl Alcohol) onto Ice Surfaces. *Cryst. Growth Des.*, 3(5): 747–752, sep 2003.

[115] S. G. Spain, M. I. Gibson, and N. R. Cameron. Recent advances in the synthesis of well-defined glycopolymers. *J. Polym. Sci. Part A Polym. Chem.*, 45(11):2059–2072, jun 2007.

[116] R. Y. Tam, C. N. Rowley, I. Petrov, T. Zhang, N. A. Afagh, T. K. Woo, and R. N. Ben. Solution Conformation of C-Linked Antifreeze Glycoprotein Analogues and Modulation of Ice Recrystallization. *J. Am. Chem. Soc.*, 131 (43):15745–15753, nov 2009.

[117] H.-Y. Wang, T. Inada, K. Funakoshi, and S.-S. Lu. Inhibition of nucleation and growth of ice by poly(vinyl alcohol) in vitrification solution. *Cryobiology*, 59(1):83–89, aug 2009.

[118] B. Wowk and G. M. Fahy. Inhibition of bacterial ice nucleation by polyglycerol polymers. *Cryobiology*, 44(1):14–23, feb 2002.

[119] S. Muppalaneni. Polyvinyl Alcohol in Medicine and Pharmacy: A Perspective. *J. Dev. Drugs*, 02(03), jan 2013.

[120] J.-C. Horng. Stereoelectronic effects on polyproline conformation. *Protein Sci.*, 15(1):74–83, jan 2006.

[121] S. K. Brahmachari, M. Bansal, V. S. Ananthanarayanan, and V. Sasisekharan. Structural Investigations on Poly(4-hydroxy-L-proline). 2. Physicochemical Studies. *Macromolecules*, 12(1):23–28, jan 1979.

[122] O. Mizrahy, M. Bar-Dolev, S. Guy, and I. Braslavsky. Inhibition of ice growth and recrystallization by zirconium acetate and zirconium acetate hydroxide. *PLoS One*, 8(3):e59540, mar 2013.

[123] L. Vrbka and P. Jungwirth. Brine Rejection from Freezing Salt Solutions: A Molecular Dynamics Study. *Phys. Rev. Lett.*, 95(14):148501, 2005.

[124] M. A. Carignano, E. Baskaran, P. B. Shepson, and I. Szleifer. Molecular dynamics simulation of ice growth from supercooled pure water and from salt solution. *Ann. Glaciol.*, 44(1):113–117, 2006.

[125] H. Nada and Y. Furukawa. Anisotropic growth kinetics of ice crystals from water studied by molecular dynamics simulation. *J. Cryst. Growth*, 169(3): 587–597, dec 1996.

[126] M. A. Carignano, P. B. Shepson, and I. Szleifer. Molecular dynamics simulations of ice growth from supercooled water. *Mol. Phys.*, 103(21-23):2957–2967, 2005.

[127] J. S. Kim and A. Yethiraj. The effect of salt on the melting of ice: A molecular dynamics simulation study. *J. Chem. Phys.*, 129(12):124504, sep 2008.

[128] D. Henderson, M. Holovko, and A. Trokhymchuk. Ionic Soft Matter: Modern Trends in Theory and Applications. In *Ion. Soft Matter Mod. Trends Theory Appl.*, volume 206 of *NATO Science Series II: Mathematics, Physics and Chemistry*, pages 333–359. Springer Netherlands, Dordrecht, 2005.

[129] E. J. Smith, T. Bryk, and A. D. J. Haymet. Reply to Comment on Molecular dynamics study of solvation of Cl[sup] and Na[sup +] in the ice/water interface' [J. Chem. Phys. 123, 034706 (2005)]. *J. Chem. Phys.*, 126(23):237102, jun 2007.

[130] J. W. Brady. Molecular dynamics simulations of .alpha.-D-glucose in aqueous solution. *J. Am. Chem. Soc.*, 111(14):5155–5165, jul 1989.

[131] W. Damm, A. Frontera, J. Tirado-Rives, and W. L. Jorgensen. OPLS all-atom force field for carbohydrates. *J. Comput. Chem.*, 18(16):1955–1970, dec 1997.

[132] P. Bordat, A. Lerbret, J. P. Demaret, F. Affouard, and M. Descamps. Comparative study of trehalose, sucrose and maltose in water solutions by molecular modelling. *Europhys. Lett.*, 65(1):41–47, jan 2007.

[133] J. H. Crowe, L. M. Crowe, J. F. Carpenter, A. S. Rudolph, C. A. Wistrom, B. J. Spargo, and T. J. Anchordoguy. Interactions of sugars with membranes. *Biochim. Biophys. Acta*, 947(2):367–384, jun 1988.

[134] S. L. Lee, P. G. Debenedetti, and J. R. Errington. A computational study of hydration, solution structure, and dynamics in dilute carbohydrate solutions. *J. Chem. Phys.*, 122(20):204511, may 2005.

[135] C. Branca, S. Magazu, G. Maisano, and P. Migliardo. Anomalous cryoprotective effectiveness of trehalose: Raman scattering evidences. *J. fo Chem. Phys.*, 111(1):281–287, jul 1999.

[136] C. Branca, S. Magazù, G. Maisano, F. Migliardo, P. Migliardo, and G. Romeo. α,α-trehalose/water solutions. 5. Hydration and viscosity in dilute and semidilute disaccharide solutions. *J. Phys. Chem. B*, 105(41):10140–10145, oct 2001.

[137] J. R. Errington and P. G. Debenedetti. Relationship between structural order and the anomalies of liquid water. *Nature*, 409(6818):318–21, 2001.

[138] L. Weng, C. Chen, and W. Li. Calorimetric and molecular simulation study on unfrozen water characteristics in aqueous sugar solutions: implications for biopreservation. *Mol. Simul.*, 41(9):691–698, may 2015.

[139] J. H. Crowe, S. B. Leslie, and L. M. Crowe. Is Vitrification Sufficient to Preserve Liposomes during Freeze-Drying? *Cryobiology*, 31(4):355–366, aug 1994.

[140] A. K. Sum, R. Faller, and J. J. de Pablo. Molecular simulation study of phospholipid bilayers and insights of the interactions with disaccharides. *Biophys. J.*, 85(11):2830–2844, nov 2003.

[141] S. Paul and S. Paul. Molecular Insights into the Role of Aqueous Trehalose Solution on Temperature-Induced Protein Denaturation. *J. Phys. Chem. B*, 119(4):1598–1610, jan 2015.

[142] E. Spiga, L. A. Abriata, F. Piazza, and M. Dal Peraro. Dissecting the Effects of Concentrated Carbohydrate Solutions on Protein Diffusion, Hydration, and Internal Dynamics. *J. Phys. Chem. B*, 118(20):5310–5321, may 2014.

[143] A. Wierzbicki, P. Dalal, T. E. Cheatham, J. E. Knickelbein, A. D. J. Haymet, and J. D. Madura. Antifreeze Proteins at the Ice/Water Interface: Three Calculated Discriminating Properties for Orientation of Type I Proteins. *Biophys. J.*, 93(5):1442–1451, sep 2007.

[144] H. Jorgensen, M. Mori, H. Matsui, M. Kanaoka, H. Yanagi, Y. Yabusaki, and Y. Kikuzono. Molecular dynamics simulation of winter flounder antifreeze protein variants in solution: correlation between side chain spacing and ice lattice. *Protein Eng.*, 6(1):19–27, jan 1993.

[145] S. M. McDonald, J. W. Brady, and P. Clancy. Molecular dynamics simulations of a winter flounder ?antifreeze? polypeptide in aqueous solution. *Biopolymers*, 33(10):1481–1503, oct 1993.

[146] A. Cheng and K. M. Merz. Ice-binding mechanism of winter flounder antifreeze proteins. *Biophys. J.*, 73(6):2851–2873, dec 1997.

[147] M. E. Houston, H. Chao, R. S. Hodges, B. D. Sykes, C. M. Kay, F. D. Sönnichsen, M. C. Loewen, and P. L. Davies. Binding of an oligopeptide to a specific plane of ice. *J. Biol. Chem.*, 273(19):11714–11718, may 1998.

[148] D. R. Nutt and J. C. Smith. Dual Function of the Hydration Layer around an Antifreeze Protein Revealed by Atomistic Molecular Dynamics Simulations. *J. Am. Chem. Soc.*, 130(39):13066–13073, oct 2008.

[149] C. P. Garnham, R. L. Campbell, and P. L. Davies. Anchored clathrate waters bind antifreeze proteins to ice. *Proc. Natl. Acad. Sci.*, 108(18):7363–7367, may 2011.

[150] S. M. Mcdonald, A. White, P. Clancy, and J. W. Brady. Binding of an Antifreeze Polypeptide to an Ice/Water Interface via Computer Simulation. *AIchE J.*, 41(4):959–973, 1995.

[151] P. Dalal, J. E. Knickelbein, A. D. J. Haymet, F. D. Sönnichsen, and D. J. Madura. Hydrogen bond analysis of Type 1 antifreeze protein in water and the ice/water interface. *PhysChemComm*, 4(7):32, jan 2001.

[152] W. L. Jorgensen, J. Chandrasekhar, J. D. Madura, R. W. Impey, and M. L. Klein. Comparison of simple potential functions for simulating liquid water. *J. Chem. Phys.*, 79(2):926, 1983.

[153] J. D. Madura, A. Wierzbicki, J. P. Harrington, R. H. Maughon, J. A. Raymond, and C. S. Sikes. Interactions of the D- and L-Forms of Winter Flounder Antifreeze Peptide with the {201} Planes of Ice. *J. Am. Chem. Soc.*, 116(1): 417–418, jan 1994.

[154] J. D. Madura, K. Baran, and A. Wierzbicki. Molecular recognition and binding of thermal hysteresis proteins to ice. *J. Mol. Recognit.*, 13(2):101–113, 2000.

[155] H. W. Horn, W. C. Swope, J. W. Pitera, J. D. Madura, T. J. Dick, G. L. Hura, and T. Head-Gordon. Development of an improved four-site water model for biomolecular simulations: TIP4P-Ew. *J. Chem. Phys.*, 120(20):9665–78, may 2004.

[156] K. Battle, S. E. Alan, E. R. Wesley, and A. Wierzbicki. Potential of mean force calculation of the free energy of adsorption of Type I winter flounder antifreeze protein on ice. *J. Cryst. Growth*, 312(8):1257–1261, apr 2010.

[157] H. Nada, J. P. V. D. Eerden, and Y. Furukawa. A clear observation of crystal growth of ice from water in a molecular dynamics simulation with a six-site potential model of H2O. *J. Cryst. Growth*, 266(1-3):297–302, may 2004.

[158] H. Nada and Y. Furukawa. Growth Inhibition Mechanism of an IceWater Interface by a Mutant of Winter Flounder Antifreeze Protein: A Molecular Dynamics Study. *J. Phys. Chem. B*, 112(23):7111–7119, jun 2008.

[159] H. Nada and Y. Furukawa. Growth inhibition at the ice prismatic plane induced by a spruce budworm antifreeze protein: a molecular dynamics simulation study. *Phys. Chem. Chem. Phys.*, 13(44):19936, 2011.

[160] H. Nada and Y. Furukawa. Antifreeze proteins: computer simulation studies on the mechanism of ice growth inhibition. *Polym. J.*, 44(7):690–698, mar 2012.

[161] K C Chou. Energy-optimized structure of antifreeze protein and its binding mechanism. *J. Mol. Biol.*, 223(2):509–517, jan 1992.

[162] D. Wen and R.a. Laursen. A model for binding of an antifreeze polypeptide to ice. *Biophys. J.*, 63(6):1659–1662, 1992.

[163] O. A. Karim and A. D. J. Haymet. The ice/water interface. *Chem. Phys. Lett.*, 138(6):531–534, aug 1987.

[164] D. Rozmanov and P. G. Kusalik. Temperature dependence of crystal growth of hexagonal ice (Ih). *Phys. Chem. Chem. Phys.*, 13(34):15501, 2011.

[165] K. Modig, J. Qvist, C. B. Marshall, P. L. Davies, and B. Halle. High water mobility on the ice-binding surface of a hyperactive antifreeze protein. *Phys. Chem. Chem. Phys.*, 12(35):10189, 2010.

[166] G. Todde, C. Whitman, S. Hovmöller, and A. Laaksonen. Induced Ice Melting by the Snow Flea Antifreeze Protein from Molecular Dynamics Simulations. *J. Phys. Chem. B*, 118(47):13527–13534, 2014.

[167] G. Todde, S. Hovmöller, and A. Laaksonen. Influence of Antifreeze Proteins on the Ice/Water Interface. *J. Phys. Chem. B*, page 150210124511005, 2015.

[168] M. J. Kuiper, C. J. Morton, S. E. Abraham, and A. Gray-Weale. The biological function of an insect antifreeze protein simulated by molecular dynamics. *Elife*, 4:1–14, 2015.

[169] S. Park, R. J. Radmer, T. E. Klein, and V. S. Pande. A new set of molecular mechanics parameters for hydroxyproline and its use in molecular dynamics simulations of collagen-like peptides. *J. Comput. Chem.*, 26(15):1612–1616, nov 2005.

[170] D. Yu, M. Hennig, R. A. Mole, J. C. Li, C. Wheeler, T. Strässle, and G. J. Kearley. Proline induced disruption of the structure and dynamics of water. *Phys. Chem. Chem. Phys.*, 15(47):20555, dec 2013.

[171] E. B. Naziga, F. Schweizer, and S. D. Wetmore. Solvent Interactions Stabilize the Polyproline II Conformation of Glycosylated Oligoprolines. *J. Phys. Chem. B*, 117(9):2671–2681, mar 2013.

[172] S. Hezaveh, S. Samanta, G. Milano, and D. Roccatano. Molecular dynamics simulation study of solvent effects on conformation and dynamics of polyethylene oxide and polypropylene oxide chains in water and in common organic solvents. *J. Chem. Phys.*, 136(12):124901, mar 2012.

[173] H. Lee, R. M. Venable, A. D. Mackerell, and R. W. Pastor. Molecular dynamics studies of polyethylene oxide and polyethylene glycol: hydrodynamic radius and shape anisotropy. *Biophys. J.*, 95(4):1590–1599, aug 2008.

[174] S. A. Oelmeier, F. Dismer, and J. Hubbuch. Molecular dynamics simulations on aqueous two-phase systems - Single PEG-molecules in solution. *BMC Biophys.*, 5(1):14, jan 2012.

[175] W. A. Elam. Rational Design of Selective Industrial Performance Chemicals Basedon Molecular Modeling Computations. In Beena Ra, editor, *Mol. Model. Des. Nov. Perform. Chem. Mater.*, volume 87, chapter 2, pages 57–58. Yale Journal of Biology and Medicine, dec 2014.

[176] Y. Tamai, H. Tanaka, and K. Nakanishi. Molecular Dynamics Study of Water in Hydrogels. *Mol. Simul.*, 16(4-6):359–374, sep 1996.

[177] Y. Tamai, H. Tanaka, and K. Nakanishi. Molecular Dynamics Study of PolymerWater Interaction in Hydrogels. 1. Hydrogen-Bond Structure. *Macromolecules*, 29(21):6750–6760, 1996.

[178] Y. Tamai and H. Tanaka. Effects of polymer chains on structure and dynamics of supercooled water in poly(vinyl alcohol). *Phys. Rev. E. Stat. Phys. Plasmas. Fluids. Relat. Interdiscip. Topics*, 59(5 Pt B):5647–54, may 1999.

[179] F. Muller-Plathe and W. F. van Gunsteren. Solvation of poly (vinyl alcohol) in water, ethanol and an equimolar water-ethanol mixture: structure and dynamics studied by molecular dynamics simulation. *Polymer (Guildf).*, 38 (9):2259–2268, 1997.

[180] F. Müller-Plathe. Diffusion of water in swollen poly(vinyl alcohol) membranes studied by molecular dynamics simulation. *J. Memb. Sci.*, 141(2):147–154, apr 1998.

[181] C. Wu. Cooperative behavior of poly(vinyl alcohol) and water as revealed by molecular dynamics simulations. *Polymer (Guildf).*, 51(19):4452–4460, sep 2010.

[182] Q. G. Zhang, Q. L. Liu, Y. Chen, J. Y. Wu, and A. M. Zhu. Microstructure dependent diffusion of waterethanol in swollen poly(vinyl alcohol): A molecular dynamics simulation study. *Chem. Eng. Sci.*, 64(2):334–340, jan 2009.

[183] G. Tesei, G. Paradossi, and E. Chiessi. Poly(vinyl alcohol) Oligomer in Dilute Aqueous Solution: A Comparative Molecular Dynamics Simulation Study. *J. Phys. Chem. B*, 116(33):10008–10019, aug 2012.

[184] J. S. Bermejo and C. M. Ugarte. Influence of water content on structure and mobility of polyvinyl alcohol: A molecular dynamics simulation. *J. Chem. Phys.*, 129(15):154907, oct 2008.

[185] A. Noorjahan and P. Choi. Thermodynamic properties of poly(vinyl alcohol) with different tacticities estimated from molecular dynamics simulation. *Polymer (Guildf).*, 54(16):4212–4219, jun 2013.

[186] F. Corzana, J. H. Busto, M. G. De Luis, A. Fernández-Tejada, F. Rodríguez, J. Jiménez-Barbero, A. Avenoza, and J. M. Peregrina. Dynamics and hydration properties of small antifreeze-like glycopeptides containing non-natural amino acids. *European J. Org. Chem.*, 2010(18):3525–3542, jun 2010.

[187] J. S. Kim, S. Damodaran, and A. Yethiraj. Retardation of ice crystallization by short peptides. *J. Phys. Chem. A*, 113(16):4403–7, apr 2009.

[188] M. Davidovic, C. Mattea, J. Qvist, and B. Halle. Protein cold denaturation as seen from the solvent. *J. Am. Chem. Soc.*, 131(3):1025–1036, jan 2009.

[189] Z. Hu and J. Jiang. Assessment of biomolecular force fields for molecular dynamics simulations in a protein crystal. *J. Comput. Chem.*, 31(2):NA–NA, jan 2009.

[190] A. D. MacKerell, J. Wiorkiewicz-Kuczera, and M. Karplus. An all-atom empirical energy function for the simulation of nucleic acids. *J. Am. Chem. Soc.*, 117(48):11946–11975, dec 1995.

[191] A D MacKerell, N Banavali, and N Foloppe. Development and current status of the CHARMM force field for nucleic acids. *Biopolymers*, 56(4):257–65, jan 2001.

[192] W. D. Cornell, P. Cieplak, C. I. Bayly, I. R. Gould, K. M. Merz, D. M. Ferguson, D. C. Spellmeyer, T. Fox, J. W. Caldwell, and P. A. Kollman. A Second Generation Force Field for the Simulation of Proteins, Nucleic Acids, and Organic Molecules. *J. Am. Chem. Soc.*, 117(19):5179–5197, may 1995.

[193] L. D. Schuler, X. Daura, and W. F. van Gunsteren. An improved GROMOS96 force field for aliphatic hydrocarbons in the condensed phase. *J. Comput. Chem.*, 22(11):1205–1218, 2001.

[194] W. L. Jorgensen and J. Tirado-Rives. The OPLS [optimized potentials for liquid simulations] potential functions for proteins, energy minimizations for crystals of cyclic peptides and crambin. *J. Am. Chem. Soc.*, 110(6):1657–1666, mar 1988.

[195] D. V. D. Spoel, E. Lindahl, B. Hess, A. R. V. Buuren, E. Apol, P. J. Meulenhoff, D. P. Tieleman, A. L. T. M. Sijbers, K. A. Feenstra, R. V. Drunen, and H. J. C. Berendsen. *Gromacs User Manual version 4.5.4.* 2010.

[196] C. Sagui and T. A. Darden. Molecular dynamics simulations of biomolecules: long-range electrostatic effects. *Annu. Rev. Biophys. Biomol. Struct.*, 28:155–79, jan 1999.

[197] T. Darden, D. York, and L. Pedersen. Particle mesh Ewald: An Nlog(N) method for Ewald sums in large systems. *J. Chem. Phys.*, 98(12):10089, jun 1993.

[198] U. Essmann, L. Perera, M. L. Berkowitz, T. Darden, H. Lee, and L. G. Pedersen. A smooth particle mesh Ewald method. *J. Chem. Phys.*, 103(19):8577, nov 1995.

[199] M. W. Mahoney and W. L. Jorgensen. A five-site model for liquid water and the reproduction of the density anomaly by rigid, nonpolarizable potential functions. *J. Chem. Phys.*, 112(20):8910, 2000.

[200] C. Vega, J. L. F. Abascal, M. M. Conde, and J. L. Aragones. What ice can teach us about water interactions: a critical comparison of the performance of different water models. *Faraday Discuss.*, 141:251–276, nov 2009.

[201] P. Mark and L. Nilsson. Structure and Dynamics of the TIP3P, SPC, and SPC/E Water Models at 298K. *J. Phys. Chem. A*, 105(43):9954–9960, 2001.

[202] Oren M. B. and M. Karplus. *A Guide to Biomolecular Simulations*, volume 4 of *Focus on Structural Biology*. Springer-Verlag, Berlin/Heidelberg, 2006.

[203] B. Guillot. A reappraisal of what we have learnt during three decades of computer simulations on water. *J. Mol. Liq.*, 3(101):219–260, 2002.

[204] J. L. F. Abascal, E. Sanz, R. García Fernández, and C. Vega. A potential model for the study of ices and amorphous water: TIP4P/Ice. *J. Chem. Phys.*, 122(23):234511, 2005.

[205] R.W Hockney, S.P Goel, and J.W Eastwood. Quiet high-resolution computer models of a plasma. *J. Comput. Phys.*, 14(2):148–158, 1974.

[206] G. Bussi, D. Donadio, and M. Parrinello. Canonical sampling through velocity rescaling. *J. Chem. Phys.*, 126(1):014101, jan 2007.

[207] H. C. Andersen. Molecular dynamics simulations at constant pressure and/or temperature. *J. Chem. Phys.*, 72(4):2384, jul 1980.

[208] H. J. C. Berendsen, J. P. M. Postma, W. F. van Gunsteren, A. DiNola, and J. R. Haak. Molecular dynamics with coupling to an external bath. *J. Chem. Phys.*, 81(8):3684, 1984.

[209] W. G. Hoover.

[210] M. Parrinello. Polymorphic transitions in single crystals: A new molecular dynamics method. *J. Appl. Phys.*, 52(12):7182, 1981.

[211] J.-P. Ryckaert, G. Ciccotti, and H. J. C. Berendsen. Numerical integration of the cartesian equations of motion of a system with constraints: molecular dynamics of n-alkanes. *J. Comput. Phys.*, 23(3):327–341, mar 1977.

[212] B. Hess, H. Bekker, H. J. C. Berendsen, and J. G. E. M. Fraaije. LINCS: A linear constraint solver for molecular simulations. *J. Comput. Chem.*, 18(12): 1463–1472, sep 1997.

[213] S. Miyamoto and P. A. Kollman. Settle: An analytical version of the SHAKE and RATTLE algorithm for rigid water models. *J. Comput. Chem.*, 13(8): 952–962, oct 1992.

[214] D. V. D. Spoel and E. Lindahl. Brute-Force Molecular Dynamics Simulations of Villin Headpiece: Comparison with NMR Parameters. *J. Phys. Chem. B*, 107(40):11178–11187, oct 2003.

[215] C. Vega, J. L. F. Abascal, E. Sanz, L. G. MacDowell, and C. McBride. Can simple models describe the phase diagram of water? *J. Phys. Condens. Matter*, 17(45):S3283–S3288, 2005.

[216] J. D. Bernal and R. H. Fowler. A Theory of Water and Ionic Solution, with Particular Reference to Hydrogen and Hydroxyl Ions. *J. Chem. Phys.*, 1(8): 515, 1933.

[217] M. M. Conde, C. Vega, and A. Patrykiejew. The thickness of a liquid layer on the free surface of ice as obtained from computer simulation. *J. Chem. Phys.*, 129(1):014702, jul 2008.

[218] H. J. C. Berendsen, J. R. Grigera, and T. P. Straatsma. The Missing Term in Effective Pair Potentials. *J. Phys. Chem.*, 91(24):6269–6271, 1987.

[219] R. García Fernández, J. L. F. Abascal, and C. Vega. The melting point of ice Ih for common water models calculated from direct coexistence of the solid-liquid interface. *J. Chem. Phys.*, 124(14):144506, apr 2006.

[220] J. L. F. Abascal and C. Vega. The melting point of hexagonal ice (Ih) is strongly dependent on the quadrupole of the water models. *Phys. Chem. Chem. Phys.*, 9(22):2775–8, jun 2007.

[221] C. Vega, E. Sanz, and J. L. F. Abascal. The melting temperature of the most common models of water. *J. Chem. Phys.*, 122(11):114507, mar 2005.

[222] Y. Koyama, H. Tanaka, G. Gao, and X. C. Zeng. Melting points and thermal expansivities of proton-disordered hexagonal ice with several model potentials. *J. Chem. Phys.*, 121(16):7926–31, oct 2004.

[223] J. Wang, S. Yoo, J. Bai, J. R. Morris, and X. C. Zeng. Melting temperature of ice Ih calculated from coexisting solid-liquid phases. *J. Chem. Phys.*, 123 (3):036101, 2005.

[224] E. Sanz, C. Vega, J. L. F. Abascal, and L. G. MacDowell. Phase Diagram of Water from Computer Simulation. *Phys. Rev. Lett.*, 92(25):255701, jun 2004.

[225] M. M. Conde and C. Vega. Determining the three-phase coexistence line in methane hydrates using computer simulations. *J. Chem. Phys.*, 133(6):064507, 2010.

[226] H. Nada, J. P. V. D. Eerden, and M. P. J. Jan. An intermolecular potential model for the simulation of ice and water near the melting point: A six-site model of H[sub 2]O. *J. Chem. Phys.*, 118(16):7401, apr 2003.

[227] J. L. Aragones, E. G. Noya, J. L. F. Abascal, and C. Vega. Properties of ices at 0 K: a test of water models. *J. Chem. Phys.*, 127(15):154518, oct 2007.

[228] M. Levitt, M. Hirshberg, R. Sharon, K. E. Laidig, and V. Daggett. Calibration and Testing of a Water Model for Simulation of the Molecular Dynamics of Proteins and Nucleic Acids in Solution. *J. Phys. Chem. B*, 101(25):5051–5061, jun 1997.

[229] W. L. Jorgensen, D. S. Maxwell, and J. Tirado-Rives. Development and Testing of the OPLS All-Atom Force Field on Conformational Energetics and Properties of Organic Liquids. *J. Am. Chem. Soc.*, 7863(15):11225–11236, 1996.

[230] S. W. I. Siu, K. Pluhackova, and R. A. Böckmann. Optimization of the OPLS-AA Force Field for Long Hydrocarbons. *J. Chem. Theory Comput.*, 8(4): 1459–1470, apr 2012.

[231] J. Chandrasekhar, D. C. Spellmeyer, and W. L. Jorgensen. Energy component analysis for dilute aqueous solutions of lithium(1+), sodium(1+), fluoride(1-), and chloride(1-) ions. *J. Am. Chem. Soc.*, 106(4):903–910, feb 1984.

[232] B. Hess, C. Kutzner, D. V. D. Spoel, and E. Lindahl. GROMACS 4 : Algorithms for Highly Efficient, Load-Balanced, and Scalable Molecular Simulation. *J. Chem. Theory Comput.*, 4(3):435–447, 2008.

[233] S. Pronk. Solvation free energy of ethanol. In *Mol. Simul. Methods with Gromacs*, pages 1–25. GROMACS, 2013.

[234] S. Nosé. A molecular dynamics method for simulations in the canonical ensemble. *Mol. Phys.*, 52(2):255–268, aug 2006.

[235] C. H. Bennett. Efficient estimation of free energy differences from Monte Carlo data. *J. Comput. Phys.*, 22(2):245–268, 1976.

[236] R. W. Zwanzig. High-Temperature Equation of State by a Perturbation Method. I. Nonpolar Gases. *J. Chem. Phys.*, 22(8):1420–1426, 1954.

[237] J. G. Kirkwood. Statistical Mechanics of Fluid Mixtures. *J. Chem. Phys.*, 3 (5):300, 1935.

[238] M. R. Shirts and V. S. Pande. Comparison of efficiency and bias of free energies computed by exponential averaging, the Bennett acceptance ratio, and thermodynamic integration. *J. Chem. Phys.*, 122(14):1–16, 2005.

[239] R. Radhakrishnan and B. L. Trout. Nucleation of hexagonal ice (Ih) in liquid water. *J. Am. Chem. Soc.*, 125(25):7743–7, jun 2003.

[240] M. Matsumoto, S. Saito, and I. Ohmine. Molecular dynamics simulation of the ice nucleation and growth process leading to water freezing. *Nature*, 416 (6879):409–13, mar 2002.

[241] A. K. Soper and M. G. Phillips. A new determination of the structure of water at 25C. *Chem. Phys.*, 107(1):47–60, aug 1986.

[242] K. Watanabe and M. L. Klein. Effective pair potentials and the properties of water. *Chem. Phys.*, 131(2-3):157–167, mar 1989.

[243] J. M. M. Cordeiro. Monte Carlo thermodynamic and structural properties of the TIP4P water model: dependence on the computational conditions. *Quim. Nova*, 21(6):698–701, nov 1998.

[244] C.P. Lawrence and J.L. Skinner. Flexible TIP4P model for molecular dynamics simulation of liquid water. *Chem. Phys. Lett.*, 372(5-6):842–847, may 2003.

[245] C. Vega, C. McBride, E. Sanz, and J. L. F. Abascal. Radial distribution functions and densities for the SPC/E, TIP4P and TIP5P models for liquid water and ices Ih, Ic, II, III, IV, V, VI, VII, VIII, IX, XI and XII. *Phys. Chem. Chem. Phys.*, 7(7):1450–1456, 2005.

[246] W. L. Jorgensen and C. Jenson. Temperature dependence of TIP3P, SPC, and TIP4P water from NPT Monte Carlo simulations: Seeking temperatures of maximum density. *J. Comput. Chem.*, 19(10):1179–1186, 1998.

[247] M. P. Allen and D. J. Tildesley. *Computer Simulation of Liquids*. Clarendon Press, 1989.

[248] R. Mills. Self-diffusion in normal and heavy water in the range 1-45.deg. *J. Phys. Chem.*, 77(5):685–688, mar 1973.

[249] W. S. Price, H. Ide, and Y. Arata. Self-Diffusion of Supercooled Water to 238 K Using PGSE NMR Diffusion Measurements. *J. Phys. Chem. A*, 103(4): 448–450, jan 1999.

[250] G. W. Robinson, S. B. Zhu, S. Singh, and M. W. Evans. *Water in biology, chemistry and physics: Experimental Overviews and Computational Methodologies*, volume 9. World Scientific Publishing Co, 1996.

[251] I. C. Yeh and G. Hummer. System-size dependence of diffusion coefficients and viscosities from molecular dynamics simulations with periodic boundary conditions. *J. Phys. Chem. B*, 108(40):15873–15879, 2004.

[252] D. V. Zlenko. Computing the self-diffusion coefficient for TIP4P water. *Biophysics (Oxf).*, 57(2):127–132, 2012.

[253] J. Zielkiewicz. Structural properties of water: Comparison of the SPC, SPCE, TIP4P, and TIP5P models of water. *J. Chem. Phys.*, 123(10):104501, 2005.

[254] H. Xu, H. A. Stern, and B. J. Berne. Can water polarizability be ignored in hydrogen bond kinetics? *J. Phys. Chem. B*, 106(8):2054–2060, 2002.

[255] A. Rastogi, A. K. Ghosh, and S. J. Suresh. Hydrogen bond interactions between water molecules in bulk liquid, near electrode surfaces and around ions. In Juan Carlos Moreno-Pirajan, editor, *Thermodyn. - Phys. Chem. Aqueous Syst.*, chapter 13, pages 1–14. InTech, 2011.

[256] S. Han, P. Kumar, and H. E. Stanley. Hydrogen-bond dynamics of water in a quasi-two-dimensional hydrophobic nanopore slit. *Phys. Rev. E*, 79(4):041202, apr 2009.

[257] A. L. Norbert and J. A. Dean. *Lange's Handbook of Chemistry.* McGraw-Hill, 10th edition, 1973.

[258] D. Bandyopadhyay, S. Mohan, S. K. Ghosh, and N. Choudhury. Correlation of structural order, anomalous density, and hydrogen bonding network of liquid water. *J. Phys. Chem. B*, 117(29):8831–43, jul 2013.

[259] A. K. Soper. Supercooled water: Continuous trends. *Nat. Mater.*, 13(7): 671–673, jun 2014.

[260] C. A. Angell. Supercooled water: Two phases? *Nat. Mater.*, 13(7):673–5, jul 2014.

[261] Y. I. Jhon, K. T. No, and M. S. Jhon. Common Features of Orientational Order at the Temperature of Maximum Density for Various Water Models: Molecular Dynamics Study. *J. Phys. Chem. B*, 111(33):9897–9899, aug 2007.

[262] A. J. Easteal, W. E. Price, and L. A. Woolf. Diaphragm cell for high-temperature diffusion measurements. Tracer Diffusion coefficients for water to 363 K. *J. Chem. Soc. Faraday Trans. 1 Phys. Chem. Condens. Phases*, 85 (5):1091, jan 1989.

[263] G. S. Kell. Effects of Isotopic Composition, Temperature, Pressure, and Dissolved Gases on the Density of Liquid Water *. *J. Phys. Chem. Ref. Data*, 6 (4):1109–1131, 1977.

[264] K. Krynicki, C. D. Green, and D. W. Sawyer. Pressure and temperature dependence of self-diffusion in water. *Faraday Discuss. Chem. Soc.*, 66:199, jan 1978.

[265] K. T. Gillen. Self-diffusion in liquid water to 31C. *J. Chem. Phys.*, 57(12): 5117, sep 1972.

[266] S. H. Lee. Temperature dependence on structure and self-diffusion of water: a molecular dynamics simulation study using SPC/E model. *Bull. Korean Chem. Soc.*, 34(12):3800–3804, 2013.

[267] K D. Sharma, N. Rai, and P. Biswal. *Molecular dynamics study of TIP3P, SPC/E and TIP4P water models at room temperature.* Msc, National Institute of Technology Rourkela, 2013.

[268] S.-B. Zhu and G. W. Robinson. Molecular-dynamics computer simulation of an aqueous NaCl solution: Structure. *J. Chem. Phys.*, 97(6):4336, 1992.

[269] D. H. Powell, A. C. Barnes, J. E. Enderby, G. W. Neilson, and P. S. Salmon. The hydration structure around chloride ions in aqueous solution. *Faraday Discuss. Chem. Soc.*, 85:137, jan 1988.

[270] J. Mähler and I. Persson. A study of the hydration of the alkali metal ions in aqueous solution. *Inorg. Chem.*, 51(1):425–438, 2012.

[271] Y. Marcus. Ionic radii in aqueous solutions. *J. Solution Chem.*, 12(4):271–275, 1983.

[272] A. K. Soper, G. W. Neilson, J. E. Enderby, and R. A. Howe. A neutron diffraction study of hydration effects in aqueous solutions. *J. Phys. C Solid State Phys.*, 10(11):1793–1801, jun 1977.

[273] A. H. Narten. Diffraction pattern and structure of aqueous lithium chloride solutions. *J. Chem. Phys.*, 58(11):5017, aug 1973.

[274] T. Koishi, S. Tamaki, and T. Ebisuzaki. Large scale molecular dynamics simulation of aqueous NaCl solutions. In K Yasuoka M Nakahara, N Matubayashi, M Ueno and K Watanabe, editors, *14th Int. Conf. Prop. Water Steam Kyoto*, pages 212–215, Kyoto, 2004.

[275] A. P. Lyubartsev and A. Laaksonen. Concentration effects in aqueous NaCl solutions. A molecular dynamics simulation. *J. Phys. Chem.*, 100(40):16410–16418, 1996.

[276] M. Patra and M. Karttunen. Systematic comparison of force fields for fi-croscopic fimulations of NaCl in aqueous solutions: diffusion, free energy of hydration, and structural properties. *J. Comput. Chem.*, 25(5):678–689, 2004.

[277] D. H. Powell, G. W. Neilson, and J. E. Enderby. The structure of Cl- in aqueous solution: an experimental determination of g ClH (r) and g ClO (r). *J. Phys. Condens. Matter*, 5(32):5723–5730, aug 1993.

[278] G. W. Neilson and J. E. Enderby. Chapter 7. Neutron and X-ray diffraction studies of concentrated aqueous electrolyte solutions. *Annu. Rep. Prog. Chem., Sect. C Phys. Chem.*, 76(0):185–220, 1979.

[279] S. B. Rempe and L. R. Pratt. The hydration number of Na+ in liquid water. *Fluid Phase Equilib.*, 183-184:121–132, jul 2001.

[280] H. Ohtaki and T. Radnai. Structure and dynamics of hydrated ions. *Chem. Rev.*, 93(3):1157–1204, may 1993.

[281] D. E. Smith and L. X. Dang. Computer simulations of NaCl association in polarizable water. *J. Chem. Phys.*, 100(5):3757, 1994.

[282] R. Mancinelli, A. Botti, F. Bruni, M. A. Ricci, and A. K. Soper. Hydration of sodium, potassium, and chloride ions in solution and the concept of structure maker/breaker. *J. Phys. Chem. B*, 111(48):13570–7, 2007.

[283] J. Brodholt. Molecular dynamics simulations of aqueous NaCl solutions at high pressures and temperatures. *Chem. Geol.*, 151(1-4):11–19, 1998.

[284] J. S. Kim, Z. Wu, A. R. Morrow, A. Yethiraj, and A. Yethiraj. Self-diffusion and viscosity in electrolyte solutions. *J. Phys. Chem. B*, 116(39):12007–12013, 2012.

[285] W. L. Jorgensen. Optimized intermolecular potential functions for liquid alcohols. *J. Phys. Chem.*, 90(7):1276–1284, 1986.

[286] L. Saiz, J. A. Padró, and E. Guardia. Dynamics and hydrogen bonding in liquid ethanol. *Mol. Phys.*, 97(7):897–905, oct 1999.

[287] J. A. Padró, L. Saiz, and E. Guàrdia. Hydrogen bonding in liquid alcohols: a computer simulation study. *J. Mol. Struct.*, 416(1-3):243–248, oct 1997.

[288] A. Coccia, P.L. Indovina, F. Podo, and V. Viti. PMR studies on the structures of water-ethyl alcohol mixtures. *Chem. Phys.*, 7(1):30–40, jan 1975.

[289] K. Mizuno, Y. Miyashita, Y. Shindo, and H. Ogawa. NMR and FT-IR Studies of Hydrogen Bonds in Ethanol-Water Mixtures. *J. Phys. Chem.*, 99(10):3225–3228, mar 1995.

[290] S. Burikov, T. Dolenko, S. Patsaeva, Y. Starokurov, and V. Yuzhakov. Raman and IR spectroscopy research on hydrogen bonding in water-ethanol systems. *Mol. Phys.*, 108(18):2427–2436, sep 2010.

[291] I. Bakó, T. Megyes, S. Bálint, T. Grósz, and V. Chihaia. Water-methanol mixtures: topology of hydrogen bonded network. *Phys. Chem. Chem. Phys.*, 10(32):5004–11, aug 2008.

[292] N. Zhang, W. Li, C. Chen, J. Zuo, and L. Weng. Molecular Dynamics Investigation of the Effects of Concentration on Hydrogen Bonding in Aqueous Solutions of Methanol, Ethylene Glycol and Glycerol. *Bull. Korean Chem. Soc.*, 34(9):2711–2719, 2013.

[293] P. F. B. Gonçalves and H. Stassen. Calculation of the free energy of solvation from molecular dynamics simulations. *Pure Appl. Chem.*, 76(1), jan 2004.

[294] Y. Yonetani. Liquid water simulation: a critical examination of cutoff length. *J. Chem. Phys.*, 124(20):204501, may 2006.

[295] D. V. D. Spoel, P. J. V. Maaren, and H. J. C. Berendsen. A systematic study of water models for molecular simulation: Derivation of water models optimized for use with a reaction field. *J. Chem. Phys.*, 108(24):10220–10230, 1998.

[296] Y. Yonetani. A severe artifact in simulation of liquid water using a long cut-off length: Appearance of a strange layer structure. *Chem. Phys. Lett.*, 406(1-3): 49–53, apr 2005.

[297] P. Auffinger and D. L. Beveridge. A simple test for evaluating the truncation effects in simulations of systems involving charged groups. *Chem. Phys. Lett.*, 234(4-6):413–415, mar 1995.

[298] M. Lsal, J. Kolafa, and I. Nezbeda. An examination of the five-site potential (TIP5P) for water. *J. Chem. Phys.*, 117(19):8892, oct 2002.

[299] T. Bryk and A. D. J. Haymet. The Ice/Water Interface: DensityTemperature Phase Diagram for the SPC/E Model of Liquid Water. *Mol. Simul.*, 30(2-3): 131–135, 2004.

[300] N. Samadashvili, B. Reischl, T. Hynninen, T. Ala-Nissilä, and A. S. Foster. Atomistic simulations of friction at an ice-ice interface. *Friction*, 1(3):242–251, sep 2013.

[301] N. Pertaya, C. B. Marshall, C. L. DiPrinzio, L. Wilen, E. S. Thomson, J. S. Wettlaufer, P. L. Davies, and I. Braslavsky. Fluorescence microscopy evidence for quasi-permanent attachment of antifreeze proteins to ice surfaces. *Biophys. J.*, 92(10):3663–73, may 2007.

[302] R. K. Kar and A. Bhunia. Will It Be Beneficial To Simulate the Antifreeze Proteins at Ice Freezing Condition or at Lower Temperature? *J. Phys. Chem. B*, 119(35):11485–11495, 2015.

[303] N. Zięb acz, S. A. Wieczorek, T. Kalwarczyk, M. Fiałkowski, and R. Hołyst. Crossover regime for the diffusion of nanoparticles in polyethylene glycol solutions: influence of the depletion layer. *Soft Matter*, 7(16):7181, 2011.

[304] C.-S. Wu. *Handbook Of Size Exclusion Chromatography And Related Techniques: Revised And Expanded*, volume 4. CRC Press, 2003.

[305] R. Y. Tam, S. S. Ferreira, P. Czechura, J. L. Chaytor, and R. N. Ben. Hydration Index: A Better Parameter for Explaining Small Molecule Hydration in Inhibition of Ice Recrystallization. *J. Am. Chem. Soc.*, 130(51):17494–17501, dec 2008.

[306] S. Kundu and D. Roy. Structural analysis of Ca2+ dependent and Ca2+ independent type II antifreeze proteins: A comparative molecular dynamics simulation study. *J. Mol. Graph. Model.*, 38:211–219, 2012.

[307] F.-H. Lin, L. A. Graham, R. L. Campbell, and P. L. Davies. Structural modeling of snow flea antifreeze protein. *Biophys. J.*, 92(5):1717–23, mar 2007.

[308] S. A. Bagherzadeh, S. Alavi, J. A. Ripmeester, and P. Englezos. Why Ice-Binding Type I Antifreeze Protein Acts as a Gas Hydrate Crystal Inhibitor. *Phys. Chem. Chem. Phys.*, 17(604):9984–9990, 2015.

[309] B. L. Pentelute, Z. P. Gates, J. L. Dashnau, J. M. Vanderkooi, and S. B. H. Kent. Mirror Image Forms of Snow Flea Antifreeze Protein Prepared by Total Chemical Synthesis Have Identical Antifreeze Activities. *J. Am. Chem. Soc.*, 130(30):9702–9707, 2008.

[310] D. H. Nguyen, M. E. Colvin, Y. Yeh, R. E. Feeney, and W. H. Fink. The dynamics, structure, and conformational free energy of proline-containing antifreeze glycoprotein. *Biophys. J.*, 82(6):2892–905, jun 2002.

[311] H. Nada and Y. Furukawa. Anisotropy in growth kinetics at interfaces between proton-disordered hexagonal ice and water: A molecular dynamics study using the six-site model of H2O. *J. Cryst. Growth*, 283(1-2):242–256, sep 2005.

[312] J. A. Hayward and A. D. J. Haymet. The ice/water interface: Molecular dynamics simulations of the basal, prism, {2021}, and {2110} interfaces of ice Ih. *J. Chem. Phys.*, 114(8):3713, 2001.

[313] J. R. Espinosa, E. Sanz, C. Valeriani, and C. Vega. Homogeneous ice nucleation evaluated for several water models. *J. Chem. Phys.*, 141(18):18C529, 2014.

[314] R. Politi, L. Sapir, and D. Harries. The impact of polyols on water structure in solution: a computational study. *J. Phys. Chem. A*, 113(26):7548–55, jul 2009.

[315] Z. Qin and M. J. Buehler. Carbon dioxide enhances fragility of ice crystals. *J. Phys. D. Appl. Phys.*, 45(44):445302, 2012.

[316] L. Corcilius, G. Santhakumar, R. S. Stone, C. J. Capicciotti, S. Joseph, J. M. Matthews, R. N. Ben, and R. J. Payne. Synthesis of peptides and glycopeptides with polyproline II helical topology as potential antifreeze molecules. *Bioorg. Med. Chem.*, 21(12):3569–81, jun 2013.

[317] M. D. Hanwell, D. E. Curtis, D. C. Lonie, T. Vandermeersch, E. Zurek, and G. R Hutchison. Avogadro: an advanced semantic chemical editor, visualization, and analysis platform. *J. Cheminform.*, 4(1):17, jan 2012.

[318] A. Wierzbicki, M. S. Taylor, C. A. Knight, J. D. Madura, J. P. Harrington, and C. S. Sikes. Analysis of shorthorn sculpin antifreeze protein stereospecific binding to (2-1 0) faces of ice. *Biophys. J.*, 71(1):8–18, jul 1996.

[319] V. S. Ananthanarayanan and C. L. Hew. Structural studies on the freezing-point-depressing protein of the winter flounder Pseudopleuronectes americanus. *Biochem. Biophys. Res. Commun.*, 74(2):685–689, jan 1977.

[320] C. J. Capicciotti, M. Leclère, F. A. Perras, D. L. Bryce, H. Paulin, J. Harden, Y. Liu, and R. N. Ben. Potent inhibition of ice recrystallization by low molec-

ular weight carbohydrate-based surfactants and hydrogelators. *Chem. Sci.*, 3 (5):1408, 2012.

[321] B. Wathen, M. Kuiper, V. Walker, and Z. Jia. A new model for simulating 3-d crystal growth and its application to the study of antifreeze proteins. *J. Am. Chem. Soc.*, 125(3):729–737, 2003.

[322] N. J. English. Massively parallel molecular-dynamics simulation of ice crystallisation and melting: The roles of system size, ensemble, and electrostatics. *J. Chem. Phys.*, 141(23):234501, 2014.

[323] A. H. Nguyen and V. Molinero. Identification of Clathrate Hydrates, Hexagonal Ice, Cubic Ice, and Liquid Water in Simulations: the CHILL+ Algorithm. *J. Phys. Chem. B*, 2014.

[324] S. J. Cox, S. M. Kathmann, B. Slater, and A. Michaelides. Molecular simulations of heterogeneous ice nucleation. I. Controlling ice nucleation through surface hydrophilicity. *J. Chem. Phys.*, 142(18):184704, 2015.